CHARACTERIZATION OF BACKGROUND NEUTRAL FLOWS IN VACUUM TEST FACILITIES AND IMPACTS ON HALL EFFECT THRUSTER OPERATION

A Dissertation
Presented to
The Academic Faculty

by

Jason David Frieman

In Partial Fulfillment
of the Requirements for the Degree
Doctor of Philosophy in Aerospace Engineering

Georgia Institute of Technology

August 2017

CHARACTERIZATION OF BACKGROUND NEUTRAL FLOWS IN VACUUM TEST FACILITIES AND IMPACTS ON HALL EFFECT THRUSTER OPERATION

Approved by:

Professor Mitchell Walker, Advisor
School of Aerospace Engineering
Georgia Institute of Technology

Dr. John Yim
Electric Propulsion Systems Branch
NASA Glenn Research Center

Professor Glenn Lightsey
School of Aerospace Engineering
Georgia Institute of Technology

Dr. Mark Crofton
Propulsion Science Department
The Aerospace Corporation

Professor Wenting Sun
School of Aerospace Engineering
Georgia Institute of Technology

Date Approved: May 3, 2017

Do or do not. There is no try.
-*Yoda*
Star Wars Episode V: The Empire Strikes Back

To my grandmother, Jackie, and Andy; gone, but never forgotten

ACKNOWLEDGEMENTS

Once during a STEM outreach event, a young student raised their hand and timidly asked me my grade level. After standing there stumped for a second, I began to calculate, and, at the time of writing this, I can proudly say I am in the 21st grade. I start with that anecdote not to underscore the number or years that went into this document and degree, but, rather to emphasize how many people I have interacted with over the past 21 years of education that have helped me get to this point, and, therefore, just how many people I have to thank for my name now ending in the letters "Ph.D."

I would first like to thank the members of my committee for their gracious service; without you, this literally would not have been possible. Thank you for taking the time out of your schedules to read this tome, listen to my presentation, and provide your feedback; I am certain that this research effort is stronger because of your efforts.

Amongst the committee members, the biggest thank you must go to my adviser, Professor Mitchell Walker. You once told one of the other lab members that you viewed grad school as weight training, and that you are our spotter; your job is to push us to make sure we can lift our maximum weight, but you are always there on standby to catch the bar and stop it from choking us should we hit our limits. A truer analogy about grad school has probably never been spoken. Thank you for taking me on as a student, finding funding when I needed it, pushing me to achieve my best, and always being there for advice along the way. I wish you all the best as you continue to grow the lab into one of the premier university EP research groups.

Supporting the committee and all of us in the department is one of the best groups of support staff that I have ever seen. Thank you to all of you (especially Tiwanna) for always being there to answer my questions and help me with everything from shipping to purchasing to reserving a room for my defense. Thank you to the National Science Foundation, the ARCS Foundation, ARCS Atlanta, and Lockheed Martin for your financial support. My relationships with these organizations have been deeply fulfilling and I could not have gotten to this point without their support.

The next round of acknowledgements goes to my many colleagues at HPEPL. To Gabe and Logan (aka "Lab Tyrant"), you started grad school with an empty corner of a warehouse and left with two working vacuum chambers, and, somehow, through it all you always found time to answer my questions and provide me advice, even after you graduated. Your mark on the lab will never be forgotten and all past, present, and future students owe you a tremendous debt of gratitude. Alex, thank you for showing me the finer points of MacGyvering and always being there with advice throughout my time as an undergrad. Lake, thank you for showing me the ropes when I was a know-nothing undergrad. The meaningful tasks you gave me, whether it was fixing the Bell Jars or running the CNCC experiments, got me hooked on lab work and gave me the foundation from which I still operate today. Scott, thank you for taking me under your wing when I transitioned into grad school and being so patient with me as I learned the finer details of building and running HETs. I still remember that first summer of grad school when you were there with me the whole way as I built, broke, and rebuilt the T-140 repeatedly. But, it finally worked, and when it did, you were there to teach me how to run it, take data, and write a paper.

Sam, whether you knew it or not, you were the soul of the lab while you were here. Your optimism and love of grad school were infectious and got us all through our worst days. You were always the first to volunteer to stay late with me as I was scrambling to get an apparatus built or a test finished and I probably learned more from your plasma thought experiments than I ever did reading textbooks. In fact, it was during one of those late nights that you uttered my favorite description of the life of an experimentalist. As we were waiting on the nitrogen system to cool down, you turned to me and said, "science is really just staring at dials and being upset with them." Looking back, I now realize just how true those words were. Natalie, if Sam was the soul of the lab, you were the personality. Your stories (both the true ones and the plots from the "show") are legendary. They brought much-needed levity as we toiled to get our experiments and/or chambers to work and are still among my favorite memories to recount to the younger students. Thank you to both of you and Jonathan for everything you did for me and the lab and best of luck to all of you out in the real world.

To the current crop of students (Connie Liu, David Jovel, and Nathan Brown) thank you all for your support as I finished out this crazy road that is grad school. Connie, I am confident the lab is in good hands under your leadership and I am sure you and the other baby ducks will safely make your way across the river of grad school. David, thank you for always being there with a smile, and, if needed, a horde of undergrads ready to tackle any problem. Nathan, thank you for all your support as an undergrad and I wish you the best of luck as you get your laser up and running. I am sure if you all stick together, you will not only survive, but thrive at HPEPL.

To the VTF-1 consortium, Eugina Mendez-Ramos and Nathan Prestridge, thank you for organizing and running the VTF-1 undergrad army and always being a set of friendly faces around the lab. I would be remiss if I did not acknowledge the contributions of all the lab undergrads (past and present). Although your names are too numerous to list, you each helped us all achieve so much, and for that, we all thank you.

Last, but certainty not least amongst my colleagues, is Dr. Thomas Liu. Your job as the resident "lab adult" is probably the hardest I have ever seen and you handle it with an amazing amount of grace. Whether it is dealing with an overheating diffusion pump, an underperforming cryogenerator, or an arcing HET, you are always there to provide calm advice and troubleshooting tips. You have been here with me through the entire roller coaster ride, starting with the "40-hour weekend" in which we went from nothing to a fully assembled and working HET, plasma diagnostics package, and cathode in less than 72 hrs and ending with the latest customer testing marathon. I have learned more from you than anyone else and I hope to be half as effective in my new job as you are in yours. Thank you for your constant advice, counsel, and friendship; without you I absolutely could not have made it here.

Although technically a professional/academic endeavor, anyone who has gone to grad school knows just how deeply it impacts all aspects of your life. As such, I would be remiss if I did not acknowledge all the support I received from friends and family. To all the current and past members of "Schoolhouse Spock" aka "Tyler Perry Presents Team Number Nine," Mel, Phil, Eric, Nathaniel, Aaron, Steve, Alyssa, Alisha, and Seth, playing trivia with you all has been a highlight of my week for as long as I can remember. Thank you for providing innumerable memories and laughs and for your friendship. To Jason

Zutty and Justin Davis, it is incredible to think that we met almost ten years ago when you guys took me out to Arby's. You guys have been my best friends since then and I cannot thank you enough for all the adventures and laughs we have shared throughout my time at Georgia Tech.

To my parents Jan and Ron Frieman, you always encouraged me to get an education and follow my dreams. And, in typical Jason fashion, I overdid it and here we are 21 grades later! I cannot thank you for your constant love, advice, support, and guidance. You provided me the best childhood and life anyone could ever hope for. To Nikki, you have been here with me at Tech through it all. Thank you for your love and friendship; you are going to kill it up in DC. To Aunt Nan, thank you for the best birthday present ever year after year. I will never forget my experiences in Augusta that were only possible because of you.

Last, but certainly not least, thank you to my wonderful girlfriend Suzie Heitfeld. Over the past four years, you have been there with me as I went on crazy three-month testing marathons, got called to the lab at 3 AM, and worked more weekends and nights than I can count. You have helped with more set-ups and pump downs than some graduates of HPEPL all while holding down a real job at the CDC. No matter what time of day, you were always there to listen and provide support and love. I love you and absolutely could not have done this without you. Thank you from the bottom of my heart and I look forward to our future in Cleveland!

TABLE OF CONTENTS

LIST OF TABLES

LIST OF FIGURES

NOMENCLATURE

AFRL	Air Force Research Laboratory
ARM	NASA Asteroid Retrieval Mission
A_c	collector area
A_{exit}	thruster exit plane area
B	magnetic field strength
$\bar{B}$	magnetic field
BA	Bayard-Alpert
CEX	charge exchange
CFM	cubic-feet per minute
e	elementary charge
EP	electric propulsion
$\bar{E}$	electric field
F_{S+}	mass flow rate crossing surface S moving in the positive direction
$f(V_{ion})$	ion voltage distribution
$f(v_i)$	ion velocity distribution
$FWHM$	full width at half maximum
g_o	gravitational constant
HET	Hall effect thruster
I_c	collector current
I_e	electron emission current
I_i	ion beam current

I_p	probe current
I_{sp}	specific impulse
JPL	NASA Jet Propulsion Laboratory
k	Boltzmann's constant
L_i	length of the ionizing space in a Bayard-Alpert hot-cathode gauge
LVDT	linear voltage differential transformer
LVTF	the Large Vacuum Test Facility at the University of Michigan
m	molecular mass of the background neutral
m_e	electron mass
m_f	final spacecraft mass
m_i	ion mass
m_o	initial spacecraft mass
m_{prop}	propellant mass
$\dot{m}$	net mass flow rate of gas
$\dot{m}_a$	anode mass flow rate
$\dot{m}_{ing}$	ingestion mass flow rate of the background neutrals
n	number density
n_b	background neutral number density
n_i	ion number density
n_j	ion number density of charge state j
n_r	number density of particles moving in the radial direction
n_S	number density of particles crossing surface S
n_{S+}	total number density of particles crossing surface S moving in the positive direction

n_{S+i}	number density of particles of population *i* crossing surface S moving in the positive direction
n_{S-i}	number density of particles of population *i* crossing surface S moving in the negative direction
NI	National Instruments
P	pressure
P_b	base pressure
P_c	corrected pressure
P_i	indicated pressure
P_o	stagnation pressure
P_∞	static pressure
PDF	probability density function
$p_{survival}$	kinetic survival probability
q	ion charge
q_{eff}	effective ion charge
q_j	charge of ion charge state j
RPA	retarding potential analyzer
R^2	coefficient of determination
S	surface area
S_c	chamber cross-sectional area
SEE	secondary electron emission
S_{ig}	ion gauge sensitivity factor
S_{pd}	total surface area of downstream pump surfaces
S_{pe}	total surface area of end dome pump surfaces

S_{pu} total surface area of upstream pump surfaces

s_d ratio of total surface area of the downstream pump surfaces to the chamber cross-sectional area

s_e ratio of total surface area of the end dome pump surfaces to the chamber cross-sectional area

s_u ratio of total surface area of the upstream pump surfaces to the chamber cross-sectional area

T gas temperature

T_b temperature of the background neutrals

T_e electron temperature

T_F thrust

T_i temperature of particles of population i

T_p pump surface temperature

T_w chamber wall temperature

$\bar{V}_{exit}$ average propellant exit velocity

V_{ion} effective ion voltage

V_{grid} ion repulsion grid voltage

V_i thermal-diffusive velocity of particles of population i

V_{mp} most-probable ion voltage

V_p probe voltage

V_s thermal-diffusive velocity of particles crossing surface S

v_i ion velocity

$\langle v_i \rangle$ average ion velocity

$v_{i,crit}$ critical ion velocity

Z	ratio of the background neutral bulk and thermal velocities
α	pump sticking coefficient
Δn	percent difference in the number densities detected between the upstream and downstream-facing ion gauge
Δn_{radial}	percent difference in the number densities detected between the radial and downstream-facing ion gauge
ΔV	velocity change imparted to a spacecraft
ΔV_{grid}	difference between electron repelling and ion retarding grid voltage
Δx	axial span of the grid region
θ	cone half-angle
λ	collisional mean free path
λ_d	Debye length
ν	total collision frequency
σ_i	ionization cross section
Φ	ingestion flux due to random motion of background neutrals
$\Phi_{incident}$	incident ion flux
ϕ	plume divergence half-angle
Ω_e	electron Hall parameter

SUMMARY

Hall effect thrusters (HETs) are a type of electrostatic electric propulsion device characterized by high specific impulses, thrust efficiencies, and thrust densities. These performance attributes make HETs an appealing choice for use as the primary propulsion system onboard a number of Earth-orbiting and interplanetary satellite missions. However, extensive ground testing of HETs has revealed that HET operation, performance, and plume properties are impacted by facility-dependent parameters such as pumping capacity. Specifically, it has been shown that increases in facility pressure result in artificial increases in device thrust and efficiency due to the ingestion of ambient background neutrals present in the vacuum facility. Although several analytical and semi-empirical models of HET neutral ingestion exist, none have been shown to be able to accurately predict empirical observations across a range of HETs and test facilities.

This work focuses on investigating the hypothesis that a bulk background flow of neutrals exists inside vacuum test facilities that varies as a function of facility-specific design and operating parameters (i.e., pump placement and pressure modulation technique) and contributes to HET neutral ingestion and the concomitant impacts on performance and plume characteristics. The first portion of this work determines if a bulk background flow exists inside ground test facilities, and characterizes how this flow field changes as a function of facility-specific parameters including pump placement. To do this, a general analytic model of the organized flow of background neutrals inside ground test facilities is created and validated using existing empirical measurements taken using several different facilities and HETs. This model is used to analytically determine the sensitivity of the

background flow field to facility variables including pump placement and pressure modulation technique. These studies are repeated empirically and confirm the accuracy of the model as well as the existence of the bulk background flow, its relationship to HET ingestion, and its sensitivity to facility operating parameters.

The second portion of this work seeks to quantify the impact of the background flow field (and concomitant neutral ingestion) on HET operation. Empirical measurements of the time-resolved discharge current, ion energy distribution, thrust, plume plasma properties, and ion current density profile of three HETs are performed and confirm the hypothesis that a full description of the background flow field can better explain the observed sensitivity of certain plume properties to changes in facility pressure than can pressure magnitude. Changes in the background flow field are shown to be unable to fully describe changes in discharge current oscillation characteristics, however, changes in facility pressure are shown to directly cause mode transitions, thus suggesting that optimal magnetic field settings may change between test facilities.

CHAPTER 1. INTRODUCTION

1.1 Electric Propulsion Overview

Primary spacecraft propulsion systems are responsible for the delivery of a given payload to its operational orbit and maintaining or modifying that orbit to prolong mission lifetime or achieve mission goals [1]. The propulsive capability required to complete each of these responsibilities is expressed in terms of the velocity increment (ΔV) that must be imparted to the spacecraft and can be computed as a function of the specific impulse (I_{sp}) of the propulsion system, the gravitational constant (g_o), the initial mass of the spacecraft before the propulsive maneuver (m_o), and the final mass of the spacecraft after the propulsive maneuver (m_f) using the ideal rocket equation shown in Eq. (1.1) [1]:

$$\Delta V = \mathrm{g_o} I_{sp} \ln\left(\frac{m_o}{m_f}\right) \tag{1.1}$$

The specific impulse shown in Eq. (1.1) is a measure of the energy content of the propellant and the efficiency of the process that converts energy into thrust [1]. It can be expressed as a function of the thrust of the propulsion system (T_F), mass flow rate of propellant ($\dot{m}$), and the average propellant exit velocity ($\bar{V}_{exit}$) as shown in Eq. (1.2) [1, 2]:

$$I_{sp} = \frac{T_F}{\dot{m} g_o} = \frac{\bar{V}_{exit}}{g_o} \tag{1.2}$$

Since the mass loss during a propulsive maneuver is due to the expulsion of propellant from the spacecraft, the initial mass of the spacecraft can be rewritten as the sum of the final mass and the expended propellant mass (m_{prop}). Furthermore, Eq. (1.1) can be rearranged to solve for the propellant mass required to complete a specified propulsive maneuver [1]:

$$m_{prop} = m_f \left[\exp\left(\frac{\Delta V}{g_o I_{sp}} \right) - 1 \right] \tag{1.3}$$

The relationship between specific impulse and required propellant mass expressed in Eq. (1.3) is illustrated for a 3,600 kg spacecraft with a 8,742 m/s required ΔV in Figure 1.1; these specifications are similar to those for the planned NASA Asteroid Retrieval Mission (ARM) [3]. As shown in Figure 1.1 and Eq. (1.3), propulsion systems with higher specific impulses can complete a given mission profile with exponentially reduced propellant masses, or, equivalently, spacecraft with a fixed propellant mass can achieve exponentially more ΔV. This reduction in required propellant mass also results in a concomitant reduction in mission costs for systems with higher specific impulses [1].

Historically, the majority of spacecraft propulsion systems have been comprised of chemical rockets [1]. These systems generate thrust by converting the chemical energy of the propellant to kinetic energy via combustion and subsequent flow expansion through a

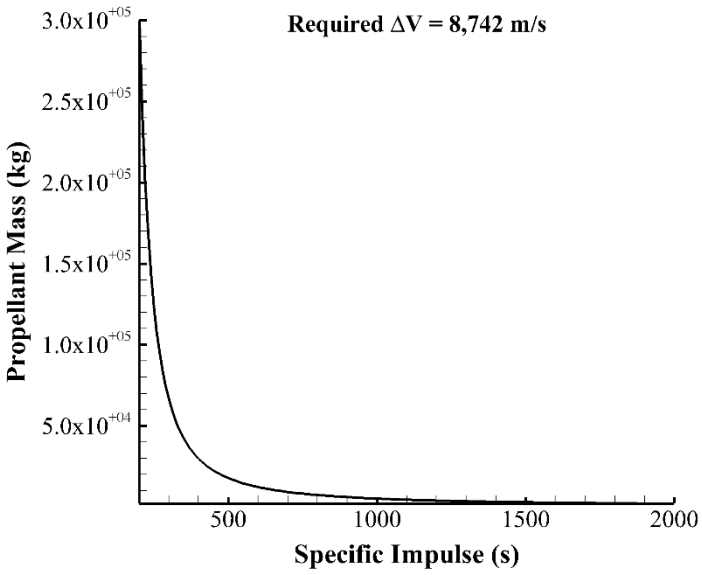

Figure 1.1: Propellant mass required by NASA ARM as a function of specific impulse.

nozzle [1]. The amount of energy that can be released by these systems is thus limited to the energy stored in the chemical bonds of the propellant. As such, the maximum specific impulses that these systems can achieve is limited to approximately 400 s [1].

By contrast, in electric propulsion (EP) systems, outside electrical energy is used to energize and/or accelerate the propellant, thus decoupling the thrust generation process from the chemical energy of the propellant [1, 2]. This removes the aforementioned performance limitation associated with chemical rockets and allows EP systems to achieve typical specific impulses of over 1,000 s [1]. As noted previously, this increase in specific impulse results in an exponential decrease in required propellant mass for a given mission or an exponential increase in propulsive capability for a given spacecraft. Thus, EP systems are an appealing choice for use as the primary propulsion system onboard a number of different satellite missions.

There are three general categories of EP systems. The first is electrothermal. In these systems a resistive heating element or arc is used to heat the propellant that is then expanded through a nozzle in order to generate thrust [1, 2, 4]. Examples of these types of devices are resistojets and arcjets [1, 2, 4]. The second category of EP systems is electromagnetic and includes magnetoplasmadynamic thrusters, pulsed inductive thrusters, and pulsed plasma thrusters [2, 4]. In these devices, the Lorentz force generated by perpendicular electric and magnetic fields is used to accelerate ionized propellant [2, 4]. The final category of EP device is electrostatic. In these systems, thrust generation is accomplished via the use of large electric fields to accelerate ionized propellant [1, 2, 4]. Prominent examples of this type of device are gridded ion engines and Hall effect thrusters (HETs) [1, 2, 4].

1.2 Hall Effect Thruster Overview

In comparison to ion engines, the high thrust density provided by HETs make them a particularly appealing choice for use as the primary propulsion system onboard a number of commercial and government Earth-orbiting satellite missions and has increasingly made them prime candidates for more ambitious deep space missions [3]. A schematic of a typical HET is shown in Figure 1.2. It is important to note that this schematic is for a magnetic-layer-type HET. This configuration has long insulating ceramic channel walls relative to the channel width [5]. There is also another type of HET known as the anode layer type. This configuration has short conductive walls relative to the channel width [5]. Unless otherwise stated, all HETs referenced in this work are of the magnetic layer type.

During HET operation, an axial electric field ($\bar{E}$) is established between the device anode and an external cathode. Electrons emitted by the cathode are drawn by the resulting electrostatic gradient into the HET discharge channel and towards the anode. During this transit, the electrons encounter a radial magnetic field ($\bar{B}$) generated by a set of electromagnetic coils and guided by a magnetic circuit composed of ferromagnetic pole pieces. The impact of the magnetic field on the motion of the cathode electrons can be described using the electron Hall parameter (Ω_e). The Hall parameter is defined as a function of the elementary charge (e), magnetic field strength (B), electron mass (m_e), and the total collision frequency (ν) in Eq. (1.4) [2, 6]:

$$\Omega_e = \frac{eB}{m_e \nu} \tag{1.4}$$

Overall, the magnetic field causes the electrons to undergo cyclotron motion. The electron Hall parameter is a measure of the number of gyroradii completed around a magnetic field

line by an electron during this cyclotron motion per collision with a neutral atom, ion, or the channel walls [2, 6]. As cross-field motion of the electron towards the anode is enabled by these collisions, the higher the electron Hall parameter, the smaller the electron mobility towards the anode [7].

In HETs, the magnetic field strength is chosen such that the electron Hall parameter is large (i.e., $\Omega_e^2 >> 1$) but the ion Hall parameter is small. The magnetic field thus prevents the electrons from traveling towards the anode without first undergoing a collision with the wall or another particle, but does not impact the motion of the ions in the channel [2, 5]. Furthermore, the orthogonal orientation of the applied electric and magnetic fields causes an azimuthal drift of electrons in the azimuthal or $\bar{E} \times \bar{B}$ direction; this azimuthal electron drift is known as the Hall current [2, 5].

As shown at location one in Figure 1.2, neutral propellant is injected into the discharge channel by the anode; typically, the anode also serves as the propellant distributor in HETs. During its transit through the channel, the neutral propellant encounters the Hall current and collides with the trapped electrons as shown at location two in Figure 1.2. This collision ionizes the propellant atom. As shown at the bottom of Figure 1.2, the reduced axial electron mobility caused by the imposed radial magnetic field permits the generation of strong electric fields in the plasma. This causes the majority of the potential drop between the anode and near-field plasma potential to occur near the region of maximum magnetic field strength (i.e., near the ionization zone) [5]. The newly created ion is thus accelerated by this potential gradient and expelled from the device to generate thrust as shown at location three [2, 5].

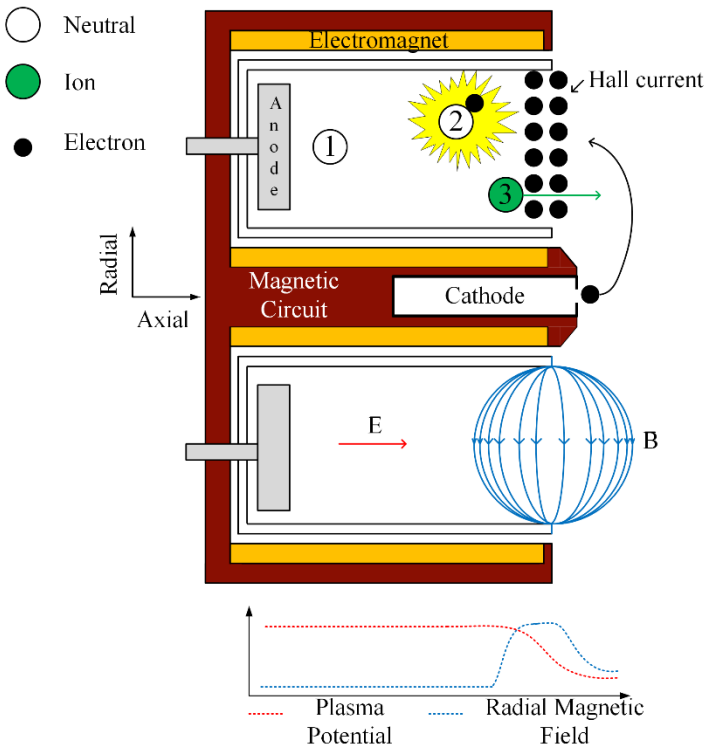

Figure 1.2: Schematic of a typical HET (not to scale).

1.3 Motivation

1.3.1 Previous Work on Facility Effects

The growth in interest and popularity of HETs has been driven by the aforementioned performance attributes and has caused a corresponding increase in the quantity of vacuum facilities engaged in HET research and testing. Despite the physical similarities among the HETs operated and characterized at each of these facilities, the wide range of facility geometries, sizes, materials, and pumping capacities have been shown to make it difficult for researchers to compare data sets without including facility-dependent corrections [8]. Therefore, it is necessary to develop an understanding of how to quantify ground-based vacuum facility effects on measured HET operation, performance, and plume

characterization so that facility-dependent testing artifacts can be corrected for and a facility-independent understanding of device performance can be achieved.

In general, there are two broad categories of HET-facility interactions. The first is the electrical coupling between the HET plasma and the conductive walls of the test facility. Previous work has shown that the facility walls collect a significant fraction of the discharge current, and as such, act as an alternate recombination site for plume ions and electrons that have not undergone recombination prior to reaching the facility walls [9, 10]. Current collection by the facility walls could significantly alter the path of the electrons in the plume by serving as an alternative lower resistance pathway (as compared to transit through the plasma plume) [9, 10]. This alternate pathway is an artificial effect introduced by the presence of the vacuum facility and is expected to be absent on orbit. Thus, any process dependent upon the path of the electrons through the plasma (including plasma reactance and resistance) may be significantly different between ground operation and operation on orbit [9–13].

The second type of identified facility effect is the impact of facility backpressure on plume properties and device operation. Previous studies have shown that increases in facility pressure result in artificial increases in device thrust and efficiency [2, 14–29]. Work has also been conducted linking background pressure to parasitic facility effects caused by resonant charge exchange (CEX) collisions. Specifically, studies have shown that higher facility pressures lead to increased CEX collisions. These collisions, in turn, introduce additional plume components and artificially increase the ion current density measured by Faraday probes in the regions of the HET plume at large angles with respect to thruster centerline [14, 30–32]. Finally, more recent work has indicated a link between

facility pressure and the ionization and acceleration processes within the HET itself. The ionization and acceleration zones have been observed to shift upstream in the channel with increasing background pressure. This shift has been accompanied by an increase in the number of multiply-charged ion species in the HET plume, a broadening of the plume ion energy distribution, and an increase in the characteristic frequency related to the ionization processes in the HET [15, 18–20, 28, 33].

In many of these previous studies, the observed changes in HET performance have been attributed to the ingestion, and subsequent ionization and acceleration, of background neutrals in the vacuum facility due to the random flux of these neutrals across the exit plane of the thruster [16, 17, 21, 23, 25, 29]. In this model (hereafter referred to as the thermal model), the corresponding ingestion flux of background particles (Φ) can be expressed as a function of Boltzmann's constant (k) as well as the number density (n_b), temperature (T_b), and molecular mass of the background neutrals (m) using the following equation [16, 17, 21–23, 29]:

$$\Phi = \frac{1}{4} n_b \left(\frac{8kT_b}{\pi m} \right)^{\frac{1}{2}} \tag{1.5}$$

The corresponding ingested mass flow rate of neutrals into the HET ($\dot{m}_{ing}$) can then be found by multiplying the ingestion flux from Eq. (1.5) by the molecular mass of the background gas and the thruster exit plane area (A_{exit}) as done in Eq. (1.6) [21, 29]:

$$\dot{m}_{ing} = \Phi m A_{exit} \tag{1.6}$$

In Eq. (1.5), the number density of the background neutrals is most often found via in-situ pressure measurements, thus linking the ingested neutral flux to the facility background pressure [16, 17, 21, 23, 25, 29].

The thermal model has been successfully applied to explain trends observed in early empirical measurements of the SPT-100 HET and was used to generate the recommendation that all HETs should be tested at a facility pressure below 5.0×10^{-5} Torr in order to keep neutral ingestion below the threshold required to generate reliable predictions of in-orbit performance [21, 25]. However subsequent investigations with different HETs in different facilities have shown that the results generated by the thermal model underpredict the empirically-observed changes in discharge current for cases with constant anode mass flow rate [16, 17, 22–24, 29]. The thermal mode has also been shown to underpredict observed changes in the required anode mass flow rate to achieve a fixed discharge current or thrust [16, 17, 22–24, 29]. Specifically, previous studies have shown that the ingestion mass flow rates predicted by the thermal model are 2-14 times too small to account for the empirically-observed changes in discharge current, required anode mass flow rate, or thrust and have been unable to provide insight into the observed changes in ionization and acceleration characteristics with changing background pressure [15, 18, 19, 22, 24, 28, 29].

These underpredictions have prompted proposals replacing the exit plane area in Eq. (1.6) with an empirically-determined larger effective ingestion area to account for ionization and acceleration of background neutrals in regions of the near-field plume where the electron temperature is still high enough to ionize neutral gas [19, 22, 23]. This approach has been disputed because it relies on the assumption that neutrals ingested across a reference surface in the plume are ionized and accelerated equivalently to neutrals supplied through the HET gas distributor [15, 23]. Other proposals suggest using empirical techniques to compute neutral ingestion by HETs. In these techniques, empirically-

measured changes in discharge current as a function of pressure are used to approximate the neutral ingestion mass flow rate [29].

A final set of proposals attributes the observed shortcomings in the thermal model to variations in the type and location of the gauges used to measure facility pressure [34, 35]. Previous empirical work has shown that the pressure inside the ground test facility varies spatially during HET operation [32, 36]. Thus, variations in pressure gauge placement relative to the thruster could result in concomitant variations in measured background pressures, and, thus in the computed ingestion mass flow rates using the thermal model [34, 35]. This final set of proposals seeks to eliminate these variations by standardizing the selection and placement of pressure probes during HET testing so that the measured pressure is the one most relevant for quantification of the impact of facility backpressure on HET operation [34, 35].

However, application of any of the aforementioned approaches requires the acquisition of empirical measurements and, thus, does not provide any ability to predict neutral ingestion characteristics *a priori*. Furthermore, although these approaches have been successfully applied to data taken with individual HET and facility combinations, they have not been shown to be broadly applicable across multiple devices and facilities [15, 23]. These shortcomings prevent the accurate determination of HET neutral ingestion and hinder the ability to accurately gauge changes in HET operating characteristics as a function of ingestion mass flow rate [16, 17, 22–24, 29].

1.3.2 Previous Work on Background Neutral Flows

In addition to the aforementioned shortcomings, the thermal model assumes that all motion of background neutrals is random (i.e., thermal) in nature. However, previous work

modeling the rarefied background flow inside a HET test facility found that the background neutrals could not be treated simply as a static gas field with only thermal velocity components [37, 38]. Instead, an organized background flow field was found to exist within the test facility during HET operation and that background neutrals achieved bulk axial velocities of over 100 m/s [37, 38]. These models were successfully used to replicate the empirically-observed spatial pressure distribution within the Large Vacuum Test Facility (LVTF) at the University of Michigan as well as the VF-5 vacuum facility at NASA Glenn Research Center.

The presence of an organized background flow within the facility has been independently supported by empirically-observed changes in pressure measurements as a function of the orientation of the gauge inlet within the facility [15, 39]. These works attributed these changes to an additional "dynamic pressure" within the facility caused by the bulk motion of background neutrals in a direction parallel to the thrust vector (i.e., in the HET axial direction) [15, 39]. However, as of yet, this bulk motion of background neutrals has not been studied, and, as such, the impact of facility design parameters such as pump placement on the background flow field is not known. Furthermore, despite the fact that this bulk axial motion of background neutrals is in the proper orientation for HET ingestion, these concepts have not been applied to assess the potential impact that the bulk flow of background neutrals could have on HET neutral ingestion or on explaining previously-acquired HET facility effects data.

1.4 Research Goals and Methodology

The hypothesis of this work is that a bulk background flow of neutrals exists inside vacuum test facilities and changes as a function of facility-specific design and operating

parameters (e.g., pump placement and pressure modulation technique). It is further hypothesized that this bulk background flow, in addition to the random flux of background neutrals, is a non-negligible contributor to HET neutral ingestion and the concomitant impacts on performance and plume characteristics.

The overall goal of this work is to test this hypothesis both analytically and empirically. From this overarching goal, it is possible to distill the research goals of this work into finding the answers to two overarching questions (RQ 1 and RQ 2) and two corollary questions (RQ 1A and RQ 1B):

RQ 1: Do bulk motions constitute a non-negligible component of the background neutral flow field inside vacuum facilities?

RQ 1A: Are the bulk motions sensitive to facility-specific parameters such as pump placement and pressure modulation technique?

RQ 1B: Do the bulk motions constitute a non-negligible component of the HET ingestion flow?

RQ 2: How does HET operation change as a function of ingestion mass flow rate (instead of pressure measured at a given location)?

First, in order to determine the answers to RQ 1, RQ 1A, and RQ 1B, an analytical model capable of simulating the bulk background neutral flow in ground test facilities with different physical geometries and pump placements is developed in Chapter 2. In Chapter 3, the model-predicted bulk mass flow rates of neutrals into a given HET (i.e., across a given surface in the facility) are compared against several existing empirical data sets taken using a variety of different HETs and vacuum test facilities. These comparisons are used to determine if the flux caused by the bulk background flow matches existing empirical

observations, and, thus, if these bulk motions constitute a non-negligible component of the background neutral flow field within the test facility and the neutral ingestion flow into HETs. Once validated against these empirical measurements, the background flow model is used to assess the sensitivity of the background flow field to facility-dependent parameters including pump placement and pressure modulation technique to analytically test the stated hypothesis that these bulk motions are sensitive to these parameters.

In Chapter 5, an additional set of empirical measurements of the bulk background flow are acquired as facility variables such as pump placement and pressure modulation technique are varied. These data are used to further validate the ability of the background flow model to predict these sensitivities and provide empirical evidence to determine if a bulk background flow exists, and, if so, how it varies as a function of facility-specific parameters. The results from this portion of the work provide the first experimentally-derived insight into the bulk motions of the rarefied gas flow field inside finite vacuum vessels, how these motions change as a function of facility design and operation, and how they impact HET ingestion, thus providing analytic and empirical answers to RQ 1, RQ 1A, and RQ 1B. Although presented with a focus on HET testing, the impact of these findings is far-reaching due to the ubiquitous presence of vacuum facilities in a variety of fields including materials processing.

The work presented in Chapters 3 and 5 provides empirical measurements of the ingestion mass flow rate into HETs as well as an analytic method of predicting these mass flow rates as a function of facility design and operation. The second portion of this work, described in Chapter 6, seeks to determine how HET operation changes as a function of the ingestion mass flow rate directly, in contrast to the previously-employed method of

correlating these changes to the facility background pressure. The background flow field (and thus the ingestion mass flow rate into the HET) is adjusted by varying the number of active cryopumps and introducing a bleed flow of propellant while the time-resolved discharge current, thrust, ion voltage distribution, ion current density profile, and plume plasma properties of the HET are measured. The variation in ion voltage distribution, thrust, and discharge current characteristics such as breathing mode frequency are used to directly quantify the impact of the changing background flow on the ionization and acceleration processes in the HET. The variation in ion current density profiles and plume plasma properties quantifies the effect of the background flow on the HET plume. These data characterize how HET operation changes as a function of ingestion mass flow rate (instead of the pressure measured at a given location) and, thus, enables a better understanding of the observed sensitivity of HETs to the pressure environment within the vacuum test facility. These results also serve to help determine the minimum test conditions required to minimize facility effects and maximize the fidelity of ground-based testing, thus providing answers to RQ 2.

CHAPTER 2. BACKGROUND FLOW MODEL DEVELOPMENT

2.1 Overview of HET Vacuum Test Facilities

Figure 2.1(a) shows a schematic of a typical vacuum test facility used for HET testing. These test facilities are usually stainless-steel cylindrical vacuum chambers measuring 4 m or more in length and 2 m or more in diameter equipped with cryopumps in order to achieve and maintain operating pressures on the order of 10^{-5} Torr or less [9, 15, 30, 35, 37]. The cryopumps operate by cooling a plate or series of plates to an operating temperature of approximately 15 K using gaseous helium [37]. When incident particles strike the pump surface, a fraction of the particles is condensed onto to the pump surface while the remaining particles reflect with a thermal speed characterized by the pump surface temperature [37]. The probability that incident particles are condensed on the pump surface is known as the sticking coefficient (α), with the probability that an incident particle reflects off the pump expressed as 1-α [37]. Thus, the sticking coefficient is a metric of pump performance and quantifies how effectively the pumps act as sinks of neutral particles from the background flow field [37]. The number and location of these pumps varies between different facilities as does the facility geometry [10, 15, 37].

In operation, a HET is mounted inside the vacuum facility to a test stand typically located at one end of the facility. A low-density plasma flow (i.e., the HET plume) is exhausted from the HET in the axial direction towards the downstream end of the facility. Although some of the emitted ions and electrons recombine prior to striking the downstream facility surfaces, the ion-electron recombination mean free path is generally longer than the characteristic axial facility dimensions, thus, most of these charged particles

strike the downstream facility surfaces, recombine, and reflect as neutrals with a thermal speed characterized by the chamber wall temperature [9, 10, 37]. Upon reflection, these neutrals are then able to traverse the vacuum facility until they strike and are condensed on one of the cryopumps. This motion of neutrals through the vacuum facility is known as the background neutral flow and is the focus of this model.

2.2 Assumptions and Basic Relations

2.2.1 Assumptions

In order to model the flow environment described above, several simplifying assumptions were made. These assumptions, as well as the corresponding justifications underlying them, are detailed below.

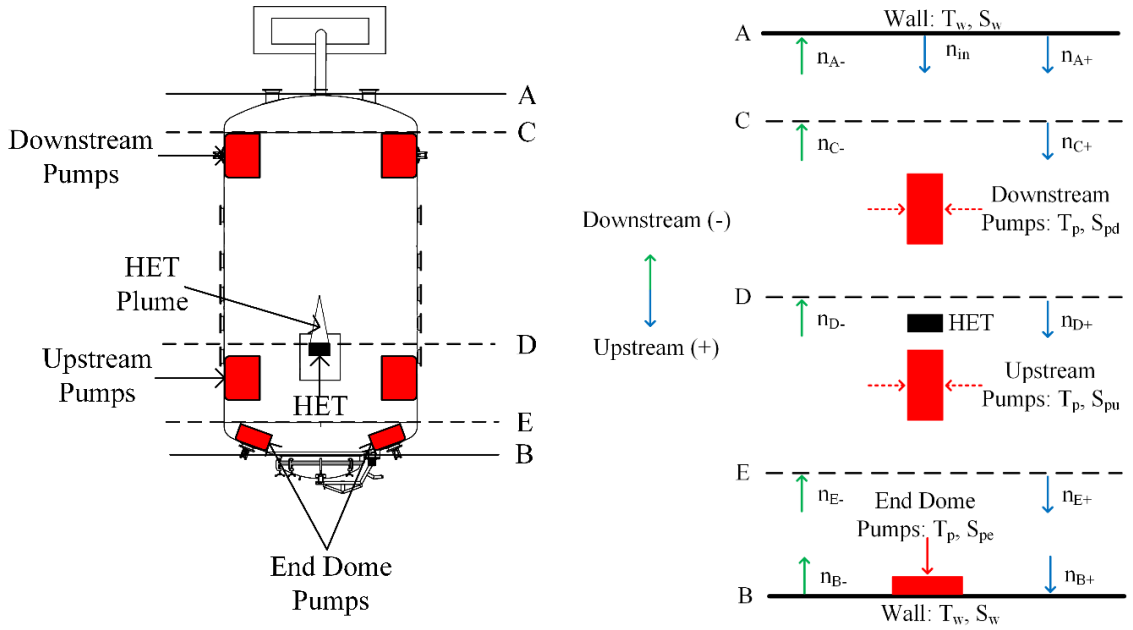

(a) **(b)**

Figure 2.1: (a) Schematic and (b) background flow model representation of a typical HET test facility.

The first set of assumptions concerns the background flow environment. First, it is assumed that the background flow in the test facility is in the free molecular regime (i.e., the mean free path of the background neutrals is larger than the facility length). Previous work has shown that, because HET test facilities typically operate at pressures of 10^{-5} Torr-Xe or below, the Knudsen number (i.e., the ratio of the mean free path to the facility length) in these facilities is of order unity [37]. This is well within the range considered to be characteristic of a free molecular flow environment [40]. It is also assumed that the background flow is one-dimensional along the thrust axis of the HET. This assumption is consistent with previous studies into background neutral flows that have yielded good agreement with more complex numerical simulations and empirical measurements [37, 41]. The accuracy of the 1-D assumption is further examined in Section 3.3. Finally, it is assumed that the background flow is in thermodynamic equilibrium. This implies all variables that impact the background flow (i.e., the temperatures of the chamber wall and pump surfaces as well as the anode mass flow rate) are in steady-state. This restricts the model to predictions of time-averaged ingestion mass flow rates. This restriction is appropriate for this model as the focus is on replicating empirical results acquired on the time scale of seconds to minutes (i.e., measurements of average discharge current and thrust) and not on the oscillation characteristics of HETs that occur at characteristic frequencies on the order of 20 kHz [33]. It is also important to note that this assumption is only strictly valid for facilities in which the pumping surfaces (or other non-wall temperature surfaces) do not occupy a significant fraction of the chamber area, as is the case for the majority of HET test facilities [9, 15, 30, 35, 37].

The next set of assumptions pertains to the vacuum test facility. Within the model, the chamber wall temperature and pump surface temperature are assumed to be constant and equal to 300 K and 15 K, respectively. For this work, the term "pump surface temperature" refers to the temperature of the helium cryosail and not the temperature of any liquid-nitrogen-cooled shrouds. The assumed pump surface temperature is consistent with reported empirical measurements in HET test facilities [30]. Furthermore, all cryopumps are assumed to have a constant sticking coefficient of 0.4. It is important to note that typical values for the sticking coefficient of noble gases on bare cryogenic panels are typically within a range of 0.6 to 0.8 [42]. However, since the pumps installed in many HET test facilities are surrounded by liquid-nitrogen-cooled, louvered shrouds, the effective sticking coefficient for these pumps can be lower than the values achieved for a bare cryosurface; the assumed sticking coefficient of 0.4 is in agreement with previous analytical and empirical studies of cryosurfaces with louvered shrouds [30, 37]. The sensitivity of the model to these assumptions are assessed in Section 3.2.5.

The final set of assumptions concerns the behavior of the individual particles composing the HET plume and background flow. First, it is assumed that neutrals fully accommodate to the surfaces they strike and reflect specularly. Previous analysis has shown that the differences in results generated between diffuse and specular reflection assumptions are small; thus the impact of this assumption is expected to be minor [41]. Next, it is assumed that all particles injected into the HET anode travel unimpeded to the downstream facility surfaces, thermalize, and reflect. Thus, the downstream facility surfaces are considered as a source of neutral xenon entering the chamber at the thruster anode mass flow rate, through the chamber cross-sectional surface area, and at the wall temperature. This assumption is

consistent with previous work into background flow modeling in HET test facilities [37]. It is furthermore supported by empirical measurements of the velocity distributions within HET plumes; these measurements show that both ions and neutrals exhausted by the HET have large axial velocity components in the direction of the downstream chamber surfaces [43]. Further empirical evidence indicates that the majority of the ions are unlikely to undergo a recombination collision prior to reaching the downstream facility surfaces [10]. Thus, the most likely pathway for these particles to begin traveling back towards the thruster is by reflection from the downstream facility surfaces. It is nevertheless important to note that this assumption does not capture two processes present in facilities with downstream pumping surfaces. First, it does not capture the loss of unionized propellant exhausted by the HET due to contact with pump surfaces during the initial transit from the HET to the downstream facility surfaces. Second, it does not capture the effective reduction in chamber area caused by the shadowing of these downstream surfaces by the cryopumps. Fortunately, these processes have offsetting effects on the number density. Specifically, the first process reduces the effective inflow number density while the second increases it. Furthermore, as typical HET mass utilization efficiencies are on the order of 90%, this oversight only impacts a very small percentage of the HET propellant flow [2].

Finally, it is assumed that the HET plume flow collisionally scatters background flow neutrals traveling towards the HET exit plane. The only collisions that are considered are the elastic collisions between the background neutrals and the unionized propellant exhausted by the HET. The collisional cross-sections are computed using models employed in previous HET plume models [44]. In order to compute the cross-sections, it was assumed that the neutral density at the exit plane of all HETs was approximately 1×10^{18} m^{-3}; this

estimate is taken from previous empirical measurements using the 1.5-kW SPT-100 and 5-kW P5 HETs, both of these thrusters are used as points of comparison for this work [32, 44]. The neutral density is furthermore assumed to follow an inverse-square dependency; this variation is derived by modeling the neutral density as the isotropic emissions of a rarefied flow from a disk with a diameter equal to the thruster exit area and is commonly applied in HET plume models [2]. The velocity of plume neutrals is taken to be approximately 200 m/s, consistent with previous empirical measurements [43]. It is important to note that the large relative velocity (i.e., greater than 20,000 m/s) between the ions exhausted by the HET and the neutral background flows results in an elastic collisional cross-section more than an order of magnitude smaller than the computed cross-section for the elastic collisions between the background neutrals and the unionized propellant exhausted by the HET; thus this ion-neutral collision process is ignored for this work. No additional considerations of conductance losses or equivalent processes are included in the model beyond the described collisional scattering effects.

2.2.2 Basic Relations

Before the background flow model can be mathematically developed, a few basic relations regarding the flow of rarefied gas in equilibrium must be presented. The net mass flow rate ($\dot{m}$) of a rarefied gas at rest across a surface in one direction for a one-dimensional flow is given by Eq. (2.1):

$$\dot{m} = m n_S S \sqrt{(8kT)/(\pi m)}\,/4 = m n_{S+} S \sqrt{(2kT)/(\pi m)} \tag{2.1}$$

where S is the area of the surface, T is the temperature of the particles crossing the surface, and n_{S+} is the number density of particles crossing surface S moving in the positive direction (equal to half the total number density of particles at the surface as there are only

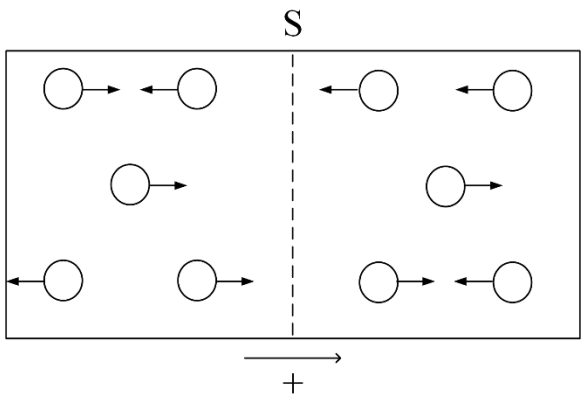

Figure 2.2: One-dimensional motion of a rarefied gas.

two potential directions of motion), and all other variables retain their meaning from previous equations [37]. The situation described by Eq. (2.1) is illustrated in Figure 2.2. For convenience, the simplified thermal-diffusive velocity term (V_s) from Eq. (2.1) will be defined as shown in Eq. (2.2):

$$V_S = \sqrt{(2kT)/(\pi m)} \tag{2.2}$$

Finally, from the law of mass conservation and Eq. (2.1), the number of particles of incoming temperature (T_1) reflected from a surface at a different temperature (T_2) is given by Eq. (2.3) [37]:

$$n_1\sqrt{T_1} = n_2\sqrt{T_2} \tag{2.3}$$

In Eq. (2.3), n_1 is the number density of the incoming particles and n_2 is the number density of the reflected particles.

2.3 Model Development

Using the assumptions from Section 2.2, the typical HET test facility shown in Figure 2.1(a) is transformed into the one-dimensional background flow model shown in Figure

2.1(b). In order to help correlate the model to the test facility, identical reference surfaces are drawn on both the schematic of the HET chamber shown in Figure 2.1(a) and the model representation in Figure 2.1(b). These reference surfaces demarcate the different chamber regions of interest: the downstream wall region is located between surfaces A and C, the downstream pump region is located between surfaces C and D, the upstream pump region is located between surfaces D and E, and the end dome pump region is located between surfaces E and B. For this work, the dividing line between the upstream and downstream regions is the HET exit plane. In other words, all pumps located downstream of the HET exit plane and not on the end domes of the vacuum test facility are considered to be in the downstream pump region while those located upstream of the HET exit plane and not on the end domes of the vacuum test facility are considered to be in the upstream pump region. As shown in Figure 2.1(b), because this is a one-dimensional model, the number density of particles (and the corresponding flux) crossing each of these surfaces can be further decomposed into an upstream (i.e., positive) and downstream (i.e., negative) component.

The analytical model needed to compute the ingestion mass flow rate due to the background neutral flow is built from the identified assumptions, basic relations, and modeling domain. In order to arrive at this final solution, expressions for the flux and number density of background neutrals crossing each of the surfaces in both directions need to be obtained. These expressions can then be combined into a system of equations that can be solved for the ingestion number density (n_{D^+}) and mass flow rate (F_{D^+}). The model will be presented region-by-region in order to explicitly show the unique aspects associated with each type of region. Furthermore, the resulting equations will compose a

toolkit that can readily be applied to build a model of any facility geometry or pump configuration.

2.3.1 Pump Regions

The model development starts by examining the flow environment in the upstream and downstream pump regions. There are three potential outcomes for background particles that enter a pump region: 1) the particles can proceed unimpeded through the region and exit at the temperature at which they entered, 2) the particles can strike a pump and condense, that removes them from the flow, or 3) the particles can strike a pump and reflect at the pump temperature. These outcomes are shown in Figure 2.3. Thus, the mass flow rate of particles of population *i* exiting the pump region (F_{D+_i}) can be written as [37]:

$$F_{D+_i} = mS_c n_{C+_i} V_i - m\, S_{p_d} n_{C+_i} V_i + (1-\alpha) n_{C+_i} S_{p_d} m V_p \sqrt{T_i/T_p} \qquad (2.4)$$

Note that Eq. (2.4) is written using the flux across surface D in the positive direction as an example exit surface from a pump region. In Eq. (2.4), S_c is the chamber cross-sectional area, S_{p_d} is the total surface area of cryopumps located in the relevant pump region (for this example it would be the downstream pump region), n_{c+_i} is the number density of particles of population *i* entering the pump region (for this example, it is the number density of particles of population *i* crossing surface C in the positive direction), V_i is the thermal-diffusive speed characterized by the temperature of particles of population *i* (T_i), V_p is the thermal-diffusive speed characterized by the pump surface temperature (T_p), and all other terms retain their meanings from previous expressions.

Each of the summation terms in Eq. (2.4) represents one of the possible outcomes discussed above. The first term represents all particles that entered the pump region, the

second term represents the particles that struck a pump surface, and the third term represents the fraction of particles that struck a pump surface, but did not condense and instead reflected at a thermal-diffusive speed characterized by the pump surface temperature. The difference between the first and second term thus represents the particles that traversed the pump region unimpeded. Finally, it is important to note that Eq. (2.4) is also written for a single population of particles (i.e., a group of neutral characterized by a single velocity). If additional populations are entering the pump region, then Eq. (2.4) would be applied to each population and the total exit mass flow rate would be equal to the sum of the exit mass flow rates for each population. Such a situation could arise for adjacent pump regions (i.e., the upstream and downstream pump regions for a chamber similar to the one shown in Figure 2.1(a)) as, after traversing the first pump region, the flux entering the second pump region would be composed of a population of particles at the original entry temperature and another at pump surface temperature made up of those particles that struck but were not trapped by a pump in the first pump region.

The number density of particles of population i exiting the pump region (n_{D+_i}) can similarly be written as [37]:

$$n_{D+_i} = (1 - s_d)n_{C+_i} + (1 - \alpha)n_{C+_i}s_d\sqrt{T_i/T_p} \tag{2.5}$$

In Eq. (2.5), s_d is the ratio of pump surface area to facility cross-sectional area in the region of interest and all other terms retain their meaning from previous expressions. The first term of Eq. (2.5) represents the number density of particles that proceeded unimpeded through the pump region while the second is the number density of those that reflected from a pump and are now moving at a thermal-diffusive speed characterized by the pump surface temperature. As with Eq. (2.4), Eq. (2.5) is written for a single population of

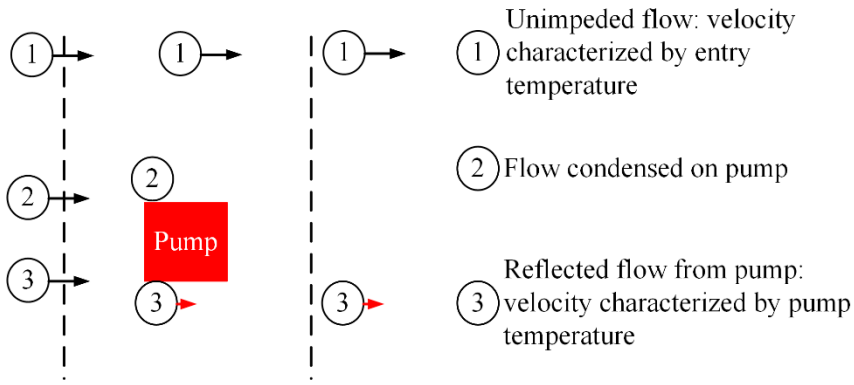

Figure 2.3: Three potential outcomes for particles in pump regions.

particles, the total exit number density would be equal to the sum of the number densities for each population.

2.3.2 Wall Regions

The next class of regions to consider are wall regions without end dome pumps. Such a region is shown between surfaces C and A in Figure 2.1(b). All particles entering this region strike the facility walls, thermally accommodate to the facility wall, and then reflect with a thermal-diffusive speed characterized by the facility wall temperature. This process is shown in Figure 2.4. The resulting exit mass flow rate can be expressed as [37]:

$$F_{C+_i} = mS_c n_{A-_i} V_w \sqrt{T_i/T_w} \tag{2.6}$$

The corresponding exit number density is [37]:

$$n_{C+_i} = n_{C-_i} \sqrt{T_i/T_w} \tag{2.7}$$

In Eq. (2.6) and Eq. (2.7), V_w is the thermal-diffusive speed characterized by the temperature of the chamber wall (T_w) and all other variables retain their meaning from previous expressions. As with Eq. (2.4) and Eq. (2.5), both Eq.(2.6) and Eq. (2.7) must be

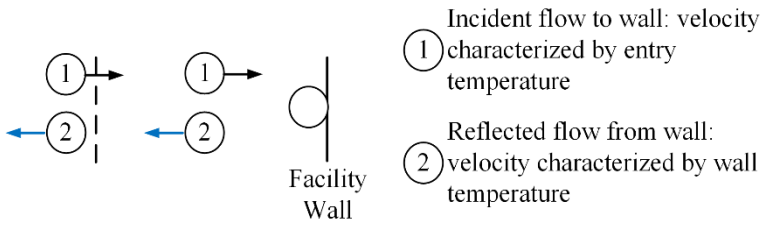

Figure 2.4: Illustration of outcome for particles in wall regions.

applied to all populations present and the total mass flow rates and number densities will be the sum of the contributions of all populations and any source terms.

2.3.3 End Dome Pump Regions

The final type of facility region is an end dome pump region. Such a region is shown between surfaces E and B in Figure 2.1(b). Particles entering this region can either: 1) strike and thermally accommodate to the facility wall then reflect with a thermal-diffusive speed characterized by the facility wall temperature, 2) strike an end dome pump and condense, or 3) strike and thermally accommodate to an end dome pump then reflect with a thermal-diffusive velocity characterized by the pump surface temperature. These outcomes are illustrated in Figure 2.5. Thus, the number density of particles of population *i* exiting the end dome pump region (n_{E-_i}) can be written as:

$$n_{E-_i} = (1 - s_e) n_{E+_i} \sqrt{T_i / T_w} + (1 - \alpha) n_{E+_i} s_e \sqrt{T_i / T_p} \tag{2.8}$$

In Eq. (2.8), s_e is the ratio of pump surface area to facility cross-sectional area in the end dome pump region and all other terms retain their meaning from previous expressions. The first term of Eq. (2.8) represents the number density of particles that strike the facility wall

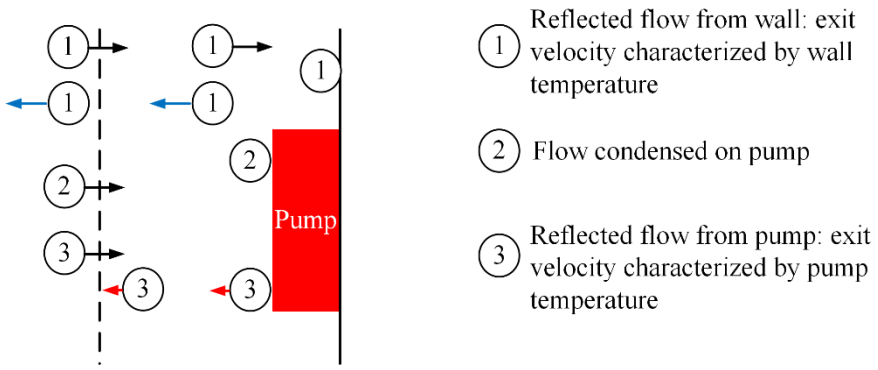

Figure 2.5: Three potential outcomes for particles in end dome pump regions.

and are reflected with a thermal-diffusive speed characterized by the facility wall temperature, while the second term is the number density of reflected particles from a pump that are now moving at a thermal-diffusive speed characterized by the pump surface temperature.

2.3.4 Final Expressions

Application of Eq. (2.5), Eq. (2.7), and Eq. (2.8) to each of the reference surfaces shown in Figure 2.1(b) results in a system of equations the can be solved simultaneously for the directional number densities crossing each surface. This system is shown for the positive directional number densities in Eq. (2.9)-(2.11). A similar system can be developed for the negative number densities crossing each surface.

$$n_{D+} = (1 - s_d)n_{C+} + (1 - \alpha)s_d n_{C+}\sqrt{T_w/T_p} \tag{2.9}$$

$$\begin{aligned} n_{E+} = {} & (1 - s_u)(1 - s_d)n_{C+} \\ & + (s_u(1 - s_d) + (1 - s_u)s_d + s_u(1 - \alpha)s_d)(1 \\ & - \alpha)n_{C+}\sqrt{T_w/T_p} = n_{B+} \end{aligned} \tag{2.10}$$

$$n_{C+} = n_{A+} = n_{in} - n_{C+}(\alpha s_d - 1)^2(\alpha s_e - 1)(\alpha s_u - 1)^2 \tag{2.11}$$

Since the HET exit plane is located just upstream of surface D, the parameter of interest for HET neutral ingestion is the mass flow rate of particles crossing surface D in the upstream direction (F_{D+}). The solution for this parameter is shown in Eq. (2.12)-(2.13):

$$n_{C+} = \frac{n_{in}}{1 + (\alpha s_d - 1)^2(\alpha s_e - 1)(\alpha s_u - 1)^2} \tag{2.12}$$

$$F_{D+} = mS_c n_{C+} V_w - m\, S_{p_d} n_{C+} V_w + (1-\alpha) n_{C+} S_{p_d} m V_p \sqrt{T_w/T_p} \tag{2.13}$$

$$n_{in} = \frac{\dot{m}_a}{mS_c}\sqrt{\frac{\pi m}{2kT_w}} \tag{2.14}$$

In Eq. (2.9)-(2.13), s_u is the ratio of pump surface area-to-facility cross-sectional area in the upstream pump region and all other terms retain their meaning from previous expressions. In Eq. (2.12), n_{in} is the input number density due to the HET anode flow computed as per the assumption regarding plume flow reflection in Section 2.2.1. For clarity, this parameter is expressed as a function of the anode mass flow rate, $\dot{m}_a$, propellant mass, and the chamber cross-sectional area in Eq. (2.14). It is important to note that, as per the discussion in Section 2.2.1, all particles injected into the HET anode are assumed to travel unimpeded to the downstream facility surfaces, thermalize, and reflect. Thus, the relevant temperature to describe the velocity of the input neutrals is the chamber wall temperature, as indicated in Eq. (2.14). Since the HET exit plane occupies only a small fraction of the cross-sectional area of surface D, computing the actual ingested mass flow rate due to the background neutral flow requires the mass flow rate computed in Eq. (2.13) to be scaled by the ratio of the HET exit plane area to the cross-sectional area of the facility. This scaling ensures that only those particles that are on a trajectory to enter the HET

channel are counted as part of the ingested mass flow rate. It is important to note that this approach neglects any ionization processes external to the HET and so may not be strictly valid for cases with significant external ionization.

As discussed in Section 2.2.1, it is assumed that the HET plume flow collisionally scatters background flow neutrals traveling towards the HET exit plane. For this work, the region of the facility downstream of the HET is discretized into a grid consisting of five regions. The number density associated with the unionized propellant exhausted by the HET in each region is assumed to be uniform and equal to the value computed at the midpoint of the region assuming an inverse-square dependency from the HET exit plane. This number density is used to compute the collisional mean free path in each region per the model described in Section 2.2.1. The probability ($p_{survival}$) that a given background flow neutral survives the transit through a given region without undergoing a scattering collision can be expressed as a function of the axial span of the region (Δx) and the collisional mean free path (λ) as shown in Eq. (2.15).

$$p_{survival} = \exp\left(-\frac{\Delta x}{\lambda}\right) \tag{2.15}$$

The total probability of a background neutral surviving the full transit from the downstream facility surfaces to the HET exit plane can then be described as the product of the survival probabilities computed for each of the five discrete downstream regions and the ingested mass flow rate can be expressed as the product of the total survival probability and the scaled mass flow rate crossing surface D in the upstream direction. It is important to note that background neutrals that do undergo a collision are assumed to continue traveling upstream without being ingested by the HET.

Although developed for the chamber shown in Figure 2.1(a), Eq. (2.12) can readily be modified to accommodate chambers of different geometric sizes and pump configurations by appropriately modifying the values of s_e, s_u, and s_d. For example, the result for a facility with no end dome pumps would be equal to Eq. (2.12) evaluated with s_e set to zero. Similarly, thrusters of different sizes or operating conditions can be accommodated by appropriately adjusting the exit area in the scaling mentioned above and the source term in Eq. (2.12).

Now that the final expressions of the model are developed, it is important to revisit the physical processes captured by Eq. (2.12)-(2.13) and how these processes might explain the empirically-observed enhancement in background neutral ingestion relative to the predictions of the thermal model. As described in detail in Section 2.2, the physical process captured by this model is the reflection of the low-density plasma flow (as neutrals) from the downstream facility surfaces and their subsequent axial motion back towards the HET. This reflected motion is caused by the finite axial dimensions and pumping speed of the facility and represents a bulk motion towards the HET exit plane that could result in an additional or enhanced ingestion flux into the HET beyond that captured by the random motions of the thermal model. It is this additional flux (of the flow reflected off the downstream facility surfaces) that is captured by Eq. (2.13) and the concomitant enhancement of local number density that is captured by Eq. (2.12). Specifically, the velocity terms in Eq. (2.13) represent the bulk axial velocity of neutrals towards the HET exit plane due to their reflection off the facility surfaces.

It is furthermore important to note that this reflective process is not unique to HETs, but is widely applicable to any directional flow of a low-density plasma in a finite vessel

including the plume produced by gridded ion engines during ground testing. However, unlike in HETs (which have open channel exit areas), neutral ingestion into gridded ion engines is conductance-limited by the grid apertures [2]. Thus, the bulk background flow is not able to freely stream into the ion engine discharge chamber and contribute to the plasma generation in this region. This significantly limits the impact of the bulk background flow on the ingestion characteristics of gridded ion engines and suggests the thermal model is sufficient for correcting the data acquired from these devices despite the model approximations [2]

2.3.5 Initial Model Validation

Two limiting test cases were used to provide initial validation of the model developed in the preceding sections. As an initial test case, the above approach was applied in order to generate the form of Eq. (2.12) relevant to a facility with upstream pumps only. Such a facility matches the original model developed for the LVTF by Cai *et al*. [37]. By setting both s_e and s_d to zero (i.e., by removing the downstream and end dome pumps from the model), the empirically-validated expression developed by Cai *et al*. is indeed recovered [37]. As an additional test case, the background flow model was used to compute the number density of particles crossing surface D in the positive direction assuming that both s_d and α were equal to one. This situation represents the limiting case of finding the number density remaining after a rarefied flow passes into a region occupied entirely by a pump surface that condenses all incident particles. As expected, the model predicts that no particles would exit this region. These two test cases confirm both the accuracy of the math underlying the model and the above approach in expanding the background flow model to

accommodate a wider variety of facility configurations. A more detailed validation of the ability of the model to replicate empirical results is presented in Chapter 3.

2.3.6 Comparisons to Existing Background Flow Models

Although the model developed in the preceding sections follows a similar approach to that taken by Cai *et al.*, it differs from this original model in several important ways [37, 41, 45]. First, all models developed by Cai *et al.* have only a single pump region with a single type of pump (i.e., either end dome pumps exposed to the flow on only one side or upstream/downstream pumps exposed to the flow on two sides) [37, 41, 45]. Because of this, in those models, all particles enter the pump region with a uniform velocity characterized by the temperature of the facility walls [37, 41, 45]. In contrast, the model developed in this work allows for the possibility of several adjoining pump regions of different types and thus the entrance of particles of several different populations with several different velocities into these regions. The ability to model adjoining pump regions and the corresponding discussion of how to account for these different populations is thus unique to this model and represents an increase in complexity over the original models developed by Cai *et al.* and is a major contribution of the model development presented in this work [37, 41, 45]. In addition, none of the original one-dimensional flow models created by Cai *et al*. account for the collisional scattering processes associated with the interaction of the background flow with the HET plume [37, 41, 45]. These processes are accounted for in this work as described in Section 2.2.1.

It is important to note that many of the additional complexities accounted for in this model are also accounted for in the more complex direct simulation Monte Carlo (DSMC) models of the background flow environment in ground test facilities developed by Yim and

Burt [38], Nakayama and Nakamura [46], and Cai [41]. However, in contrast to these DSMC models, the proposed one-dimensional model is much simpler to implement and customize to fit a given thruster and facility combination. To compare the two approaches (and therefore preliminarily assess the viability of the employed simpler approach), the background flow model was used to compute the weighted average speed of neutrals crossing surface D (i.e., those neutrals nearest the HET). These computations show a most probable speed of approximately 20-100 m/s, which is in good agreement with the velocity distribution functions generated by the more complex DSMC codes [37, 38, 45].

The final difference between the model developed in this work and those previously developed lies in the application of the model results. The models developed by Cai *et al.* [37, 41, 45], Yim and Burt [38], and Nakayama and Nakamura [46] were all used to create maps of the spatial neutral pressure distribution within ground test facilities. Although these results also indicated the presence of a bulk background flow of neutrals towards the thruster, to date, none of these models have been directly applied to compute the resultant ingestion mass flow rate into the HET due to this bulk motion nor have they been used to replicate existing empirical data sets quantifying the sensitivity of HETs to background pressure. The main contribution of this modeling effort is thus the application of these concepts to directly compute ingestion mass flow rates and assess the pressure sensitivity of HETs.

CHAPTER 3. APPLICATION AND VALIDATION OF BACKGROUND FLOW MODEL

3.1 Comparisons to Previous Empirical Data

In order to validate the applicability of the background flow modeling approach for predicting neutral particle ingestion by HETs, the model developed in Chapter 2 was used to compute the ingested mass flow rates for situations identical to several published experimental works on HET facility effects. These results were then compared against the empirical measurements of ingestion mass flow rate as well as the predictions of the thermal model.

When comparing the results of the background flow model to empirical measurements, it is assumed that background neutral particles ingested by the HET are ionized equivalently to neutrals supplied by the propellant distributor. This simple ingestion approach is similar to that taken in many previous works on facility effects and is consistent with the approach taken in all of the works used for comparison [16, 17, 22–24, 29]. Furthermore, as mentioned above, only neutrals particles that cross the HET exit plane and enter the discharge channel are counted as part of the ingested mass flow rate in the background flow model. Since the mass flow in this region of the channel is free molecular, these neutral particles are free to travel into the ionization zone of the HET and are thus subject to collisions with the high-temperature electrons within this zone as are the neutrals supplied by the gas distributor [22].

3.1.1 SPT-100 and Randolph/Thermal Model

As noted in Section 1.3, the motivation for the development of the background flow model is to address shortcomings observed with the thermal model. However, before it can be determined if the background flow model can address these shortcomings, it first must be determined if it can accurately replicate the empirical results used to generate the thermal model.

The thermal model is based on the SPT-100 testing performed by Sankovic *et al.* and analyzed by Randolph *et al.* conducted in Vacuum Facility 5 (VF-5) at the NASA Glenn Research Center (GRC) [21, 47]. Figure 3.1 shows a schematic of this facility. VF-5 is 4.6 m in diameter and 19 m long and is equipped with a helium cryopump system with an effective pumping area of 41 m^2 and operating temperature of 20 K surrounded by a liquid nitrogen-cooled shroud [21, 47]. Despite also being equipped with 20 diffusion pumps, during testing of the SPT-100, only the cryopump system was employed [35, 47]. At the time of the SPT-100 performance evaluation, the entire cryopump system was located in the downstream section of the facility extending axially from the middle of the chamber to the downstream end dome [47]. During the tests discussed by Randolph *et al.*, the SPT-100 was placed in the 1-m test port attached to the upstream facility end dome opposite the cryosurfaces [47]. Facility pressure was modulated by bleeding in excess propellant using an orifice located near the downstream end of the facility [47].

In the data analyzed in the work of Randolph *et al.*, the sensitivity of the SPT-100 to facility background pressure was determined by varying the anode mass flow rate supplied to the SPT-100 in order to maintain a constant discharge power as the facility pressure was varied using a bleed flow of propellant [21, 47]. The authors noted that lower anode mass flow rates were required to achieve a given discharge power at higher facility pressures

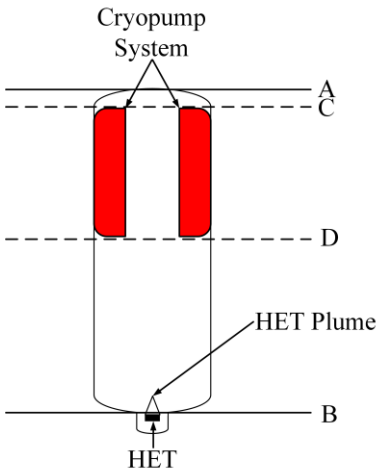

Figure 3.1: Schematic of NASA GRC VF-5 HET test facility.

and attributed the resultant change in required anode mass flow rate to an increase in neutral ingestion [21, 47]. The background flow model was similarly used to compute the ingestion mass flow rate for the SPT-100 HET in VF-5 due to both the thermal and bulk motions of the facility background neutrals. Consistent with the approach taken in Randolph *et al.*, the results are reported as the ratio of the ingestion mass flow rate to anode mass flow rate and are shown as a function of facility pressure in Figure 3.2 [21].

As shown in Figure 3.2, the ingestion mass flow rate into the SPT-100 HET due to the thermal motions of the background neutrals represents an average of 99% of the total ingestion mass flow rate across the full range of tested facility pressures. Thus, the background flow model predicts that, for the chamber configuration used to generate the data analyzed by Randolph *et al.*, the ingestion mass flow rate due to bulk motions of the background neutrals is negligibly small. This matches the key result presented by Randolph *et al.*, namely, that HET neutral ingestion could be modeled by considering only the thermal motions of the background neutrals.

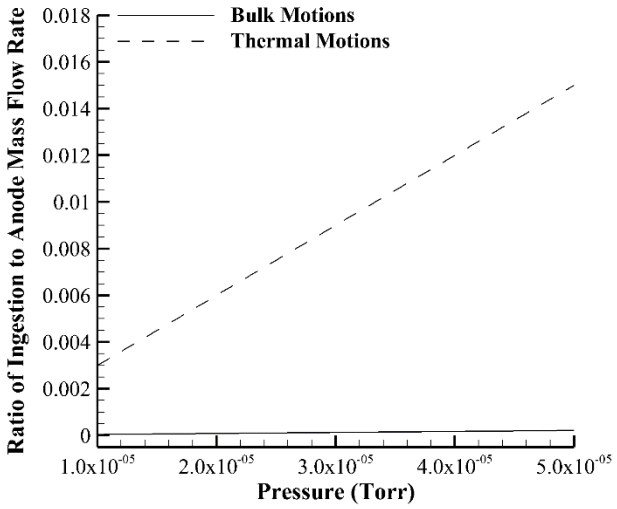

Figure 3.2: SPT-100 ingestion mass flow rate with facility pressure due to bulk and thermal motions of background neutrals.

It is important to note that the orientation of the bleed flow inlet relative to the HET thrust vector is omitted from the published descriptions of the SPT-100 testing [21, 47]. Due to the one-dimensional nature of the background flow model, radial injection of propellant cannot be directly modeled. Instead, the bleed flow was approximated as another source entering the chamber as per the assumption regarding plume flow reflection in Section 2.2.1. The impact of this will be explored in more detail in Section 3.1.3, where it will be shown that modeling the bleed flow as an additional source entering the chamber via the downstream end dome yields an overestimation of the ingestion mass flow rate due to the bulk motion of the background neutrals. This resultant overestimation due to the assumed orientation of the bleed flow inlet only further confirms the key result that, in the configuration analyzed by Randolph *et al.*, the background flow model correctly predicts that the contribution to the ingestion mass flow rate due to the bulk motions of the background neutrals is vanishingly small [21].

It is also important to note that the predictions of the background flow model are consistent with published on-orbit data taken with the SPT-100 [48]. Specifically, in the work of Pidgeon *et al.*, the authors note that the on-orbit performance of the SPT-100 matches the ground test data obtained by Sankovic *et al.* [47, 48]. The resolution of the on-orbit discharge current measurements are listed as ± 0.1 A [49]. As shown in Figure 3.2, the ingestion mass flow rate composes less than 1% of the total flow rate supplied to the SPT-100 ground testing. The absence of the ingestion mass flow rate should thus result in a corresponding change in on-orbit discharge current that is less than the resolution of the on-orbit measurements as observed [48].

3.1.2 P5 HET in the LVTF

The next data used for model validation were collected using the P5 HET in the LVTF at the University of Michigan. The P5 is a laboratory-model Hall thruster developed jointly by the Air Force Research Laboratory (AFRL) and the University of Michigan [29]. The P5 has a nominal operating power of 5 kW [29]. The LVTF is a stainless-steel clad vacuum chamber measuring 9 m in length and 6 m in diameter and is equipped with seven cryopumps located upstream of the HET test station for a combined total upstream pump surface area of 7.26 m^2 [16, 29, 37].

The first P5 HET data set used for validation was acquired by Hofer *et al*. [16]. In this work, the anode mass flow rate supplied to the P5 was varied in order to maintain a constant discharge current as the number of active pumps in the LVTF was varied from four to seven [16]. The authors noted that higher anode mass flow rates were required to achieve a given discharge current at lower facility pressures and attributed the resultant change in required anode mass flow rate to a decrease in neutral ingestion [16]. For instance, approximately

10 mg/s of anode flow was required, on average, to achieve a discharge current of 10 A in the four pump configuration, whereas 10.21 mg/s of anode flow was required, on average, in order to achieve the same discharge current in the seven pump configuration [16]. Thus, the change in ingested mass flow rate between the two conditions can be approximated as 0.21 mg/s. The background flow model was similarly used to compute the difference in ingestion mass flow rate for the P5 in the LVTF as the number of active cryopumps was changed from four to seven. The results are shown as a function of anode mass flow rate along with the empirical results in Figure 3.3(a). Also shown in Figure 3.3(a) are the changes in ingestion mass flow rate predicted by the thermal model. Consistent with the approach taken in Hofer *et al.*, the number densities used for the thermal model calculations correspond to the average of the values acquired by a pair of hot-cathode ion gauges: one was located on located on the wall of the LVTF near the exit plane of the HET and the other was located on the wall at an axial distance equal to half the length of the LVTF [16]. Previous work has shown that the pressures reported at these two locations in the LVTF vary by an average of 70%; the error bars shown for the thermal model predictions correspond to the uncertainty in the thermal model computations associated with this variance in the pressure measurements [36]. The error bars shown for the empirical data in the figure correspond to the reported uncertainty of the measurements. It is important to note that the point taken at 10 mg/s is characterized by a relative uncertainty; this is likely because 10 mg/s is the nominal design point for the P5, thus increasing the stability and repeatability of the HET relative to the other flow rates.

As shown in Figure 3.3(a), the changes in ingestion mass flow rate predicted by the thermal model are 7-15 times smaller than the empirical observations. However, the

computed changes in ingestion mass flow rate generated by the background flow model are within the empirical error bars for all but one of the anode mass flow rates. For that mass flow rate (10 mg/s), there is less than a 10% difference between the upper uncertainty bound and the prediction of the background flow model. Thus, for this data set, the predictions generated by the background flow model are on average, 70% closer to the empirical values than the predictions generated by the thermal model. The background flow model therefore captures the empirically-observed strong sensitivity of the P5 to facility pressure.

It is important to note that the background flow model consistently overpredicts the change in ingestion mass flow rate for the 5 mg/s and 10 mg/s anode mass flow rates, but underpredicts this change for the 12.5 mg/s and 15 mg/s anode mass flow rates. The reason for this is likely due to the employed collision model. As noted in Section 2.2.1, neutral

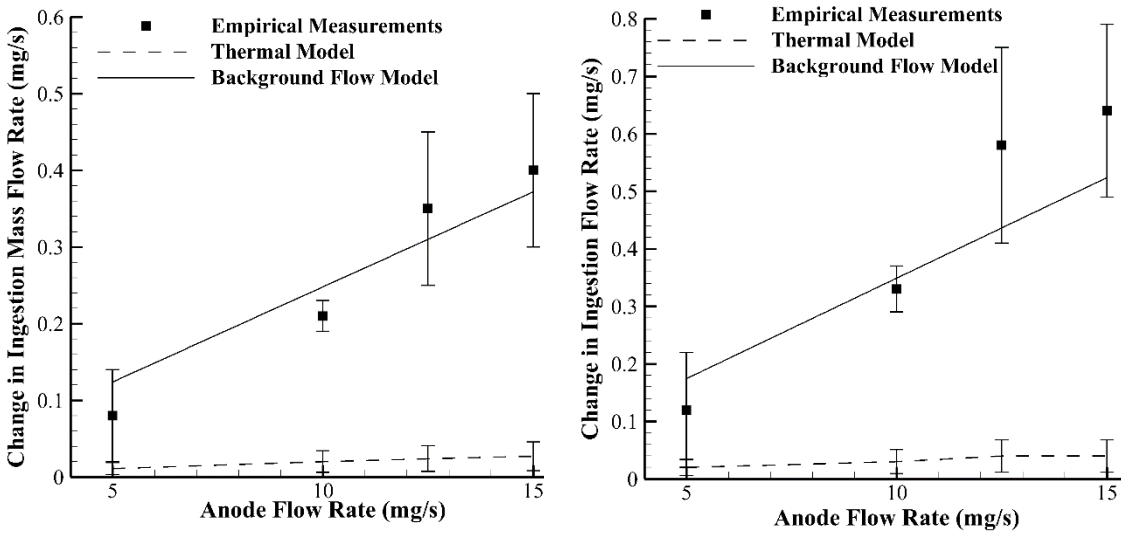

(a) **(b)**

Figure 3.3: Change in P5 ingestion mass flow rate between: (a) four and seven cryopumps and (b) seven cryopumps and vacuum.

particles exhausted by the HET are assumed to travel at a constant speed regardless of the HET operating condition. However, HET wall and anode temperature have been empirically shown to increase with increasing discharge power [50]. This results in a corresponding increase in the temperature (and thus velocity) of unionized neutrals exhausted by the HET, with the corresponding reduction in the collisional cross-section for the modeled elastic collisions between the background neutrals and the unionized propellant exhausted by the HET [51, 52]. Since the background flow model does not capture this change in cross-section, it overpredicts the number of collisions that a background neutral undergoes (and thus underpredicts the ingestion mass flow rate) for operating conditions with high anode mass flow rates and vice versa for the low anode mass flow rate conditions.

In order to estimate the difference in operating characteristics between the LVTF and test conditions with no background pressure, Hofer *et al*. used the aforementioned data to generate linear fits that could be extrapolated to predict the anode mass flow rate that would be required to achieve a given discharge current in true vacuum conditions [16]. The difference between this value and the anode mass flow rate required to achieve the same discharge current in the LVTF represents the ingested mass flow rate of neutrals by the P5 in the LVTF with all seven cryopumps operating. The background flow model was similarly used to compute the ingestion mass flow rate for the P5 in the LVTF with all seven pumps on. The results are shown as a function of anode mass flow rate along with the empirical results in Figure 3.3(b). As done by Hofer, *et al*, the empirical data shown in Figure 3.3(b) represents the average of the values acquired for each flow rate across four discharge voltages, while the error bars correspond to the standard deviation of these values

[16]. Also shown in the figure is the ingestion mass flow rate predicted by the thermal model for the P5 in the LVTF with all seven cryopumps operating. The number densities used for the thermal model calculations were determined identically the procedure described for the data shown in Figure 3.3(a) [16].

As was the case for the data shown in Figure 3.3(a), the results shown in Figure 3.3(b) indicate that the predictions made by the background flow model are significantly closer to the empirical observations than the predications generated using the thermal model. Specifically, the ingestion mass flow rates predicted by the thermal model are 11-24 times smaller than the empirical observations. By contrast, the difference between the estimates generated by the background flow model and the empirical measurements are less than the empirical error for all of the tested anode mass flow rates.

The next empirical data set used to validate the background flow model was acquired by Walker and Gallimore using the same thruster and test facility [29, 30]. In this work, the anode mass flow rate supplied to the P5 was held constant and the resultant average discharge current was measured as the number of active pumps in the LVTF was varied from two to four to seven [29, 30]. The authors noted that higher average discharge currents were observed at higher facility pressures and attributed the resultant change in discharge current to an increase in neutral ingestion [29, 30]. For instance, the discharge current of the P5 operating at a discharge voltage of 400 V and an anode mass flow rate of 5.25 mg/s was observed to be approximately 5 A with seven cryopumps on and 5.2 A with four cryopumps on. Using flow unit conversions, it can be shown that single ionization of 1 mg/s of xenon flow results in approximately 0.7 A of ion current [2]. In HETs, the ratio of the ion beam current to the discharge current is typically on the order of 70% and has been

shown to remain close to this value even at elevated ingestion mass flow rates; thus, an increase in ion current of approximately 0.7 A should result in a concomitant increase of 1 A in the discharge current [27, 53]. Thus, the observed change of 0.2 A of discharge current can be approximated as being due to a 0.2 mg/s reduction in ingestion mass flow rate between the four and seven cryopump configurations. It is important to note that this conversion is a rough approximation as compared to the direct measurements of anode mass flow changes acquired by Hofer *et al*. [16]. In order to quantify the error associated with this approximation, the average percent difference between the P5 discharge current predicted using the above mass flow rate to discharge current conversion and those measured empirically were computed for all of the discharge voltages and mass flow rates used by Walker and Gallimore. The average percent difference between the estimated and empirical results is approximately 1%, which approximates the overall error associated with the employed estimation technique.

The background flow model was similarly used to compute the difference in ingestion mass flow rate for the P5 in the LVTF as the number of active cryopumps was changed from two to seven. The results are shown as a function of anode mass flow rate along with the empirical results in Figure 3.4. Consistent with the approach of Hofer *et al.*, the empirical data shown in Figure 3.4 represents the average of the values acquired for each mass flow rate across four discharge voltages, while the error bars correspond to the standard deviation of these values. Also shown in the figure are the changes in ingestion mass flow rate predicted by the thermal model. Consistent with the approach taken by Walker and Gallimore, the number densities used for the thermal model calculations correspond to the empirical measurements taken using a single hot-cathode ionization

gauge located on the wall of the LVTF downstream of the HET test station [29]. The uncertainty in the computed ingestion mass flow rates using the thermal model due to the reported 20% pressure measurement uncertainty is captured by the line thickness.

As shown in Figure 3.4, the average percent difference between the empirical measurements and the predictions of the background flow model is 9% as the number of active pumps is increased from two to seven. By comparison, the change in ingestion mass flow rate predicted by the thermal model is 14-17 times smaller than the empirical measurements, resulting in an average percent difference of 93%. It is important to note that a similar analysis performed by Walker and Gallimore indicated that the thermal model underpredicted the observed changes by only 2-14 times [29]. However, that analysis is based on measurements of thrust, not of discharge current, and incorporates an assumed ionization efficiency of 80% for ingested neutrals [29]. If this same ionization efficiency is applied to the results presented in this work, then the change in ingestion mass flow rate predicted by the thermal model shrinks to between 11 and 14 times smaller than the observations, which is consistent with the range listed by Walker and Gallimore [29].

The accuracy of the background flow model in predicting the empirical data is comparable to that of the current increment technique originally proposed by Walker and Gallimore [29]. In this technique, empirically measured changes in discharge current as a function of pressure are used in order to approximate the neutral ingestion flow rate [29]. However, application of this technique requires measurements of the operating characteristics of a given thruster across a range of facility backpressures. The comparable accuracy of the predictions of the background flow model to this empirical technique

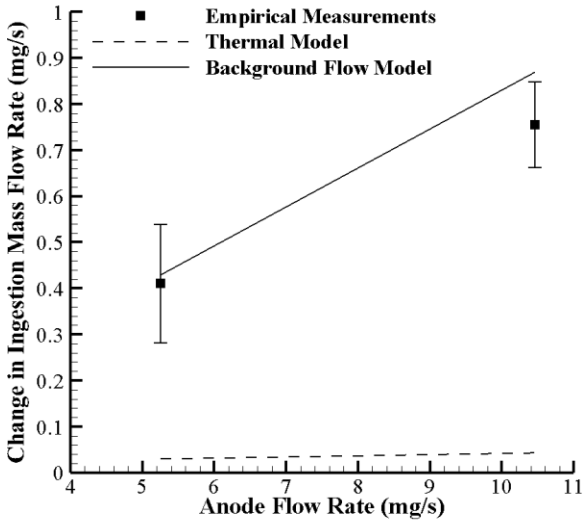

Figure 3.4: Change in P5 ingestion mass flow rate between two and seven cryopumps.

suggest that the model may be implemented in order to obtain these estimates of neutral ingestion without needing to perform the empirical mapping. Thus, taken together with the previously presented comparisons to the work of Hofer *et al.*, these results indicate that the background flow model can able to accurately replicate the empirically-observed neutral ingestion characteristics of the P5 in the LVTF and offers a 60% to 70% improvement in accuracy over the thermal model [16].

3.1.3 H6 in the LVTF

The background flow model was developed without any considerations of HET-specific characteristics. As such, the model should be able to maintain the previously-observed accuracy when predicting the ingestion characteristics of another thruster in the same facility. To evaluate this assertion, the predictions of the background flow model were compared to another data set collected by Reid using the H6 HET in the LVTF [22, 23].

The H6 is a 6-kW laboratory-model HET developed by AFRL in collaboration with the NASA Jet Propulsion Lab and the University of Michigan [54]. In this work, Reid held the anode mass flow rate supplied to the H6 constant and the resultant average discharge current was measured as the pressure in the LVTF was varied using a bleed flow of propellant [22, 23]. As was the case with the P5, higher discharge currents were observed at higher facility pressures and attributed to an increase in neutral ingestion [22, 23]. The observed change in discharge current can be used to estimate the concomitant change in effective anode mass flow rate using the method described previously.

The background flow model was similarly used to compute the ingestion mass flow rate for the H6 in the LVTF as a function of bleed mass flow rate for a discharge voltage of 300 V. The results are shown as a function of bleed mass flow rate along with the empirical results in Figure 3.5. The changes in ingestion mass flow rate predicted by the thermal model are also shown in Figure 3.5. Consistent with the approach taken by Reid, the number densities used for the thermal model correspond to the average values acquired by a pair of ion gauges located on opposite walls at an axial distance equal to half the length of the LVTF [22, 23]. Data presented by Reid shows that the pressures reported at these two locations in the LVTF vary by an average of 70%; the error bars shown for the thermal model predictions correspond to the uncertainty in the thermal model computations associated with this variance in the pressure measurements [22]. The error bars shown for the empirical data in the figure correspond to the reported uncertainty in the measurements [22, 23]. The results are reported as the change in ingestion mass flow rate relative to the baseline value obtained for an operating pressure of 1.9×10^{-5} Torr-Xe, which corresponds to a bleed flow of approximately 12 mg/s. It is important to note that, during the

experiment, the bleed flow orifice was located beneath the thruster and oriented such that the flow of propellant impacted the underside of the thrust stand mounting structure [22]. Due to the one-dimensional nature of the background flow model, the radial injection of propellant cannot be directly modeled. Instead, the bleed flow was approximated as another source entering the chamber as per the assumption regarding plume flow reflection in Section 2.2.1.

As shown in Figure 3.5, the values predicted by the thermal flow model are, on average, 10 times smaller than the empirical results. Even if the empirical measurements are all assumed to be equal to the lower uncertainty bound, the average percent difference between the predictions of the thermal model and the empirical results is 55%. However, the values predicted by the background flow model are of the same order as the empirical measurements and are within the uncertainty of the empirical measurements for the measurements taken at bleed mass flow rates of approximately 7.5 mg/s and 5 mg/s. For the final measurement, the predictions of the background flow model are only 8% different from the upper uncertainty bound. Thus, the predictions of the background flow model are approximately 50% closer to the empirical measurements than those generated using the thermal model. These results are identical to those for the 400 V operating condition also presented in the work by Reid [22, 23].

The accuracy of the background flow model in predicting the empirical data is comparable to that of the empirically-derived technique originally proposed by Reid [22, 23]. In this technique, the effective ingestion area is assumed to be a hemisphere equal in diameter to the thruster outer diameter; all neutrals that cross this surface are assumed to

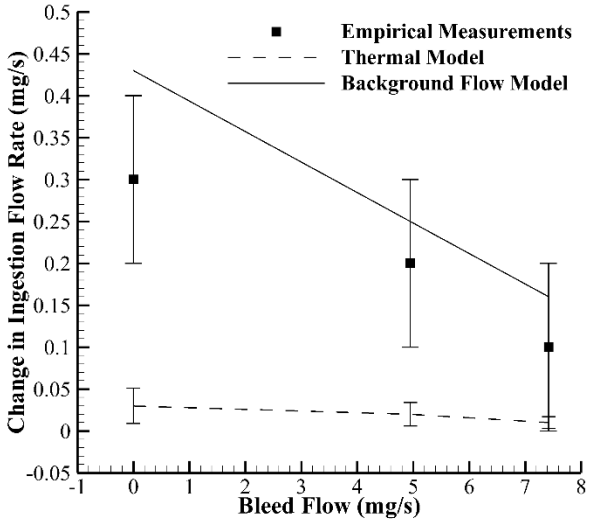

Figure 3.5: Change in H6 ingestion mass flow rate as a function of bleed flow rate in the LVTF. Values are measured relative to the 12 mg/s bleed flow rate case.

undergo the same ionization process as the neutrals supplied to the anode [22, 23]. However, as noted previously, this assumption has been disputed by other researchers [15]. The comparable accuracy of the predictions of the background flow model to this empirical technique suggests that the background flow model may be implemented in order to obtain estimates of the neutral ingestion mass flow rate without needing to make any assumption about ionization in the HET near-field plume. Taken together with the previously presented comparisons to the P5 in the LVTF, these results indicate that the background flow model can accurately replicate the empirically-observed neutral ingestion characteristics of two different thrusters in the LVTF and offers a significant improvement in accuracy over the thermal model.

3.1.4 SPT-100 in Aerospace Corporation Facility

In order to assess the ability of the model to accurately predict trends in different facility types, a final data set collected by Diamant *et. al*. using the SPT-100 HET in the vacuum facility at the Aerospace Corporation was used for model validation [15]. The SPT-100 is a flight-model HET developed and built by the Fakel Experimental and Design Bureau with a nominal operating power of 1.35 kW [15]. The Aerospace vacuum facility is a stainless-steel vacuum chamber measuring 9.8 m in length and 2.4 m in diameter and is equipped with ten total cryosurfaces [15]. There are four cryopumps in the downstream pump region, four 1.2-m diameter cryotubs in the upstream pump region, and two cryopumps on the upstream end dome [15]. Because the cryopumps used in the Aerospace facility are the same model as those used in the LVTF, all of these cryosurfaces are assumed to be similar in terms of sticking coefficient and surface temperature to the cryopumps used in the LVTF.

In this work, the anode mass flow rate supplied to the SPT-100 was varied in order to maintain a constant discharge current as the vacuum facility pressure was varied via a combination of bleed mass flow addition and changing the number of active cryopumps [15]. As with the P5 and H6, the authors noted that higher anode mass flow rates were required to achieve a given discharge current at lower facility pressures and attributed the resultant change in anode mass flow rate to a decrease in neutral ingestion [15]. Using these data, the authors estimated the difference in mass flow rate between operation at the lowest achievable facility pressure (as measured by an ion gauge internally mounted adjacent to the HET) and vacuum conditions. Based on this estimate, the authors predicted a total ingestion mass flow rate of 0.03 mg/s. The background flow model was similarly used to compute the ingestion mass flow rate for the SPT-100 in the Aerospace facility with all

pumps on and no bleed flow. The background flow model predicted an ingested mass flow rate of approximately 0.02 mg/s, while the thermal model predicted an ingestion mass flow rate of 0.008 mg/s. The predictions of the background flow model are thus 40% closer to the empirical results than those of the thermal model and were computed without needing to obtain any empirical pressure measurements.

Although the above data set will be explored in more detail in a later section, these initial results as well as those for the SPT-100 in VF-5, the P5, and the H6 indicate that the background flow model is significantly more accurate than the thermal model in predicting the ingestion characteristics of several different thrusters tested in different facilities with different pressure modulation techniques. These results furthermore suggest that the physical mechanisms captured by the model offer a potential framework to explain the original results observed by Randolph as well as the enhanced ingestion rates observed in subsequent facility effects studies. It is important to note, however, that existing empirical evidence suggests that the modeled additional ingestion flow caused by bulk background flows is likely one of the contributors to the observed enhanced sensitivity of HETs to facility pressure beyond what would be predicted by the thermal model. Previous work has suggested that factors including spatial shifts in near-field plasma properties and the concomitant effects on electron transport can also contribute to HET operational changes as a function of facility pressure [17]. Nevertheless, the ability of the background flow model to obtain the predictions detailed in this section without empirical measurements as well as the accuracy of the model across the described range of thruster and facility characteristics has not previously been demonstrated with any other mass ingestion or HET

facility effects model [2, 14–29]. These results therefore lend credibility to the background flow modeling approach.

3.2 Model Studies

The background flow model has been validated against several empirical data sets. In the remainder of this chapter, the model is more generally used to explore how parameters that often vary between different HET test facilities or test campaigns affect the neutral particle ingestion mass flow rates experienced by the HET being tested.

3.2.1 Impact of Facility Parameters on Randolph Criterion

As noted previously, subsequent studies with the SPT-100 HET in other vacuum test facilities have shown enhanced neutral ingestion mass flow rates beyond that predicted by the thermal model [15]. As the background flow model has been able to correctly capture both the enhanced neutral ingestion observed in other works as well as the neutral ingestion due only to thermal motions observed by Randolph *et al*., it can be used to provide insight into what aspects of VF-5 in the configuration used during the SPT-100 minimized the enhanced ingestion mass flow rates observed in other facilities.

The similarities between the other vacuum test facilities in which SPT-100 backpressure sensitivity studies have been conducted permit the creation of a generalized reference facility whose characteristics are representative of all of these facilities [16, 17, 22–24, 29]. This reference facility is assumed to have a length of 8 m and a diameter of 2.5 m. The pumps in the reference facility are assumed to have a total pump surface area of 10 m^2, have the same sticking coefficient as those in VF-5, and be distributed such that 50% of the pump surface area is upstream of the HET and 50% of the pump surface area is

downstream of the HET. With this facility defined, it is now possible to identify the key differences between it and VF-5 in order to determine which facility parameters most impact the neutral ingestion characteristics of the HETs being tested.

The first major difference between VF-5 and the reference facility is the placement of the pumping surfaces. During the SPT-100 testing in VF-5, all of the cryopumps were located downstream of the HET exit plane [47]. By contrast, in the reference facility, the cryopumps are distributed around the facility at stations located upstream and downstream of the HET [15]. To determine the impact of this on the ingestion characteristics of the SPT-100, the background flow model was used to compute the ratio of ingestion to anode mass flow rate for this HET as a function of downstream pump fraction for a facility of equal dimensions to VF-5. The results are shown in Figure 3.6. Also shown in the figure are reference lines that demarcate the downstream pump fraction for VF-5 and the reference facility. As compared to a facility with a 50% downstream pump fraction (*e.g.*, the reference facility), there is an 83% reduction in ingestion mass flow rate for a facility of equal size with a 100% downstream pump fraction (*e.g.*, VF-5). Consistent with results from previous work, this suggests that maximizing the downstream pump fraction minimizes the ingestion mass flow rate into a given HET [55].

The next difference between VF-5 and the reference facility is the total effective pumping area of the cryopanels in each facility. In the configuration used to test the SPT-100 HET, VF-5 had an effective pumping area of 41 m^2, whereas the reference facility has an effective pumping area of less than 15 m^2 [15, 47]. To determine how this changes the ingestion characteristics of the SPT-100 HET, the background flow model was used to compute the ratio of ingestion to anode mass flow rate as a function of total effective pump

area for a facility of equal size to VF-5 with all the pumping surfaces located downstream of the SPT-100. The results are shown in Figure 3.6. Consistent with the results discussed previously, also shown in the figure are reference lines that demarcate the approximate total effective pump areas for the reference facility and VF-5 during SPT-100 HET testing. As shown in Figure 3.6, the increase in total effective pumping area results in an 86% reduction in ingestion mass flow rate for VF-5 relative to the reference facility. This result is fully expected as increasing the pump surface area directly increases the outflux or sink terms in the background flow model formulation and thus reduces the overall ingestion mass flow rate.

The final difference between these two facilities is the facility length. VF-5 is 19 m long whereas the reference facility is assumed to be 8 m long. To determine the impact of this on the ingestion characteristics of the SPT-100, the background flow model was used to compute the ratio of ingestion to anode mass flow rate as a function of facility length for a facility of equal diameter to VF-5 with the same cryopump area and positioning. The results are shown in Figure 3.6. Also shown in the figure are reference lines that demarcate the length of VF-5 and the reference facility. The increased length of VF-5 results in a 94% reduction in ingestion mass flow rate as compared to reference facility. The reason for this is that the increased chamber length reduces the effective conductance of the bulk background neutral flow to the thruster. In other words, the longer path between the downstream chamber surfaces and the SPT-100 HET exit plane results in a larger percentage of background neutrals undergoing an elastic scattering collision prior to reaching the thruster and, thus, the ingestion of a smaller percentage of these neutrals [56].

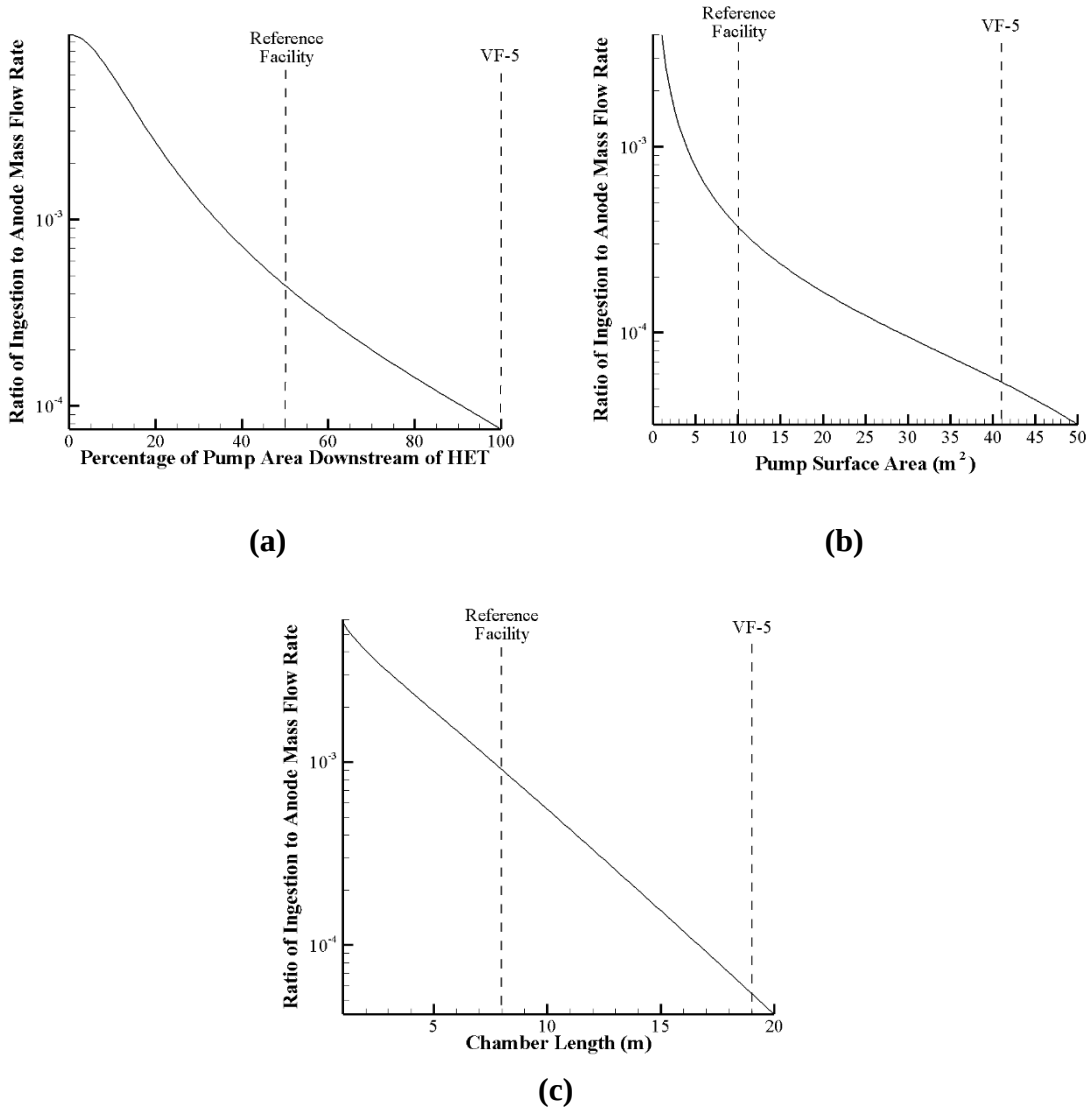

Figure 3.6: Impact of (a) pump placement, (b) pump surface area, and (c) chamber length on SPT-100 ingestion characteristics.

This effect is shown explicitly by Eq. (2.15). The increase in facility length results in longer transit paths (Δx) and thus a lower total survival probability for the background neutrals.

Taken together, these facility parameter differences yield an increase in ingestion mass flow rate of 135 times for the reference facility relative to VF-5 for similar operating pressures [15, 21]. However, because both ingestion mass flow rates are so small relative to the anode mass flow rate supplied to the HET, the total mass flow rate (*i.e.*, the sum of the ingestion and anode mass flow rates) supplied to the HET varies by only 1% between VF-5 and the reference facility. Finally, it is important to note that, although the diameter varies between VF-5 and the reference facility, the one-dimensional axial nature of the background flow model prohibits a full analysis of the impact of this parameter on HET neutral ingestion.

3.2.2 Pump Placement

The next parameter to be evaluated will be how pump placement within the test facility impacts HET ingestion. Although an initial exploration of the impact of this parameter on HET neutral ingestion was performed in Section 3.2.1, that analysis was limited to only look at a subset of existing HET test facilities (i.e., those in which the SPT-100 has been tested). As noted previously, facilities used for HET testing come in a wide variety of geometries and sizes [8]. These differences in geometric properties result in variations between facilities in the pump placement relative to the HET. Evidence of this can be seen from the above descriptions of the LVTF (in which all pumps are located upstream of the HET test station), VF-5 (in which all pumps are located downstream of the HET test station), and the Aerospace facility (in which the pumps are distributed upstream and downstream of the HET test station as well as on the upstream end dome) [15, 29]. Current

HET testing standards provide guidance regarding minimum facility pumping speeds and pressure measurement locations, but often do not mention how pump placement within the facility could impact the background neutral flow environment or the operation of the HET itself [8, 35].

In order to more generally determine the impact of pump placement on the neutral ingestion characteristics of a HET, the background flow model was used to compare the ingestion mass flow rates of a given HET in a given facility as the pump locations were varied. Specifically, the ingestion mass flow rate of the P5 in the LVTF was computed for an anode mass flow rate of 15 mg/s and a discharge voltage of 300 V as the number of active cryopumps was increased from two to twelve. These calculations were repeated for five different common pump geometries: upstream pumps only, downstream pumps only, distributed pumps with a 50%/50% upstream/downstream pump split, distributed pumps with a 40%/60% upstream/downstream pump split, and distributed pumps with a 20%/20%/60% end dome/upstream/downstream pump split. For convenience, hereafter the upstream/downstream splits will be shown without the percent signs. The results comparing the first three configurations are shown in Figure 3.7(a) while the results comparing the different distributed pump distributions are shown in Figure 3.7(b).

As shown in Figure 3.7(a), the facility configuration with downstream pumps only has the lowest ingestion mass flow rate for all values of active cryopumps. As compared to the downstream pump only configuration, the ingestion mass flow rate is between 3% and 21% higher if the only cryopumps are located upstream of the thruster with a mean percent difference of 12 ± 7% across all values of active cryopumps. The reported uncertainty represents one standard deviation of the data set. Similarly, the ingested mass flow rate is

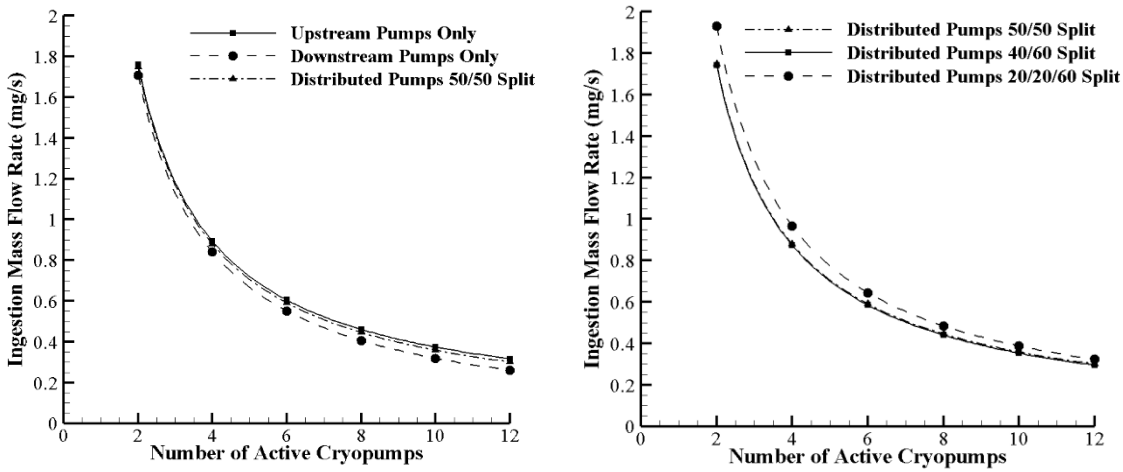

(a) **(b)**

Figure 3.7: Ingestion mass flow rate of the P5 operating at an anode flow rate of 15 mg/s comparing: (a) upstream, downstream, and distributed pumps and (b) different distributed pump configurations.

between 2% and 15% higher for the distributed pump configuration with a 50/50 upstream/downstream pump split as compared to the configuration with downstream pumps only with a mean value of 9 ± 5%.

As shown in Figure 3.7(b), the distributed pump configuration with the lowest ingestion mass flow rate is that with a 40/60 upstream/downstream pump split. As compared to the downstream pump only configuration shown in Figure 3.7(a), the distributed pump configuration with a 40/60 upstream/downstream pump split has a 2% to 13% higher ingestion mass flow rate with a mean of 7 ± 4% across all values of active cryopumps. The distributed pump configuration with a 20/20/60 end dome/upstream/downstream pump split is the worst performing pump configuration and has an ingestion mass flow rate that is 13% - 24% higher than the downstream pump only configuration with a mean percent difference of 18 ± 4%. Although the relative difference in ingestion mass flow rates

between the different pump configurations is significant, overall, the ingestion mass flow rate for most values of active cryopumps represents less than 5% of the total mass flow rate supplied to the thruster (i.e., the sum of the anode mass flow rate and the ingestion mass flow rate). Thus, the overall deviation in total mass flow supplied to the HET is less than 1% between the configuration with the highest ingestion mass flow rates (i.e., the 20/20/60 end dome/upstream/downstream distributed pump split) and the one with the lowest ingestion mass flow rate (i.e., the downstream pumps only).

In order to understand why there is only a minimal difference in total mass flow supplied to the HET as a function of pump placement, the path an ingested neutral particle must take through the facility in order to be ingested by the HET must be discussed. As shown in Figure 2.1(b), the only neutrals that can be ingested by the HET are those that cross surface D traveling in the upstream direction. By assuming only one-dimensional motion, there are then only two paths that a given neutral can take in order to be ingested. The first (i.e. Pathway 1) is the neutral can reflect off the downstream pump surfaces and travel through the downstream region to the thruster exit plane without striking, and sticking to, a pump or being collisionally scattered by the HET plume. Neutrals that complete this transit must be on a trajectory to intersect the thruster exit plane in order to be ingested. Neutrals that follow a trajectory that lies outside of the thruster exit plane area must follow a second pathway (i.e., Pathway 2) to be ingested. These neutrals must travel through the upstream chamber region, reflect off the upstream chamber surfaces (and/or travel through the upstream end dome pump region), travel in the downstream direction back through the upstream and downstream pump regions, reflect off the downstream facility surfaces, and then travel back through the downstream pump region on a trajectory to intersect the

thruster exit plane without being pumped or collisionally scattered in order to be ingested. Neutrals can repeat this second pathway as many times as needed until they are either pumped or ingested. Both pathways are illustrated in Figure 3.8.

It is thus possible to define two components of the ingestion flow, one each contributed by the two pathways discussed above. The magnitude of the first component (i.e., ingestion due to neutrals that traverse the downstream pump region on an intersecting trajectory with the HET exit plane) is inversely related to the pump surface area in the downstream pump region. Since for a given number of pumps, the downstream only pump configuration maximizes the downstream pump area, this component of the ingestion flow rate is thus minimized for this pump configuration. The magnitude of the second component (i.e.

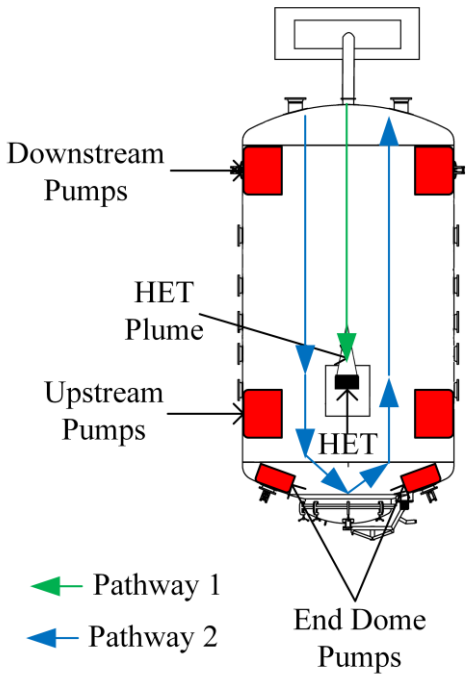

Figure 3.8: Bulk background flow ingestion pathways.

ingestion due to neutrals that have traversed the entire facility) is inversely related to the pump surface area in upstream and end dome pump regions. This component is thus maximized for the downstream only pump configuration, but is minimized for the other chamber configurations. As shown by the results in Figure 3.8, these two competing effects largely offset each other and result in a minimal difference in ingestion flow rate as a function of pump configuration.

A similar analysis regarding the impact of pump placement on the background flow field was conducted by Nakayama and Nakamura [46]. In that work, a two-dimensional DSMC code was used to assess the sensitivity of the background neutral pressure map to pump location and facility aspect ratio. The model developed in this work is unable to provide similar guidance on facility aspect ratio due to the assumption of one-dimensional motion. Furthermore, in the cited work, only the distance between the pumps and the HET were varied [46]. Despite these differences, both works suggest that maximization of the number of downstream pump surfaces minimizes the number of background neutrals near the thruster exit plane, thus indicating good agreement between the more complex DSMC approach and the one-dimensional approach applied here [46].

3.2.3 Pressure Modulation Technique

As shown by the empirical data sets referenced in Section 3.1, existing empirical investigations into HET facility effects change the nominal operating pressure in the test facility by some combination of varying the gas load via the introduction of a bleed flow of propellant and modulating the effective pumping speed by changing the number of active cryopumps [57]. However, since the nominal operating pressure in a HET test facility can be expressed as the ratio of the gas load to the effective facility pumping speed,

there are many combinations of bleed mass flow rate and pumping speed that can yield a given operating pressure [57]. To illustrate this point, the pressure in the LVTF during P5 operation at an anode mass flow rate of 10.46 mg/s was computed as a function of the number of active cryopumps and the bleed mass flow rate of propellant. The results are shown in Figure 3.9. For these computations, it was assumed that the gas load of the P5 was 1.25 Torr l/s and the nominal xenon pumping speed of the facility with all seven pumps on was 240,000 l/s. These numbers are consistent with values reported in previous investigations using the LVTF and were linearly scaled to account for the addition of bleed flow or the modulation of facility pumping speed [30]. Using this approach, the pressure, P, that would be measured by an ion gauge mounted on the wall of the LVTF near the exit plane of the HET can be computed as a function of the bleed flow rate of propellant, $\dot{m}_b$, and the number of active pumps, n_p, using Eq. (3.1):

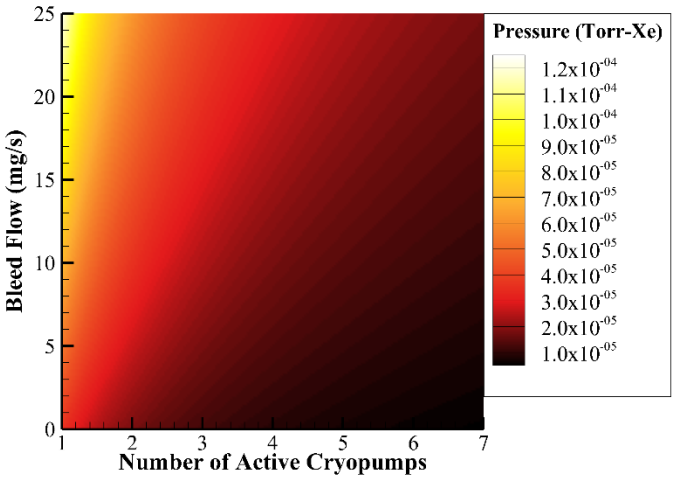

Figure 3.9: LVTF operating pressure during P5 operation at an anode mass flow rate of 10.46 mg/s as a function of active pump quantity and bleed flow.

$$P = \frac{1.25\left(\frac{\dot{m}_b + 10.46}{10.46}\right)}{240000\left(\frac{n_p}{7}\right)} \tag{3.1}$$

Despite the fact that each of the colored surfaces shown in Figure 3.9 yield the same facility operating pressure, previous work has shown that the method used to achieve this pressure (i.e., the combination of bleed flow and pumping speed) can impact the concomitant response of the HET [17, 38]. In order to determine if HET neutral ingestion due to the bulk background flow is similarly affected by the method used to achieve a given facility pressure, the background flow model was used to compute the ingestion mass flow rate of neutrals into the P5 during operation at an anode mass flow rate of 10.46 mg/s in the LVTF for all combinations of bleed flow and pumping speed (i.e., number of active cryopumps) yielding a facility operating pressure of 2×10^{-5} Torr-Xe. The results are shown in Figure 3.10. As done previously in the comparisons to empirical work with the H6, the bleed flow was approximated as another source entering the chamber as per the assumption regarding plume flow reflection in Section 2.2.

As shown in Figure 3.10, at a fixed facility pressure of 2×10^{-5} Torr-Xe, the ingestion mass flow rate is not constant and varies depending on the combination of bleed flow and pumping speed used to achieve that pressure. Specifically, the ingestion mass flow rate varies from a minimum value of 0.69 mg/s (7% of the anode mass flow rate) to a maximum value of 1.31 mg/s (12.5% of the anode mass flow rate). The percent difference between these maximum and minimum possible ingestion mass flow rates is thus 91%. These changes in ingestion mass flow rate furthermore result in up to a 5.6% variation in total mass flow rate (i.e., the sum of the constant anode mass flow rate and ingestion mass flow rate) supplied to the HET. This variation is larger than the approximately 2% variation seen

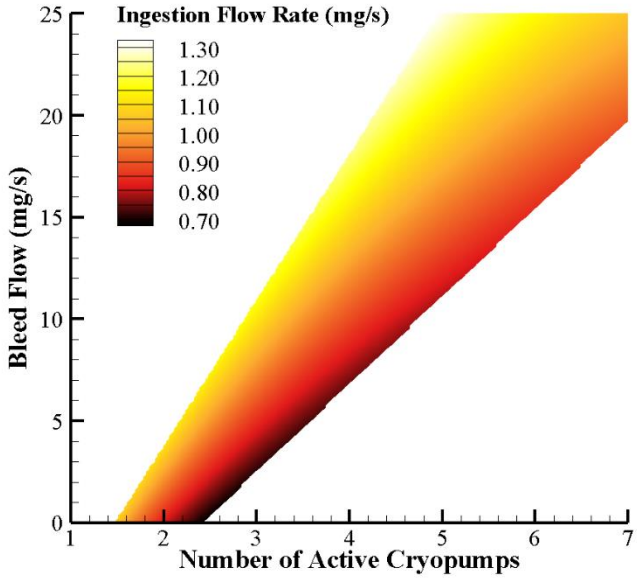

Figure 3.10: Computed ingestion mass flow rates for P5 operation at an anode mass flow rate of 10.46 mg/s in the LVTF at a pressure of 2×10^{-5} Torr-Xe.

by Hofer *et al*. in Ref. 16 for the P5 in the LVTF when the facility pumping speed was halved and was achieved without changing the facility operating pressure. These results are furthermore consistent with previous works that have shown that the background neutral distribution within the test facility and the HET ingestion characteristics vary depending on the method used to modulate the facility pressure [17, 38]. Overall, these results indicate that pressure magnitude (measured in a single location) is not a sufficient parameter to understand and predict neutral ingestion by a HET and that significant variation in total mass flow rate (or, equivalently discharge current) could be observed at a fixed facility pressure depending on how that pressure is achieved.

It is important to note that, in practice, many researchers orient bleed flows such that they are injected radially or in the cross-stream direction relative to the HET plume [15,

22]. Because of the one-dimensional nature of the background flow model, this radial motion cannot directly be captured and all bleed flow is assumed to enter the facility traveling axially. This could cause the impact of bleed flow on ingestion mass flow rate to be overstated in the background flow model computations. To account for this, the ingestion mass flow rate was again computed assuming that only one-quarter of the bleed flow was travelling axially in the facility. This reduction in number density corresponds to assuming that the bleed flow motion is two-dimensional (i.e., can travel in the axial and radial directions) and that the bleed flow has an equal probability of traveling in any of these directions. Even with this reduction to account for the radial motion of the bleed flow, the results of the background flow model indicate up to a 4% variation in total mass flow rate supplied to the HET at a facility operating pressure of 2×10^{-5} Torr-Xe depending on how that pressure was achieved. This is still greater than the variation previously observed when the pumping speed in the LVTF was halved [16]. Furthermore, this variation is observed at a pressure below the thresholds recommended Dankanich *et. al* [35].

3.2.4 SPT-100 Performance Variation

To further explore how pressure modulation techniques may impact HET neutral ingestion, the thrust data collected by Diamant *et al.* for the SPT-100 HET in the vacuum facility at the Aerospace Corporation as a function of facility backpressure was revisited [15]. The measurements in this work indicated that the thrust of the SPT-100 decayed exponentially with decreasing facility pressure [15]. This trend is unlike the linear decay seen with other thrusters and facilities and is not accounted for by any existing model of neutral ingestion [2, 14–29]. In this work, the facility pressure was varied via a combination of bleed flow and modulating the number of active pumps [15]. As shown previously,

depending on how each pressure was achieved, this could result in a range of possible ingestion mass flow rates, and, therefore, a corresponding range of possible thrust values. If this range is large enough, it may be able to capture the observed exponential trend for the SPT-100.

The background flow model was used to compute the ingestion mass flow rate of the SPT-100 HET in the Aerospace facility for all combinations of bleed flow and pumping speeds yielding operating pressures between 1×10^{-5} Torr-Xe and 7×10^{-5} Torr-Xe (which matches the range over which empirical measurements were taken) [15]. In order to estimate the resultant impact of these ingestion mass flow rates on the performance of the SPT-100, the empirically-estimated vacuum thrust value was linearly scaled by the ratio of the total mass flow rate supplied to the HET at a given pressure to that estimated for the zero-backpressure case. This approach implicitly assumes that all ingested neutrals were ionized and accelerated identically to neutrals supplied via the thruster gas distributor and that the ingested neutrals do not change the ionization and acceleration processes within the HET. As noted previously, this simple ingestion approach is similar to that taken in many previous works on facility effects, and, furthermore, it is applied only to get a first-order estimate for the performance changes; these computations are not intended to fully predict the performance of the SPT-100 or capture all of the mode or operational changes that may be associated with neutral ingestion [16–18, 22–24, 29]. The results are shown in Figure 3.11 along with the empirical trend line originally presented by Diamant *et al*. [15].

As noted above and shown in Figure 3.11, the range of potential ingestion mass flow rates at a given pressure results in a range of possible thrust values. Only thrust values

corresponding to the maximum and minimum predicted ingestion mass flow rates at each pressure are shown. In other words, the points composing the maximum prediction line correspond to the predicted thrust values that would be measured for those facility conditions that yield the highest ingestion mass flow rate at each of the pressures shown on the abscissa, while the minimum prediction line contains the points corresponding to the predicted thrust values that would be measured for those facility conditions that yield the lowest ingestion mass flow rate at each pressure. Between these two lines is a range of points that represent all of the thrust values that could be measured at each pressure according to the background flow model.

As shown in Figure 3.11, this range is large enough to encompass the exponential decay in thrust observed by Diamant *et al.* within the stated experimental uncertainty of approximately 0.5 mN [15]. These results therefore suggest that the observed exponential decay could have been the result of the pathway used to achieve each pressure and the resultant non-linear impact on neutral ingestion by the HET. In other words, due to the size of the range of possible thrust values at each pressure, the background flow model suggests that it is possible to plot a pathway through this range that would yield an apparent exponential decay in thrust with facility pressure. To the author's knowledge, this is the first analytical model to be able to offer insight into these observed trends [15]. It is important to note that although the background flow model is consistent with the observed empirical trends, it is not able to replicate the observed asymptote at pressures above 5.0×10^{-6} Torr-Xe. This asymptote is discussed further in Section 5.2.1.

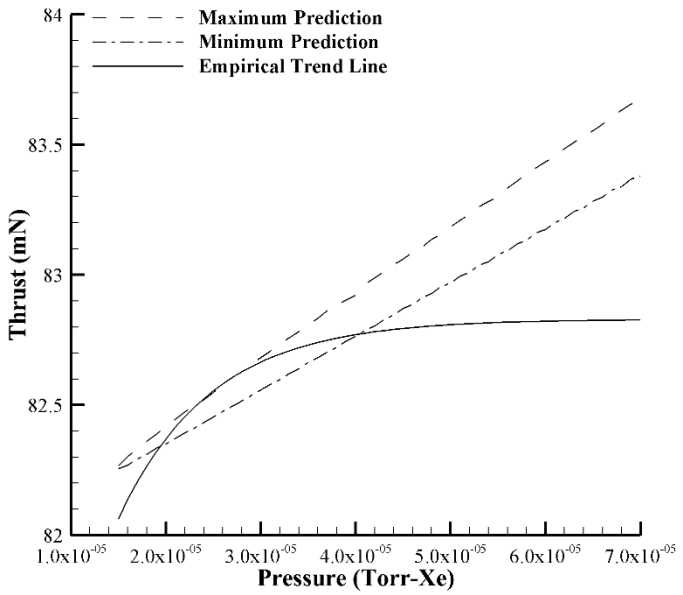

Figure 3.11: Predicted and measured thrust of the SPT-100 HET as a function of Aerospace facility pressure.

3.2.5 Parameter Sensitivities

As shown in Eq. (2.12) and Eq. (2.13), the predicted ingestion mass flow rate computed by the background flow model is impacted directly by three parameters whose values have been assumed: the chamber wall temperature, the pump surface temperature, and the pump sticking coefficient. Since these factors could vary between different facilities, the assumption of a uniform value for these three parameters may have introduced uncertainty in the estimates made by the background flow model. In order to quantify this potential uncertainty, the sensitivity of the predictions made by the background flow model to these parameters must be determined.

The first parameter sensitivity to be evaluated is that related to the facility wall temperature. This sensitivity is of particular importance as, in many HET test facilities, the

plume is directed towards a graphite beam dump that is separate from the facility walls. As the beam dump is directly impinged upon by the plume, the beam dump surface temperature may be higher than the facility wall temperature, thus, the neutrals reflecting off this surface could have a velocity characterized by a higher temperature. For this sensitivity study, the background flow model was used to compute the ingestion mass flow rate for the P5 in the LVTF at the 10.46 mg/s operating condition as a function of chamber wall temperature holding all other variables constant. The results are shown for three different types of pump configurations in Figure 3.12(a) and indicate that the predicted ingestion mass flow rate varies by approximately 3.5% as the facility wall temperature is changed from 273 K to 350 K for all pump configurations. In terms of total mass flow rate supplied to the HET, the variation over that temperature range is less than 0.1%.

In order to determine the sensitivity of the background flow model to the assumed pump surface temperature, the background flow model was used to compute the ingestion mass flow rate of the P5 in the LVTF at the 10.46 mg/s operating condition as a function of pump surface temperature holding all other variables constant. The results are shown for three different types of pump configurations in Figure 3.12(b) and indicate that the predicted ingestion mass flow rate varies by less than 0.1% as the pump surface temperature is changed from 10 K to 50 K for all pump configurations. The chosen temperature range encompasses all reported surface temperatures of cryosurfaces used to pump xenon during HET testing [37, 58]. It is important to note that the vapor pressure of xenon rises with temperature and that the pumping speed of a cryopanel decreases with increasing vapor pressure [37, 58]. Thus, the selected temperature range also encompasses the range of

xenon vapor pressures across which the pumping speed of a cryopanel will not decrease significantly [37, 58].

The final parameter to be evaluated is the pump sticking coefficient. For this sensitivity study, the background flow model was used to compute the ingestion mass flow rate of the P5 in the LVTF at the 10.46 mg/s operating condition as a function of pump sticking coefficient holding all other variables constant. The results are shown for three different types of pump configurations in Figure 3.12(c). The observed sensitivity to pump sticking coefficient is larger than that observed for either chamber wall temperature or pump surface temperature. As the pump sticking coefficient is changed from 0.3 to 0.8, the HET ingestion mass flow rate decreases by an average of 60% for all pump configurations.

This large variation is expected as the pump sticking coefficient determines the effectiveness with which the cryosurfaces remove xenon from the background flow environment, and, thus can have a similar influence to the addition of extra pumping surfaces. However, because the ingestion flow rate represents such a small fraction of total flow supplied to the HET, the variation in total mass flow is less than 3%. Furthermore, the assumed sticking coefficient of 0.4 was empirically determined for the LVTF using detailed maps of the neutral density inside of the facility during HET operation [30, 37]. As the majority of the empirical results used for comparison were acquired in the LVTF, it is expected that the error associated with this choice of sticking coefficient is minimal. Therefore, overall, the background flow model shows minimal sensitivity to the assumed empirical parameters.

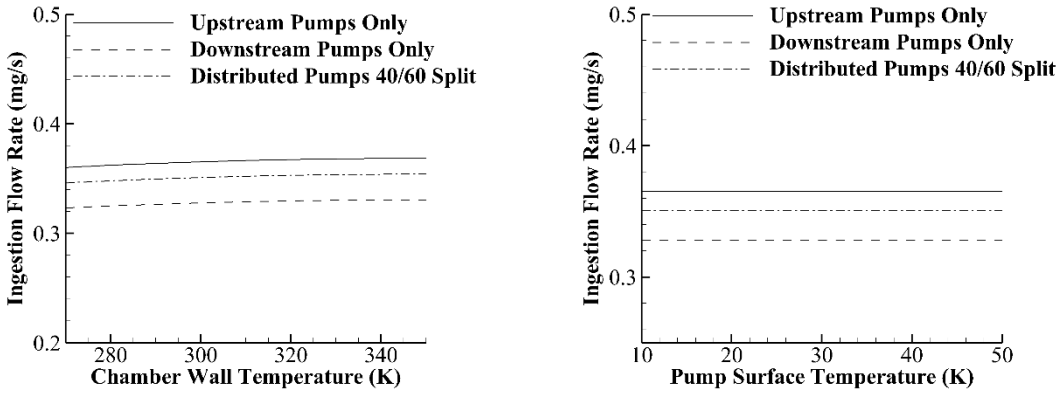

(a) **(b)**

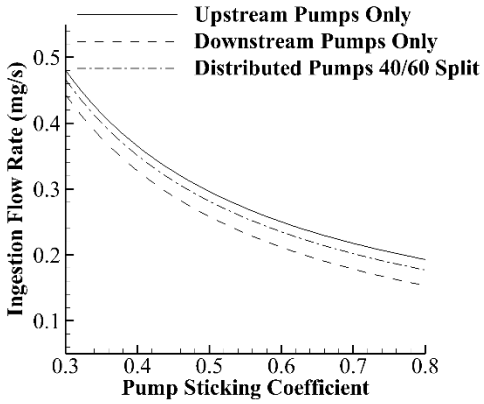

(c)

Figure 3.12: Results sensitivity to: (a) chamber wall temperature, (b) pump surface temperature, and (c) pump sticking coefficient.

3.3 Discussion of the One-Dimensional Flow Assumption

Among the assumptions discussed in Section 2.2, perhaps the most restrictive is the assumption of a one-dimensional background flow. Although consistent with the approach taken by Cai *et al.*, it is nonetheless worthwhile to discuss the relevance of this assumption as well as the resultant impacts on the model and the results it generates [37, 41, 45]. The first implication of this assumption is that the background neutrals are constrained to move only in the axial direction. In order to assess the validity of this constraint, it is necessary to discuss the typical reflection geometry in HET ground test facilities. In the facilities mentioned in this chapter, the HET plume flow is directed towards a carbon beam dump composed of several flat graphite panels [59]. As the ions in the HET plume are axially accelerated, the incident particles specularly reflect off these flat surfaces with a bulk velocity that is primarily oriented in the axial direction, thus minimizing the error associated with the one-dimensional flow assumption for the facilities used in this work [60]. This rationale has been empirically supported by pressure measurements, which have found minimal bulk background gas entrainment into radially-facing gauges but significant entrainment into gauges facing axially [38]. This suggests that the bulk flow of the background gas is primarily in the axial direction. The impact of non-flat plume reflection geometries on the validity of the one-dimensional flow assumption is discussed in Section 5.3.1.

By assuming a one-dimensional flow, all collisions between the background neutrals and facility side walls are also neglected. These collisions modify the speed distribution of the background neutrals. As per the assumed thermal accommodation coefficient of unity discussed in Section 2.2, upon colliding with the facility sidewall, an incident neutral will

thermalize and thus be reflected with an axial speed characterized by the facility wall temperature. For incident particles with speeds characterized by another temperature (i.e., those at pump temperature), these collisions will then result in a change in velocity and a concomitant change in number density as per Eq. (2.3). In order to assess the error associated with neglecting this effect, the background flow model was used to compute the ingestion mass flow rate for the P5 HET operating in a facility with 10 pumps located downstream of the HET. The downstream pump only configuration was selected as it maximizes the population of neutrals crossing surface D in the upstream direction with a speed characterized by a temperature other than the facility wall temperature. This facility configuration thus maximizes the error associated with neglecting the side wall effects. The ingestion mass flow rate was then computed again assuming all particles not at wall temperature undergo a sidewall collision prior to crossing surface D, which again represents the worst-case deviation from the model assumptions. The deviation between this result and the one computed neglecting the side wall effects is less than 1%.

A more detailed discussion of side wall effects on the validity of the one-dimensional approximation is included in the work of Cai *et al.* [45]. In this work, the model is modified in two different ways to account for the impact of the side walls. In the first, all neutrals were assumed to remain at wall temperature throughout the modeling domain. This is the same approach as taken in this work and represents a case in which all neutrals are assumed to collide with the side walls at least once during their transit through the facility. In the second approach, the model was modified to more generally consider sidewall effects by defining a geometric factor that incorporates chamber dimensions and view factors to compute the probability of a given neutral undergoing a side wall collision. The first

modification therefore represents an asymptotic case of the second with the probability of a side wall collision set to unity. Both model modifications were compared to results generated using a DSMC code and the predictions of the first modification (i.e., the one in which all neutrals were assumed to undergo a sidewall collision) were found to be consistently more accurate than those of the second [45]. This supports the approach taken in this work to quantify the error associated with the one-dimensional approximation.

3.4 Summary of Modeling Work

The work detailed in Chapters 2 and 3 expanded the background flow model first proposed by Cai *et al.* and explored the applicability of this approach to modeling neutral ingestion by HETs [37]. The original model was further developed and generalized to describe the background flow environment in facilities with any combination of end dome, upstream, and downstream pumps and analytic expressions were developed for the ingestion mass flow rate of a HET due to the background neutral flow within the facility. The predictions generated by these expressions were compared against empirical data taken with the P5, H6, and SPT-100 HETs in several different facilities and found to match the empirical observations to within the experimental uncertainty. These predictions were furthermore shown to be 40% to 70% more accurate than those generated using the thermal model most commonly used to predict and estimate neutral ingestion by HETs and equally as accurate as specific semi-empirical models developed for the P5 and H6 without requiring any empirical inputs such as in-situ pressure measurements [22, 23, 29]. The demonstrated improvement over the thermal model as well as the demonstrated accuracy in predicting empirical measurements for a variety of thrusters and facilities is, to the author's knowledge, unique to the background flow model, thus lending credibility to this

modeling approach and supporting its value as a predictive analytical tool [2, 14–29]. Furthermore, these results suggest that the physical mechanisms captured by the background flow model offer a potential framework to explain both the results observed by Randolph *et al.* and the enhanced ingestion rates observed in subsequent facility effects studies. This capability is to the author's knowledge, also unique to the background flow model [16, 17, 22–24, 29].

The validated background flow model was used to assess the impact of parameters that often vary between different test facilities and test campaigns on HET neutral ingestion. It was shown that neutral ingestion due to bulk motions of the background neutrals is minimized for facilities in which the downstream pump fraction, effective pump surface area, and length are maximized. Furthermore, it was shown that neutral ingestion can vary by as much as 24% depending on where the pumps are placed within a test facility; the lowest ingestion mass flow rates occurred for facilities with the maximum number of pumps located downstream of the HET. The impact of pressure modulation techniques on HET neutral ingestion was investigated, and it was shown that the ingestion mass flow rate of a HET can vary by as much as 91% at a fixed facility pressure of 2×10^{-5} Torr-Xe, depending on the combination of bleed flow and pumping speed used to achieve that pressure. This results in a band of possible ingestion mass flow rates and performance characteristics at a given pressure that is large enough to capture the empirically-observed exponential decay of the thrust of the SPT-100 with decreasing facility pressure [15]. The sensitivity of these results to the assumed parameters of chamber wall temperature, pump surface temperature, and pump sticking coefficient were assessed and shown to be less than 3% of the predicated total HET flow. Overall, these results indicate that pressure magnitude

is not a sufficient variable for quantifying neutral ingestion by a HET, and that other test variables (i.e., pressure modulation technique) must be specified and held constant in order to fully describe HET ingestion characteristics. Taken as a whole, these results provide strong initial confirmation of the proposed hypothesis regarding the presence of a bulk flow of background neutrals inside finite vacuum vessels and the impact of this flow on HET neutral ingestion.

CHAPTER 4. FACILITIES AND DIAGNOSTICS

As discussed in Section 1.4, the overall goal of this work is to test the proposed hypothesis regarding the presence of a bulk flow of background neutrals inside finite vacuum vessels and the impact of this flow on HET neutral ingestion both analytically and experimentally. The analytical results were presented in Chapter 3. This chapter outlines the empirical apparatus and approach used to test this hypothesis. Details of the employed facility, HETs, and diagnostics are presented in Sections 4.1, 4.2, and 4.3, respectively while the empirical approach and test matrix is detailed in Section 4.4.

4.1 Vacuum Test Facility

All experiments detailed in this work were performed in Vacuum Test Facility 2 (VTF-2) at the Georgia Institute of Technology High-Power Electric Propulsion Laboratory (HPEPL). A general schematic of this facility is shown in Figure 4.1. VTF-2 is a stainless-steel chamber measuring 9.2 m in length and 4.9 m in diameter. VTF-2 is evacuated to rough vacuum using one 495 cubic-feet per minute (CFM) rotary-vane pump and one 3800 CFM blower. High-vacuum is achieved using 10 CVI TMI re-entrant cryopumps. As shown in Figure 4.1, the cryopumps are distributed both upstream and downstream of the HET test station; 6 of the cryopumps are in a symmetric (relative to chamber centerline) azimuthal ring adjacent to the downstream end dome and 4 of the cryopumps are mounted in a symmetric (relative to chamber centerline) half-circle adjacent to the upstream end dome. The cryopump shrouds are fed using the Stirling Cryogenics SPC-8 RL special closed-loop nitrogen liquefaction system detailed by Kieckhafer and Walker [61]. The

facility has a combined nominal pumping speed of 350,000 l/s on xenon and can achieve a base pressure of 1.9×10^{-9} Torr.

The pressure in VTF-2 was monitored using one Agilent BA 571 hot filament ionization gauge controlled by an Agilent XGS-600 Gauge Controller. As per the recommendations in the EP pressure measurement standard, the gauge was mounted external to the chamber at the same axial location as the HET exit plane [35, 62]. In order to prevent plume ions from having a direct line of sight to the ionization gauge filament of the exterior ion gauge and potentially affecting the pressure measurement, a grounded neutralizer screen was attached to the gauge orifice [30, 35]. Unless otherwise noted, the facility pressure reported in this work corresponds to the corrected pressure measured by this ion gauge. The corrected pressure (P_c) is found by relating the indicated pressure (P_i) and the vacuum

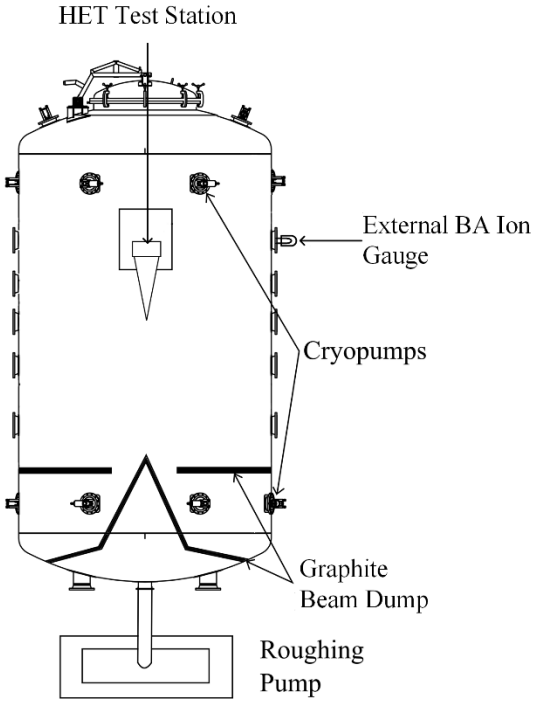

Figure 4.1: Schematic of VTF-2 (not to scale).

chamber base pressure (P_b) to a gas-specific constant using Eq. (4.1) [57]. It is important that, as written, Eq. (4.1) is only valid for correcting the pressure measurement for xenon [57].

$$P_c = \left[\frac{P_i - P_b}{2.87}\right] + P_b \tag{4.1}$$

4.2 Hall Effect Thrusters

4.2.1 IHD2000-EM11

The first thruster used in this work was the EM11 variant of the IHD2000 HET developed and manufactured by the IHI Corporation of Japan and shown in Figure 4.2 [63, 64]. The IHD2000 is a 2-kW class HET with a target operational range of 0.2 kW – 3 kW discharge power [63, 64]. The performance of the IHD2000 has been mapped by prior

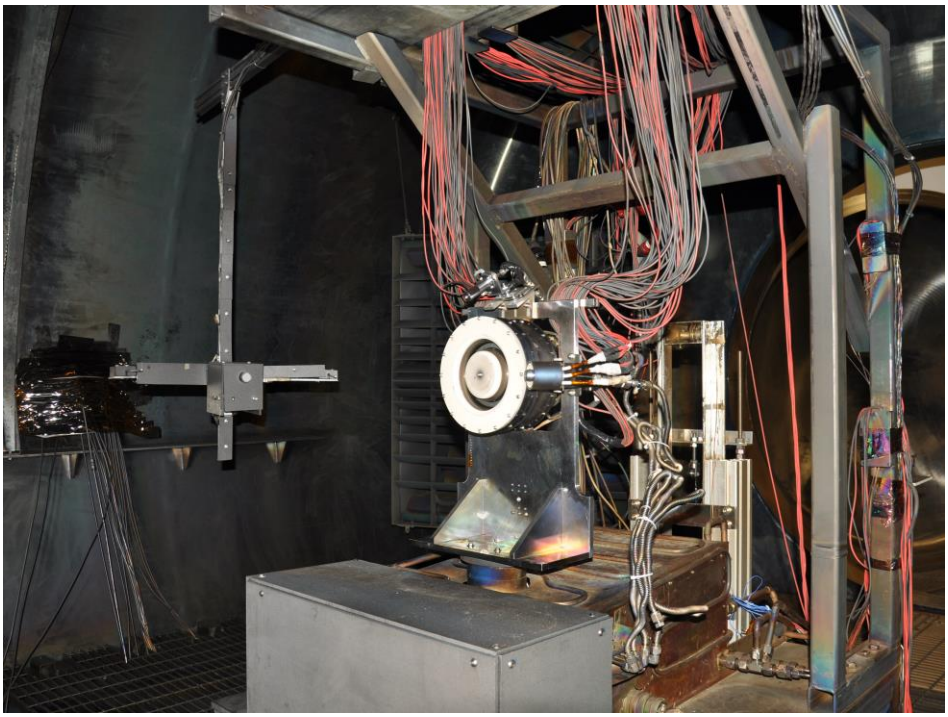

Figure 4.2: IHD2000-EM11 HET installed in VTF-2.

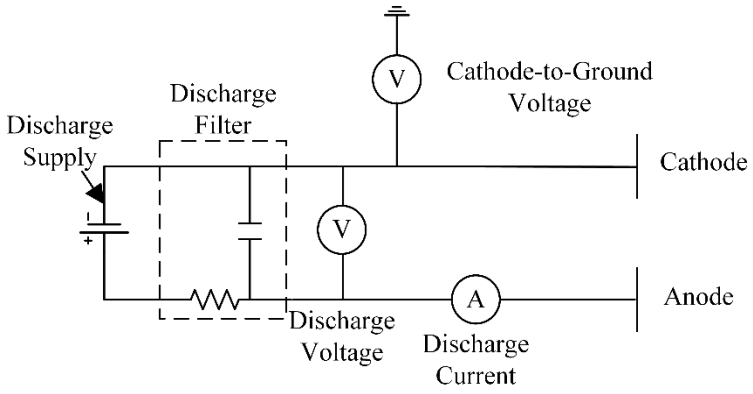

Figure 4.3: IHD2000-EM11 HET discharge circuit and thruster telemetry measurement locations.

investigations in Japan [63, 64]. For this work the IHD2000 was operated using an externally-mounted Veeco HCN-252 hollow cathode located at the three o'clock position of the thruster; the cathode mass flow rate was fixed to be 10% of the anode mass flow rate. An Electric Propulsion Laboratory HCPEE 375-series cathode was also installed as an auxiliary option at the 12 o'clock position of the thruster but not used in this work. All data presented in this work were collected with the IHD2000 operating at a discharge voltage of 300 V and anode mass flow rate of 4 mg/s. All HETs used in this work were fired for a minimum of three hours prior to data acquisition on the first day at vacuum to permit any absorbed moisture or vapors that could act as an additional gas source to fully outgas from the HET channel and cathode emitters. In addition, each HET was fired for a minimum of 1 hour each subsequent day prior to data acquisition to permit initial heating of the system to near thermal equilibrium.

Research-grade (99.9995%) xenon propellant was supplied to the thruster and cathode using stainless-steel lines metered with MKS 1179A mass flow controllers. The controllers

were calibrated before each test by measuring gas pressure and temperature as a function of time in a known control volume [65]. The mass flow controllers have an uncertainty of approximately ± 0.5% of the set point for the cathode, anode, and bleed flow [65].

The IHD2000-EM11 discharge was controlled using a Magna-Power TSA800-54 power supply; the inner and outer magnets were powered using TDK-Lambda GEN80-42 power supplies. A TDK-Lambda GEN600-2.6 and GEN60-25 were used for the cathode keeper and heater, respectively. All electrical connections entered VTF-2 through separate feedthroughs to eliminate potential electromagnetic interference concerns. The thruster discharge supply was connected to a discharge filter consisting of a 95-μF capacitor and 1.3-Ω resistor to prevent oscillations over 1.4 kHz in the discharge current from reaching the discharge supply. Figure 4.3 shows the circuit used for the IHD2000-EM11 HET in this work. All electrical/telemetry measurements were acquired using an Agilent 34980A Data Acquisition System (DAQ); these signals were sampled at the power supply terminals and corrected for the resistive voltage loss through the discharge filter and lines.

The discharge current oscillations of the IHD2000-EM11 HET were recorded using a Teledyne LeCroy CP030A current probe connected to a Teledyne LeCroy HDO6104 oscilloscope. The minimum sensitivity and bandwidth of the current probe are 1 mA/div and 50 MHz. The mean discharge voltage and cathode-to-ground voltage of the IHD2000-EM11 were measured differentially using a pair of Teledyne LeCroy PPE2kV 100:1 high-voltage probes connected to the same Teledyne LeCroy oscilloscope. Since the HET oscillations have a characteristic frequency of approximately 20-30 kHz, measurements were acquired at a sampling frequency of 12.5 Ms/s for a capture period 20 ms [33]. The chosen frequency is sufficient to satisfy the Nyquist criterion and permit capture of 400

fundamental periods [13]. Figure 4.3 shows the location of each telemetry measurement in the IHD2000-EM11 circuit.

4.2.2 H6

The second HET used in this work is the H6 HET shown in Figure 4.4. As discussed in Section 3.1.3, the H6 is a 6-kW laboratory-model HET developed by AFRL in collaboration with the NASA Jet Propulsion Lab and the University of Michigan in order to serve as a standardized test-bed for research of HET physics [54]. The tested H6 variant was from AFRL and was not magnetically shielded. The performance and sensitivity to background pressure of the H6 have been extensively mapped by previous investigations [17, 23, 52, 66]. The H6 was operated with a center-mounted LaB_6 hollow cathode developed by JPL at a mass flow rate equal to 7% of the anode mass flow rate [22].

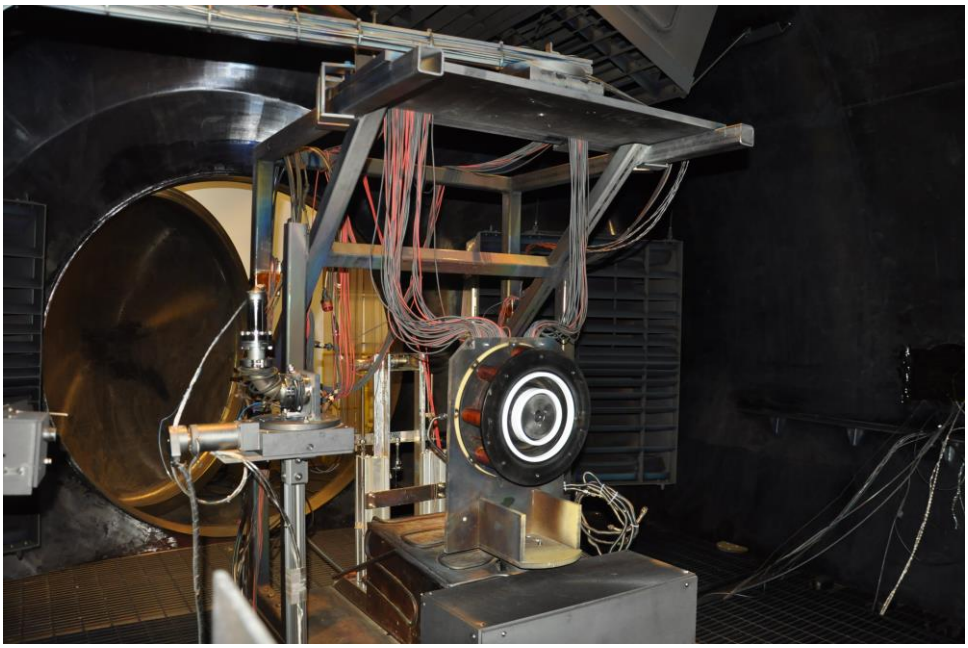

Figure 4.4: H6 HET installed in VTF-2.

All data presented in this work were collected with the H6 operating at its nominal discharge voltage and anode mass flow rate of 300 V and 20 mg/s, respectively [22]. The HET circuit and mass flow system used with the H6 HET were largely identical to the one described in Section 4.2.1, except time-resolved measurements of the discharge current were acquired using a Teledyne LeCroy CP030 current probe instead of the CP030A probe used with the IHD2000-EM11. The minimum sensitivity and bandwidth of the CP030 current probe are 10 mA/div and 50 MHz.

4.2.3 6-kW Laboratory HET

The final HET used in this work is a 6-kW class laboratory HET. For this work, it was chosen to operate this HET with a centrally-mounted cathode and in a magnetically-shielded configuration. The cathode was operated with a mass flow rate equal to 10% of the anode mass flow rate. The HET circuit and mass flow system used with the 6-kW HET were nearly identical to the one described in Section 4.2.2. The only change was that a TDK-Lambda GEN40-38 was used for the cathode heater for this HET instead of the GEN60-25, which was used for the cathode keeper. All data presented in this work were collected with the 6-kW HET operating at its nominal discharge voltage and anode mass flow rate of 300 V and 20 mg/s, respectively.

4.3 Diagnostics

4.3.1 Thrust Stand

Thrust was measured using the null-type, inverted pendulum thrust stand of NASA Glenn Research Center design detailed in the work of Xu and Walker [67]. The employed

thrust stand consists of a pair of parallel plates connected by a series of four flexures that support the top plate and permit it to deflect in response to an applied force. The position of the upper plate is measured using a linear voltage differential transformer (LVDT) and is controlled using two electromagnetic actuators. During operation, the current through each actuator is controlled using a pair of Stanford Research Systems SIM960 proportional-integral-derivative control loops that use the LVDT signal as the input and then modulate the current through the actuators to remove any vibrational noise (damper coil) and hold the upper plate stationary (null coil). The thrust is correlated to the current through the null coil that is required to keep the upper plate stationary. In order to maintain thermal equilibrium during thruster firings, the thrust stand is actively cooled using three parallel loops: one each through the structure, the null coil, and the outer radiation shroud. Cooling water is supplied by a 1100-W VWR International 1173-P refrigerated recirculation chiller and does not vary by more than 5° C as compared to the thruster-off condition [67].

The thrust stand is calibrated by loading and off-loading a set of known weights that span the full range of expected thrust values. A linear fit is then created to correlate the null coil current to the force applied to the thrust stand. In order to minimize the thermal drift of the zero position, the thrusters were shut down periodically so that a recalibration could be performed. The thrust stand uncertainty is reported as the standard error of the estimate associated with the calibrations performed immediately before and after each operating condition; the standard error of the estimate accounts for the uncertainty associated with both the drift of the zero position and that associated with the linear calibration fit. In this work, the average thrust stand uncertainty was approximately 1.5% full-scale.

4.3.2 Motion Stages

In this work, four motion stages were used to control the position of the plasma and pressure diagnostics. Linear motion was controlled using a pair of Parker Daedal 406XR precision linear motion stages. These stages both have a 2,000 mm travel, a positional repeatability of ± 159 μm, and a positional uncertainty of approximately ± 20 mm (relative to thruster centerline) [12]. Rotary motion was controlled using a pair of Parker Daedal 200RT series rotary tables, which have positional precisions of ± 0.17º and a positional uncertainty of approximately ± 1º (relative to thruster centerline) [12]. All four tables were actuated simultaneously using a LabVIEW Virtual Instrument that interfaces with a National Instruments (NI) MID-7604 4-axis stepper motor drive and a NI-Motion PCI-7314 4-axis stepper controller.

4.3.3 Bayard-Alpert Hot-Cathode Ionization Gauge

4.3.3.1 Theory of Operation

As shown in Figure 2.1(b) and discussed in Section 2.3, the relevant parameters for describing the aspects of the background neutral flow most germane for HET ingestion are the one-directional number densities (i.e., n_{D+} and n_{D-}) crossing the surface immediately in front of the HET exit plane (i.e., surface D). Measurements of these directional number densities were acquired in this work using a Bayard-Alpert (BA) hot-cathode ionization gauge. A schematic of this type of gauge is shown in Figure 4.5.

In a hot-cathode ionization gauge, a heated thermionic cathode filament emits a current of electrons which are then accelerated towards a positively-biased internal grid [62]. During their transit, these electrons strike and ionize the background gas that enters the

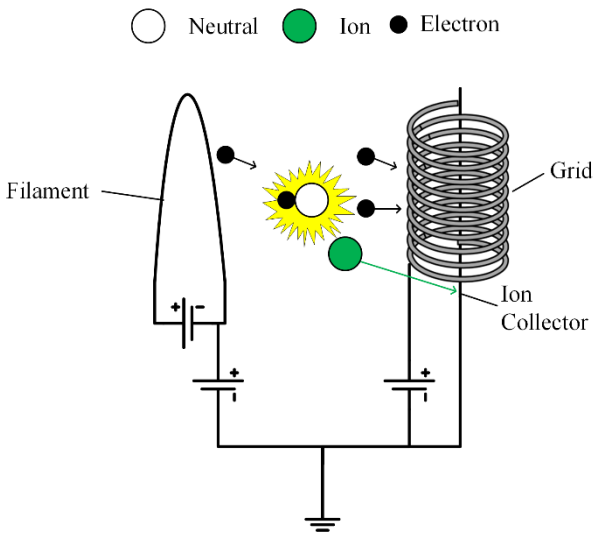

Figure 4.5: Schematic of a hot-cathode ionization gauge.

gauge [62]. The resulting ions are attracted to a grounded collector; the number of ions generated and collected is linearly proportional to the background gas number density, and thus, the background gas pressure [30]. This linear relationship between pressure (P) and the collected ion current (I_c) can be expressed as shown in Eq. (4.2) below [30].

$$I_c = \left[\frac{L_i \sigma_i}{kT}\right] I_e P = S_{ig} I_e P \tag{4.2}$$

The bracketed term in Eq. (4.2) is a function of several gas- and gauge-specific parameters including the length of the ionizing space (L_i), the ionization cross-section (σ_i) and gas temperature (T). For convenience, this term it is often expressed as a singular gauge sensitivity factor (S_{ig}) as shown in Eq. (4.2) [30]. The linear relationship between pressure and collector current shown in Eq. (4.2) has been validated for pressures between 10^{-4} Torr and 10^{-9} Torr. This range encompasses the full range of pressures observed in this work and in most HET testing applications [30].

4.3.3.2 Design and Implementation

The in-chamber BA hot-cathode ionization gauge used in this work is a Granville-Phillips Stabil-Ion Series 370 gauge connected to a Granville-Phillips Stabil-Ion Series 370 controller. In order to prevent plume ions from having a direct line of sight to the ionization gauge filament and potentially affecting the measurements, a neutralizer tube identical to the one used in previous works was attached to the gauge orifice [15, 30, 35, 62]. The selected gauge and controller meet all of the design recommendations put forth in the recently published pressure measurement standard including having a precision-wound supported anode and acceleration grid, an all-metal construction, and tensioned dual filaments [62, 68]. Finally, it is important to note that the as-implemented in-chamber gauge is identical to those used in many previous facility effects studies, thus allowing for direct comparison between data sets without needing to worry about variations between types of BA hot-cathode ionization gauges [15, 27, 28, 69, 70].

4.3.3.3 Uncertainty Analysis

In general, there are two primary sources of uncertainty associated with BA hot-cathode ionization gauges. The first is associated with variations in internal gauge geometry during operation due to gravity-induced sagging of the internal components (i.e., anode, acceleration grid, and filaments). These variations alter gauge stability by impacting the ionization and current collection characteristics of the gauge, and thus alter the sensitivity factor shown in Eq. (4.2) [62]. Such effects are exacerbated if the gauge is mounted with the anode, grid, and filaments oriented horizontally [62]. BA hot-cathode ionization gauges with designs that do not address these issues have been shown to have uncertainties of 30% to 50% [62].

The second source of uncertainty is driven by the operation of the gauge. Although most BA hot-cathode ionization gauges are calibrated by the manufacturer, this calibration is typically done using air or nitrogen at a given temperature [62]. Using these gauges with different gases results in a change in the ionization cross-section, and thus the sensitivity factor shown in Eq. (4.2) [62]. Noting this, most manufacturers provide gas correction factors in order to allow the measured pressure to be corrected for the relevant gas [62]. Although these factors vary with pressure, studies have shown that they provide accurate and reliable correction across the range of pressures relevant for HET testing even if the pressure sensitivity of the correction factor is neglected [62]. Similarly, operating the gauges at a temperature other than that at which it was calibrated has been shown to cause changes in the collected ion current by 0.075%/K [62]. Since in-chamber temperatures in this work did not vary greatly from room-temperature, the error associated with temperature effects is negligible [62].

A more detailed discussion of the sources of uncertainty for BA hot-cathode ionization gauges can be found in the aforementioned pressure measurement standard for electric propulsion testing [62]. In addition, the standard provides guidelines on how to minimize the error associated with this type of pressure gauge. These include selecting a gauge designed to minimize gravity-induced sag, paring the gauge with one of the recommended controllers, using properly shielded signal cables, orienting the gauge with the filaments vertical, and letting the gauge operate for at least 2 hours prior to data acquisition in order for it to reach thermal equilibrium [62]. All of these recommendations were followed in this work, yielding an uncertainty of 4% to 6% for all measurements taken with the in-chamber Stabil-Ion Series 370 gauge [62]. It is important to note that the exterior Agilent

BA 571 gauge described in Section 4.1 does not include the design features specified in the pressure measurement standard and thus has an uncertainty of 20% to 30% for all measurements [62].

4.3.4 Retarding Potential Analyzer

4.3.4.1 Theory of Operation

The ion energy distribution in the thruster plume was measured using a four-grid retarding potential analyzer (RPA). A schematic of this probe is shown in Figure 4.6. The RPA uses a set of electrostatically-biased grids to act as a high-pass energy filter and selectively filter ions based on the ion energy [71, 72]. The grids are (in order from the plasma to the collector): the floating grid, the electron repelling grid, the ion retarding grid, and the electron suppression grid. The floating grid minimizes plasma perturbations caused by the presence of the probe. The electron repelling grid is biased negative relative to facility ground in order to prevent plasma electrons from reaching the collector. The electron suppression grid is also biased negative relative to facility ground to repel any secondary electrons emitted by the collector and promote the recollection of these secondary electrons by the collector. Recollection of these secondary electrons removes their effects from the I-V characteristic.

The final grid is the ion retarding grid; this grid is biased positive relative to ground to impede the motion of the incident ions, and thus filter the ion population based upon directed kinetic energy per unit charge. For an ion to proceed past this grid, it must have a kinetic energy greater than the electric potential energy of the grid. A critical velocity can thus be defined as that required to give an ion equal kinetic energy to the electrostatic potential energy of the ion retarding grid [73]. As shown in Eq. (4.3) and (4.4), this critical

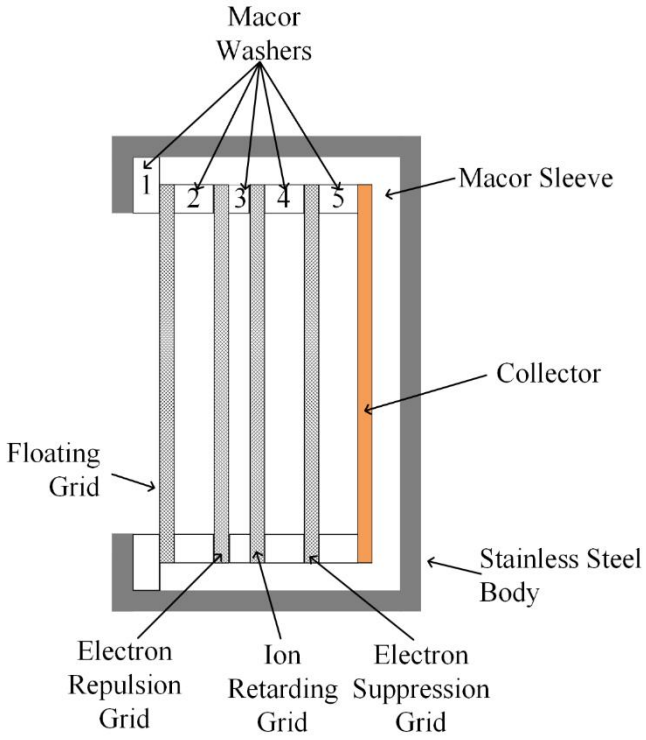

Figure 4.6: Schematic of a four-grid RPA.

velocity ($v_{i,crit}$) is a function of the ion mass (m_i), the ion charge (q), the grid voltage (V_{grid}), and the elementary charge (e).

$$\frac{1}{2}m_i v_{i,crit}^2 = qeV_{grid} \tag{4.3}$$

$$v_{i,crit} = \sqrt{\frac{2qeV_{grid}}{m_i}} \tag{4.4}$$

The ion current collected by the RPA will thus only consist of those ions with a velocity higher than the critical velocity. In general, this current can be expressed as a function of the collector area (A_c) and incident ion flux ($\Phi_{incident}$) using Eq. (4.5) [6, 56, 73].

$$I_c = qeA_c\Phi_{incident} \tag{4.5}$$

The incident ion flux can further be decomposed into the product of the ion number density (n_i) and average incident ion velocity ($\langle v_i \rangle$) as shown in Eq. (4.6) [6, 56, 73].

$$I_c = qeA_c n_i \langle v_i \rangle \tag{4.6}$$

Noting that the only ions that can reach the collector are those with a velocity higher than the critical velocity, the average incident ion velocity term can be rewritten as shown in Eq. (4.7). In this expression, $f(v_i)$ is the velocity distribution function of the ions and all other terms in Eq. (4.7) retain their meaning from previous equations [6, 56, 73].

$$I_c = qeA_c n_i \int_{v_{i,crit}}^{\infty} v_i f(v_i) dv \tag{4.7}$$

Finally, since the plume of a HET is composed of ions belonging to several different charge states, the total current collected by the RPA for a fixed ion repulsion voltage is thus the sum of the current contributions from the ions of each charge state (j) as shown in Eq. (4.8) [74, 75].

$$I_c = A_c e \sum_j n_j q_j \int_{v_{i,crit}}^{\infty} v_i f(v_i) dv \tag{4.8}$$

During operation, the ion repulsion voltage is swept in order to determine the ion energy distribution function [73]. As such, it is useful to perform a change of variables from ion velocity (v) to effective ion voltage (V_{ion}) defined as the ion's kinetic energy per unit charge. For convenience, it is also useful to define an effective charge state (q_{eff}) as per Eq. (4.9) in order to simplify the handling of multiply charged ions in the HET plume.

$$q_{eff} = \frac{\sum_j n_j q_j}{\sum_j n_j} \tag{4.9}$$

Applying both the definition of the effective ion voltage and charge state yields the expression shown in Eq. (4.10).

$$I_c = -\frac{A_c n_i e^2 q_{eff}^2}{m_i} \int_{V_{grid}}^{\infty} f(V_{ion}) dV_{ion} \tag{4.10}$$

An expression for the ion voltage distribution function ($f(V_{ion})$) can then be obtained by differentiating Eq. (4.10) with respected to voltage. As shown in Eq. (4.11), the ion voltage distribution function is thus related to the derivative of the current collected by the RPA with respect to the voltage of the ion repulsion grid [73]. The most-probable ion voltage (V_{mp}) is the peak of this derivative profile.

$$\left.\frac{dI_c}{dV_{ion}}\right|_{V_{ion}=V_{grid}} = \frac{-A_c n_i e^2 q_{eff}^2}{m_i} f(V_{ion}) \tag{4.11}$$

It is important to emphasize that Eq. (4.11) is strictly an expression for the ion voltage (i.e., the ion energy per unit charge) distribution and not the ion energy distribution [73]. The reason for this is that the grid voltage required to screen an ion traveling with a given kinetic energy is identical to that required to screen a doubly-charged ion traveling with twice that kinetic energy [73]. The two ions are thus indistinguishable using the RPA.

4.3.4.2 Design and Implementation

The RPA used in this work is of the four-grid design previously used by Xu and shown schematically in Figure 4.6 [14, 74]. The RPA consists of a stainless-steel body, a Macor sleeve to insulate the body from the grids, and the grid assembly. All four grids in the assembly are made from a photo-chemically etched screen of 316 stainless steel with 229 micron holes and an open area of 31% [76]. The grids are separated by a series of Macor washers of varying thicknesses. These washers are labeled 1-5 in Figure 4.6 and the thickness of each washer is shown in Table 4.1.

Table 4.1 Thickness of washers separating RPA grids.

Washer	Thickness (mm)
1	1,6
2	3.2
3	1.6
4	6.3
5	6.3

For the RPA to effectively filter ions, two design requirements must be met. The first is that the grid holes must be small enough to permit the sheath to extend across the opening. The reason for this is that Debye shielding prevents the bias placed on the grid from being felt by the plasma outside of the sheath [6, 77, 78]. Thus, for an RPA in which the sheath sizes are smaller than the grid openings, the retarding voltages will not be felt uniformly across the holes and the plasma will be able to proceed directly to the collector. Since the sheath size is on the order of several (typically 5-10) Debye lengths, this requirement effectively implies that the hole diameter should be no larger than the local Debye length (λ_d) [78].

The next design requirement is that the probe must be designed so as to avoid the space-charge limitation from occurring between the electron repelling and ion retarding grids [78]. In this region of the probe, most of the electrons that entered the probe should have been screened by the electron repelling grid. This could yield a situation in which there is an excess of positive charge in front of the ion retarding grid that could cause the effective ion retarding voltage to be greater than the potential energy applied to the grid. In order to prevent this from occurring, the ion retarding grid must be placed in the sheath downstream of the electron repelling grid [78]. Mathematically, this yields the requirement that the

spacing between the electron repelling and ion repulsion grids (t_3) must satisfy the expression shown in Eq. (4.12).

$$t_3 \leq 1.02\,\lambda_d \left(\frac{e\Delta V_{grid}}{kT_e}\right)^{3/4} \tag{4.12}$$

In Eq. (4.12), ΔV_{grid} is the difference between the voltage applied to the electron repelling and ion retarding grids, T_e is the electron temperature, and all other variables retain their meaning from previous expressions.

Using published data for the H6 HET, the design of the selected probe was evaluated against these two design criteria. Unfortunately, it was found that the plasma number densities at the standard measurement location of 1 m downstream of the HET exit plane were too high to permit the sheath to fully extend over the grid apertures. Thus, measurements for the H6 and 6-kW HET were taken 1.6 m downstream of the HET exit plane so that the number densities were sufficiently low to permit effective screening by the RPA grids. The number densities for the IHD2000-EM11 were sufficiently low that the sheaths fully extended over the grid apertures thus permitting RPA data acquisition at the standard 1 m distance. It is important to note that this approach to overcoming probe limitations is similar to that employed is other published HET performance evaluations [79].

Consistent with previous work with the H6, during operation, the electron suppression and repulsion grids were biased to -30 V using a Xantrex XEL 60-1.5 power supply [22]. The ion repulsion grid bias was controlled by a Keithley 2410 1100V SourceMeter and the collector current was measured using a Keithley 6487 Picoammeter. The SourceMeter and picoammeter were simultaneously controlled using a LabVIEW Virtual Instrument to

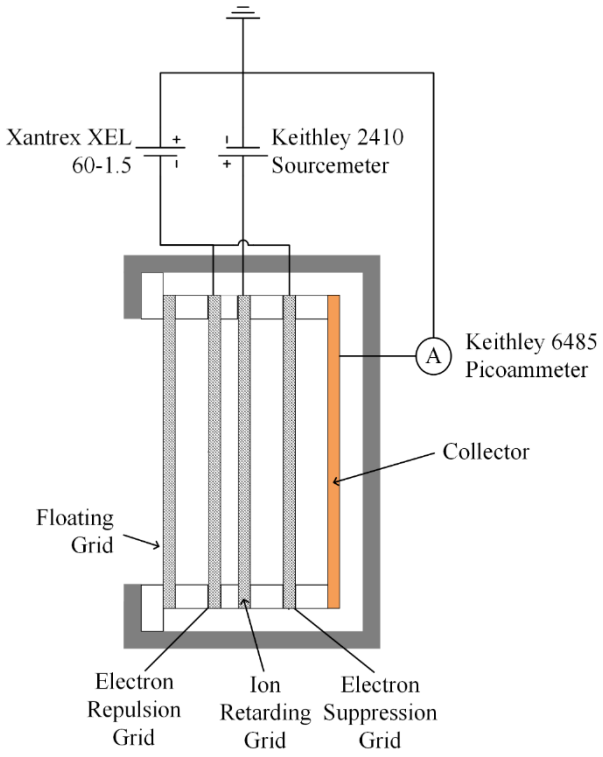

Figure 4.7: Schematic of the RPA measurement circuit.

ensure synchronous recording of the ion repulsion voltage and collector current. The measurement circuit is shown schematically in Figure 4.7.

During each measurement, the ion repulsion voltage was typically swept between 0 V and 50-100 V above the discharge voltage in 1V increments with a 300ms dwell time. Four sweeps of the ion repulsion voltage were taken at each measurement condition. The data from each of these sweeps were differentiated using Newton's Difference Quotient. The derivative curves were smoothed using a robust locally-weighted scatter plot smoothing algorithm (RLOESS) to remove noise. As discussed in Section 4.3.4.1, the resultant derivative peaks correspond to the most-probable ion voltages. These energies were corrected for the plasma potential by subtracting the plasma potential from the resultant most-probable values. A representative RPA trace is shown in Figure 4.8.

4.3.4.3 Uncertainty Analysis

A detailed analysis of the uncertainty associated with RPA measurements is presented in previous work by Beal and Gallimore [80]. In this work, measurements of the ion energy per charge distribution in the plume of a HET cluster were acquired with both an RPA as well as a proven parallel-plate electrostatic energy analyzer (ESA). The two data sets were then analyzed and compared in order to determine how accurately the RPA was able to replicate the results from the ESA. The results showed that the RPA results had a conservative uncertainty bound of approximately ± 10 V for the most-probable voltage and ± 20 V full width at half maximum (FWHM) [53, 80]. This uncertainty measurement includes the uncertainty associated with correcting the most-probable voltage by the local plasma potential.

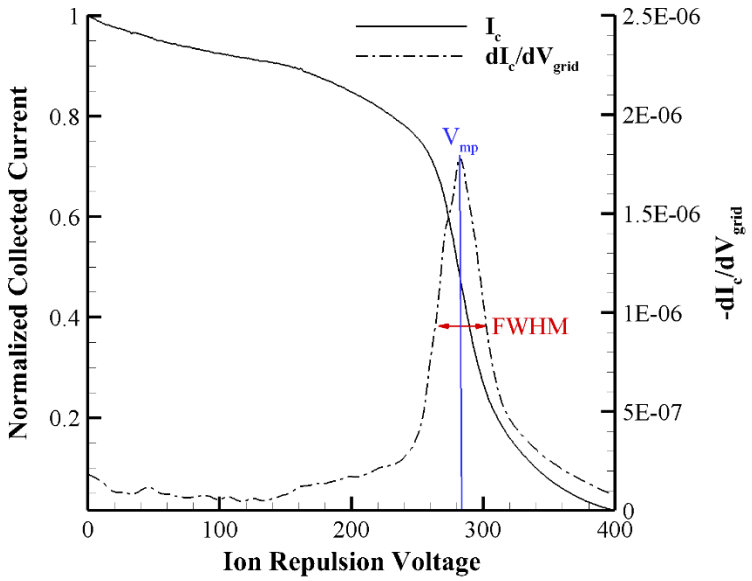

Figure 4.8: Representative RPA trace acquired using a 6-kW HET operating at an anode mass flow rate of 20 mg/s and facility pressure of 1×10^{-5} Torr-Xe.

4.3.5 Faraday Probe

4.3.5.1 Theory of Operation

In its most basic form, a Faraday probe consists of a negatively-biased planar metal electrode that is swept through the HET plume along a constant-radius arc in order to measure the ion current density distribution [14, 81]. These current density distribution measurements can then be spherically integrated to determine the total ion beam current and the plume divergence half-angle. The ion beam current is used to determine what fraction of the discharge current is exhausted into the plume and used to generate thrust whereas the divergence half-angle is a measure of the off-axis acceleration of the plume ions [14].

4.3.5.2 Design and Implementation

A JPL-style nude Faraday probe similar in design to the ones previously used by Walker and Xu was used for this work [31, 74]. A schematic of this probe is shown in Figure 4.9 and all relevant dimensions are given in the work by Walker [31]. As shown in Figure 4.9, the chosen probe implements several improvements over the most basic Faraday probe described in Section 4.3.5.1. The first of these is the inclusion of an additional aluminum guard electrode surrounding the main collector. This guard electrode is electrically isolated from the collector by a small gap. During operation, the guard electrode is biased to the same potential as the collector in order to create a flat, uniform sheath across the collector face and prevent edge effects from impacting the ion current density measurements [14, 31]. If left unaddressed, these edge effects can artificially increase the effective area of the collector and therefore artificially inflate the measured ion current density [14, 31].

The second design improvement seeks to minimize the impacts of secondary electron emission (SEE) on the measurements. SEE occurs when an ion strikes the collector with sufficient energy to cause the emission of an electron from the surface [6, 31, 73, 77]. This electron emission artificially increases the collected current because an emitted electron appears identical to a collected ion in terms of measured current. To limit the impact of SEE, the aluminum collector was spray coated with tungsten, a material with low SEE yield. This technique has been proven effective in limiting the impact of SEE on the ion current density measurements [14, 31].

The circuit used to obtain Faraday probe measurements for this work is shown in Figure 4.9. During operation, the guard and collector electrodes were both biased using a Xantrex XEL 60-1.5 power supply. The electrode bias was selected by taking I-V characteristics of the probe collector at a position 1-m downstream along the centerline of each of the HETs tested in this work [82]. Based on these characteristics, a bias of -30 V was shown to be able to repel electrons without causing sheath expansion and thus artificially increasing the collection area. The collector signal was passed through a 100-Ω shunt and the resultant

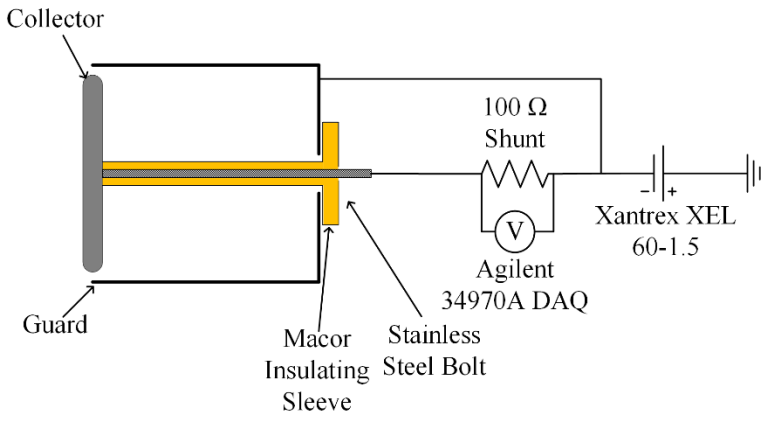

Figure 4.9: Faraday probe schematic.

voltage drop across the resistor was measured using an Agilent 34970A Data Acquisition/Data Logger Switch Unit (DAQ).

The angular traverse of the probe through the plume and the DAQ were simultaneously controlled using a LabVIEW Virtual Instrument to ensure synchronous recording of the angular position of the probe and the spatially-resolved collected current. To reduce any systematic directional bias, two angular sweeps of the Faraday probe were taken in succession at each measurement condition in opposing directions (i.e., one sweep was taken each from -90º to 90º and from 90º to -90º relative to HET centerline). For all measurements reported in this work, the Faraday probe was placed on an arc located 1 m downstream of the exit plane of the HETs and swept at a speed of 2 deg/s. The reported ion beam currents and plume divergence half-angles represent the average of the results computed for each of the two angular sweeps taken for each condition. A representative Faraday probe scan is shown in Figure 4.10.

4.3.5.3 Uncertainty Analysis

A detailed analysis of the uncertainty associated with Faraday probe measurements is presented in previous work by Brown and Gallimore [14, 79]. Among the sources of error identified in this work are changes in the effective collection area to account for ions striking the lateral faces of the collector via the gap between the collector and guard electrodes as well as variations in probe angle and path length relative to channel centerline as the probe is swept through the plume caused by the geometric offset between the axis of rotation of the Faraday probe sweep (i.e., thruster centerline) and the location where ions are generated and accelerated (i.e., channel centerline). Brown and Gallimore also developed a detailed analysis procedure including corrections for these various effects

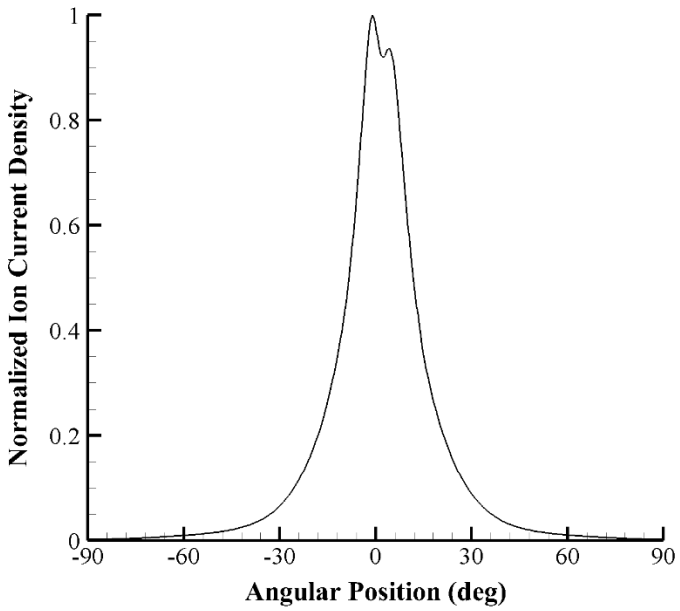

Figure 4.10: Representative Faraday probe scan acquired using a 6-kW HET operating at an anode mass flow rate of 20 mg/s and facility pressure of 1×10^{-5} Torr-Xe.

capable of yielding uncertainties of approximately ± 5% for the ion beam current and ± 1.5% for the 95% plume divergence half-angle [14, 79]. As the analysis and measurement techniques used in this work are identical to those detailed by Brown and Gallimore, these uncertainties are also used for all data presented in this work.

4.3.6 Cylindrical Langmuir Probe

4.3.6.1 Theory of Operation

In this work, measurements of the electron temperature, ion and electron number densities, and auxiliary measurements of the plasma potential were obtained using cylindrical Langmuir probes. Relative to the other probes used in this work, the operating principle of the cylindrical Langmuir probe is relatively simple. During operation, the

probe circuit varies the voltage applied to the probe tip and measures the current collected yielding a current-voltage (or I-V) characteristic [73, 83]. A representative I-V characteristic is shown in Figure 4.11. Following the standard convention, positive current corresponds to electron current collection.

As indicated in Figure 4.11, the I-V characteristic generated by a Langmuir probe can be further subdivided into three regions [73, 83]. At low bias voltages, the probe tip collects mainly ions and the resultant current is known as the ion saturation current [73, 83]. At high bias voltages, the probe tip collects mainly electrons and the resultant current is known as the electron saturation current [73, 83]. Between these two regions is the transition region in which the probe collects both ions and electrons [73, 83]. Measurements of the plasma number densities, electron temperature, and plasma potential can be made via analysis of each of these three regions.

For plasmas with Maxwellian electron distributions, the transition region will exhibit exponential behavior (as it does in Figure 4.11). If plotted on a semi-log plot, this region will thus appear as a straight line, and the electron temperature is proportional to the inverse of the slope of the electron current in this region [73, 83]. In order to isolate the electron current, the ion current is approximated by fitting a line through the ion saturation region and extrapolating it through the transition region. This ion current is then subtracted from the total collected current thus yielding only the electron current collected by the probe tip [77]. The plasma potential can similarly be found by fitting straight lines to the transition and electron saturation regions on a semi-log plot of the I-V characteristic of the electron current. The voltage at which these lines intersect is the plasma potential [6, 73, 83]. It is important to note that the electron distribution in a HET plume may not be strictly

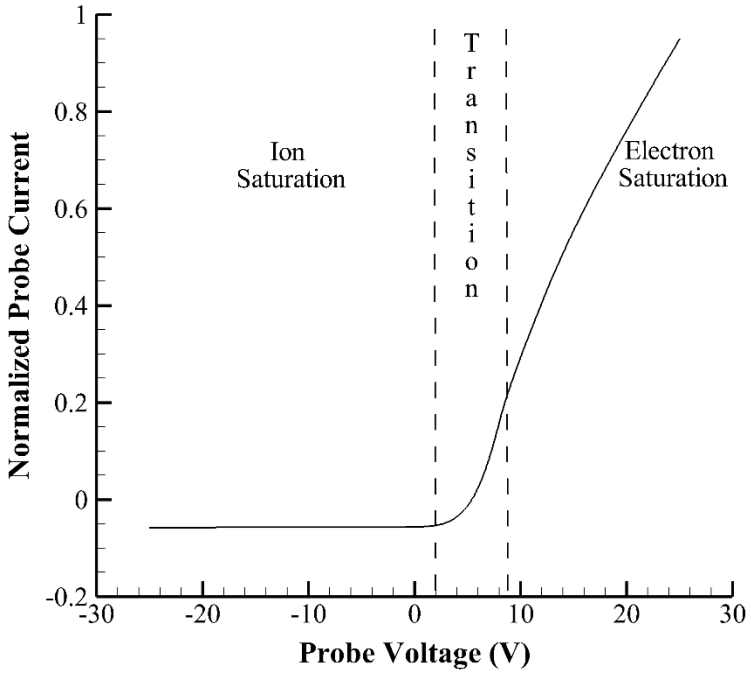

Figure 4.11: Representative Langmuir probe I-V characteristic acquired using a 6-kW HET operating at an anode mass flow rate of 20 mg/s and facility pressure of 1 × 10^{-5} Torr-Xe.

Maxwellian, nevertheless, the above approach can still be used to determine the electron temperature [84].

The electron and ion number densities are found via analysis of the electron and ion saturation regions, respectively. Unlike the electron temperature and plasma potential, these parameters cannot be found directly from the I-V characteristic. Instead, an appropriate probe theory describing the motion of the ions and electrons relative to the probe tip must be applied in order recover the species number density from the ion and electron saturation currents [6, 73, 83]. For this work, orbital-motion-limited (OML) theory was used. It is important to note that the plasma in the plume of a HET can be considered quasi-neutral [2, 6, 12, 77]. Thus, the ion and electron number densities are approximately equal and can be referred to jointly as the plasma number density.

4.3.6.2 Design and Implementation

The probes used in this work were constructed using a tungsten tip measuring 0.13 mm in diameter and approximately 22 mm long housed inside an alumina tube. The tip was bent into a right angle such that the normal to the collecting surface was oriented parallel to the device centerline axis. The transverse orientation of the collecting surface relative to the ion flow direction was chosen in order to avoid the increased ion collection due to collisional and end effects observed for Langmuir probes oriented parallel to the direction of bulk motion in supersonic flowing plasmas [85].

The sizing of the probe tip was driven by the requirements associated with application of OML theory. Specifically, application of this theory requires that the probe radius and length be much smaller and larger, respectively, than the calculated sheath thickness. For the HETs used in this work, the minimum Debye length in the vicinity of the Langmuir probe can be calculated using previous measurements of the average ion number density and electron temperature taken using the 6-kW HET. Specifically, using an average ion number density of 5×10^{16} m^{-3} and electron temperature of 1 eV, the Debye length can be estimated to be on the order of 0.03 mm. As the sheath size can be approximated as 5-10 Debye lengths (0.15 mm to 0.3 mm), the employed probe tips thus satisfy all requirements for accurate application of OML theory [2, 6, 77, 81, 83].

A Keithley 2410 1100 V SourceMeter was used to control the probe tip bias and measure the collected current. During each current-voltage sweep, the tip voltage was varied over a range of -30 V to 30 V in 0.2-V increments with a 300-ms dwell time. The SourceMeter was controlled and logged in real-time using a LabVIEW Virtual Instrument to ensure synchronous recording of the probe bias voltage and collected current. A

minimum of five sweeps were taken per measurement. The analyzed results were then averaged together to determine the mean value for each condition; the standard deviation between the five scans was also computed to determine the repeatability of the measurement.

4.3.6.3 Uncertainty Analysis

A detailed analysis of the uncertainty associated with Langmuir probe measurements is presented in detailed review of electric probes for plasmas by Demidov, Ratynskaia, and Rypdal [83]. The sources of error identified in this work include local plasma perturbations by the probe holder, SEE from the probe tip driven by impurities on the probe surface and material imperfections leading to an uneven work function across the probe tip, systematic errors associated with the measurement electronics, and perturbations of the local plasma due to current collection by the probe [83]. Taken together, these effects yield uncertainties of ± 20% for electron temperature, ± 50% for ion and electron number densities, and ± 3 V for the plasma potential [73, 83, 86].

4.3.7 Emissive Probe

4.3.7.1 Theory of Operation

In this work, measurements of the plasma potential were obtained using emissive probes. The theory of operation of emissive probes is very similar to that of Langmuir probes described in Section 4.3.6.1. As with Langmuir probes, during operation, the probe circuit varies the voltage applied to the probe tip and measures the collected current to generate a current-voltage characteristic [87]. However, unlike with Langmuir probes, the

probe tips in emissive probes are actively heated to a sufficient threshold to cause thermionic emission of electrons [87].

The emission of electrons from the probe tip changes the nature of the I-V characteristic. Instead of measuring which charged species are collected from the plasma (as with a Langmuir probe) the I-V characteristic of an emissive probe measures how many of the emitted electrons are able to enter the bulk plasma [87]. At bias voltages below the plasma potential, all emitted electrons can enter the plasma and are measured as emitted current. As the bias voltage increases, the emitted current decreases exponentially as only those electrons with the highest energy are able to escape the probe sheath and enter the plasma [87]. Much as the slope of a Langmuir probe I-V characteristic is proportional to the inverse of the electron temperature in the transition region when plotted on a semi-log plot, the slope in the transition region of the emissive probe characteristic is proportional to the inverse of the emitter temperature [87]. Since the emitter temperature is usually much smaller than the electron temperature, the knee in the transition region associated with the plasma potential becomes much more defined for emissive probes and the plasma potential can be determined more accurately [87].

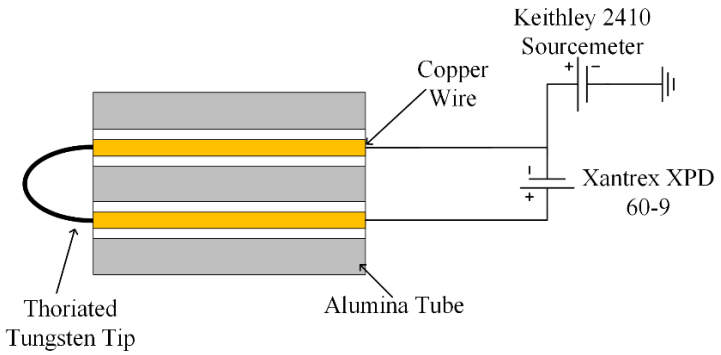

Figure 4.12: Emissive probe schematic and electrical circuit.

4.3.7.2 Design and Implementation

The emissive probes used in this work are identical in design to those used by Xu [74] and Langendorf [88]. The probes were constructed from a 0.13-mm-diameter loop of thoriated tungsten wire bent into a "hairpin" tip with a bend radius of approximately 0.75 mm. The filaments were connected via a mechanical press-fit to PTFE-insulated copper wire housed in a 4.8-mm-diameter double-bore alumina tube [88]. The probe heating current was controlled using a Xantrex XPD 60-9 power supply. A Keithley 2410 1100 V SourceMeter was used to control the probe tip bias and measure the collected current. A schematic of the probe and measurement used in this work is shown in Figure 4.12.

The inflection point method was used for data collection and analysis. During each measurement, the heating current to the emissive probe filament was varied over five heating current values. These heating current values varied throughout the probe lifetime,

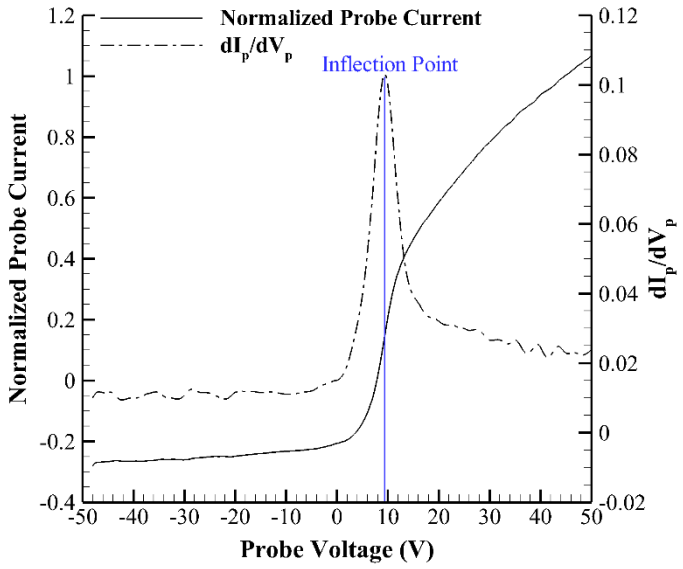

Figure 4.13: Representative emissive probe I-V characteristic acquired using a 6-kW HET operating at an anode mass flow rate of 20 mg/s and facility pressure of 1 × 10^{-5} Torr-Xe.

but were within a range between 1.6 A and 1.8 A. One bias sweep was taken per heating current. During each bias sweep, the probe voltage (V_p) was varied over a range of -50 V to 50 V in 1 V increments with a 300 ms dwell time. The inflection point was then found in each of the I-V traces, and the plasma potential was found by linearly extrapolating these values to zero emission current [87]. The inflection point was found by determining the maximum of the derivative of the current collected by the probe (I_p) with respect to probe voltage; these curves were smoothed using a RLOESS algorithm to remove noise. The emission current for a given trace was determined by averaging the emitted electron current in the region biased below the plasma potential and then subtracting the collected ion saturation current from an I-V characteristic acquired when the probe was not emitting [88]. A sample I-V characteristic is shown in Figure 4.13 and a sample extrapolation to

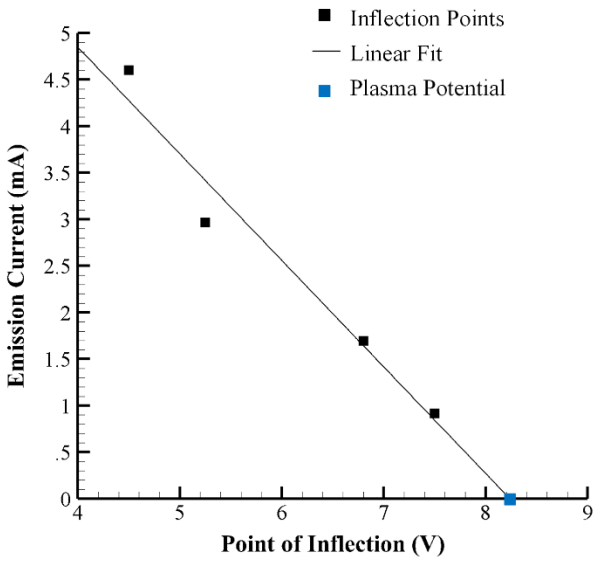

Figure 4.14: Representative extrapolation of emissive probe I-V characteristic inflection points to determine plasma potential. Data acquired using a 6-kW HET operating at an anode mass flow rate of 20 mg/s and facility pressure of 1×10^{-5} Torr-Xe.

zero emission current is shown in Figure 4.14.

4.3.7.3 Uncertainty Analysis

Previous work investigating the uncertainty associated with using the inflection point method indicated that the resultant uncertainty in plasma potential (ΔV_p) can be approximated using the electron temperature and fundamental charge as shown in Eq. (4.13).

$$\Delta V_p = \frac{T_e}{10e} \tag{4.13}$$

Peak electron temperatures (as determined using Langmuir probe measurements) near the emissive probes are approximately 3 eV for the HETs used in this work, thus yielding an uncertainty of ± 0.3 V for the plasma potential measurements.

However, the use of a DC current to heat the emissive probe results in an offset between the voltage sourced by the SourceMeter and the voltage applied to the probe tip due to the voltage drop across the lines and the probe tip itself. This voltage offset yields an additional systematic uncertainty for the plasma potential measurements that can be estimated using the voltage required to source the probe heating current [87]. Combining the uncertainties associated with the inflection point method and the probe tip voltage offset yields a conservative combined uncertainty estimate of ± 1.5 V.

4.4 Experimental Approach

4.4.1 Restatement of Research Goals

Although enumerated in Section 1.4, for convenience, it is useful to restate the hypothesis and research goals of this work to motivate the experimental approach outlined

in this section and clearly correlate the performed experiments to the sated objectives. The overall hypothesis of this work is that a bulk background flow of neutrals exists inside vacuum test facilities and changes as a function of facility-specific design and operating parameters (e.g., pump placement and pressure modulation technique). It is further hypothesized that this bulk background flow, in addition to the random flux of background neutrals, is a non-negligible contributor to HET neutral ingestion and the concomitant impacts on performance and plume characteristics.

To test this hypothesis, the research goals of this work can be distilled into finding the answers to two overarching questions (RQ 1 and RQ 2) and two corollary questions (RQ 1A and RQ 1B):

RQ 1: Do bulk motions constitute a non-negligible component of the background neutral flow field inside vacuum facilities?

RQ 1A: Are the bulk motions sensitive to facility-specific parameters such as pump placement and pressure modulation technique?

RQ 1B: Do the bulk motions constitute a non-negligible component of the HET ingestion flow?

RQ 2: How does HET operation change as a function of ingestion mass flow rate (instead of pressure measured at a given location)?

Accordingly, two experiments were performed, one to answer each research question. These experiments are outlined in the remainder of this section and the results are presented and analyzed in Chapters 5 and 6, respectively.

4.4.2 Experiment 1: Background Neutral Flow Field Characterization

4.4.2.1 Phase 1: IHD2000-EM11

The goal of the first experiment was to empirically investigate the existence of a bulk background flow of neutrals within the ground test facility and characterize the sensitivity approach detailed in Section 3.1, observed changes in the mean discharge current can be used to approximate changes in ingestion mass flow rate into the HET. Comparing these empirical results to predictions generated by the background flow model yields an additional data set with which to validate the model and provide further information to determine if the bulk motions described by the model are present in the vacuum test facility and, if so, how they influence HET ingestion. These data will thus provide further answers to RQ 1 and RQ 1A.

A schematic of the VTF-2 configuration used for this phase of the experiment is shown in Figure 4.15. The chamber operating conditions used during this phase of the experiment are shown in Table 4.2. These chamber conditions were selected to empirically replicate

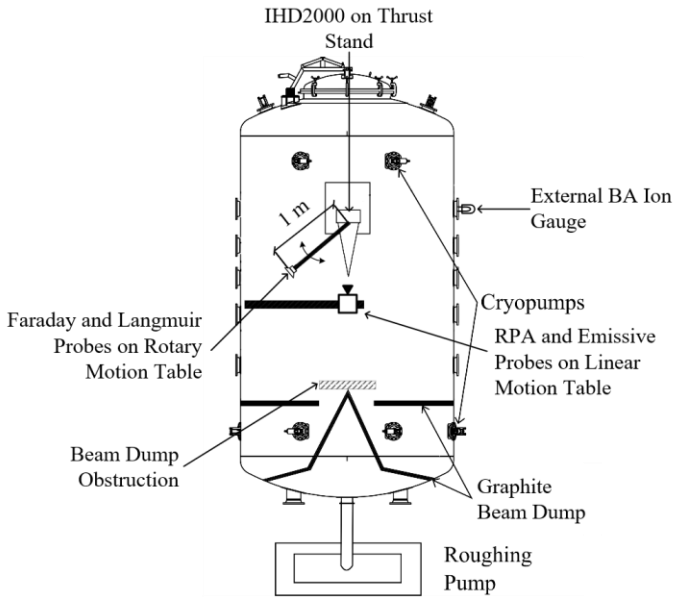

Figure 4.15: Schematic of VTF-2 configuration for IHD2000-EM11 testing (not to scale).

Table 4.2 Chamber operating conditions used during IHD2000-EM11 testing.

Chamber Configuration	Number of Active Cryopumps		Bleed Flow (mg/s)	Bleed Flow Direction	Facility Pressure (Torr-Xe)
	Upstream	Downstream			
Baseline	4	6	0	-	1×10^{-6}
			10	Axial	5×10^{-6}
			16	Axial	9×10^{-6}
			16	Radial	9×10^{-6}
			35	Axial	2×10^{-5}
			35	Radial	2×10^{-5}
Downstream Pumps	0	4	0	-	9×10^{-6}
			2	Axial	9×10^{-6}
			2	Radial	9×10^{-6}
			10	Axial	2×10^{-5}
			10	Radial	2×10^{-5}
			35	Axial	5×10^{-5}
Upstream Pumps	4	0	0	-	9×10^{-6}
			2	Axial	9×10^{-6}
			2	Radial	9×10^{-6}
			10	Axial	2×10^{-5}
			10	Radial	2×10^{-5}
			35	Axial	5×10^{-5}

the analytical model studies performed in Section 3.2. Specifically, the sensitivity of the background flow field to pump placement was assessed by acquiring measurements with only the four upstream pumps on and then again with four of the six downstream pumps on. To control variables, the four chosen downstream pumps were in the same azimuthal position relative to the thruster as the upstream pumps. Data were also acquired by arriving at several common pressures (i.e., 1×10^{-5} Torr-Xe, 2×10^{-5} Torr-Xe, and 5×10^{-5} Torr-Xe) different ways to empirically validate the model-predicted sensitivity of ingestion flow rate to pressure modulation technique. Finally, the measurements were acquired twice at several chamber conditions: once each with the bleed flow orifice parallel and perpendicular to the thrust vector to assess the sensitivity of the results to this assumption and further evaluate the sensitivity of ingestion mass flow rate to the method of pressure

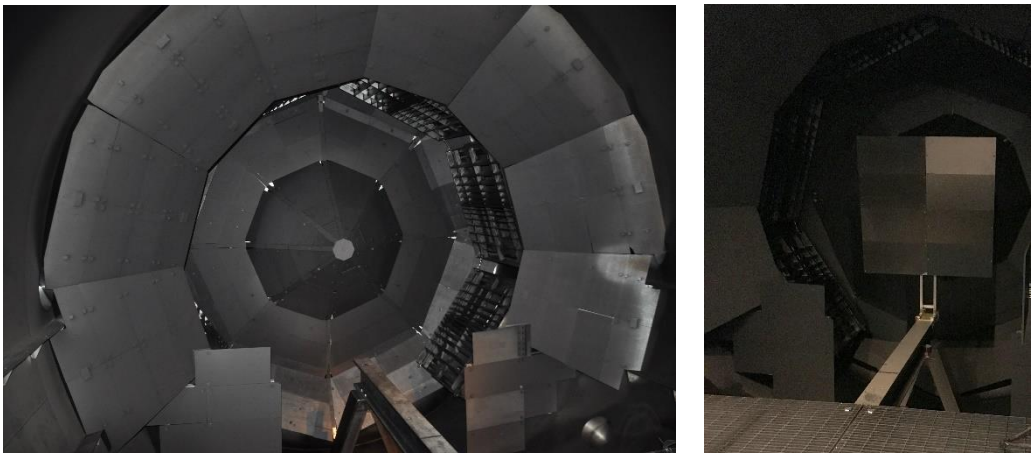

(a) **(b)**

Figure 4.16: (a) Conic and (b) flat plate beam dump configurations for VTF-2.

modulation. Identical to the approach taken by Reid during H6 testing in the LVTF, the radial bleed flow orifice was located beneath the thruster and oriented such that the flow of propellant impacted the underside of the thrust stand mounting structure [22]. To control variables, the axial bleed flow orifice was placed in the same location, but was oriented to inject flow in the downstream direction. Toggling between these two orifices was accomplished without breaking vacuum or halting thruster operation using a pair of Peter Paul E22G9DCCM in-situ solenoid valves that could be actuated from outside the vacuum facility. Overall, these data are used to further validate the background flow model and provide empirical answers to RQ 1B.

As noted in Section 3.3, the facilities used to generate the data used for initial validation of the background flow model have beam dumps composed of flat plates of graphite. Unlike these facilities, VTF-2 nominally has the conic beam dump configuration shown in Figure 4.16(a). To more closely replicate the downstream reflection surfaces in these other facilities as well as remove any impact on the results from variations in this geometry, for

this phase of the experiment, the removable flat plate beam dump shown in Figure 4.16(b) was installed in front of the nominal beam dump. The flat plate beam dump was composed of identical graphite panels to those used in the conic beam dump and measured 0.6 m long and 0.6 m wide. The size was selected to completely obstruct the center conic portion of the nominal beam dump when viewed from the HET test station.

4.4.2.2 Phase 2: H6 and 6-kW HET

The data acquired in the first phase of this experiment ultimately provides measurements of a quantity (i.e., mean discharge current) that changes because of variations in the background flow field; it is not a direct measurement of the changes in the flow field itself. As shown in Figure 2.1(b), the relevant flow field parameters for describing the aspects of the background neutral flow most germane for HET ingestion are the one-directional number densities at the surface immediately downstream of the HET exit plane (i.e., n_{D+} and n_{D-}). In the second phase of this experiment, these quantities and their variation with facility parameters were directly measured using the Stabil-Ion Series 370 gauge discussed in Section 4.3.3 during operation of the H6 and 6-kW HET.

A schematic of the chamber configuration used for this phase of the experiment is shown in Figure 4.17. As also shown in Figure 4.4, the Stabil-Ion gauge was mounted to a rotary motion stage located approximately 0.5 m radially outward from and centered about 0.1 m upstream of the HET exit plane. At each facility operating condition, measurements were taken with the gauge facing upstream and downstream to quantify the positive and negative fluxes across surface containing the HET exit plane. To quantify the flow in the radial direction and thus assess the validity of the one-dimensional flow assumption, measurements were also taken for the gauge facing the HET (i.e., radially).

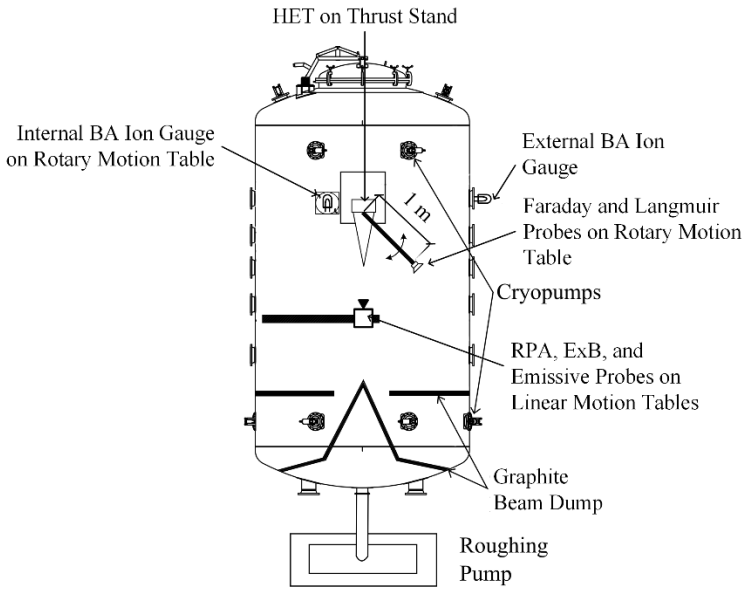

Figure 4.17: Schematic of VTF-2 configuration for H6 and 6-kW HET testing (not to scale).

The chamber operating conditions used during this phase of the experiment are shown in Table 4.3. As with those detailed in Section 4.4.2.1, these chamber conditions were again selected to empirically replicate the analytical model studies performed in Section 3.2. Specifically, chamber conditions were again chosen to achieve several common pressures (i.e., 1×10^{-5} Torr-Xe, 2×10^{-5} Torr-Xe, and 4×10^{-5} Torr-Xe) different ways in order to test the further test the finding from Section 3.2.3 that pressure magnitude is an insufficient parameter to describe the ingestion mass flow rate into HETs. In order to garner insight into the impact of beam dump geometry on the background flow field, for this phase of the experiment, the flat plate beam dump was removed and data was acquired using the conic beam dump configuration shown in Figure 4.16(a). When combined with the data from phase 1, the data generated by this experiment should provide empirical evidence to support the analytical attempts in Chapter 3 to answer RQ 1 and its two corollaries RQ 1A and RQ 1B.

Table 4.3 Chamber operating conditions used during H6 and 6-kW HET testing.

Chamber Configuration	Number of Active Cryopumps		Bleed Flow (mg/s)	Bleed Flow Direction	Facility Pressure (Torr-Xe)	HETs Tested
	Upstream	Downstream				
Baseline	4	6	0	-	1×10^{-5}	H6, 6-kW HET
			5	Axial	1×10^{-5}	H6
			12.5	Axial	2×10^{-5}	H6
			12.5	Radial	2×10^{-5}	H6
			20	Axial	2×10^{-5}	H6
			20	Radial	2×10^{-5}	H6
Six pumps	3	3	0	-	2×10^{-5}	H6, 6-kW HET
			5	Axial	2×10^{-5}	H6
			12.5	Axial	3×10^{-5}	H6
			20	Axial	4×10^{-5}	H6, 6-kW HET
			25	Axial	4×10^{-5}	H6
			40	Axial	5×10^{-5}	H6, 6-kW HET

4.4.3 Experiment 2: Hall Effect Thruster Performance Characterization

The goal of the background neutral flow field characterization detailed in Section 4.4.2 is to establish the link between the bulk background flow of neutrals in the test facility and neutral ingestion by HETs. The second experiment performed in this work seeks to quantify the concomitant effects on HET operation and determine how the observed HET sensitivity to facility backpressure correlates to the background flow field to provide answers to RQ 2. To accomplish this, measurements of thrust, ion voltage distribution, ion current density profile, and plume plasma properties (i.e., plasma potential, ion/electron number density, and electron temperature) were acquired for the H6, 6-kW HET, and

IHD2000-EM11. As noted in Section 4.3, the diagnostics used to acquire these measurements were the thrust stand, RPA, Faraday probe, and Langmuir and emissive probes, respectively. As shown in Figure 4.18 and Figure 4.19, for this work, the RPA and emissive probes were positioned using the linear motion stages whereas the Faraday probe and Langmuir probes positioned using the rotary motion stage. It is important to note that, as shown in Figure 4.18, although an ExB probe was also mounted on the linear motion stages, it was not used as part of this work. Measurements of the time-resolved discharge current were also acquired for each HET to allow analysis of the discharge current oscillations and help pinpoint how ingestion impacts the ionization processes in the HET.

The performance and plume measurements were acquired concurrently with the measurements taken as part of the background neutral flow field characterization. As such, data were acquired for the IHD2000-EM11 for the chamber configuration shown in Figure 4.15 and the conditions shown in Table 4.2, while data for the H6 and 6-kW HET were acquired for the chamber configuration shown in Figure 4.17 and the conditions listed in

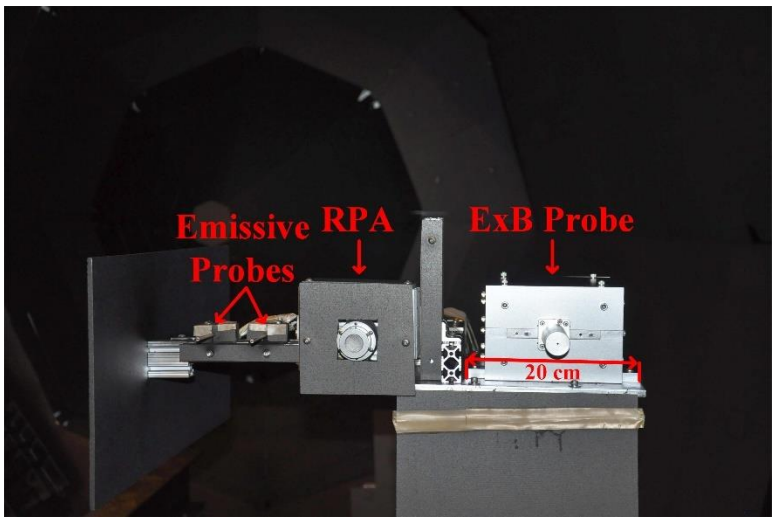

Figure 4.18: Diagnostics mounted on the linear motion stage: emissive probes (2x), RPA, and ExB probe.

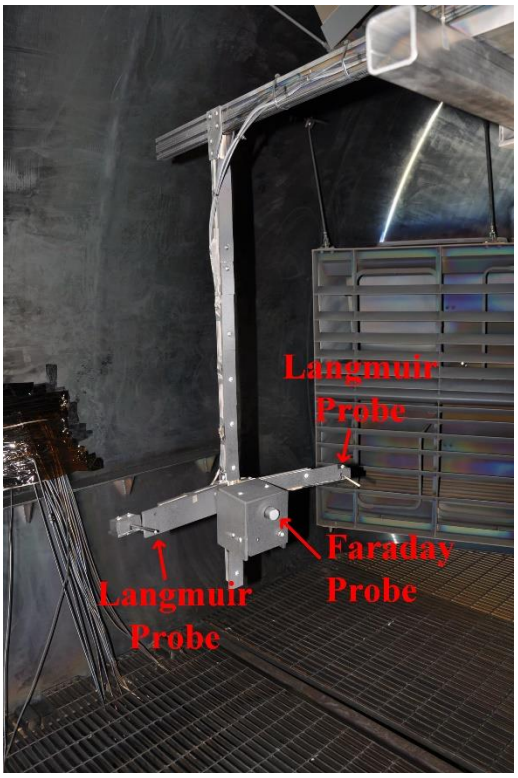

Figure 4.19: Diagnostics mounted on the rotary motion stage: Langmuir probes (2x) and Faraday probe.

Table 4.3.

In order to determine the relationship between magnetic field topography, ingestion mass flow rate, and HET stability, once plume and pressure measurements were acquired for the H6 and 6-kW HET, the peak radial magnetic field strength was varied by changing the magnitude of the current supplied to each magnet while maintaining a constant ratio of current supplied to the inner, outer, and trim magnets as done in the works of Hofer and Sekerak [54, 89]. The peak radial magnetic field strength was varied between 60% and 120% of the nominal value in increments of 10% with a dwell time of 5 minutes at each condition for the H6. For the 6-kW HET, the peak magnetic field strength was varied between approximately 70% and 190% of the nominal value in increments of

approximately 12% with a dwell time of 3 minutes at each condition. Time-resolved measurements of the discharge current were acquired at each of these magnet settings for all chamber conditions listed in Table 4.3.

CHAPTER 5. BACKGROUND FLOW FIELD CHARACTERIZATION

5.1 Chapter Overview

This chapter is focused on presenting and analyzing the data acquired as part of both phases of the background flow field characterization experiment outlined in Section 4.4.2. The results from the first phase of the experiment (i.e., the test conducted using the IHD2000-EM11) are presented in Section 5.2 whereas those from the second phase (i.e., the test conducted using the H6 and 6-kW HET) are presented in Section 5.3.

Each section of this chapter is structured identically. First, the empirical results are presented and compared to the predictions of the background flow model. This comparison serves to further validate the model and determine if the physical mechanisms it describes (i.e., the bulk motion of background neutrals) exist and how they impact HET ingestion characteristics. Based on these comparisons, if needed, changes to the model are suggested and developed to refine its description of the bulk background flow field and provide answers to RQ 1 and RQ 1A.

Next, results are presented and discussed showing the impact of varying various facility operating parameters on the bulk background flow. The purpose of these discussions is twofold. First, it provides direct answers to RQ 1B and validates the analytical investigation presented in Section 3.2. This additional validation ensures that the physical description of these sensitivities is correct in the background flow model. Second, these empirical trade studies will help inform vacuum facility designers and operators on how to vary test facility parameters to control and modulate the background neutral flow field.

5.2 IHD2000-EM11 Results

5.2.1 Comparison of Background Flow Model and Empirical Results

As noted in Section 4.4.2.1, during this phase of the experiment, measurements of the mean discharge current of the IHD2000-EM11 were acquired as the pressure in VTF-2 was varied across the chamber conditions shown in Table 4.2. Using the approach detailed in Section 3.1, measured changes in the mean discharge current can be used to approximate changes in ingestion mass flow rate into the HET. The results are shown as a function of bleed mass flow rate in Figure 5.1(a) for the baseline chamber configuration, Figure 5.1(b) for the downstream pumps configuration, and Figure 5.1(c) for the upstream pumps configuration. The values in Figure 5.1 correspond to the change in ingestion mass flow rate (or equivalently discharge current) relative to the baseline case of 10 active cryopumps with no bleed flow. A minimum of ten measurements of the mean discharge current were acquired at each chamber operating condition with each measurement encompassing approximately 400 fundamental periods. The empirical data shown in Figure 5.1 represents the average across these ten measurements, while the error bars correspond to the standard deviation.

Consistent with the approach taken in Chapter 3, the background flow model was similarly used to compute the difference in ingestion mass flow rate for the IHD2000-EM11 in VTF-2 for the same chamber configurations. The results are plotted alongside the empirical results in Figure 5.1. Also shown in the figure are the changes in ingestion mass flow rate predicted by the thermal model. Consistent with the approach taken by Walker and Gallimore, the number densities used for the thermal model calculations correspond to

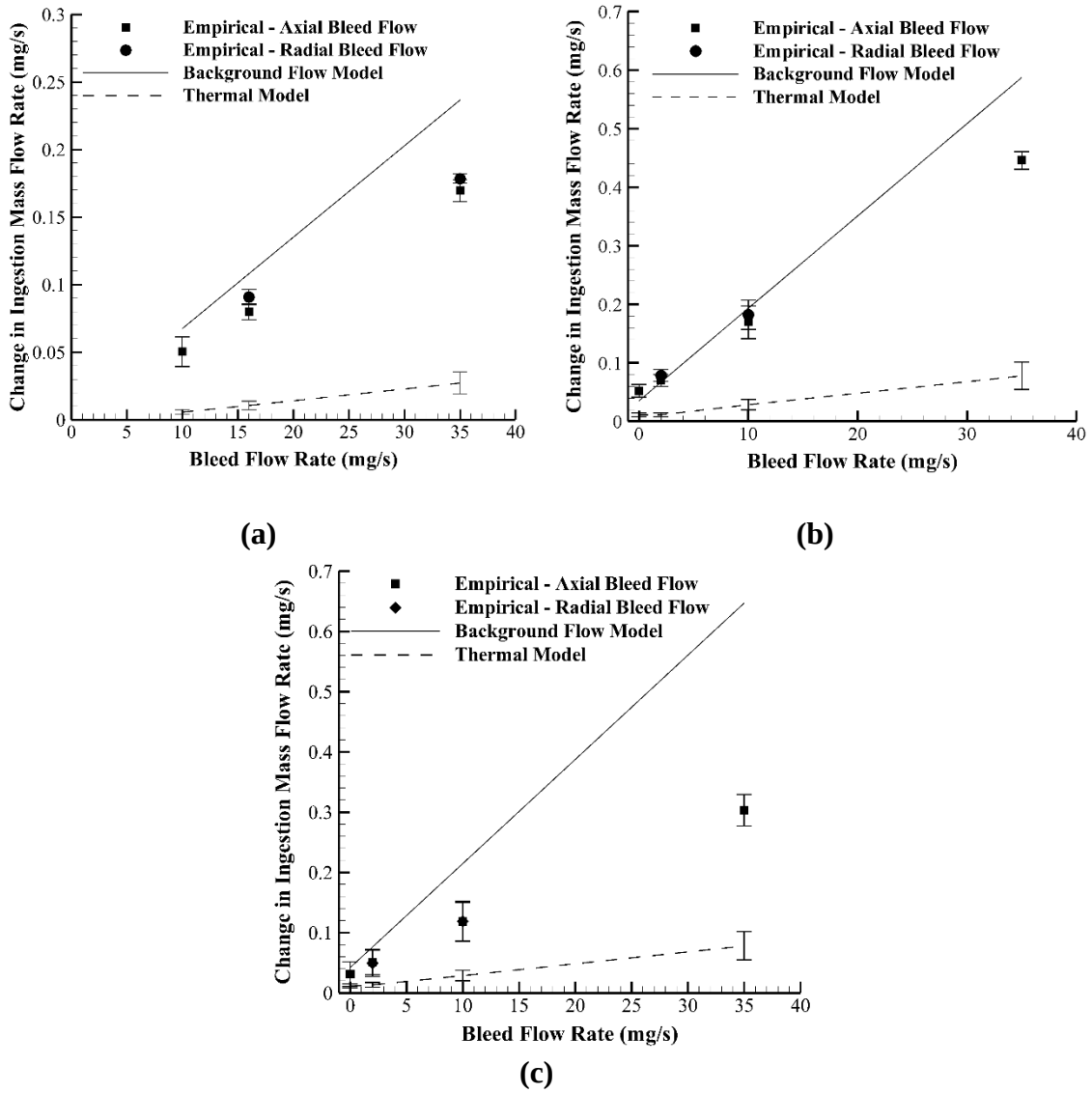

Figure 5.1: Change in IHD2000-EM11 ingestion mass flow rate for the (a) 10 pump, (b) downstream pump, and (c) upstream pump chamber configurations.

the empirical measurements taken using the single exterior hot-cathode ionization gauge described in Section 4.1 [29]. The uncertainty in the computed ingestion flow rates from the thermal model due to the reported 20% pressure measurement uncertainty is captured by the displayed error bars.

Consistent with previous results, the predictions of the thermal model are, on average, 80% less than the empirical results. By contrast, the predictions of the background flow model are, on average, 34% greater than the empirical measurements. Although the predictions of the background flow model are 50% closer (on average) than those of the thermal model, the deviation between these predictions and the empirical results is much larger than was seen during the initial validation performed in Chapter 3. During those validation studies, the average percent difference between the predictions of the background flow model and the empirical results was on the order of 10%. A closer inspection of the results in Figure 5.1 reveals that the tendency of the background flow model to overestimate the empirical measurements worsens at higher bleed mass flow rates. As an example, for the downstream pumps configuration shown in Figure 5.1(b), the percent difference between the background flow model and the empirical results is less than the empirical uncertainty for bleed mass flow rates of 0 mg/s and 10 mg/s, whereas it grows to 32% for the 35 mg/s bleed mass flow rate.

The reason for this stems from a pair of shortcomings in the assumptions used to introduce bleed flow into the modeling domain and describe the collisional scattering of the background neutrals. As discussed in Section 2.2.1, consistent with previous work into background flow modeling in HET test facilities, it is assumed that all particles injected into the HET anode travel unimpeded to the downstream facility surfaces, thermalize, and

reflect [37]. Thus, the downstream facility surfaces are considered as a source of neutral xenon entering the chamber at the thruster anode mass flow rate, through the chamber cross-sectional surface area, and at wall temperature. As discussed in Section 3.1.3, it is assumed that any bleed flow enters chamber in the same way (i.e., bleed flow is assumed to enter the modeling domain via a source located on the downstream facility surfaces).

This assumption did not cause significant error during the initial validation performed in Chapter 3 as the bleed flow orifices in those works were either located near the downstream facility surfaces or the introduced bleed flow was small enough that these neutrals only composed a small fraction of the background flow field. However, for the experiments performed as part of this work, the bleed flow orifice was located near the HET exit plane, oriented (for the axial bleed flow cases) to inject the bleed flow parallel to the thrust vector towards the downstream facility surfaces, and used to inject mass flow rates up to 8.75 times the anode mass flow rate to the HET. Thus, in order to be ingested, these particles (which now compose a more significant fraction of the background flow field) must first survive an initial transit through the downstream pump region without striking and condensing on a pump before joining the reflected background flow and traveling upstream towards the thruster. The loss of neutrals during this initial transit is not captured by the assumptions discussed above and could contribute to the overestimation of the ingestion mass flow rate by the background flow model. It is important to note that, as discussed in Section 2.2.1, this loss mechanism is also neglected for unionized propellant exhausted from the HET. However, as typical HET mass utilization efficiencies are on the order of 90%, this oversight only impacts a very small percentage of the HET propellant flow and so did not generate significant error during the analytical studies [2].

To correct for this additional bleed flow loss mechanism, the model was modified to separately account for the influx of particles into the chamber due to the bleed flow orifice (n_{bleed}). An updated model representation of VTF-2 capturing this change is shown in Figure 5.2. In this updated model, it is assumed that the neutrals injected as part of the bleed flow enter the modeling domain at the thermal-diffusive speed characterized by chamber wall temperature traveling in the downstream direction from surface D. Applying this assumption yields an updated expression for the number density of neutrals used to compute the ingestion mass flow rate into the HET (i.e., n_{C+}). This updated expression is shown in Equation (5.1). In Equation (5.1), the n_{bleed} term is computed identically to the n_{in} term by replacing the anode mass flow rate with the bleed mass flow rate in Equation (2.14).

$$n_{C+} = \frac{n_{in} + n_{bleed} - \alpha s_d n_{bleed}}{1 + (\alpha s_d - 1)^2(\alpha s_e - 1)(\alpha s_u - 1)^2} \tag{5.1}$$

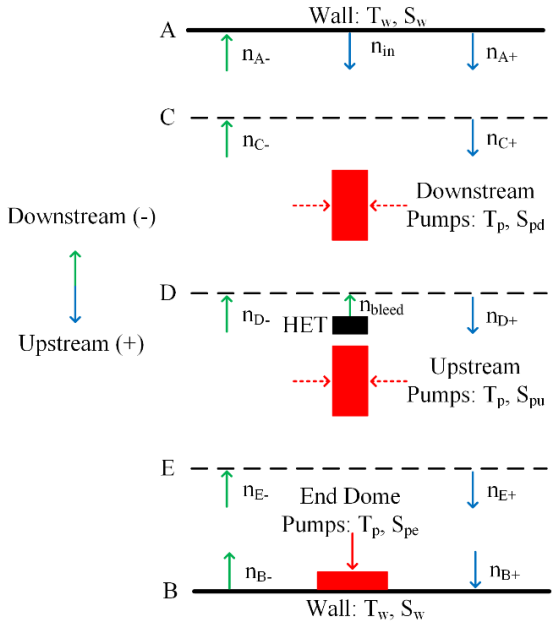

Figure 5.2: Updated background flow model representation of VTF-2 to account for axial bleed flow injection.

The second shortcoming of the original model lies in the assumptions used to describe the impact of the HET plume on the bulk motions of the background neutrals. As discussed in Section 2.2.1, the HET plume flow is assumed to collisionally scatter background neutrals traveling towards the HET exit plane. However, the only collisions that are considered are the elastic collisions between the background neutrals and the unionized propellant exhausted by the HET. Thus, collisions between background neutrals and bleed flow neutrals as well as between background neutrals moving in opposite directions are neglected as being small in comparison. While sufficient to describe the collisional dynamics downstream of the HET in the limit of low bleed mass flow rate and low background neutral density relative to the plume flow, in this work, the bleed flow introduced during IHD2000-EM11 was greater than the mass flow rate through the HET anode. This caused a background neutral density of the same order as the neutral density due to unionized propellant in the plume. Furthermore, the bleed orifice was located at the same axial location of the HET exit plane. Thus, (for the case of the axially-oriented bleed flow orifice) all injected bleed flow particles would have entered the region downstream of the HET exit plane and, due to the quantity of flow injected, been a significant contributor to the collisional scattering of the bulk background flow traveling in the upstream direction. In order to account for these additional interactions, the employed collisional model needs to be updated.

As discussed in Section 2.2.1, the collisional cross-sections employed in the original background flow model are computed assuming that the neutral density at the exit plane of all HETs is approximately 1×10^{18} m^{-3} regardless of chamber condition; this estimate is taken from previous empirical measurements using the 1.5-kW SPT-100 and 5-kW P5

HETs [32, 44]. Included in this measurement are the combined contributions to the near-field number density from both the background flow as well as the unionized propellant exhausted from the HET [32, 44]. Previous modeling work has shown that the injection of a bleed flow of approximately 35 mg/s of propellant increases the neutral number density on the order of 1×10^{17} m^{-3} in the vicinity of the orifice [38]. Accordingly, in the modified background flow model, the number density at the exit plane of the HET (n_{exit}) was scaled to account for the contributions from the bleed flow orifice as shown in Eq. (5.2):

$$n_{exit} = 1 \times 10^{18} + 0.1 \frac{\mathrm{m_{bleed}}}{35} \times 10^{18} \tag{5.2}$$

It is important to note that Eq. (5.2) implicitly assumes that the number density perturbation scales linearly with the amount of bleed flow injected. This first-order approximation is consistent with previous modeling results [38]. As discussed in Section 3.2.2, the background flow model predicts that the percentage of bleed flow neutrals able to reach the HET increases by approximately 25% when all pumps are oriented upstream of the HET. A first-order approximation of this effect is included by scaling the second term in Eq. (5.2) by a factor of 1.25 for the upstream only pump configuration.

After implementing these two changes, the background flow model was again used to compute the difference in ingestion mass flow rate for the IHD2000-EM11 in VTF-2 for the chamber configurations from Table 4.2. The results are plotted alongside the empirical results and predictions from the thermal model in Figure 5.3(a) for the baseline chamber configuration, Figure 5.3(b) for the downstream pumps configuration, and Figure 5.3(c) for the upstream pumps configuration.

Overall, the implemented changes to the background flow model greatly improved the accuracy of the model to replicate the empirical results. Whereas the original predictions

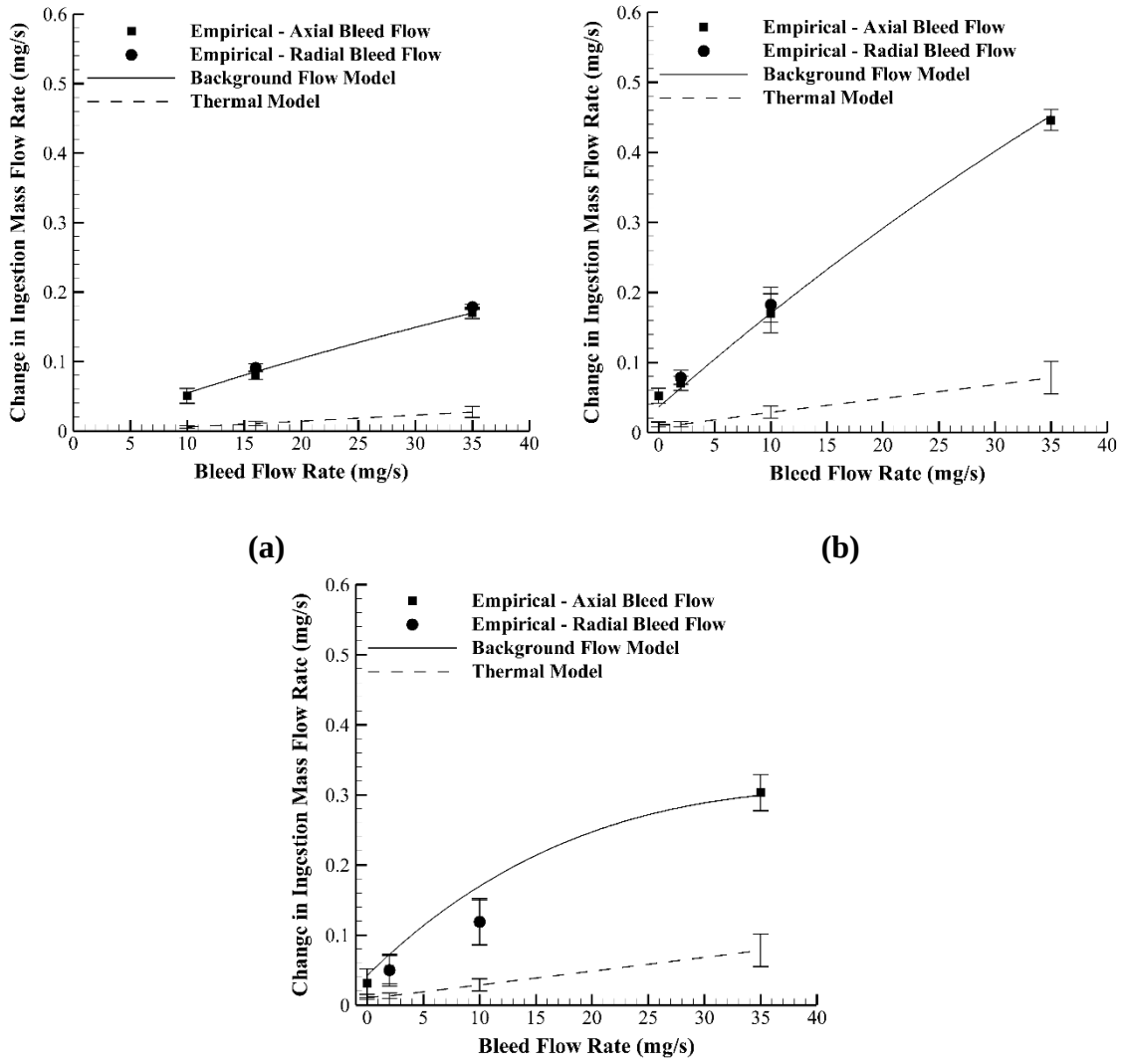

Figure 5.3: Change in IHD2000-EM11 ingestion mass flow rate for the (a) 10 pump, (b) downstream pump, and (c) upstream pump chamber configurations with modified background flow model predictions.

shown in Figure 5.1 deviated from the empirical results for the baseline and downstream pumps chamber configuration by an average of 32% and 18%, respectively, the predictions generated by the modified background flow model lie within the empirical uncertainty for all points taken in these two chamber configurations. A similar improvement in accuracy is also shown for the upstream pumps chamber configuration. Whereas the original background flow model over-estimated the empirical results by an average of 70%, the modified background flow model replicated all but one of the measurements to within the empirical uncertainty. The sole outlier is the 10 mg/s bleed flow case. For this bleed flow the modifications to the model decrease the over-estimation of the empirical result by 50%, thus generating an error of only 13% between the model predictions and the upper empirical uncertainty bound.

As shown in Figure 5.3, the implemented modifications to the model also changed the slope of the model predictions as a function of bleed mass flow rate relative to what was seen for the unmodified model in Figure 5.1. Specifically, although the change in ingestion mass flow rate predicted by the original model was linear for all bleed mass flow rates, the slope for the modified model is logarithmic. This change in slope represents an additional set of physics captured by the implemented modifications to the model. In the limit of high bleed mass flow rate, the increases in near-field number density result in the collisional scattering process dominating the increase in reflected flow back towards the HET. Thus, an increasing percentage of background neutrals are scattered prior to being ingested and the average HET discharge current becomes less sensitive to increases in bleed flow. This provides additional insight into the behavior of the bulk background flow field at high bleed mass flow rates beyond what was presented in the analytical studies in Chapter 3.

It is important to note that this asymptotic behavior qualitatively matches the performance trends observed during testing of the SPT-100 [15]. As discussed in Section 3.2.4, the original background flow model was unable to capture this trend much in the same way it overpredicted the empirically-observed changes for the IHD2000-EM11. To determine if collisional scattering could also explain the asymptotic behavior of the SPT-100, the study presented in Section 3.2.4 was repeated with the modified background flow model. Specifically, the modified background flow model was used to compute the ingestion mass flow rate into the SPT-100 HET in the Aerospace Corporation facility for all combinations of bleed flow and pumping speeds yielding operating pressures between 1×10^{-5} Torr-Xe and 7×10^{-5} Torr-Xe (which matches the range over which empirical measurements were taken) [15]. The results are shown in Figure 5.4 along with the empirical trend line originally presented by Diamant *et al*. [15].

Consistent with the approach taken in Section 3.2.4, only thrust values corresponding to the maximum and minimum predicted ingestion mass flow rates at each pressure are shown. In other words, the points composing the maximum prediction line correspond to the predicted thrust values that would be measured for those facility conditions that yield the highest ingestion mass flow rate at each of the pressures shown on the abscissa, while the minimum prediction line contains the points corresponding to the predicted thrust values that would be measured for those facility conditions that yield the lowest ingestion mass flow rate at each pressure. Between these two lines is a range of points that represent all of the thrust values that could be measured at each pressure according to the modified background flow model.

.

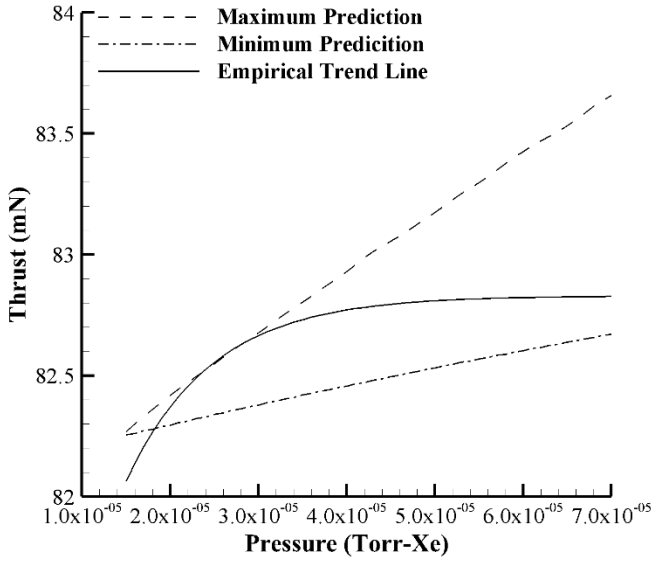

Figure 5.4 Measured and predicted (using modified background flow model) thrust of the SPT-100 HET as a function of Aerospace facility pressure.

As with the IHD2000-EM11 results, inclusion of these additional collisions allows the range of thrust values predicted by the modified background flow model to correctly replicate the emergence of the high-pressure performance asymptote for the SPT-100 HET and thus fully capture the observed logarithmic pressure sensitivity for that thruster. To the author's knowledge, this is the first analytical model to be able to capture the SPT-100 pressure sensitivities observed by both Sankovic *et al.* and Diamant *et al.* [15, 47]

It is important to verify that the implemented modifications do not alter the ability of the model to accurately reproduce the various empirical results used for validation in Chapter 3. To check this, the percent change in total mass flow rate (i.e., the sum of the ingestion and anode mass flow rates) predicted by the original and modified models was computed for a range of bleed mass flow rates for the upstream pumps chamber configuration. This configuration was chosen for two reasons. First, as shown in

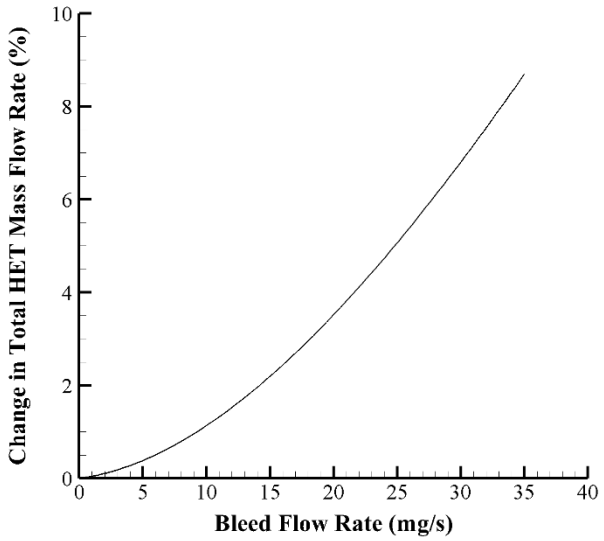

Figure 5.5: Percent change in predicted total mass flow to the IHD2000-EM11 between the original and modified background flow models.

Figure 5.1(c) and Figure 5.3(c), it is the chamber configuration for which the modified and original models show the largest deviation, and thus represents the worst-case scenario. Second, as discussed in Section 3.1, most data used for initial chamber validation were taken in the LVTF at the University of Michigan, which is a chamber with upstream pumps only. Thus, it is most pertinent to determine the deviation between the modified and original models for this chamber configuration when assessing how the modifications may impact the previously-performed validation study. The results are shown for the IHD2000-EM11 in Figure 5.5 and indicate that for bleed mass flow rates less than 100% of the anode flow (which encompasses all of the studies used for comparison in Chapter 3), the predictions of the modified background flow model deviate from those of the original by less than 1%. Thus, the changes to the background flow model implemented to improve accuracy at high bleed mass flow rates should not impact the ability of the model to replicate the results at lower bleed mass flow rates such as those analyzed in Chapter 3. This has particular relevance for the comparisons to the H6 testing performed by Reid

discussed in Section 3.1.3 due to the use of the same bleed flow location as used in this work [22, 23].

Finally, it is important to verify that the implemented first-order modifications do not train the model to correctly predict the ingestion mass flow rate at the expense of generating unphysical results for other parameters. Since the modifications impacted the model estimates of neutral number density downstream of the HET, this is the primary area of concern. To ensure that the implemented changes improved the fidelity of background flow model without comprising its physical basis, the modified model was used to generate a spatial profile of the neutral number density downstream of the IHD2000-EM11 for the downstream pumps only configuration and 35 mg/s bleed flow. Consistent with previous DSMC models of HET plumes operating at similar facility pressures, the spatial profile shows an inverse-square decay in the near field and asymptotically approaches a number density on the order of $1 \times 10^{17}\ m^{-3}$ at a distance 2 m downstream of the HET exit plane [36, 37]. This suggests that first-order modifications to the number density profile downstream of the HET plume did improve the fidelity of the collision model without introducing any unphysical results.

5.2.2 Impact of Facility Parameters on Background Flow Field

In addition to providing evidence for the existence of a bulk background flow of neutrals inside the vacuum test facility, the empirical data shown in Figure 5.3 also provide insight into the sensitivity of these bulk motions to facility operating parameters. These sensitivities are discussed in this section.

5.2.2.1 Pump Placement

The first facility parameter of interest is pump placement relative to the HET. Following the approach taken in Section 3.2.2, the sensitivity of the bulk background flow field (and the concomitant HET neutral ingestion) to this parameter can be found by comparing the results shown in Figure 5.3(b) and (c) for the downstream and upstream pumps cases, respectively. Overall, the ingestion mass flow rate into the IHD2000-EM11 was 34% higher for the downstream pumps case than the upstream pumps case. However, the ingestion mass flow rate represents less than 10% of the total mass flow rate supplied to the thruster (i.e., the sum of the anode mass flow rate and the ingestion mass flow rate) for all bleed flow cases. Thus, the overall average deviation in total mass flow supplied to the HET was less than 1.5%.

A closer inspection of these data reveals that the sensitivity of these results to pump placement varies with bleed mass flow rate. For bleed mass flow rates less than 200% of the anode mass flow rate, the difference between the ingestion mass flow rates for the upstream and downstream pumps cases is less than the empirical uncertainty and the change in total mass flow rate supplied to the HET is less than 0.5%. For bleed mass flow rates greater than 200% of the anode mass flow rate, the ingestion mass flow rates for these two chamber configurations begin to diverge. For these cases, the difference between the ingestion mass flow rates for the upstream and downstream pump configurations is greater than the empirical uncertainty. Furthermore, the change in total mass flow rate to the HET grows to 1.5% for the 10 mg/s bleed mass flow rate and 3.3% for the 35 mg/s bleed mass flow rate. In both cases, the ingestion mass flow rate is higher for the downstream pumps case.

These results are contrary to those from Section 3.2.2, in which the downstream pumps only configuration was shown to minimize the ingestion mass flow rate into the HET. The reason for these divergent results lies in the fact that the results shown in Section 3.2.2, do not account for the additional scattering collisions discussed in Section 5.2.1. As discussed previously, at high bleed mass flow rates, these collisions begin to dominate and lessen the number of background neutrals able to reach the thruster. This scattering process will be greater for the upstream pumps only configuration due to higher number density in the downstream region for facilities without downstream pumps thus resulting in reduced ingestion mass flow rates relative to the downstream pumps configuration.

However, care must be taken when interpreting these results. A significant deviation between the two pump configurations was only seen for bleed flows over 200% of the anode mass flow rate. Such a high bleed mass flow rate is atypical for HET tests [16, 17, 22–24, 29]. Thus, for most testing applications, the empirical results match those of the model in suggesting there is only a minimal difference in HET total mass flow rate between facilities with pumps located downstream and upstream of the HET test station.

5.2.2.2 Bleed Flow Orientation

As discussed in Section 3.1.3, in many facility effects tests, the bleed flow orifice is oriented to inject propellant radially (i.e., perpendicular to the thrust vector) [15, 23, 24]. Due to the one-dimensional nature of the background flow model, the radial injection of propellant cannot be directly modeled. Instead, the bleed flow is approximated as being injected axially. In order to determine the error associated with this assumption, two bleed mass flow rates for each chamber configuration were repeated. One trial each was conducted with the bleed flow oriented to inject flow axially and radially. The results are

shown for each chamber configuration in Figure 5.3. For all cases, the difference in discharge current between the axial and radial injection cases was less than the empirical uncertainty, thus suggesting that HET ingestion for facilities with flat plate beam dumps has limited sensitivity to bleed flow direction. This finding is consistent with those of previous modeling work and supports the approach taken in Section 3.1.3, thus further validating the results presented in that section [38].

5.2.2.3 Pressure Modulation Technique

A key finding from the analytical studies performed in Section 3.2 was that the total mass flow rate supplied to a HET at a fixed facility operating pressure could vary on the order of 4% depending on how that pressure was achieved. This finding suggests that pressure magnitude is an insufficient parameter to describe facility effects on HETs. To

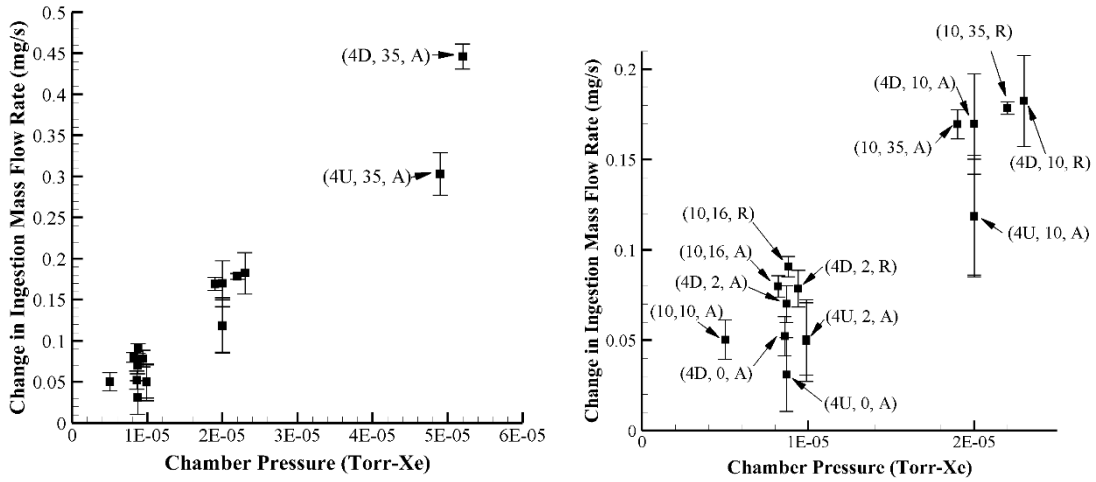

(a) **(b)**

Figure 5.6: Change in IHD2000-EM11 ingestion mass flow rate for chamber pressures up to: (a) 5×10^{-5} and (b) 2×10^{-5} Torr-Xe. Labels correspond to: (number of pumps, bleed mass flow rate in mg/s, bleed flow direction). U/D indicates upstream/downstream pumps and A/R indicates axial/radial bleed flow.

test this assertion, three common pressures (i.e., 1×10^{-5} Torr-Xe, 2×10^{-5} Torr-Xe, and 5×10^{-5} Torr-Xe) were achieved using different combinations of bleed flow and active pump modulation during IHD2000-EM11 testing. The results are shown for the full range of tested pressures in Figure 5.6(a). For clarity and ease of interpretation, the results from the lowest achieved pressures are isolated and replicated in Figure 5.6(b). It is important to note that the pressures correspond to the measurements made using the external pressure gauge discussed in Section 4.1. The observed spread in abscissa around the three indicated common pressures is due to the uncertainty in pressure reading associated with this gauge.

The results shown in Figure 5.6(a) and (b) confirm the analytical finding that a range of ingestion mass flow rates are possible at a fixed pressure depending on how that pressure is achieved. At pressures of 1×10^{-5} Torr-Xe, 2×10^{-5} Torr-Xe, and 5×10^{-5} Torr-Xe the ingestion mass flow rate into the HET varies by 200%, 50%, and 50%, respectively, yielding changes in total HET mass flow rate of 1% to 3.5% depending on how each pressure is achieved. All observed changes are outside of the empirical uncertainty. Furthermore, all chamber pressures are within the range historically considered as acceptable for HET testing [21, 25]. These results confirm the analytical findings that pressure magnitude alone is not a sufficient parameter to describe HET neutral ingestion and that, at a fixed pressure, the total mass flow rate supplied to a HET can vary by approximately 4%. These results furthermore suggest that a full description of how a given pressure is achieved is required to comprehensively model the bulk background motions and the corresponding ingestion into the HET.

5.3 H6 and 6-kW HET Results

5.3.1 Comparison of Background Flow Model and Empirical Results

5.3.1.1 Mean Discharge Current

As noted in Section 4.4.2.2, during the second phase of the experiment, measurements of the mean discharge current of the H6 and 6-kW HET were taken for the chamber conditions shown in Table 4.3. These results were acquired and analyzed identically to those for the IHD2000-EM11 described in Section 5.2. The results are shown as a function of bleed mass flow rate in Figure 5.7(a) for the baseline chamber configuration and in Figure 5.7(b) for the six pumps configuration. Consistent with the IHD2000-EM11 results, the values in Figure 5.7 correspond to the change in ingestion mass flow rate (or equivalently discharge current) relative to the baseline case of 10 active cryopumps with no bleed flow.

The modified background flow model was similarly used to compute the change in ingestion mass flow rate for the H6 and 6-kW HET in VTF-2 for the same chamber configurations. The results are plotted alongside the empirical results in Figure 5.7. Also shown in the figure are the changes in ingestion mass flow rate predicted by the thermal model. Consistent with the approach taken for the IHD2000-EM11 results, the number densities used for the thermal model calculations correspond to the empirical measurements taken using the single exterior hot-cathode ionization gauge described in Section 4.1. The uncertainty in the computed ingestion mass flow rates from the thermal model due to the reported 20% pressure measurement uncertainty is captured by the displayed error bars.

Consistent with the previous H6 facility effects studies described in Section 3.1.3, the predictions of the thermal model under predict the empirical results by 67% to 87% for the

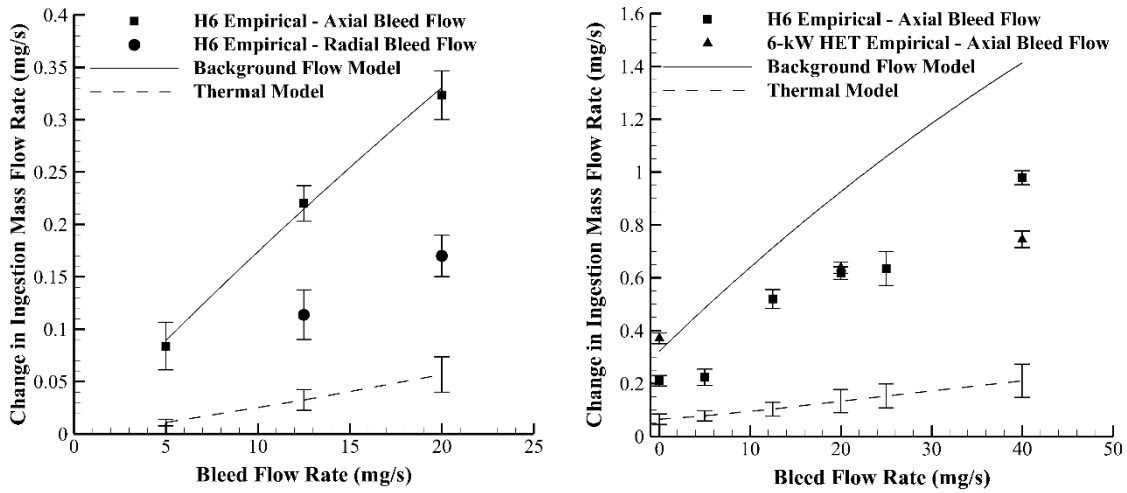

(a) **(b)**

Figure 5.7: Change in H6 and 6-kW HET ingestion mass flow rate for the (a) baseline and (b) six pumps chamber configuration.

baseline configuration and 70% to 83% for the six pumps configuration. Overall, this yields an average percent difference of 77% across all chamber configurations for both HETs. The predictions of the thermal model are thus, on average, four times lower than the empirical measurements. By contrast, as shown in Figure 5.7(a), the predictions of the background flow model match all empirical measurements to within the uncertainty for the baseline chamber configuration with axial bleed flow. This represents a 75% improvement in accuracy relative to the thermal model.

As shown in Figure 5.7(b), the accuracy of the background flow model is significantly reduced for the six pumps chamber configuration. Across all bleed mass flow rates, the predictions of the background flow model are approximately 1.5 times greater than the empirical measurements. It is important to note that the nature of this overestimation is different than that observed in Figure 5.1 when comparing the original model predictions to the data collected using the IHD2000-EM11. Whereas the difference between the

predictions of the original model and the empirical data for the IHD2000-EM11 increased with increasing bleed mass flow rate, for the H6 and 6-kW HET, the magnitude of the overestimation is largely constant and independent of bleed mass flow rate. This different behavior, along with the accurate prediction of the baseline chamber configuration data, suggest that the corrections implemented and described in Section 5.2.1 to address the identified shortcomings regarding the computation of collision cross-sections and entry of bleed flow into the modeling domain remain valid for the higher-power HETs used in this phase of the experiment. Thus, the overestimation shown in Figure 5.7(b) is likely caused by something other than these two items.

As noted in Section 4.4.2.2, an important difference between the tests performed with the IHD2000-EM11 and the H6 and 6-kW HET is that the latter two tests were performed with the conic beam dump configuration. This change in downstream reflection geometry could significantly alter the trajectory of reflected particles and thus, the magnitude of the bulk flow towards the HET. For the flat plate beam dump, all incident neutrals behave as shown in Figure 2.4. Specifically, incident neutrals strike the beam dump, thermalize, and reflect specularly in the axial direction. For the conic beam dump, incident neutrals behave

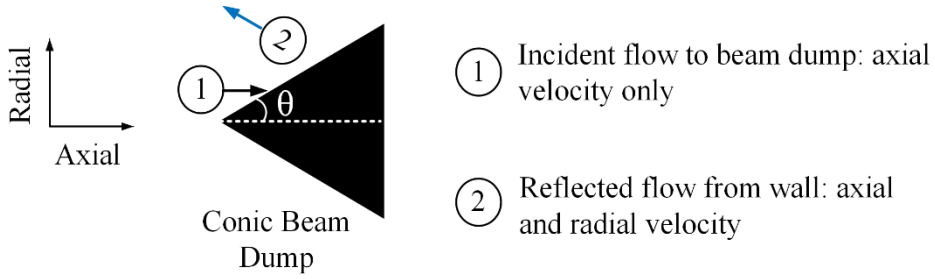

Figure 5.8: Neutral reflection from conic beam dump.

as shown in Figure 5.8 and reflect with both axial and radial velocity components. Flow traveling radially cannot travel directly back to the HET and contribute to the ingestion mass flow rate without first undergoing another collision with either the facility sidewalls or another neutral.

Due to the assumption of a one-dimensional flow field, the background flow model cannot account for losses due to radial reflection and so overestimates the ingestion mass flow rate into the HET for the conic beam dump. A first-order estimate of the impact of this change in downstream reflection geometry can be determined by defining a retention factor based on the half-angle of the conic surface (θ) shown in Figure 5.8. In the limit of a flat plate beam dump, the cone half-angle goes to 90 degrees and no flow is lost due to radial reflection (i.e., the retention factor is unity). In the limit where the cone half-angle goes to 0 degrees, the beam dump becomes an infinitely thin plate. For this case, no flow is reflected towards the HET, thus yielding a retention factor of zero. The retention factor, therefore, is the percentage of incident flow that is not lost to radial reflection and is equal to the sine of the cone half-angle.

As noted previously, the empirical results represent, on average, 65% of the background flow model predictions for the six pumps chamber configuration. Thus, for the H6 and 6-kW HET, the retention factor can be approximated as 0.65. Taking the arcsine of this value yields a corresponding cone half-angle of 41 degrees. Measurements of the conic beam dump in VTF-2 show an average cone half-angle of approximately 40 degrees. The closeness between the cone half-angle required to explain the observed overestimation and the actual half-angle of the conic beam dump, suggests that this is the likely mechanism responsible for the model overestimation of the six pumps results.

The retention ratio was used to correct the modified background flow model results for radial reflection during the six pumps configuration. The results are shown in Figure 5.9 along with the same empirical results from Figure 5.7. After correcting for radial reflection, the predictions of the background flow model match the H6 empirical results to within the experimental uncertainty for all bleed mass flow rates except 40 mg/s. For this case, the background flow model predictions are within 6% of the empirical results. This represents a 48% improvement in accuracy relative to the predictions shown in Figure 5.7(b).

Before this discussion can be concluded, a comment must be made about why the conic correction factor was not required for the model to accurately replicate the empirical results for the baseline configuration. As discussed in Section 2.3, the background flow model uses the surface area of the active pumps and the pump sticking coefficient to compute the number of neutrals that will strike and condense on the pumps during a given transit through a pump region. As shown most clearly in Figure 3.7, changing the number of active

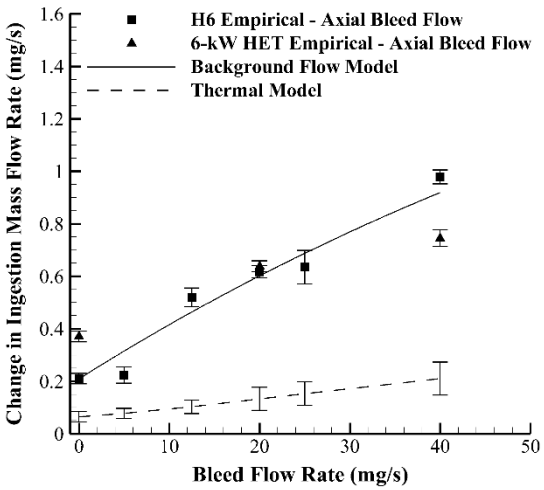

Figure 5.9: Change in H6 and 6-kW HET ingestion mass flow rate for the six pumps chamber configuration corrected for radial reflection.

pumps has a non-linear impact on the number of particles that will exit a given pump region without condensing. For the baseline chamber configuration, the model estimation of the efflux of neutrals to the pumps was sufficient to account for neutrals lost both to the pumps and via radial reflection. As shown in Figure 3.7, this loss rate decreases exponentially for the six pumps case, resulting in an insufficient estimation of the number of neutrals lost to both radial flow and condensation on the pumps. This results in an additional loss factor being required to account for this process.

Although unintentional in the formulation of the background flow model, this model behavior matches the physical situation in VTF-2 quite well. The conic beam dump in VTF-2 was constructed to reflect incident particles to the six cryopumps surrounding it. The view factor of these six pumps covers approximately 85% of the conic beam dump area. When all six cryopumps are activated, nearly all the flow lost to radial reflection also strikes the downstream cryopumps. Thus, accounting for only one of these loss mechanisms (i.e., the removal of neutral due to condensation on the pumps) is sufficient to fully capture the efflux of neutrals from the background flow in the downstream pump region. However, when the downstream pumps are deactivated, this view factor shrinks, and an appreciable number of neutrals lost to radial reflection do not contact an active pump. Therefore, the two loss paths affect different neutrals and must be accounted for separately via the inclusion of an additional loss term.

5.3.1.2 One-Directional Number Densities

The ability of the background flow model to accurately replicate the empirically-measured changes in mean discharge current suggest that the physical mechanisms captured by this model (i.e., the bulk motion of background neutrals) are responsible for

the observed changes in ingestion mass flow rate. However, these results ultimately represent a quantity (i.e., mean discharge current) that changes because of variations in the background flow field; it does not directly measure changes in the flow field itself. To ensure that changes in the background flow field are indeed the cause of the observed changes in HET ingestion mass flow rate, direct measurements of the background flow parameters relevant for describing HET ingestion were acquired and compared to the predictions of the background flow model. As shown in Figure 2.1(b), these relevant parameters are the number densities of neutrals traveling in the upstream and downstream directions at the surface immediately downstream of the HET exit plane (i.e., n_{D+} and n_{D-}). For convenience, hereafter, these number densities will be referred to as the one-directional number densities.

These quantities were directly measured using the Stabil-Ion Series 370 gauge during operation of the H6 and 6-kW HET and used to compute the percent difference in number densities as measured by the ion gauge between the upstream (n_{D+}) and downstream-facing (n_{D-}) orientations. This quantity (Δn) is shown as a function of bleed mass flow rate in Figure 5.10(a) for the baseline chamber configuration and Figure 5.10(b) for the six pumps chamber configuration. The background flow model was similarly used to compute the change in number density for the H6 and 6-kW HET in VTF-2 for the same chamber configurations. The results are plotted alongside the empirical results in Figure 5.10. The uncertainty in the empirical values due to the reported 5% pressure measurement uncertainty is captured by the displayed error bars.

The empirical results shown in Figure 5.10(a) largely match what would be expected

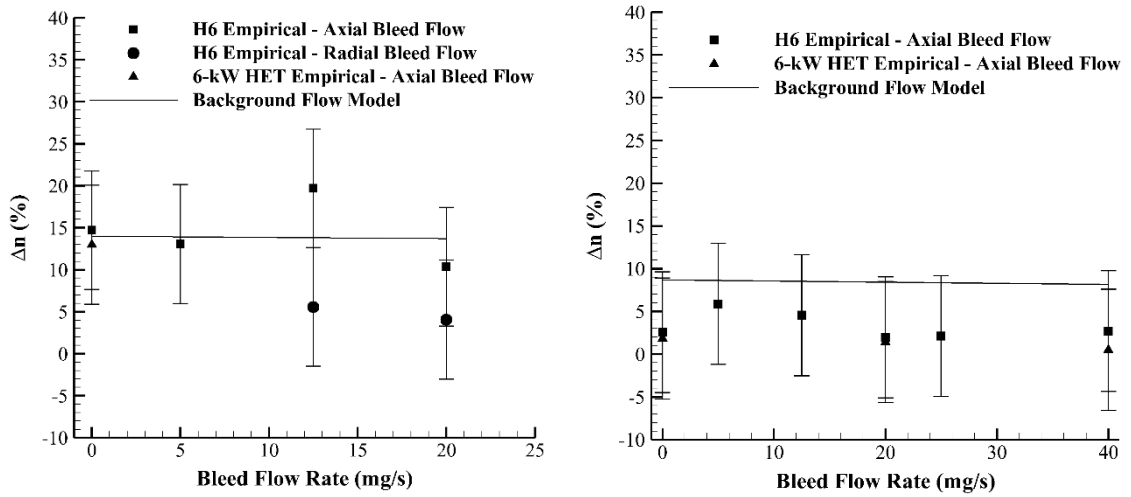

$$\Delta n = \frac{n_{D+} - n_{D-}}{n_{D-}}$$

(a) **(b)**

Figure 5.10: Percent difference in upstream and downstream-facing number densities for the (a) baseline and (b) six pumps chamber configurations.

for a vacuum facility with a bulk axial flow of neutrals. The number density measured by the upstream-facing gauge is lower than those measured by the downstream-facing gauge because the background neutrals traveling in the upstream direction have gone through an additional two transits through the upstream pump region. The magnitude of this difference is, within the empirical uncertainty, identical to the predictions of the background flow model for all axial bleed mass flow rates for both the H6 and 6-kW HET. The background flow model was also able to replicate the data acquired in the six pumps configuration shown in Figure 5.10(b) to within the empirical uncertainty. However, as was the case for the mean discharge current results presented in Section 5.3.1.1, the background flow model predictions overestimate the observed empirical changes. This is again likely caused by the radial scattering of neutrals due to collisions with the conic beam dump that is not accounted for in the model. Nevertheless, these results, when combined with those from

Sections 5.2.1 and 5.3.1.1, strongly suggest that the bulk background motions modeled by the background flow model do exist and do contribute non-negligibly to HET ingestion.

The one-dimensional flow assumption used to develop the background flow model neglects any bulk motion in the radial direction. To assess the validity of this assumption, measurements of the number density were taken with the Stabil-Ion gauge facing radially towards the HETs. These measurements were used to compute the percent difference in number densities as measured by the ion gauge between the radial (n_r) and downstream-facing orientations (n_{D-}). This quantity (Δn_{radial}) is shown as a function of bleed mass flow rate in Figure 5.11(a) for the baseline chamber configuration and Figure 5.11(b) for the six pumps chamber configuration. The uncertainty in the empirical values due to the reported 5% pressure measurement uncertainty is captured by the displayed error bars.

As shown in Figure 5.11(a), the number density of neutrals traveling radially is approximately 5% to 15% less than those traveling axially towards the HETs for the axial bleed cases in the baseline chamber configuration. This difference decreases to between 0% and 5% for the six pumps configuration shown in Figure 5.11(b). The increase in radial neutral motion for the six pumps configuration adds further support to the argument regarding radial reflection from the conic beam dump discussed in Section 5.3.1.1. Specifically, radial reflection off the conic beam dump would result in an increase in radial neutral motion as, in the six pumps configuration, not all neutrals that are radially reflected contact an active pump surface. Instead, some begin to move upstream via repeated collisions with the facility sidewalls. These additional radially-moving neutrals would result in the decrease in downstream-facing number density shown in Figure 5.10(b), the increase in radial-facing number density shown in Figure 5.11(b), and the overestimation

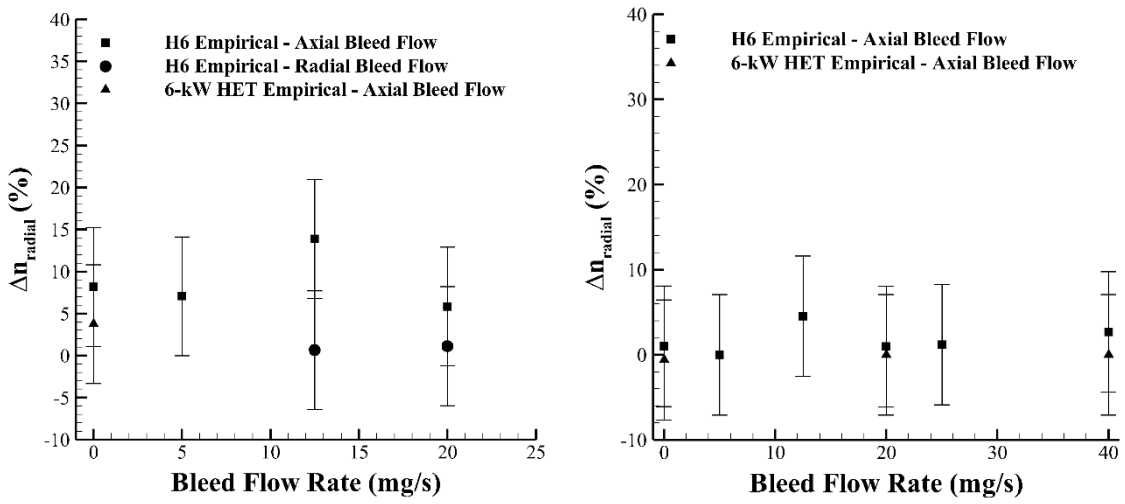

$$\Delta n_{radial} = \frac{n_{D+} - n_r}{n_r}$$

(a) **(b)**

Figure 5.11: Percent difference in radial and downstream-facing number densities for the (a) baseline and (b) six pumps chamber configuration.

of the ingestion mass flow rate by the background flow model shown in Figure 5.7(b). This suggests that radial motion is an important component of the background neutral flow field particularly for chambers with conic beam dumps. Furthermore, previous studies have shown a significant radial variation in the number density and velocity of bulk background neutrals [38]. Thus, a complete model of the background flow field must be at least two-dimensional to capture both the radial motions due to sidewall collisions as well as the radial variation of background flow field properties.

5.3.2 Impact of Facility Parameters on Background Flow Field

In addition to providing confirmation of the existence of a bulk background flow of neutrals inside the vacuum test facility, the empirical data presented in Section 5.3.1 also provides further insight into the sensitivity of this flow to facility operating parameters to

supplement the discussion from Section 5.2.2. These sensitivities are discussed in this section.

5.3.2.1 Bleed Flow Orientation

In order to determine how bleed flow orientation impacts the background flow field, two bleed mass flow rates (i.e., 12.5 mg/s and 20 mg/s) were repeated for the H6 in the baseline chamber configuration. One trial each was conducted with the bleed flow oriented to inject flow axially and radially. The results for the mean discharge current are shown in Figure 5.7(a) while those for the differential directional number densities are shown in Figure 5.10(a) and Figure 5.11(a).

As shown in Figure 5.7(a), changing the bleed flow orientation from axial to radial halves the corresponding change in discharge current (or ingestion mass flow rate). This reduction in ingestion mass flow rate corresponds to what would be expected if the bleed flow motion is two-dimensional (i.e., can travel in the axial and radial directions) and that the bleed flow has an equal probability of traveling in any of these directions. In this case, for the radial bleed flow orientation, after striking the underside of the thrust stand mounting structure, 50% of the bleed flow would travel axially, which roughly matches the empirical observations.

As shown in Figure 5.10(a), the percent difference in number densities as measured by the ion gauge between the upstream and downstream-facing orientations also decreases for the radial bleed flow orientation. Specifically, the percent differences for the axial bleed flow orientation are, on average, 3.5 times higher than those for the radial bleed flow orientation. As expected, the percent difference in number densities as measured by the ion gauge between the downstream and radial-facing orientations shown in Figure 5.11(a) also

decreases by an average of 91% for the radial bleed flow orientation relative to axial bleed flow injection. These results are consistent with flow being redirected from the axial direction to the radial direction due to the re-orientation of the bleed flow orifice.

It is important to note that, although the H6 results are self-consistent, they are different than those observed for the IHD2000-EM11. As discussed in Section 5.2.2.2, the change in ingestion mass flow rate between cases with axial bleed and radial bleed was less than the empirical uncertainty. This result is consistent with previous modeling work of VF-5, where minimal changes were seen between axial and radial injection of a bleed flow of propellant [38]. A major difference between these works is that the testing of the IHD2000-EM11 and modeling of VF-5 were done for a flat plate beam dump, whereas the H6 testing was done with a conic beam dump. Thus, the most likely cause for the observed change in sensitivity is a corresponding change flow dynamics related to the conic beam dump.

As discussed in Section 5.3.1.1, for the flat plate beam dump, all incident neutrals strike the beam dump, thermalize, and reflect specularly in the axial direction. To the first order, neutrals injected radially by bleed flow orifice can be approximated as having zero axial velocity. Thus, the collisional cross-section between these neutrals and the axial bulk background flow is large and the injected radial bleed flow can be collisionally entrained into the bulk axial flow. This minimizes the impact of radial injection on the HET ingestion characteristics. For the case of the conic beam dump, a significant fraction of the bulk background flow moves radially. Thus, less of the radially-injected bleed flow is axially entrained, and the impact of radial injection on the HET ingestion mass flow rate increases. This change in entrainment could explain the observed change in sensitivity to bleed flow orientation between the H6 and IHD2000 tests.

5.3.2.2 Pressure Modulation Technique

To further test the assertion made in Sections 3.2 and 5.2.2.3 that pressure magnitude is an insufficient parameter to describe HET neutral ingestion, three common pressures (i.e., 1×10^{-5} Torr-Xe, 2×10^{-5} Torr-Xe, and 4×10^{-5} Torr-Xe) were again achieved using different combinations of bleed flow and active pump modulation during H6 testing. It is important to note that all three of these facility pressures are within the range historically considered as acceptable for HET testing [21, 25]. The results are shown for the full range of tested pressures in Figure 5.12. It is important to note that the plotted pressures correspond to the measurements made using the external pressure gauge discussed in Section 4.1. The observed spread in abscissa around the three indicated common pressures is due to the uncertainty in pressure reading associated with this gauge.

The results shown in Figure 5.12 largely confirm the previous analytical and empirical finding that a range of ingestion mass flow rates are possible at a fixed pressure depending on how that pressure is achieved. At pressures of 1×10^{-5} Torr-Xe and 2×10^{-5} Torr-Xe, the ingestion mass flow rate into the HET varies by 100% and 118%, respectively. However, the small magnitude of the ingestion mass flow rate relative to the anode mass flow rate yields changes in total HET mass flow rate of less than 1% depending on how each pressure is achieved. All observed changes are outside of the empirical uncertainty for these two pressures. At a pressure of 4×10^{-5} Torr-Xe, no change was measured within the empirical uncertainty. However, fewer points were collected at this pressure. These results provide additional evidence that pressure magnitude alone is not a sufficient parameter to describe HET neutral ingestion and that a full description of how a given pressure is achieved is required to comprehensively model the bulk background motions

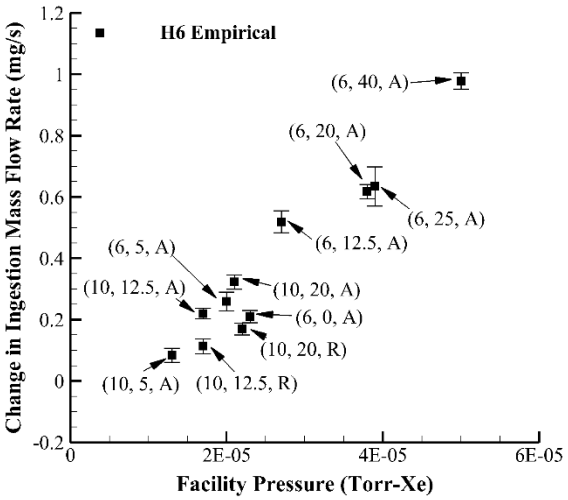

Figure 5.12: Change in H6 ingestion mass flow rate as a function of facility pressure. Labels correspond to: (number of pumps, bleed mass flow rate in mg/s, bleed flow direction). A/R indicates axial/radial bleed flow.

and the corresponding ingestion into the HET. However, they also suggest that the sensitivity of total HET mass flow rate to pressure modulation technique is lower for HETs of higher power classes.

5.4 Discussion of Enhanced Ingestion

Ultimately, final validation of the observations presented in this chapter would require direct measurements of the flux of neutrals crossing the HET exit plane. However, absent such a measurement, the acquired data can be synthesized to indirectly obtain estimates of the bulk velocity and near-field number density of the background neutrals. These estimates could prove illustrative to better understand why the thermal model underpredicts the empirically-observed changes in HET neutral ingestion mass flow rate.

As discussed by Yim and Burt, the presence of a bulk background flow as well as the use of a neutralizer tube has significant implications for the measurements obtained using

the internally-mounted Stabil-Ion Series 370 gauge [38]. Specifically, the use of the neutralizer tube with an entrance plane oriented perpendicular to the bulk flow direction creates a region of stagnated flow within the neutralizer tube; thus the pressure measured by the gauge corresponds to the stagnation pressure (P_o), not the local static pressure (P_∞) [38, 90]. The stagnation pressure of a Maxwellian free molecular flow in an infinitely long tube at a zero angle of attack relative to the flow can be described using Eq. (5.3)- (5.4):

$$\mathrm{Z} = \frac{v_B}{\sqrt{\frac{2kT_b}{m}}} \tag{5.3}$$

$$P_o = P_\infty \sqrt{\frac{T_w}{T_b}} \left\{ \left[\frac{\mathrm{Z}}{\sqrt{\pi}} + \frac{1}{2} \right] \left[e^{-\mathrm{Z}^2} + \sqrt{\pi}\mathrm{Z}(1 + \mathrm{erf}(Z)) \right] + \frac{1}{2}[1 + \mathrm{erf}(Z)] \right\} \tag{5.4}$$

where v_B is the bulk velocity of the background neutrals in the axial direction, Z is a velocity ratio between the bulk and thermal velocities of the background neutrals, and all other variables retain their meaning from previous expressions [38, 90].

Following the recommendations of Yim and Burt, two approaches can be applied to the acquired data in order to recover the bulk velocity from Eq. (5.3)-(5.4) [38]. In the first, the static pressure is assumed to be equal for the upstream- and downstream-facing gauge orientations and the bulk velocity is assumed to be equal in magnitude, but opposite in sign for these two configurations [38]. These assumptions yield a closed system of two equations (i.e., Eq. (5.4) applied to both the upstream- and downstream-facing gauge configurations) and two unknowns (i.e., the local static pressure and the bulk velocity) [38]. In the second approach, the radial-facing pressure is assumed to be equal to the local static pressure [38]. Equation (5.4) can then be solved directly for the bulk velocity using the downstream-facing pressure measurement as the local stagnation pressure [38].

Applying these approaches to the data taken in the baseline chamber configuration for the H6 yields an average bulk velocity of approximately 8 m/s and a static pressure that closely resembles the pressure measured using the radially-facing gauge. These results can then be used to compute the ingestion flow rate augmentation due to these bulk motions. Following the approach outlined in Yim and Burt, this yields a less than 10% increase in the neutral ingestion mass flow rate relative to the thermal model. These results are consistent with those of Yim and Burt who applied this technique to similar data [38]. Even though the values computed using Eq. (5.3)-(5.4) match those from previous modeling and empirical work, the resultant neutral ingestion enhancement is insufficient to explain the empirical observations. In fact, the bulk velocity required for the above approach to correctly match the empirical data is on the order of 500 m/s towards the HET exit plane, which is much larger than has been shown in previous analytical investigations [37, 38].

The background flow model predictions also diverge from those generated from application of Eq. (5.3)-(5.4) to the acquired pressure data. Specifically, the background flow model suggests that the number density near the HET exit plane is approximately one order of magnitude higher than was measured by the internal gauge and that the bulk velocity towards the HET exit plane is approximately 100 m/s for the H6 in the baseline chamber configuration. These results closely match the empirically-validated results of Cai *et al.* [37].

By comparison, the thermal model assumes that the local number density is equal to that measured by the radial-facing gauge. The velocity used by the thermal model is similar in magnitude to that of the background flow model, however, it is assumed to be isotropic,

thus background neutrals have an equal probability of traveling in any direction instead of being restricted to axial motions as done in the background flow model.

These comparisons suggest that the reason for the thermal model underpredictions is an invalid assumption of isotropy with regards to the velocity of the background neutrals, which leads to an underestimation of the number density relevant for ingestion. It is this anisotropic flux (of the flow reflected off the downstream facility surfaces) and the concomitant enhancement of local number density that is captured by Eq. (2.13) and Eq. (5.1) of the background flow model. Specifically, the velocity terms in Eq. (2.13) represent the anisotropy caused by the bulk axial velocity of neutrals towards the HET exit plane due to reflection off the downstream facility surfaces.

However, before the background flow mechanism can be accepted, it is necessary to determine why the ingestion mass flow rates computed using the measured pressures diverge from those predicted using the background model and measured using changes in mean discharge current. The first likely cause for this discrepancy is the placement of the ion gauge relative to the HET exit plane. As discussed in Section 4.4.2.2, the orifice of the internal ion gauge was located approximately 0.5 m radially outward from the HET exit plane. Previous studies have indicated that this radial distance is outside of the plume core flow and is thus characterized by much lower number densities [38]. Furthermore, this location places the gauge at the same radial location as the slanted surfaces on the conic beam dump. As discussed in Section 5.3.1, the flux measured by the gauge would thus be characterized by significant radial scattering, which would likely lessen the axial velocity detected by the gauge relative to what would be expected for a flat plate beam dump or for a location closer to the chamber centerline. This suggests that at least part of the

discrepancy between the pressure and ingestion mass flow rate measurements is caused the spatial location of the gauge. Future work should look to place the gauge radially closer to the HET exit plane to get a better measurement of the parameters relevant for computing the ingestion mass flow rate.

The next potential cause for the observed discrepancy between the pressure and ingestion mass flow rate measurements is the set of assumptions used to derive Eq. (5.3)-(5.4). As noted in the discussion regarding those equations, they are strictly only valid for a Maxwellian free molecular flow in an infinitely long tube at a zero angle of attack. The tube used in this work is of finite length and so does not satisfy these assumptions [38, 90]. However, since the length-to-diameter ratio of the employed neutralizer tube is greater than unity, previous work suggests that the error associated with this assumption is small. The more likely culprit is the assumption of a Maxwellian distribution. Previous modeling work has suggested that the velocity distribution of the background neutrals is unbalanced and cannot be approximated using a Maxwellian distribution [37, 45]. The results from this work would seem to support that finding as application of analytical solutions valid only for Maxwellian distributions yielded results that were inconsistent with the measured ingestion mass flow rates. It is important to note that the assumption of a Maxwellian distribution is also required by the thermal model [21]. Thus, if this assumption is invalid, it could also help explain why the thermal model has been unable to replicate the empirically-observed ingestion mass flow rates. As discussed in Chapter 7, future work should look to use optical diagnostics to better resolve the components of the background flow velocity distribution function to determine if they are or are not Maxwellian.

The final factor that could explain the observed discrepancy between the pressure and ingestion mass flow rate measurements is the assumed neglect of all ionization in the near-field of the HET plume. Although consistent with the approach taken in the thermal model, this assumption could prove problematic for HETs with magnetic shielding due to the location of the ionization and acceleration zone downstream of the HET exit plane [91]. If downstream ionization was significant, then the ability of the background flow model to correctly replicate the empirically-measured changes in ingestion mass flow rate would be due an incorrect inflation of the number density and velocity terms to offset the underestimation of the ingestion area.

Taken together, the results presented in this section prove illustrative for understanding both why the thermal model underpredicts the empirically-observed changes in ingestion mass flow rate and the discrepancy between the obtained measurements of pressure and ingestion mass flow rate. The underpredictions of the thermal model are driven by its failure to capture the elevation of the near-field neutral density due to the anisotropy of the background flow velocity distribution. This is compounded by evidence that the velocity distribution of the background neutrals may not be Maxwellian, as assumed by the thermal model. The discrepancy between the obtained pressure and ingestion mass flow rate measurements is could also due to the non-Maxwellian nature of the background neutrals as well as the location of the gauge outside of the core plume flow and the potential contributions of external ionization in the near-field plume.

5.5 Conclusions

The purpose of the data presented in this chapter was to provide answers to three of the research questions for this work:

RQ 1: Do bulk motions constitute a non-negligible component of the background neutral flow field inside vacuum facilities?

RQ 1A: Are the bulk motions sensitive to facility-specific parameters such as pump placement and pressure modulation technique?

RQ 1B: Do the bulk motions constitute a non-negligible component of the HET ingestion flow?

The measurements of one-directional number densities presented in Section 5.3.1.2 showed an elevated number density of neutrals traveling upstream towards the HET exit plane. These measurements are consistent with the hypothesized bulk background flow traveling in the axial direction and match the predictions of the background flow model. These results therefore confirm the existence of bulk background neutral motions and provide a definitive answer to RQ 1.

The link between the bulk motions of the background neutrals and HET ingestion were explored in Sections 5.2.1 and 5.3.1.1. In these sections, it was shown that, once modified to more accurately account for the bleed flow apparatus used in this work, the background flow model accurately replicated the observed changes in mean discharge current. Furthermore it was shown that the physics captured by the modified background flow model were able to correctly replicate the previously-unexplained high-pressure performance asymptote of the SPT-100 observed by Diamant *et al.* and replicated with the IHD2000-EM11 in this work [15, 47]. These comparisons further validate the model and confirm that the physical mechanisms it describes (i.e., the bulk motion of background neutrals) impact HET ingestion characteristics, thus answering question RQ 1B.

Question RQ 1A is answered by the empirical sensitivity studies discussed in Sections 5.2.2 and 5.3.2. In these studies, it was found that the bulk background flow is sensitive to a variety of facility-specific parameters including pump placement, bleed flow orientation, beam dump geometry, and pressure modulation technique. Specifically, it was found in Section 5.2.2.1 that the ingestion mass flow rate was reduced for the upstream only pumps configuration due to the increase in number density downstream of the HET and the concomitant effects on elastic scattering. Use of a conic beam dump was also shown to decrease HET ingestion by increasing radial losses of background neutrals. As discussed in Section 5.3.2.2, bleed flow orientation was only shown to impact HET neutral ingestion when used in combination with a conic beam dump; no change was detected between radial and axial flow injection for the flat plate beam dump. Finally, it was shown that for all three HETs tested (i.e., the IHD2000-EM11, H6, and 6-kW HET) pressure magnitude was an insufficient parameter for describing HET neutral ingestion, and that a full description of a how pressure was achieved was required to uniquely determine the background flow field and concomitant neutral ingestion. Taken together, these results largely confirm the findings of the analytical studies performed in Chapter 3 and provide answers to RQ 1, RQ 1 A, and RQ 1B.

CHAPTER 6. HET PERFORMANCE CHARACTERIZATION

6.1 Chapter Overview

As discussed extensively in Section 1.3.1, previous investigations have shown that HET plume properties and device performance are impacted by facility backpressure. Specifically, increases in facility pressure have been shown to cause artificial increases in device performance (i.e., thrust and efficiency), inflated measurements of ion current density in the regions of the HET plume at large angles with respect to HET centerline, a broadening of the plume ion energy distribution, and an increase in the thruster breathing mode frequency [2, 14–29, 33]. Although these general trends are consistent between works, attempts to quantify them using facility pressure as the only parameter of comparison have yielded results that differ depending on the employed thruster and facility combination [2, 14–29].

The results of the background flow field characterization experiment presented in Chapter 5 and the background flow modeling effort presented in Chapter 3 provide a possible explanation for why facility backpressure has proven insufficient to universally capture the observed changes in performance and plume properties. These studies confirmed the existence of the hypothesized bulk flow of background neutrals within the vacuum test facility as well as the link between these bulk motions and neutral ingestion by HETs. It was also shown that because the background flow field is sensitive to a variety of parameters, different bulk fluxes to the HET can be realized at a given pressure depending on how that pressure is achieved. These sensitivities result in pressure magnitude being an insufficient parameter to fully describe the impact of the facility on

ingestion and suggest that it may also be an insufficient parameter to fully describe the concomitant impacts on HET performance and plume properties.

In this chapter, the previously-observed changes in HET performance, plume properties, and oscillation characteristics are reanalyzed using this new understanding of the bulk background flow to determine if this description of the background neutral motions can more universally capture the observed trends. The results from the various plasma plume diagnostics are presented and analyzed in Section 6.2, while the oscillation characteristics of each of the HETs are discussed in Section 6.3 and HET performance is discussed in Section 6.4. Finally, the results of the magnet stability study are presented in Section 6.5.

6.2 Plume Properties

6.2.1 Faraday Probe

6.2.1.1 Plume Divergence Half-Angle

The plume divergence half-angles computed from the Faraday probe measurements of the ion current density profile are shown as a function of facility pressure in Figure 6.1(a) for the IHD2000-EM11 and in Figure 6.2(a) for the H6. Due to the limited data set collected with this HET, the results from the 6-kW HET are omitted throughout this section. The computed plume divergence half-angles for the IHD2000-EM11 are comparable to those of other 1-kW and 2-kW-class HETs including the SPT-140 while the computed results for the H6 are consistent with those from previous work [14, 79, 82, 92].

As shown in Figure 6.1(a) and Figure 6.2(a), the plume divergence half-angle increases for both the IHD2000-EM11 and H6 with increasing facility pressure. This finding is consistent with those from previous work [14, 30–32]. However, unlike in previous work,

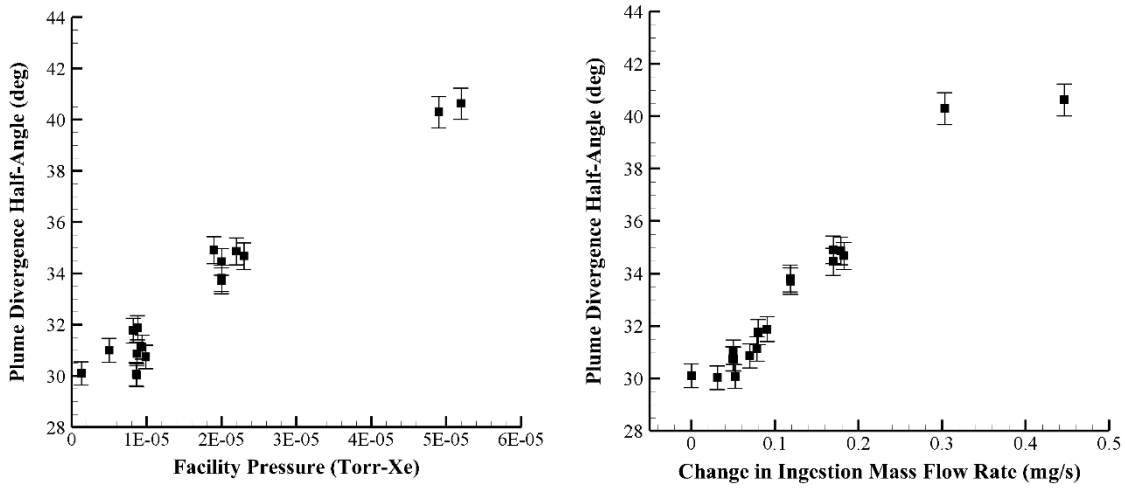

(a) **(b)**

Figure 6.1: IHD2000-EM11 plume divergence half-angle as a function of (a) facility pressure (b) ingestion mass flow rate.

the observed trend is not monotonic with facility pressure. As discussed in Sections 5.2.2.3 and 5.3.2.2, several common pressures were achieved using different combinations of bleed flow and active pump modulation for each HET to determine if the method used to achieve a given pressure affects the HET response. For the IHD2000-EM11, these pressures were 1×10^{-5} Torr-Xe, 2×10^{-5} Torr-Xe, and 5×10^{-5} Torr-Xe; for the H6 they were, 1×10^{-5} Torr-Xe, 2×10^{-5} Torr-Xe, and 4×10^{-5} Torr-Xe. As shown in Figure 6.1(a) and Figure 6.2(a), the computed divergence half-angles at several of these pressures change depending on how each pressure is achieved. At pressures of 1×10^{-5} Torr-Xe and 2×10^{-5} Torr-Xe, the plume divergence half-angle of the IHD2000-EM11 varies by 6% and 4%, respectively. Similarly, the plume divergence half-angle of the H6 varies by 4% at a facility pressure of 4×10^{-5} Torr-Xe. These observed changes are all outside of the empirical uncertainty. Consistent with the mean discharge current measurements presented in

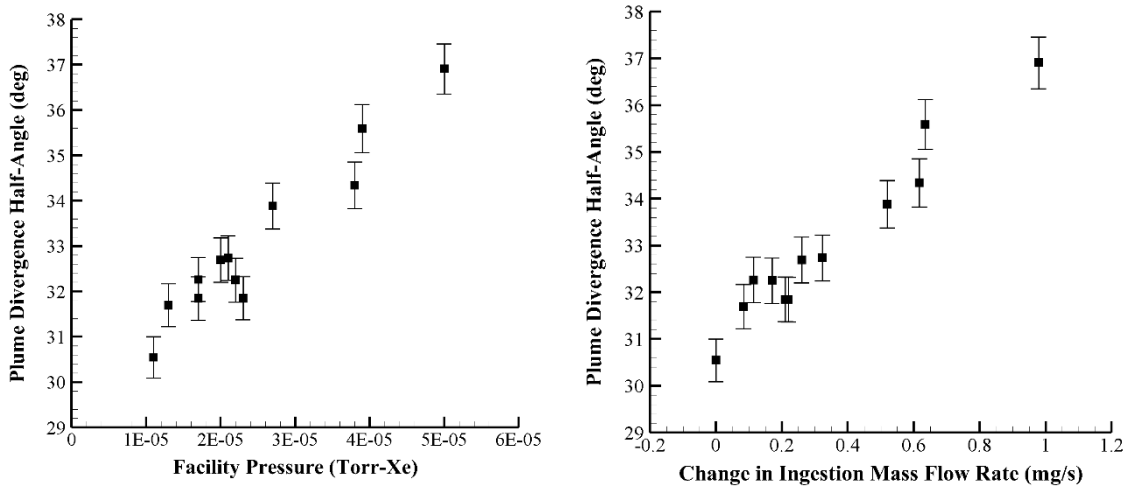

(a) **(b)**

Figure 6.2: H6 plume divergence half-angle as a function of (a) facility pressure (b) ingestion mass flow rate.

Sections 5.2.2.3 and 5.3.2.2, these results suggest that pressure magnitude is an insufficient parameter to fully describe the impact of the test facility on the HET plume.

To determine if the bulk background motions (as indicated by the ingestion mass flow rate) can more completely describe the observed trends in plume divergence half-angle, the results were replotted as a function of the empirically-measured change in ingestion mass flow rate relative to the baseline condition of ten pumps and no bleed flow computed identically to the method used in Chapter 5. These updated plots are shown in Figure 6.1(b) for the IHD2000-EM11 and in Figure 6.2(b) for the H6. When plotted against the empirically-measured change in ingestion mass flow rate, the plume divergence half-angle results become monotonic to within the empirical uncertainty as compared to being multivalued when plotted as a function of pressure in Figure 6.1(a) and Figure 6.2(a). It is also important to note the emergence of two asymptotes for the IHD2000-EM11 plume divergence half-angle results at ingestion mass flow rates less than 0.025 mg/s and above

0.3 mg/s. These asymptotes were not present when the data were plotted as a function of facility backpressure. These changes in behavior suggest that the ingestion mass flow rate due to the bulk motions of the background flow more completely describes the changes in the HET plume than does facility pressure magnitude.

The reason for this lies in the physical mechanism responsible for the broadening of the HET plume at elevated background pressures. As discussed thoroughly in previous work, during ground testing of HETs, upon being exhausted, the primary beam of accelerated ions interacts with the facility background neutrals [14, 30–32]. These interactions occur via resonant CEX collisions, which result in the charge jumping from the accelerated ion to the background neutral resulting in a fast-moving neutral and a slow-moving (or CEX) ion [14, 30–32]. Since the CEX ion was not accelerated by the HET, it does not have a large axial momentum and can follow the electric field from the core of the plume to the regions at large angles with respect to thruster centerline [14, 30–32]. As the Faraday probe is unable to distinguish primary ions from CEX ions, these CEX ions artificially increase the ion current density in these off-axis wings and cause the computed plume divergence half-angle to increase.

Consistent with other collisional processes, the CEX collision frequency increases with increasing near-field number density [14, 30–32]. As shown by the directional number density results in Figure 5.10 and Figure 5.11, the bulk motion of the background neutrals elevates the near-field neutral density beyond what would be predicted using the measurements obtained by the radial-facing pressure gauge that monitors overall facility pressure. Furthermore, the bulk velocity of the background neutrals towards the HET

reduces the relative velocity between the beam ions and the background neutrals further increasing the CEX collision cross-section [4, 44].

This mechanism also explains the asymptotic behavior observed for the IHD2000-EM11 results. At low ingestion mass flow rates, the number density associated with the bulk motion of the background neutrals is minimized and the near-field number density asymptotically approaches the value caused by thermal motions only. This results in the formation of the low-ingestion mass flow rate asymptote observed in Figure 6.1(b). As discussed in Section 5.2.1, at high ingestion mass flow rates, elastic scattering collisions begin to dominate thus lessening the increase in near-field number density associated with additional bleed flow injection. As with the observed changes in mean discharge current, this results in the formation of a high-ingestion mass flow rate asymptote for the plume divergence half-angle. Taken together, these results indicate that the empirically-measured change in ingestion flow rate is the truer indicator of the CEX collision frequency, and, thus, the better parameter to use to describe the observed changes in plume divergence half-angle.

Further evidence of the link between the observed trends in plume divergence half-angle and CEX collisions can be found by analyzing the ion current density profiles shown in Figure 6.3(a). Two ion current density profiles are shown in Figure 6.3(a): one each corresponding to the chamber conditions that yielded the highest and lowest ingestion mass flow rates for the IHD2000-EM11 at a fixed chamber pressure of 1×10^{-5} Torr-Xe. Consistent with the convention discussed in Section 4.3.5, the zero point on the abscissa corresponds to the centerline of the HET.

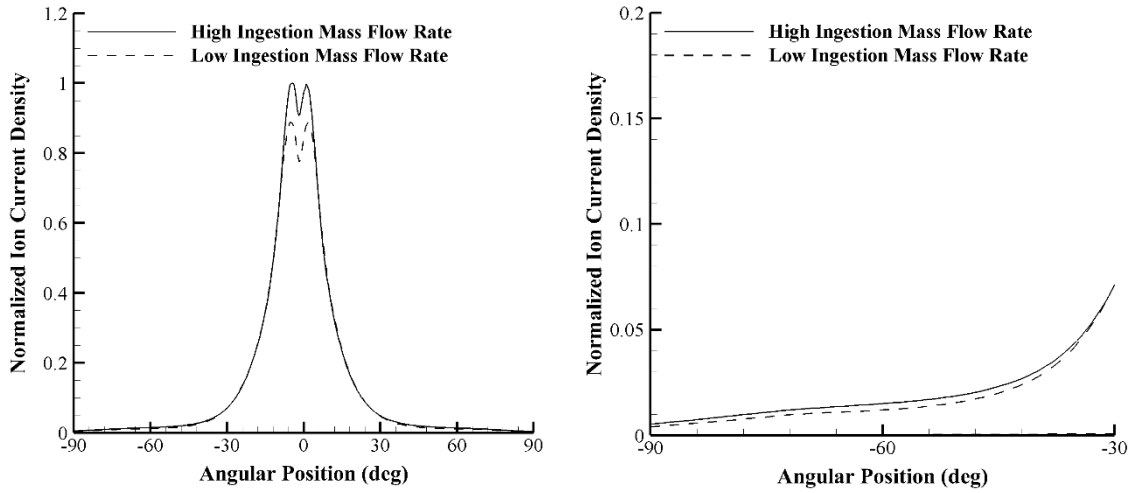

(a) **(b)**

Figure 6.3: (a) Full and (b) partial ion current density profiles of the IHD2000-EM11 corresponding to the maximum and minimum ingestion mass flow rates observed at a facility pressure of 1×10^{-5} Torr-Xe.

As discussed previously, an increase in the ion current density in the off-axis wings of the plume is an indicator of an increase in CEX ion production [14, 30–32]. For clarity and ease of interpretation, this region of the plume is isolated and shown in Figure 6.3(b). As shown in Figure 6.3(b), the ion current density is higher throughout this region of the plume for the chamber configuration corresponding to higher ingestion mass flow rate. This confirms the increase in CEX collision frequency for this chamber configuration and provides further evidence that the empirically-measured change in ingestion flow rate is the truer indicator of the increase in number density downstream of the HET exit plane due to the bulk background motions. This results in this parameter also being a truer indicator of the CEX collision frequency, and, thus, the better parameter to use to describe the observed changes in plume divergence half-angle. It is important to note that this result is not restricted to the measured change in ingestion mass flow rate. Any generalized flux

variable that accounts for the bulk motions of the background flow would also be a suitable parameter to fully capture the observed changes.

6.2.1.2 Ion Beam Current

The total ion beam current computed from the Faraday probe measurements of the plume ion current density profile are shown as a function of facility pressure in Figure 6.4 (a) for the IHD2000-EM11 and in Figure 6.5(a) for the H6. Using these results, it is possible to define a current utilization efficiency as the ratio of the ion beam current to the discharge current. This efficiency is a measure of how effectively the electrons are used to ionize the propellant [53]. Using the ion beam current results shown in Figure 6.4(a) and Figure 6.5(a) as well as the measured mean discharge current from Sections 5.2.1 and 5.3.1, the average current utilization efficiency for each HET was found to be approximately 90% for the

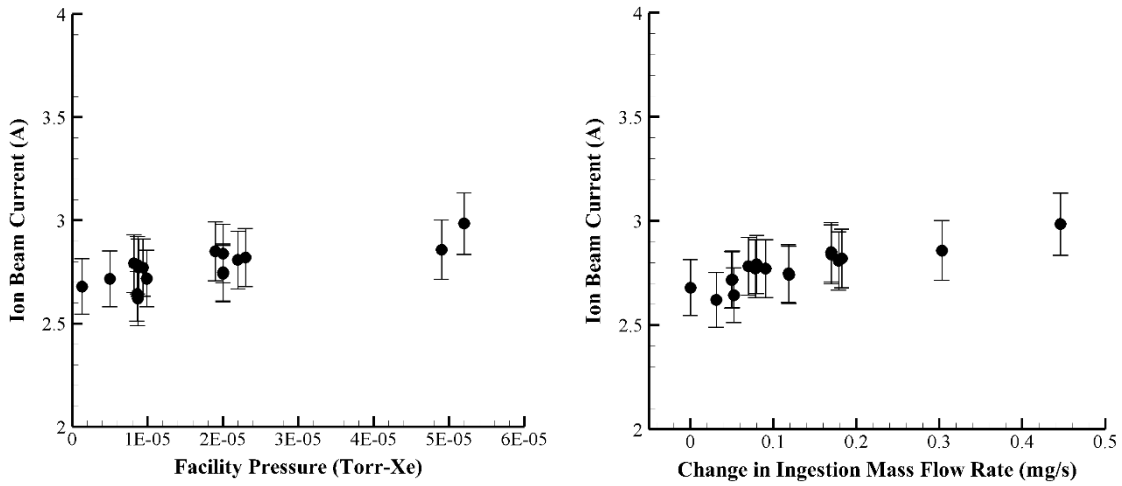

(a) **(b)**

Figure 6.4: IHD2000-EM11 ion beam current as a function of (a) facility pressure (b) ingestion mass flow rate.

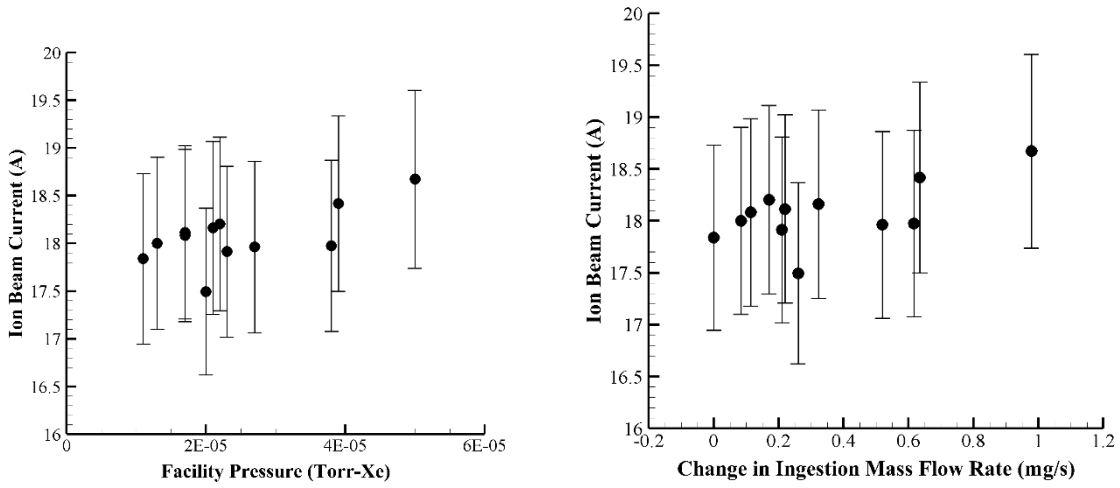

(a) **(b)**

Figure 6.5: H6 ion beam current as a function of (a) facility pressure (b) ingestion mass flow rate.

baseline case. These results are comparable with previous values published for the H6 and are consistent with typical values expected of HETs [79, 82, 93].

Overall, consistent with previous work, the mean ion beam current for both thrusters increases with facility pressure [31, 81, 94]. However, this observed trend is also not monotonic with facility pressure; the mean ion beam current varies at fixed facility pressure depending on how that pressure was achieved. Consistent with the plume divergence half-angle results shown in Section 6.2.1.1, plotting the ion beam current as a function of the change in ingestion mass flow rate (as done in Figure 6.4(b) and Figure 6.5(b)) yields a monotonic result. Further evidence of the functional relationship between ingestion mass flow rate and ion beam current is shown by the ion current density profiles in Figure 6.4(a) where the ion current density is everywhere higher for the chamber configuration that yields a higher ingestion mass flow rate at a fixed facility pressure of 1×10^{-5} Torr-Xe. This again suggests that the ingestion mass flow rate due to the bulk motions of the background

flow more completely describes the changes in the HET plume than does facility pressure magnitude. Since, the physical mechanism responsible for the increase in ion beam current at elevated background pressures is also CEX collisions, the fact that the empirically-measured change in ingestion flow rate better describes the observed changes ion beam current further supports the arguments presented in the previous section. Finally, it is interesting to note that the average rate of change for both the IHD2000-EM11 and H6 is approximately 0.7 A ion beam current per 1 A increase in measured mean discharge current. This matches the assumed ratio used to derive the flow rate to discharge current conversion discussed in Section 3.1.2 and therefore further supports the use of this technique throughout this work.

However, care must be taken when discussing the ion beam current results. Unlike with the plume divergence half-angle results, all observed changes in ion beam current are less than the empirical uncertainty. Therefore, although true for the means, the above statements cannot be fully supported until additional data is acquired with reduced uncertainty.

6.2.2 Langmuir and Emissive Probes

6.2.2.1 Number Density

The plasma density computed from the Langmuir probe I-V characteristics are shown as a function of facility pressure in Figure 6.6(a) for the IHD2000-EM11 and in Figure 6.7(a) for the H6. The results for the IHD2000-EM11 are consistent with previous results for HETs operating at a discharge power of approximately 600 W, while those for the H6 are consistent with previously published values for that HET [15, 22, 24, 95]. Consistent with previous results, the mean plasma number density for both HETs increases with facility backpressure [15, 24].

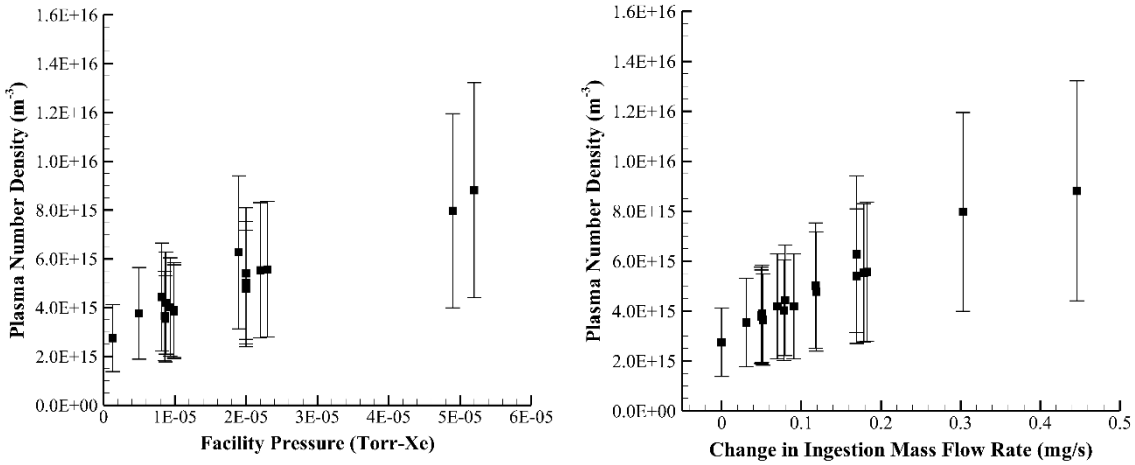

(a) **(b)**

Figure 6.6: IHD2000-EM11 plasma number density as a function of (a) facility pressure (b) ingestion mass flow rate.

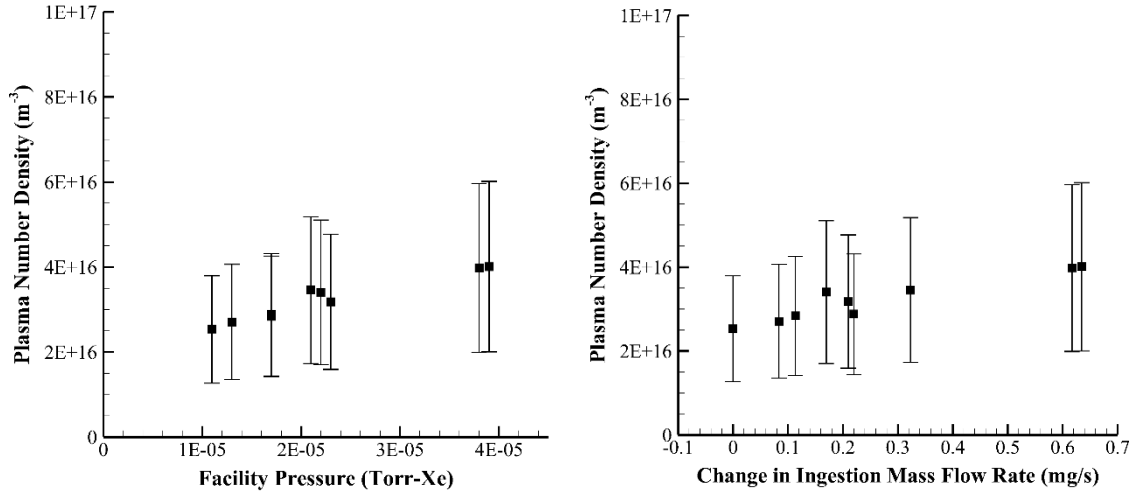

(a) **(b)**

Figure 6.7: H6 plasma number density as a function of (a) facility pressure (b) ingestion mass flow rate.

However, as with the Faraday probe results, the observed trend for the IHD2000-EM11 is not monotonic with facility pressure. Instead, variance in computed density is observed at the repeated pressures of 1×10^{-5} Torr-Xe and 2×10^{-5} Torr-Xe. Consistent with the plume divergence half-angle results shown in Section 6.2.1.1, plotting the plasma number density as a function of the change in ingestion mass flow rate (as done in Figure 6.6(b)) yields a visibly more linear and monotonic result. However, as with the ion beam current results, all observed changes in plasma density are less than the empirical uncertainty. Therefore, quantification of the variance in mean values at a given abscissa (as was done for the plume divergence half-angle) is not meaningful for this dataset.

Instead, to quantify the increase in linearity, a linear fit was created for the plasma density results using both facility pressure and change in ingestion mass flow rate as the independent variable. The corresponding coefficient of determination (or R^2) value was determined for both fit lines. When applied to regression analysis, this value is a statistical measure of how well the chosen regression model fits the observed data [96]. Since a linear model was chosen for these data, it thus serves a first-order approximation of the linearity of the data set. The computed R^2 was approximately 4% larger when the change in ingestion mass flow rate was used as the independent variable. This suggests that the ingestion mass flow rate due to the bulk motions of the background flow offers a modestly better description of the changes in plume plasma density than does facility pressure magnitude.

This finding aligns well with the observed increases in ion beam current and discharge current, which (since the current utilization efficiency remains roughly constant) suggests the generation of more plasma at elevated ingestion mass flow rates, and, thus, higher number densities. It is important to note that no significant improvement in fit was observed

with the H6 data. This is most likely due to the smaller number of measurements available at common pressures for this HET. Finally, it is interesting to note that the average rate of change for both the IHD2000-EM11 and H6 is approximately 1×10^{16} m^{-3} per 1 A increase in measured mean discharge current. The emergence of a constant rate of change is consistent with the ion beam current results presented in Section 6.2.1.2.

6.2.2.2 Electron Temperature and Plasma Potential

Measurements of the plume plasma potential and electron temperature are shown plotted as a function of facility pressure in Figure 6.8(a) and (b), respectively for the IHD2000-EM11. The equivalent data for the H6 are shown plotted in Figure 6.9(a) and (b). Unlike for the plume data thus far presented, the observed trends in electron temperature and plasma potential differ between the IHD2000-EM11 and the H6. As shown in Figure 6.8(a) and (b), plasma potential and electron temperature both decrease with increasing facility pressure for the IHD2000-EM11. Specifically, the plasma potential and electron temperature decrease by 62% and 114%, respectively, as the pressure increases from 1×10^{-6} Torr-Xe to 5×10^{-5} Torr-Xe. Both changes are greater than the empirical uncertainty. However, as shown in Figure 6.9(a) and (b), no change is observed (within the empirical uncertainty) in either quantity for the H6 as facility pressure increases.

Since electron temperature and plasma potential are both indicators of cathode coupling characteristics, this differing behavior is likely because the IHD2000-EM11 uses an externally-mounted cathode whereas the H6 uses an internally-mounted cathode. The decrease in plasma potential and electron temperature with increasing facility pressure observed for the IHD2000-EM11 is consistent with previous measurements taken using other HETs with externally-mounted cathodes including the SPT-100 and NASA-173M

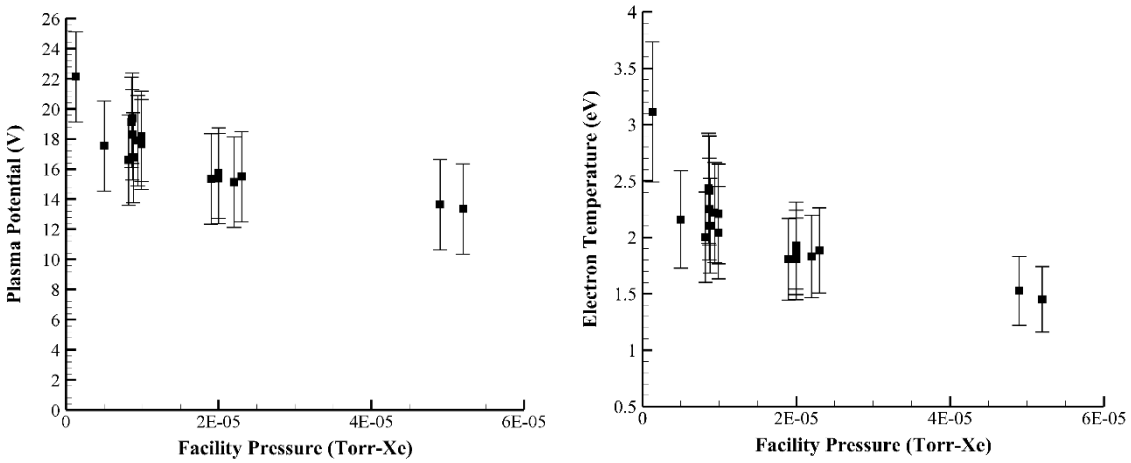

(a) **(b)**

Figure 6.8: Measurements of (a) plasma potential and (b) electron temperature for the IHD2000-EM11.

and can be explained by analyzing the impact of facility pressure on electron mobility [15, 24].

At lower background pressures, fewer collisions occur between electrons and background neutrals [15, 24]. For the nominal cathode configuration for the IHD2000-EM11, the magnetic field at the cathode orifice is high enough to magnetize the cathode electrons and force the electrons to move along the magnetic field lines towards the thruster channel and body. This decrease in cross-field electron mobility restricts all but the highest-energy electrons from moving into the plume and increases the plume electron temperature [12]. In addition, this decrease in mobility depletes electrons from the near-field plasma and pushes the plasma potential higher in order to maintain quasi-neutrality [12]. At elevated background pressures, the increase in collisions between electrons and background neutrals enhances cross-field electron mobility and eases electron transport into the plume [6, 12, 15, 24]. Lower-energy electrons are thus able to travel into the plume

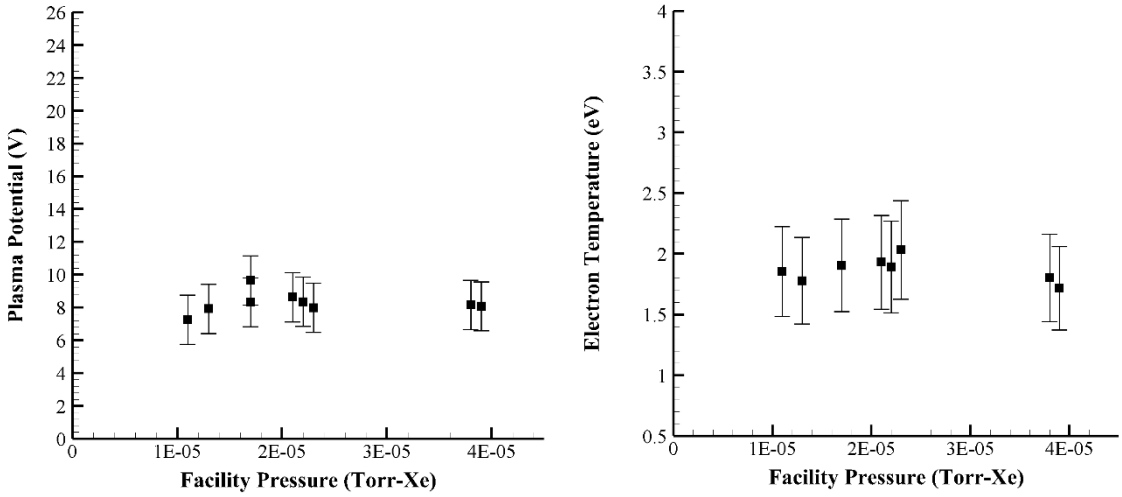

(a) **(b)**

Figure 6.9: Measurements of (a) plasma potential and (b) electron temperature for the H6.

resulting in lower electron temperatures and plasma potentials [6, 12, 15, 24].

Due to the internal mounting of the H6 cathode, for the range of pressures tested in this work, the largest contributor to the number density near the cathode orifice is unionized propellant from the HET, which, due to the fixed anode mass flow rate and mass utilization efficiency, should not have changed significantly with facility pressure. This shields the cathode electrons from changes in mobility related to changes in facility backpressure and eliminates the observed pressure sensitivity of electron temperature and plasma potential. This result is consistent with those from previous work and is one of the reasons that internally-mounted cathodes are favored for high-power HETs [17].

Another measure of the resistance to electron transport from the cathode to the anode and plume is the cathode coupling voltage, which is defined as the difference between the plasma potential and the cathode-to-ground voltage [10, 97]. The cathode coupling voltage is a loss term that determines how much of the imposed discharge voltage must be used for

electron transport, and thus cannot be used to generate thrust [10, 97]. Increases in cathode coupling voltage, therefore, correspond to reduced near-field electron mobility. The cathode coupling voltages for the IHD2000-EM11 and H6 were computed using the plasma potential measurements shown in Figure 6.8(a) and Figure 6.9(a) as well as measurements of the cathode-to-ground voltage made using an Agilent 34980A data acquisition system. The results are shown plotted as a function of facility pressure in Figure 6.10(a) for the IHD2000-EM11 and Figure 6.10(b) for the H6. The computed cathode coupling voltages confirm the increase in electron mobility (indicated by a decrease in coupling voltage of approximately 15 V) at elevated pressure for the IHD2000-EM11 and the invariance in mobility for the H6. These results are also consistent with findings from previous facility effects studies comparing internally- and externally-mounted cathodes [17].

Consistent with the Faraday probe and plasma number density results, as shown in Figure 6.8, the changes in plasma potential and electron temperature for the IHD2000-EM11 are non-monotonic and multiple values are observed at a fixed pressure. However, unlike with the previous results, plotting these changes as a function of changes in ingestion mass flow rate does yield a monotonic result. This suggests that near-field electron transport is dependent on more than just near-field neutral density and velocity. This result is expected as the reliance of cathode electron mobility on a variety of factors including magnetic field topology and strength and plasma instabilities is well-known and has been studied in a variety of works throughout the literature [2, 98–102].

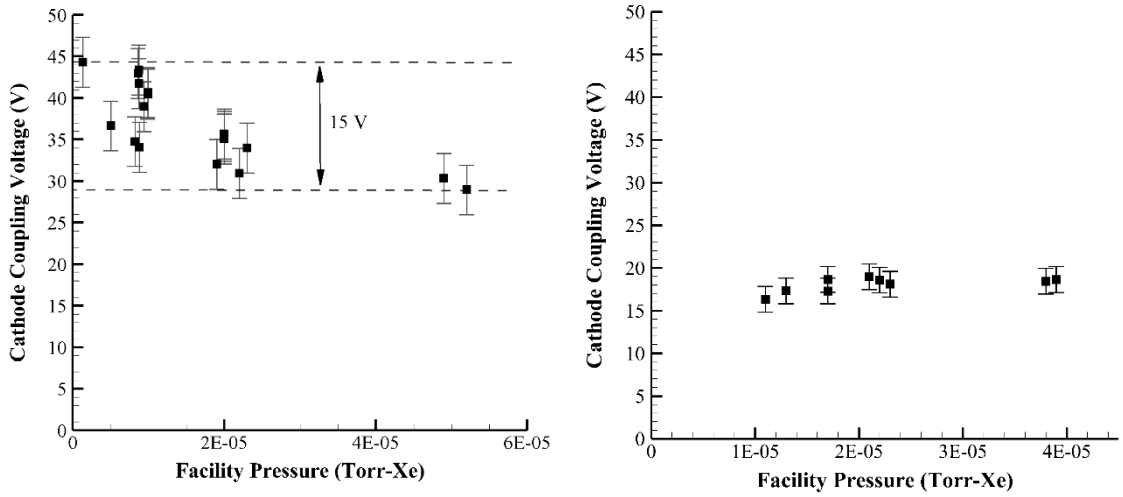

(a) **(b)**

Figure 6.10: Cathode coupling voltage as a function of facility pressure for the (a) IHD2000-EM11 and (b) H6. Cathode coupling voltage is defined as the difference between the plasma potential and cathode-to-ground voltage.

6.2.3 RPA

The final plume diagnostic used in this work was the RPA. Measurements of the most-probable ion voltage and full width at half maximum of the ion voltage distribution are shown plotted as a function of facility pressure in Figure 6.11(a) for the IHD2000-EM11 and Figure 6.11(b) for the H6. Consistent with previous facility effects studies, the most-probable ion voltage measurements for H6 is independent of facility pressure [15, 20, 27]. For IHD2000-EM11, the most-probable voltage increases by approximately 17 V as the facility pressure is increased from 1×10^{-6} Torr-Xe to 2×10^{-5} Torr-Xe. To the first-order, the average acceleration voltage of a HET can be expressed as the difference between the discharge voltage and the cathode coupling voltage [10, 97]. As discussed in Section 6.2.2.2, the cathode coupling voltage decreased by a similar value over this same range of pressures. Since the discharge voltage was fixed, the observed increase in most-probable

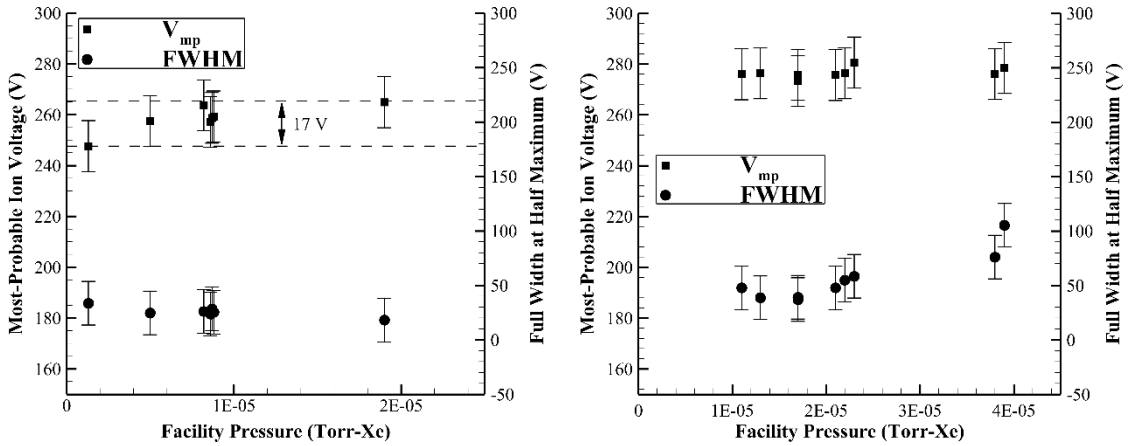

Figure 6.11: Most-probable ion voltage and full width at half-maximum as a function of facility pressure for the (a) IHD2000-EM11 and (b) H6.

ion voltage can thus be attributed to the observed decrease in cathode coupling voltage. It is important to note that a similar sensitivity for the cathode coupling voltage was observed for the BPT-4000 (now XR-5), which also uses an externally-mounted cathode [103]. This suggests that changes in cathode coupling for HETs with externally-mounted cathodes may lead to artificial increases in measured most-probable ion voltage at elevated facility pressures. However, care must be taken when interpreting these results as the observed change is less than the empirical uncertainty.

Although the FWHM measurements are also constant (within the empirical uncertainty) for the IHD2000-EM11, the FWHM increases for the H6 by 68 V or 184% as the facility pressure is increased from 1×10^{-5} Torr-Xe to 4×10^{-5} Torr-Xe. This change is larger than the empirical uncertainty associated with this measurement. The broadening of the ion energy distribution has been noted in previous facility effects studies and is, in part, attributable to CEX ion generation [15, 18–20, 28, 33]. As discussed in Section 6.2.1, CEX collisions create slow-moving ions that are not accelerated by the HET. When collected by

the RPA, these CEX ions increase the ion population at low voltage and thus cause a broadening of the ion voltage distribution. This broadening worsens at higher pressures due to the concomitant increase in CEX collisions [15, 18–20, 28, 33]. Studies have also suggested that upstream shifts in the ionization and accelerations zones at elevated background pressures can further contribute to broadening of the ion voltage distribution [20]. Unfortunately, only a partial set of RPA data were collected with both HETs due to the failure of the in-situ probe positioning stages. This prevents further analysis regarding whether facility pressure or change in ingestion mass flow rate better describes the trends in the collected data as well as an assessment on if the ion voltage distribution of the IHD2000-EM11 would have shown broadening at even higher facility pressures.

6.3 Discharge Current Oscillations

6.3.1 Discharge Current Stability

Previous studies of HET discharge oscillations have used two primary metrics to quantify the stability of the HET discharge [13, 54]. The first is the standard deviation of the discharge current, which measures the average variance around the mean. The second is the average peak-to-peak amplitude, which is a measure of the maximum variance from the mean. The smaller the magnitude of both metrics, the more stable the discharge is considered [13, 15, 54]. To determine the pressure sensitivity of the discharge current stability for each of the HETs tested, both the standard deviation and average peak-to-peak amplitude were computed using the time-resolved measurements of the discharge current described in Section 4.4.3. The resultant values of the standard deviation of the discharge current and average peak-to-peak amplitude are shown as a function of facility pressure in

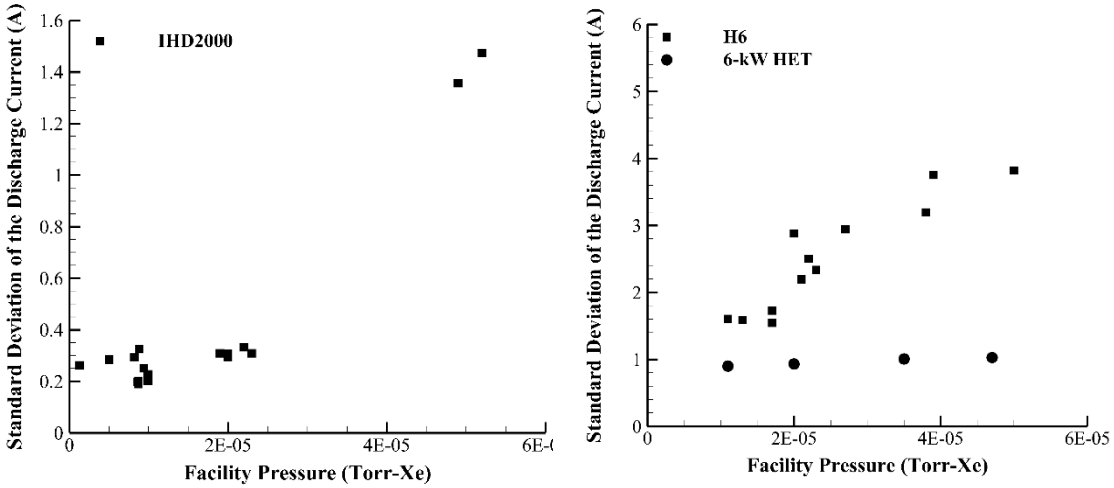

(a) **(b)**

Figure 6.12: Standard deviation of the discharge current as a function of facility pressure for the (a) IHD2000-EM11 and (b) H6 and 6-kW HET. Empirical uncertainty is represented by the symbol size.

Figure 6.12(a) and Figure 6.14(a), respectively, for the IHD2000-EM11 and in Figure 6.12(b) and Figure 6.14(b), respectively, for the H6 and 6-kW HET. A minimum of ten measurements of the time-resolved discharge current signal were acquired at each chamber operating condition with each measurement encompassing approximately 400 fundamental periods. The empirical data shown in Figure 6.12 and Figure 6.14 represent the average across these ten measurements, while the error bars correspond to the standard deviation.

Overall, both the standard deviation of the discharge current and average peak-to-peak amplitude increase with increasing background pressure for all tested HETs. As shown in Figure 6.12(a) and Figure 6.14(a), respectively, the standard deviation of the IHD2000-EM11 discharge current increased by 424% and the average peak-to-peak amplitude increased by 371% as the pressure was increased from 1×10^{-6} Torr-Xe to 5×10^{-5} Torr-Xe. As shown in Figure 6.12(b) and Figure 6.14(b), the standard deviation and average peak-to-peak amplitude of the discharge current for the H6 increased by 136% and 107%

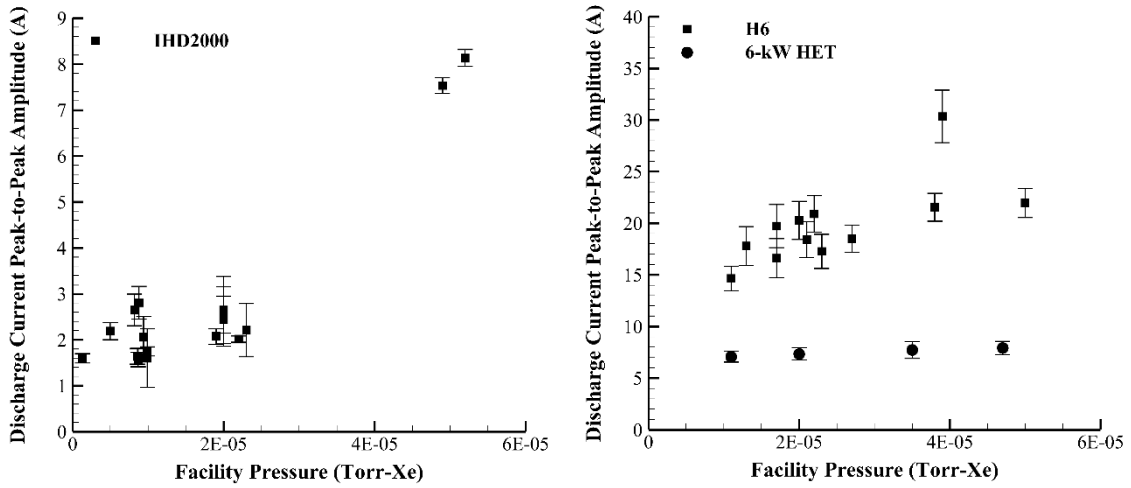

(a) **(b)**

Figure 6.13: Discharge current average peak-to-peak amplitude as a function of facility pressure for the (a) IHD2000-EM11 and (b) H6 and 6-kW HET.

respectively, while the same values for the 6-kW HET increased by 14% and 12%, respectively, as the facility pressure increased from 1×10^{-5} Torr-Xe to 5×10^{-5} Torr-Xe. The observed decrease in discharge current stability is consistent with previous work for HETs using both externally- and internally-mounted cathodes [15, 70].

6.3.2 Power Spectra

Further information on the time-resolved nature of the HET discharge as well as insight into the physical mechanisms responsible for the observed shifts in HET stability with pressure discussed in Section 6.3.1 can be found by computing the power spectrum of the discharge current. The power spectrum is obtained by applying a Fast Fourier Transform (FFT) to the discharge current signal to decompose the time-domain signal into its components in the frequency domain [104]. The frequency of maximum power within the spectrum is called the peak frequency and can be used to determine the dominant physical

process driving the observed discharge current oscillations. The peak frequency of the discharge current is shown as a function of facility pressure in Figure 6.14(a) for the IHD2000-EM11 and Figure 6.14(b) for the H6 and 6-kW HET. Identical to the approach used to compute the discharge current stability metrics in Section 6.3.1, a minimum of ten measurements of the time-resolved discharge current signal were acquired at each chamber operating condition with each measurement encompassing approximately 400 fundamental periods. The empirical data shown in Figure 6.14 represent the average across these ten measurements, while the error bars correspond to the standard deviation.

As shown in Figure 6.14(a), there are three distinct types of power spectra for the IHD2000-EM11. At the lowest achieved operating pressures (i.e., those at or below 1×10^{-5} Torr-Xe), the power spectrum is as shown in Figure 6.15(a). At these pressures, the peak frequency is approximately 10 kHz and has a power of approximately 5 dB. These spectra

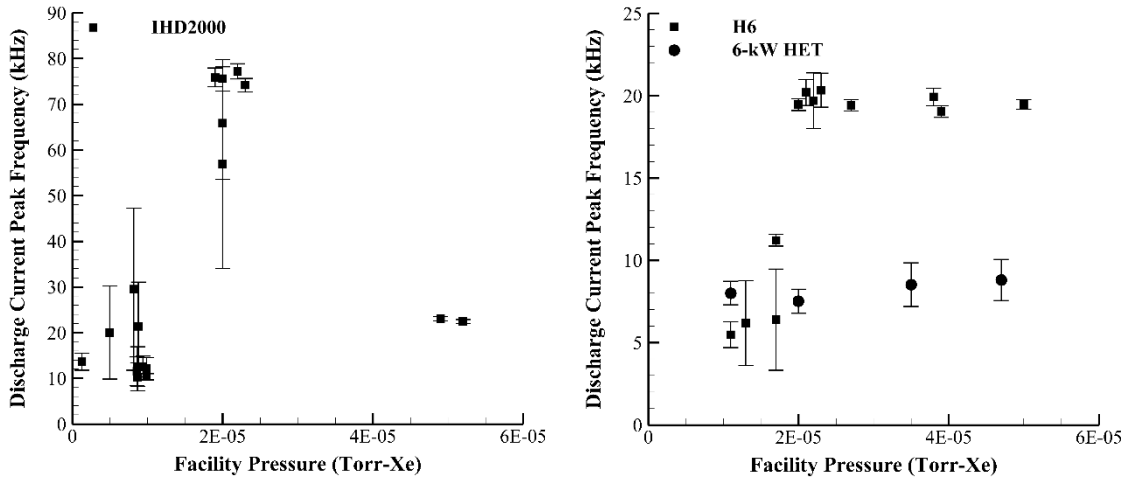

(a) **(b)**

Figure 6.14: Discharge current peak frequency as a function of facility pressure for the (a) IHD2000-EM11 and (b) H6 and 6-kW HET. Pressures achieved using the chamber configurations listed in (a) Table 4.2 and (b) Table 4.3.

also feature a prominent secondary peak at approximately 30 kHz with a power of 2 dB. Additional insight into the nature of these oscillations can be gained by computing the probability density function (PDF) of the discharge current. This approach has been used with success in recent HET oscillation studies to identify different oscillations by their unique PDF characteristics [105]. Figure 6.16(a) shows the PDF of the discharge current signal used to generate the power spectrum in Figure 6.15(a). It is important to note that the convention used in this work represents the mean discharge current as the origin of the abscissa. The magnitude of the abscissa thus represents the magnitude of the deviation from the mean.

The power spectrum peak at 10 kHz shown in Figure 6.15(a) is consistent with published values of the breathing mode frequency for thrusters of this power class [15, 33, 54, 106]. The Gaussian nature of the PDF shown in Figure 6.16(a) is also consistent with a global breathing mode oscillation [105]. The cause of the secondary peak near 30 kHz is harder to determine as it is consistent with published values of both oscillations related to azimuthal spokes and the breathing mode frequency of other 2-4-kW class thrusters such as HiVHAc [15, 18, 33, 54, 106]. The Gaussian PDF suggests that this is most likely a higher harmonic of the observed 10 kHz breathing mode frequency as oscillations associated with azimuthal spokes have been observed to cause the PDF to exhibit sinusoidal characteristics [54, 105]. However, without additional time-resolved diagnostics such as high-speed imagery, it is impossible to determine with certainty whether this secondary peak is associated with spokes or the hypothesized higher harmonic of the observed 10 kHz breathing mode frequency [15, 18, 33, 54, 106].

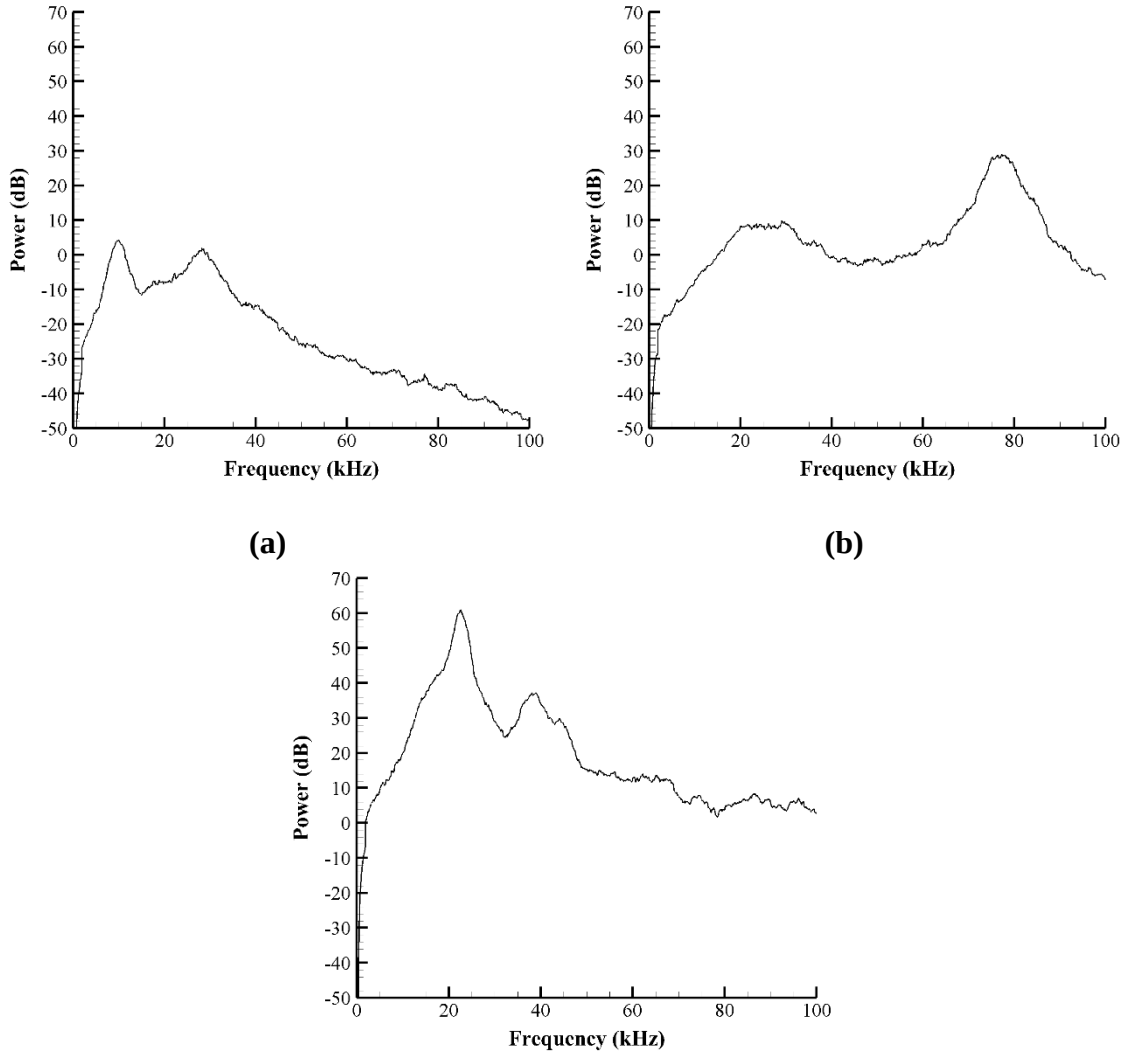

Figure 6.15: Power spectra for the IHD2000-EM11 at (a) low, (b) mid, and (c) high facility pressure.

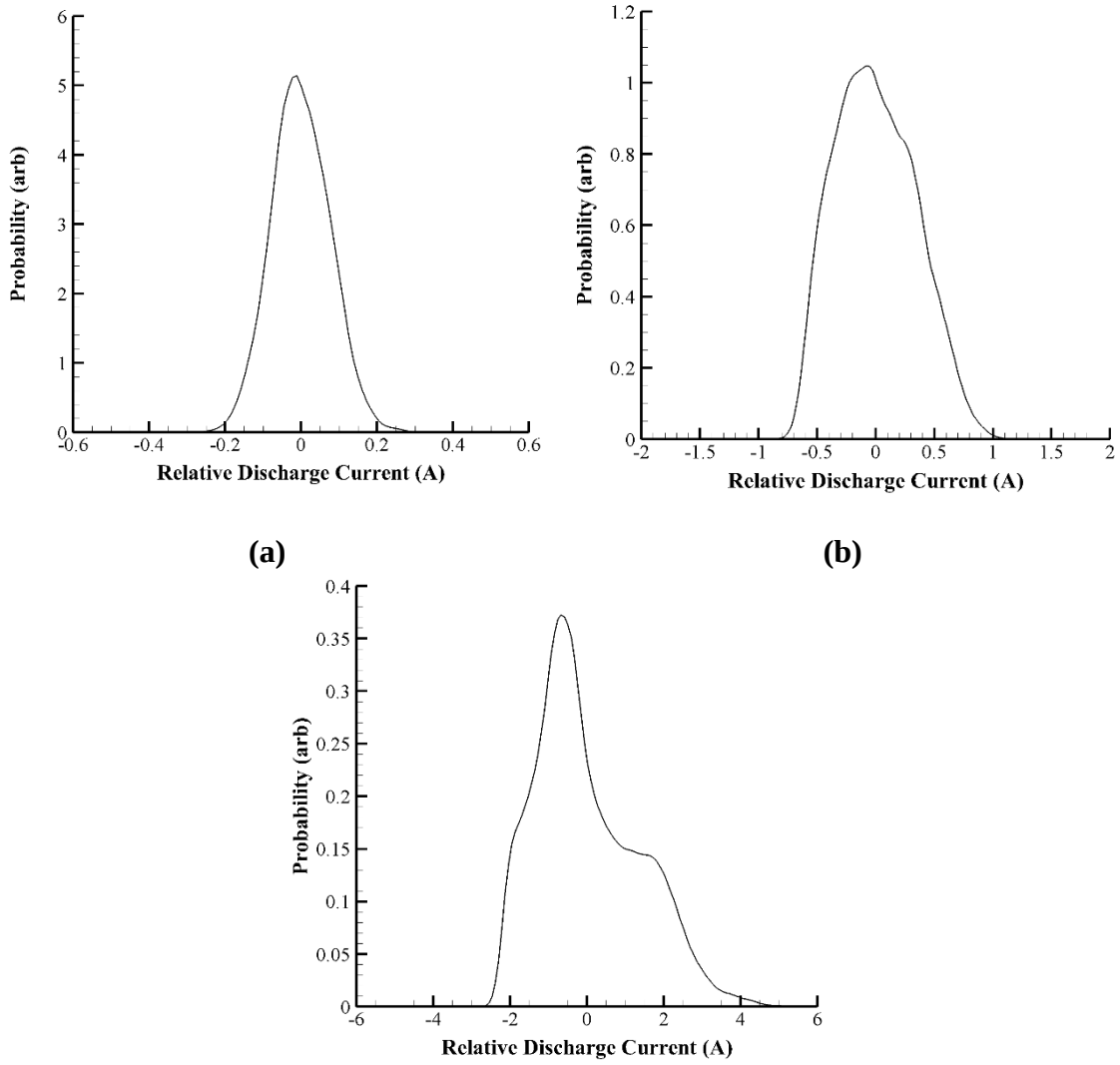

Figure 6.16: Discharge current PDFs for the IHD2000-EM11 at (a) low, (b) mid, and (c) high facility pressure.

The second type of power spectrum for the IHD2000-EM11 occurs at facility operating pressures near 2×10^{-5} Torr-Xe and is shown in Figure 6.15(b). These spectra are characterized by a stronger peak (relative to the low-pressure spectrum) at a frequency of approximately 70 kHz with an average power of approximately 30 dB. There is also a secondary peak near 30 kHz with an average power of approximately 10 dB. This secondary peak is at the same frequency as was observed in the previously-discussed low-pressure power spectrum shown in Figure 6.15(a). As shown in Figure 6.16(b), the PDF of the discharge current at this pressure exhibits characteristics of a sinusoidal PDF superimposed on a more dominant Gaussian profile [105]. Specifically, there is still one dominant peak coincident with the mean discharge current (consistent with a Gaussian PDF) and two secondary peaks spaced roughly equidistant from the mean (consistent with a sinusoidal PDF) [105].

The primary peak near 70 kHz as well as the sinusoidal characteristics of the PDF strongly resembles recently published results obtained using NASA's HERMeS HET [105]. As noted in that work, this frequency is higher than is typically observed for most common HET oscillation modes including the breathing mode and spoke mode [105]. Instead, this peak frequency most closely matches oscillations related to the recently-documented cathode gradient-driven mode [33, 105, 107]. The growth rate of this oscillation is known to be dependent on electron collision frequency [107]. As discussed in Section 6.2.2.2, measurements of the electron temperature and plasma potential strongly suggest an increase in electron collision frequency with increasing background pressure for the IHD2000-EM11. This change in frequency could therefore have excited this mode and made it the dominant oscillation at these pressures. It is important to note that this is

the first reported observation of a high-frequency sinusoidal mode in a HET that is not magnetically shielded and has an externally-mounted cathode [105]. This is also the first work to cause this mode by changing the background pressure instead of the HET throttle condition [105]. As discussed in Section 6.2.2.2, cathode processes tend to exhibit enhanced sensitivity to facility background pressure for externally-mounted cathode configurations [17]. This is likely the reason that a pressure sensitivity is observed for this mode in this work, but not in prior studies with HERMeS (which has an internally-mounted cathode).

The final type of power spectrum for the IHD2000-EM11 is shown in Figure 6.15(c) and occurs at the highest achieved facility operating pressures near 5×10^{-5} Torr-Xe. These spectra are characterized by a primary peak near 20 kHz and secondary peaks near 40 kHz. The primary peak has the highest power of any peak shown in Figure 6.15 with an average power near 60 dB, whereas the secondary peak has an average power near 40 dB, making it the second highest observed peak power. Several other facility effects studies have shown that the breathing mode frequency increases with facility pressure [15, 18, 108]. Specifically, studies using the SPT-100 have shown increases in breathing mode frequency of nearly 10 kHz over the same range of pressures tested in this work [15]. Therefore, the primary peak likely corresponds to the shifted breathing mode frequency of the IHD2000-EM11 at elevated pressure. As shown in Figure 6.16(c), the discharge current PDF at this pressure only has two defined peaks spaced equidistant from the mean discharge current, and thus more closely resembles a sinusoidal PDF than those observed at lower pressures. The sinusoidal characteristics of the PDF suggest that the secondary peak is most likely caused by an azimuthal spoke mode, which has been shown in many previous studies to

contribute to the spectrum even for discharges dominated by a strong breathing mode peak [18, 54].

It is important to note that the increase in power associated with the peak frequency of the IHD2000-EM11 spectra as well as the increase in abscissa magnitude of the PDFs with increasing pressure correspond to the observed increases in discharge current standard deviation and average peak-to-peak amplitude shown in Figure 6.13(a) and Figure 6.14(a), respectively. These observations are consistent as increases in peak frequency power correspond to increases in oscillation intensity, whereas larger PDF abscissas indicate an increased probability of larger oscillations about the mean. Both changes would manifest as increases in discharge current standard deviation and average peak-to-peak amplitude, as observed [33, 104]. Taken together, these results therefore indicate that oscillation intensity increased for the IHD2000-EM11 with increasing facility pressure.

A closer inspection of Figure 6.14(a) reveals several peak frequencies with large standard deviations relative to the other plotted points. These points correspond to situations in which the IHD2000-EM11 was jumping between the low and mid-pressure spectra shown in Figure 6.15(a) and (b), respectively. The resultant average peak frequencies lie somewhere between 10 kHz and 70 kHz, and the large standard deviation is indicative of the fact that the acquired data spanned both spectrum types. Based on the data collected, these transitional points do not appear to correspond to any systematic bias or hysteresis.

As shown in Figure 6.14(b), there are two distinct power spectra types for the H6. At the lowest achieved operating pressure of 1×10^{-5} Torr-Xe, the power spectrum is as shown in Figure 6.17(a). At this pressure, there is a broad frequency peak between approximately

5 kHz and 10 kHz with a peak power of approximately 55 dB. These spectra also feature a prominent secondary peak at approximately 20 kHz with a power of 45-50 dB. An example PDF of the discharge current measurements used to generate these spectra is shown in Figure 6.18(a). The Gaussian PDF and broad peak frequency centered near 10 kHz are both consistent with published values of the breathing mode for the H6 while the secondary peak is consistent with the m = 6 spoke mode [54, 105, 107].

A characteristic power spectrum for the H6 operating at facility pressures at and above 2×10^{-5} Torr-Xe is shown in Figure 6.17(b). The peak frequencies are identical to what was observed for the low-pressure spectrum in Figure 6.17(a), however, the power associated with the 20 kHz peak increases to approximately 70 dB, while the 10-kHz peak remains at a power of approximately 55 dB. This suggests that the H6 transitioned from operating in the global mode (which is characterized by a dominant breathing mode) at lower facility pressures to the local mode (which is characterized by a dominant spoke mode) at higher facility pressures [54]. Although this transition has previously been observed to occur in response to changes in magnetic field, this is the first work to observe it occurring in response to a change in facility pressure [54].

A characteristic PDF of the discharge current for this type of spectrum is shown in Figure 6.18(b). As compared to the low-pressure PDF in Figure 6.18(a), the high-pressure PDF displays sinusoidal characteristics including the emergence of weak secondary peaks on the negative side of the abscissa. The emergence of these characteristics is further evidence of the increasing role of the spoke mode at these pressures [54, 105]. It is also important to note the skewed nature of the PDF towards the negative half of the abscissa.

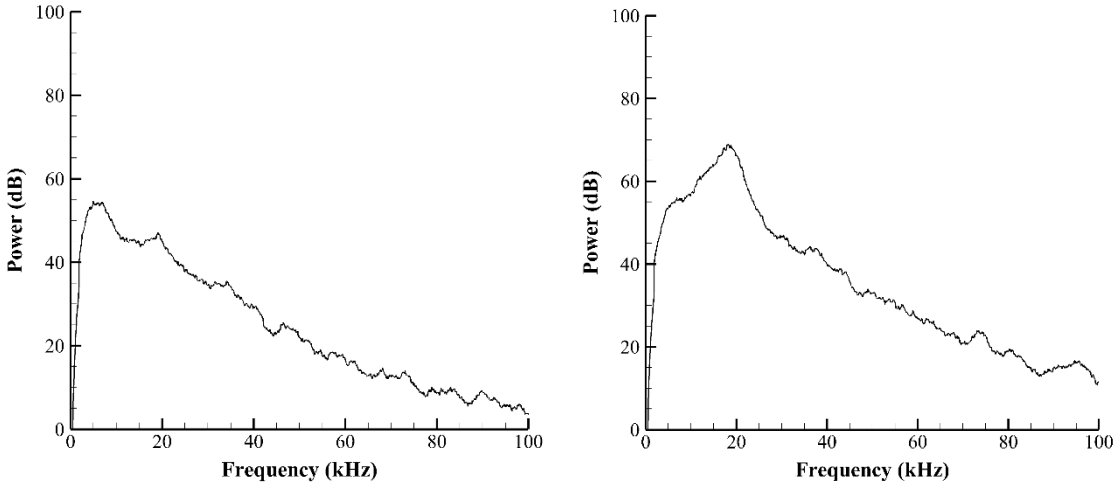

(a) **(b)**

Figure 6.17: Power spectra for the H6 at (a) low and (b) high facility pressure.

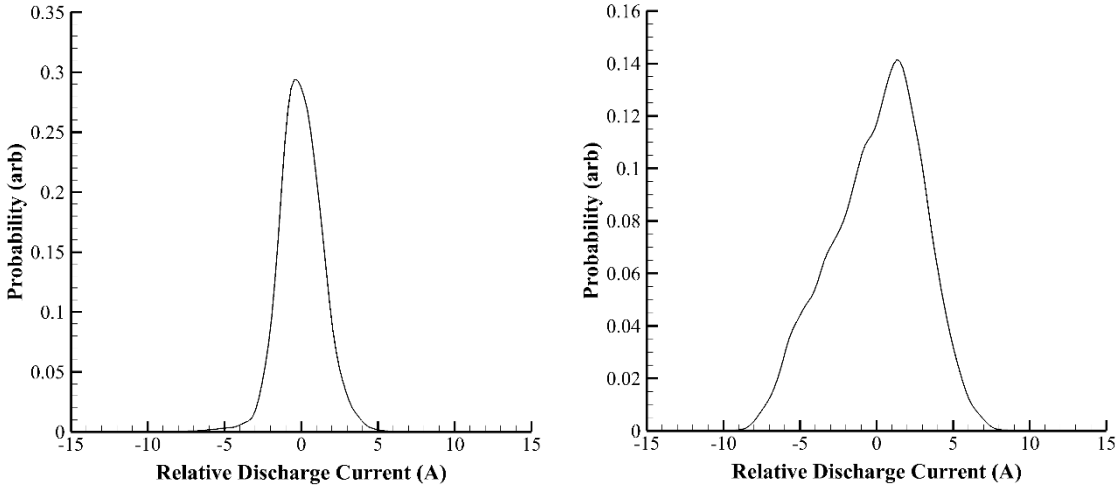

(a) **(b)**

Figure 6.18: PDFs for the H6 at (a) low and (b) high facility pressure.

Skewed PDFs have previously been observed for operating modes that exhibit periodic high-intensity oscillations [105]. The observed skew in the PDF is thus consistent with the observed increase in average peak-to-peak amplitude and standard deviation of the discharge current at elevated pressures as discussed in Section 6.3.1.

Unlike the other two HETs tested, as shown in Figure 6.14(b), the 6-kW HET only exhibited one oscillation mode across all tested facility pressures. An example power spectrum and PDF for this mode is shown in Figure 6.19(a) and (b), respectively. The power spectrum for this HET is characterized by a broad peak centered around 8 kHz with a power of approximately 50 dB while the PDF is largely Gaussian. This frequency and PDF are consistent with the breathing mode frequency for other HETs in this power class [54, 105, 107]. It is important to note that, despite staying in the breathing mode for all tested pressures, the peak frequency of the 6-kW HET did not increase as has been observed with HETs with externally-mounted cathodes including the SPT-100 and HiVHAc [15, 18]. A similar invariance was also observed during recent testing of the NASA HERMeS thruster, thus suggesting that magnetically-shielded HETs with internally-mounted cathodes may be less susceptible to changes in oscillation characteristics at elevated facility pressures [70, 105].

As most clearly seen Figure 6.14(a), the observed changes in oscillation characteristics are not monotonic with pressure for any of the tested HETs. However, much like with the electron temperature and plasma potential results discussed in Section 6.2.2.2, no increase in linearity is observed when changes in ingestion mass flow rate are used as the abscissa. This result is expected as discharge current oscillations have been shown to be complex,

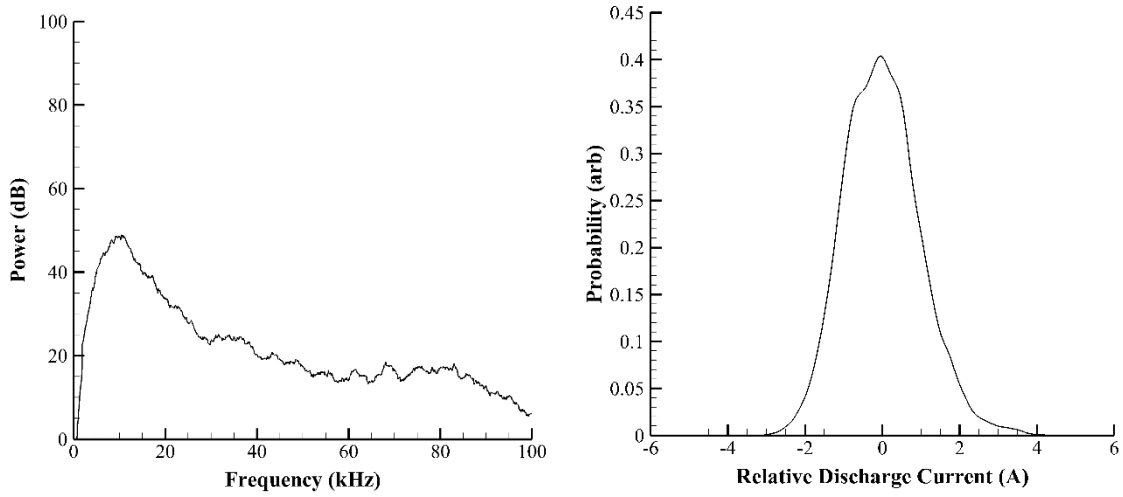

(a) **(b)**

Figure 6.19: Characteristic (a) power spectrum and (b) PDF for the 6-kW HET.

coupled phenomena with sensitivities related to a variety of factors including magnetic field topology and electron mobility [2, 54, 98–102]. The complexity associated with these phenomena is precisely why all three HETs exhibit such different oscillation characteristics. Thus, although useful for describing changes in the mean discharge current, knowledge of the bulk background motions is insufficient to fully describe the discharge current oscillation characteristics of a given HET.

6.4 Performance

Measurements of thrust are shown plotted as a function of facility pressure in Figure 6.20(a) for the IHD2000-EM11 and Figure 6.20(b) for the H6 and 6-kW HET. As with the oscillation results discussed in Section 6.3, the sensitivity to facility pressure of the thrust generated by the IHD2000-EM11 is different than that of the H6 or 6-kW HET. As shown in Figure 6.20(a), the thrust of the IHD2000-EM11 decreased by approximately 14 mN or 28% as the facility pressure increased from 1×10^{-6} Torr-Xe to 5×10^{-5} Torr-Xe. This trend

is opposite to what has been observed in previous facility effects studies; in these studies HETs operated at a fixed anode mass flow rate have generated more thrust at elevated background pressures due to the ingestion and subsequent acceleration of background neutrals [15–17, 23, 24, 27, 29]. To determine why the results from this work differ from those in previous studies, it is useful to construct a first-order analytical expression for HET thrust that exposes the sensitivity of this parameter to the previously-presented ingestion and plume results.

As shown in Eq. (6.1), the thrust of a HET can be approximated using the ion beam current (I_i), ion mass (m_i), effective ion voltage (V_{ion}), the fundamental charge (e), and the plume divergence half-angle (ϕ).

$$T_F \approx I_i \sqrt{\frac{m_i V_{ion}}{2e}} \cos\phi \tag{6.1}$$

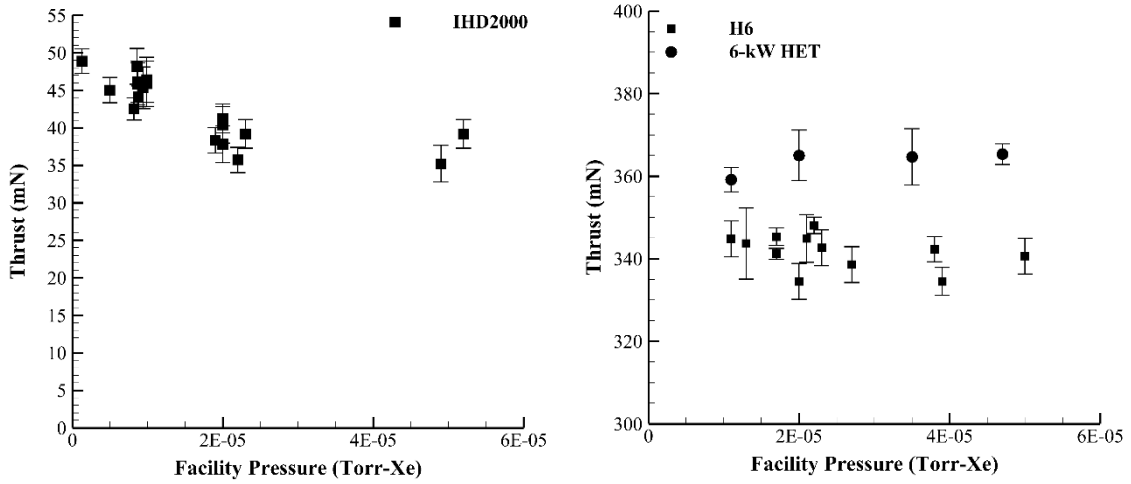

(a) **(b)**

Figure 6.20: Thrust as a function of facility pressure for the (a) IHD2000-EM11 and (b) H6 and 6-kW HET.

Each of these parameters can be estimated using the probe results presented in Section 6.2. The ion beam current and plume divergence half-angle are both computed from Faraday probe measurements as discussed in Section 6.2.1, while the effective ion voltage can be approximated as the most-probable ion voltage computed from the RPA measurements and presented in Section 6.2.3. Since the most-probable ion voltages shown in Figure 6.11(a) have no sensitivity (within the empirical uncertainty) to background pressure, this parameter is not expected to contribute to the observed thrust changes. However, as shown in Figure 6.1(a) and Figure 6.4(a), respectively, both the plume divergence half-angle and ion beam current increase with increasing facility pressure. Per Eq. (6.1), these changes have opposite effects on thrust. Specifically, the increase in ion beam current should yield higher thrust values whereas the increase in plume divergence half-angle should yield lower thrust values. To determine which effect was dominant, the thrust of the IHD2000-EM11 was computed using Eq. (6.1) and the Faraday probe results presented in Section 6.2.1. These calculations revealed that the sensitivity to plume divergence half-angle dominated, yielding a predicted thrust decrease of approximately 1.2 mN as pressure was increased from 1×10^{-6} Torr-Xe to 5×10^{-5} Torr-Xe. This result represents 8.5% of the overall observed decrease.

It is important to emphasize that care must be taken when interpreting these computations. Per the discussion in Section 6.2.1, the dominant process leading to the observed changes in ion beam current and plume divergence half-angle is CEX collisions. However, depending on where these collisions occur, they may or may not impact the thrust generated by the HET. The mechanism by which force is transferred back to the HET is the Lorentz force on the trapped Hall current of electrons [2, 4]. Thus only those CEX

ions that are created in a region of non-negligible magnetic field can influence the thrust generation process [26]. Since the HET magnetic field magnitude is known to fall to zero within tens of centimeters from the HET body, and the Faraday probe is located at a distance 1 m downstream of the HET exit plane, some CEX ions detected by the Faraday probe are created in a region of negligible magnetic field and so do not contribute to thrust augmentation. In any event, the first-order estimate of the impact of plume parameters on thrust show that these changes are insufficient to fully account for the observed thrust change even assuming all CEX ions contribute to thrust augmentation processes.

Another possibility to explain the observed thrust decrease is an artificial effect known historically as windage [109–111]. Windage refers to the force imparted on the thruster by the circulation or bulk motion of background neutrals in the test facility and has previously been identified as a concern when testing micro-propulsion devices at high pressures [109–111]. As shown in Section 5.3.1.2, a net pressure force in the negative thrust direction does arise during HET testing due to the bulk flow of neutrals in the axial direction. However, the maximum observed mass flow rate in this direction was approximately 1 mg/s, yielding a maximum force (assuming all background neutrals are moving at the thermal-diffusive speed characterized by chamber wall temperature) of less than 1 mN. Thus, for the HETs tested in this work, windage effects are negligible.

The above results suggest that the most likely possibility to explain the observed thrust decrease is thus a change in the HET power loss mechanisms with facility pressure. Previous long-duration testing of the BPT-4000 (now XR-5) revealed a thrust decrease of on the order of tens of mN during the first 500 hours of operation, which was attributed to an increase in ion power deposition to the channel [112, 113]. Studies have shown that the

ionization and acceleration zone of a HET tends to move upstream with increasing facility pressure [20]. Upstream ionization increases the effective channel view factor for ion bombardment and therefore increases the number of ions which strike the channel. Like what was observed for the BPT-4000, this increase in channel ion bombardment is accompanied by an increase in magnitude of the discharge current oscillations and a decrease in thrust [113]. Thus, increased losses to the channel wall is the most likely culprit for the observed thrust decrease at elevated background pressures. This trend represents a breakdown of the simple ingestion approach for predicting changes in HET thrust even when such an approach was adequate for predicting changes in mean discharge current as discussed in Section 5.2.1. Thus, plotting the performance variation as a function of ingestion mass flow rate does not increase the linearity or monotonic nature of the trends observed in Figure 6.20(a).

As shown in Figure 6.20(b), the changes in thrust for the H6 and 6-kW HET were less than the empirical uncertainty as the facility pressure was increased from 1×10^{-5} Torr-Xe to 5×10^{-5} Torr-Xe. Previous studies with the H6 have shown small variations in thrust of approximately 5 mN over this pressure range, which is approximately equal to the average thrust stand uncertainty during the H6 and 6-kW HET testing done in this work [17, 23]. This explains the apparent lack of thrust sensitivity to pressure for these HETs. Future work should repeat this experiment with reduced thrust stand uncertainty to better illuminate the performance trends associated with these two HETs as a function of facility pressure.

6.5 Magnetic Stability Study

During initial testing of a given HET, surfaces relating the discharge current, discharge voltage, and magnetic field strength are often compiled in order to identify what magnet

settings yield the most stable discharge current characteristics for a given mass flow rate [54, 69]. However, as discussed in Section 6.3, HET mode transitions have been observed to have a strong sensitivity to both magnetic field strength and facility background pressure [18, 54, 105, 107]. Although studies exist separately mapping the sensitivity of HET oscillations to pressure and magnetic field strength, as of yet, few have attempted to determine how pressure impacts the sensitivity of HET oscillations to magnetic field strength and vice versa [18, 54, 105, 107]. This missing knowledge is important as, without it, attempts to optimize the magnetic field for a given HET in a given facility may not hold when that HET is tested in another facility.

In order to determine how pressure impacts the magnetic field sensitivity of HET oscillations, time-resolve measurements of the discharge current of the H6 and 6-kW HET were acquired for several different peak radial magnetic field strengths. The strength of the magnetic field was varied by changing the magnitude of the current supplied to each magnet while maintaining a constant ratio of current supplied to the inner, outer, and trim magnets. This approach is identical to the one taken in previous works investigating the sensitivity of HET oscillations to magnetic field strength [54, 89]. However, unique to this work was the acquisition of data across all the various chamber configurations/pressures shown Table 4.3 in an attempt to determine the pressure sensitivity of these magnetic field strength sweeps.

6.5.1 H6

The mean, standard deviation, average peak-to-peak amplitude, and peak frequency of the H6 discharge current are shown as a function of magnetic field strength for facility pressures of 1×10^{-5} Torr-Xe, 2×10^{-5} Torr-Xe, and 4×10^{-5} Torr-Xe in Figure 6.21(a), (b),

(c), and (d), respectively. The abscissa in all panes of Figure 6.21 represents the ratio of the magnetic field strength to the nominal value. A minimum of five measurements of the time-resolved discharge current signal were acquired at each magnet condition with each measurement encompassing approximately 400 fundamental periods. The empirical data shown in all panes of Figure 6.21 represent the average across these five measurements, while the error bars correspond to the standard deviation. The uncertainty associated with the measurements of the mean and standard deviation of the discharge current (shown in Figure 6.21(a) and Figure 6.21(b), respectively) is captured by the symbol size.

Before discussing the impact of pressure, it is useful to first discuss the observed sensitivity of the discharge current characteristics to magnetic field strength at a fixed facility pressure of 1×10^{-5} Torr-Xe. As shown in Figure 6.21(b) and (c), the discharge current is the least stable for the lowest magnetic field strength tested (i.e., 60% of the nominal value). At these magnet settings, the standard deviation of the discharge current and average peak-to-peak amplitude were approximately 8 A and 62 A, respectively. Further evidence of the oscillatory nature of the discharge at these magnet settings is shown by the power spectrum Figure 6.22(a). The peak in the power spectrum has the highest power of any observed throughout this work at approximately 85 dB centered on a frequency of approximately 5 kHz. This frequency is characteristic of the breathing mode and suggests the presence of a large global oscillation inside the discharge channel [54]. As shown in Figure 6.22(b), the corresponding PDF is heavily skewed towards positive values of the abscissa, indicating the existence of large positive deviations from the mean consistent with the large average peak-to-peak amplitude. These findings match those from

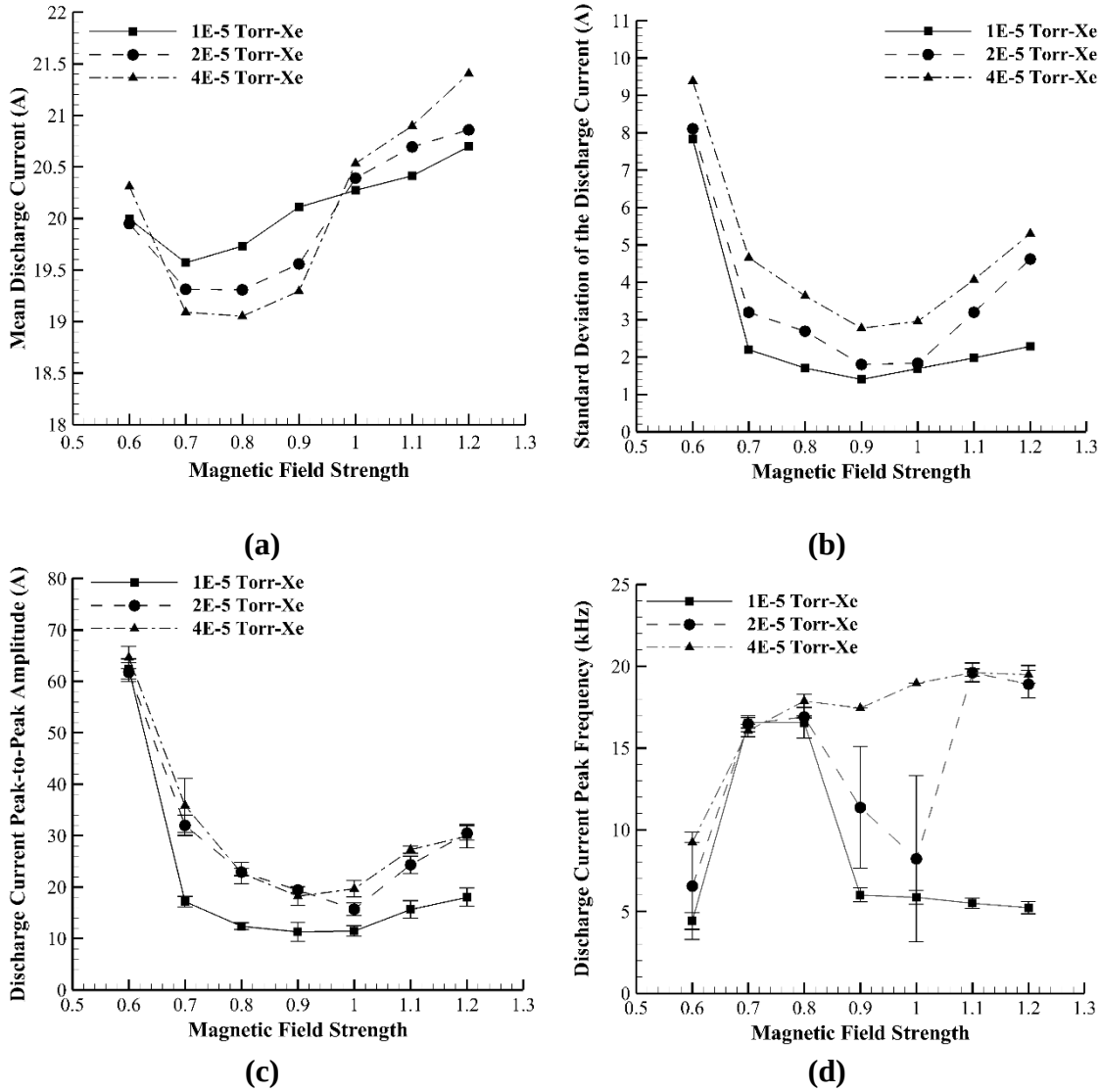

Figure 6.21: H6 discharge current (a) mean, (b) standard deviation, (c) average peak-to-peak amplitude, and (d) peak frequency as a function of magnetic field strength.

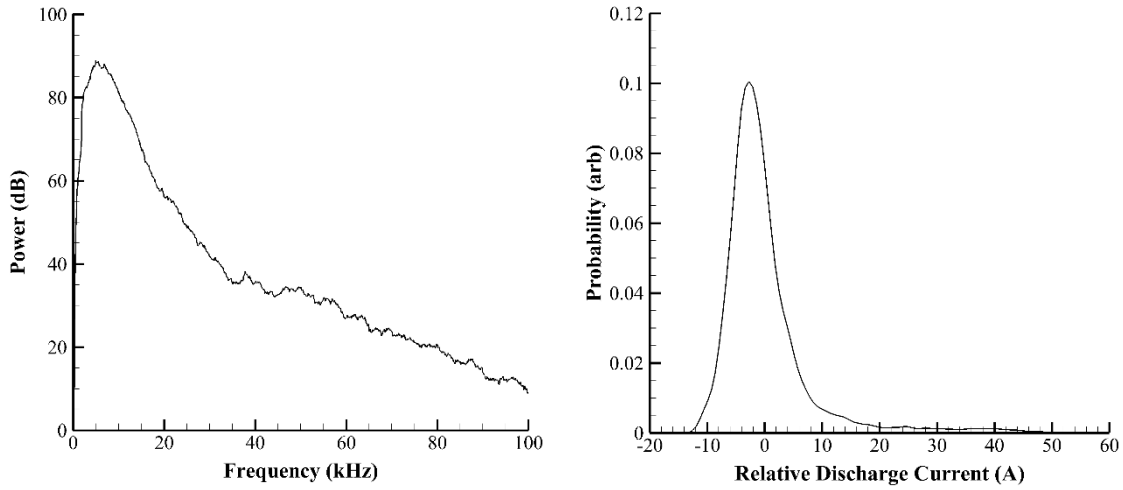

(a) **(b)**

Figure 6.22: (a) Power spectrum and (b) PDF of the H6 discharge current for operation at 60% magnetic field strength.

recent work done with the NASA HERMeS HET, which also found large oscillations and skewed PDFs at low magnetic field strengths [105].

As shown in Figure 6.21, as the magnetic field strength is increased to between 70% and 80% of the nominal value, an abrupt transition occurs. The mean, standard deviation, and average peak-to-peak amplitude of the discharge current decrease by 2%, 72%, and 72%, respectively. The peak frequency, which is shown in Figure 6.21(d) and the power spectrum in Figure 6.23(a), also increases from 5 kHz to approximately 17 kHz. As discussed in Section 6.3.2, this higher frequency is characteristic of the published value for the spoke mode for the H6 [54]. The sinusoidal characteristics of the PDF shown in Figure 6.23(b) provide further evidence of the dominance of the spoke mode. Taken together, these results suggest that the H6 transitioned from operating in the global mode (which is characterized by a dominant breathing mode) at the lowest magnetic field strength to the local mode (which is characterized by a dominant spoke mode) at magnetic field strengths

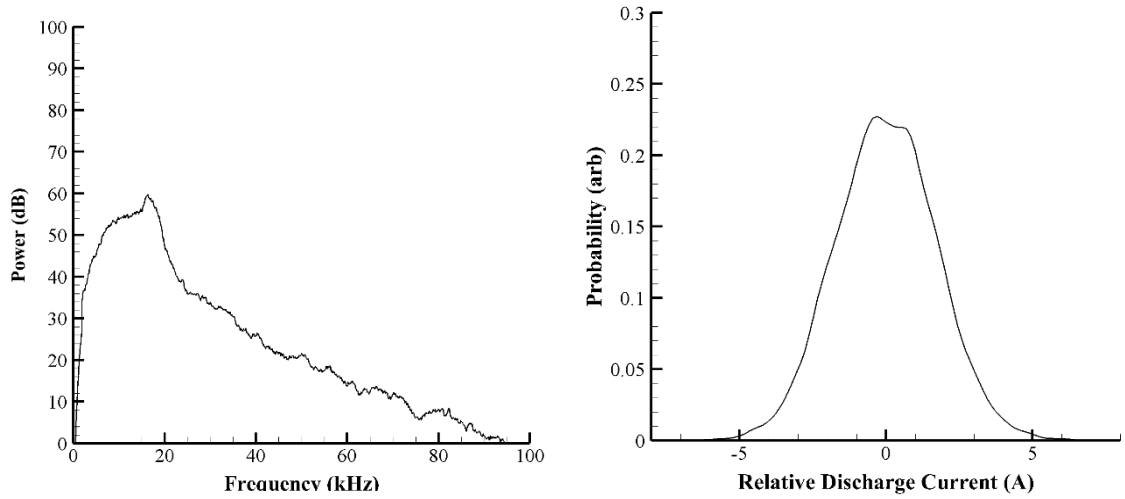

(a) **(b)**

Figure 6.23: (a) Power spectrum and (b) PDF of the H6 discharge current for operation at 70% magnetic field strength.

of 70% to 80% of the nominal value. This transition has previously been observed for this HET at similar magnetic field strengths [54]. Also consistent with this transition is the minimization of the mean discharge current at these magnet settings [54].

As shown in Figure 6.21(d) a final transition occurs as the magnetic field strength is increased to between 90% and 120% of the nominal value. For these magnetic field strengths, the peak frequency returns to a value of approximately 5 kHz. The associated power spectrum and PDF are as shown in Figure 6.17(a) and Figure 6.18(a), respectively. Consistent with previous work, the standard deviation and average peak-to-peak amplitude of the discharge current are all minimized between 90% and 100% of the nominal magnet settings then increase with increasing magnetic field strength above the nominal settings while the mean discharge current magnitude increases with increasing magnetic field strength throughout this region [54]. As discussed in Section 6.3.2, this suggests that the

H6 returned to global mode operation at these magnet settings [54]. This second transition was not observed in previous work with the H6 conducted at higher facility pressures and indicates a potential impact of pressure on the sensitivity of HET oscillations to magnetic field strength [54].

Further evidence of this pressure sensitivity is shown in Figure 6.21. At the highest operating pressure of 4×10^{-5} Torr-Xe, the second mode transition back to the global mode disappears. A representative power spectrum and PDF for operation at this pressure are shown in Figure 6.18(b) and Figure 6.24, respectively. The strong peak frequency near 20 kHz in the spectrum as well as the sinusoidal nature of the PDF both suggest the dominance of the spoke mode and that the H6 remained in local mode for all magnetic field strengths above 70% of the nominal value. As shown in Figure 6.21(d), for operation at a facility pressure of 2×10^{-5} Torr-Xe, the peak frequencies for magnetic field strengths between 90% and 100% of nominal lie between the global mode value of 5 kHz and the local mode value of 20 kHz with large standard deviation. As discussed in Section 6.3.2, these points correspond to situations in which the H6 was jumping between local and global mode. Thus, operation at this pressure appears to be transitional between the trends observed at the lowest and highest operating pressures. It is important to note that the frequency trends observed at the highest operating pressure of 4×10^{-5} Torr-Xe in this work are most consistent with those observed in previous work conducted in the LVTF at operating pressures between 1×10^{-5} Torr-Xe and 1.5×10^{-5} Torr-Xe [54]. This suggests that, just like with the changes in mean discharge current, pressure magnitude is an insufficient parameter to fully describe facility effects on mode transitions.

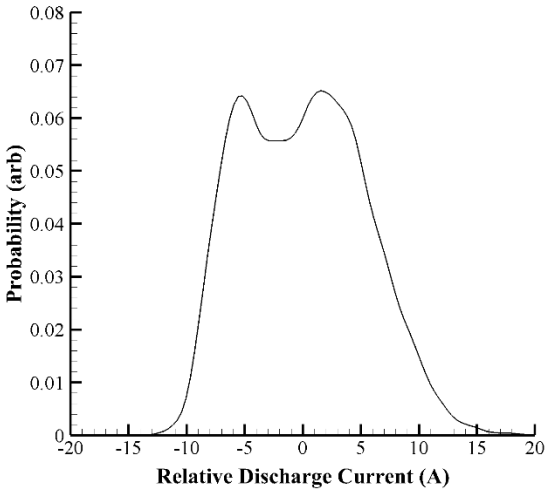

Figure 6.24: PDF of the H6 discharge current for operation at 120% magnetic field strength at a facility pressure of 4×10^{-5} Torr-Xe.

As shown in Figure 6.21(a)-(c), the peak frequency of the discharge current is not the only parameter with pressure sensitivity. Consistent with the results presented in Section 6.3.1, the average peak-to-peak amplitude and standard deviation of the discharge current increase for all magnetic field strengths with increasing pressure. As shown in Figure 6.21(a), the mean discharge current also increases with increasing pressure for magnetic field strengths below 70% and above 90% of the nominal value. However, for magnetic field strengths between 70% and 90% of the nominal value, the average discharge current decreases with increasing facility pressure. Previous work has shown that the discharge current is minimized during the transition from global mode to local mode [54]. These results therefore suggest that increases in pressure yield higher values of average discharge current in local mode and global mode, but lower values of average discharge current during the transition between these two modes.

6.5.2 6-kW HET

The mean, standard deviation, average peak-to-peak amplitude, and peak frequency of the 6-kW HET discharge current are shown as a function of magnetic field strength for facility pressures of 1×10^{-5} Torr-Xe, 2×10^{-5} Torr-Xe, and 5×10^{-5} Torr-Xe in Figure 6.25(a), (b), (c), and (d), respectively. As done for the H6, the abscissa in all panes of Figure 6.25 represents the ratio of the magnetic field strength relative to the nominal value. A minimum of five measurements of the time-resolved discharge current signal were acquired at each magnet condition with each measurement encompassing approximately 400 fundamental periods. The empirical data shown in all panes of Figure 6.25 represent the average across these five measurements, while the error bars correspond to the standard deviation. The uncertainty associated with the measurements of the mean discharge current shown in Figure 6.25(a) is captured by the symbol size.

As done with the H6, the data at the lowest operating pressure of 1×10^{-5} Torr-Xe will be discussed first to determine the sensitivity of the 6-kW HET oscillation characteristics to magnetic field strength at a fixed operating pressure. As with the H6, the standard deviation and average peak-to-peak amplitude of the discharge current are maximized at the lowest magnetic field strength of 60% of the nominal value. The power spectrum at this magnet setting is very similar to the H6 spectrum shown in Figure 6.23(a), however, the peak frequency is centered near 8 kHz with a peak power of approximately 70 dB. The PDF of the discharge current at this magnet setting is largely unchanged from the nominal Gaussian PDF for this thruster shown in Figure 6.19(b). Unlike with the H6, no skew is observed in the PDF. These results are characteristic of the breathing mode of thrusters of this power class and suggest the presence of a large global oscillation inside the discharge channel [54].

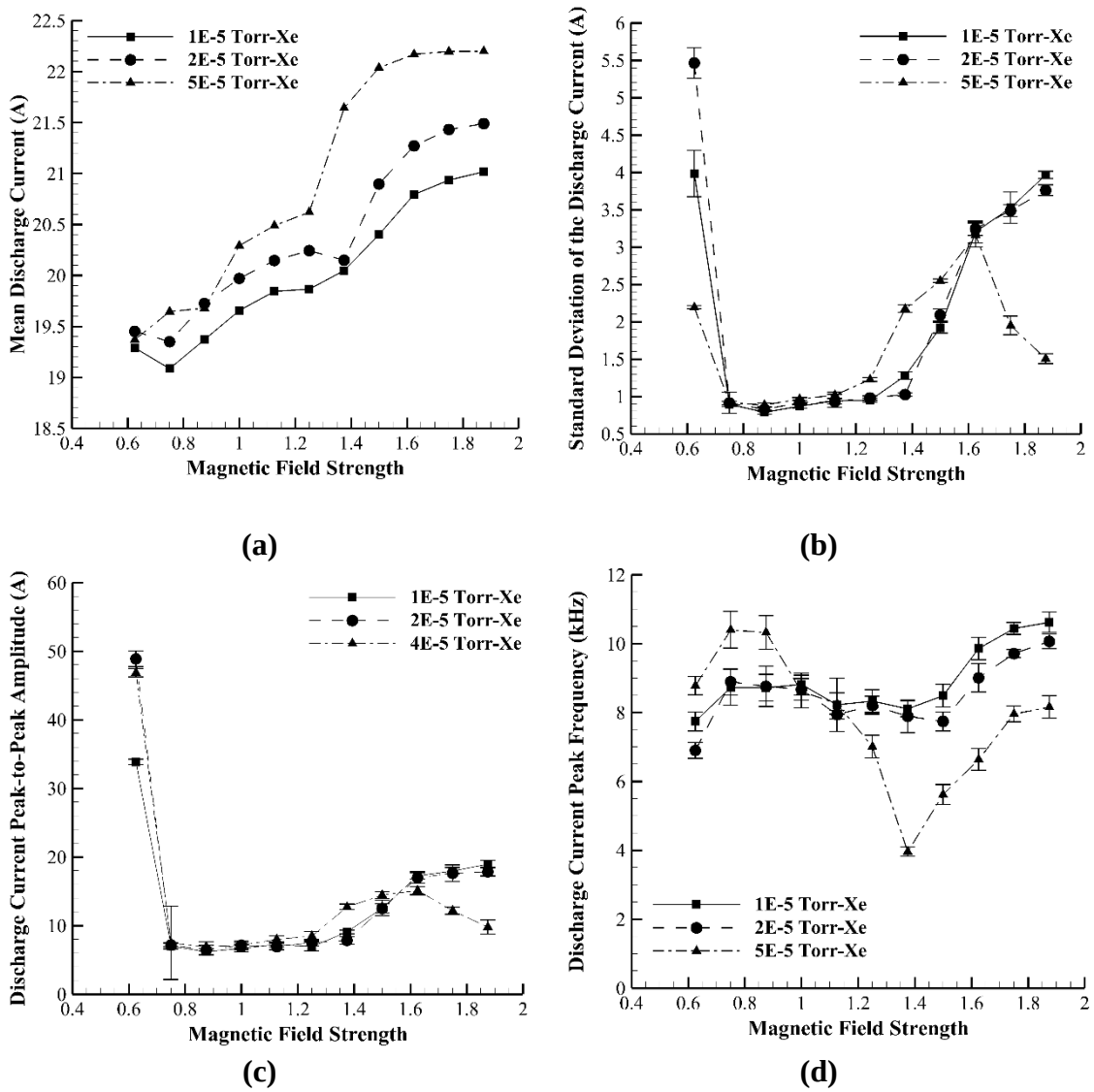

Figure 6.25: 6-kW HET discharge current (a) mean, (b) standard deviation, (c) average peak-to-peak amplitude, and (d) peak frequency as a function of magnetic field strength.

Similarly to the H6, the average peak-to-peak amplitude and standard deviation of the discharge current both decrease by 77% and 79%, respectively as the magnetic field strength is increased to approximately 75% of the nominal value. The power spectrum returns to the nominal case for the 6-kW HET shown in Figure 6.19(a) with a broad peak near 9 kHz and a peak power of less than 50 dB while the PDF retains the appearance of a weak sinusoid imposed on an overall Gaussian profile as shown in Figure 6.19(b). The reduction in peak power is consistent with the reduction in average peak-to-peak amplitude and standard deviation of the discharge current. However, unlike with the H6, the peak frequency at this magnet setting is still characteristic of the breathing mode and not of a spoke mode [54]. This suggests that the breathing mode oscillation is damped at this magnet condition, but it does not suggest the HET changed to local mode operation [54]. The absence of spoke formation at magnetic field settings near nominal has previously been observed for magnetically-shielded thrusters and it has been theorized that the absence of spoke modes is one of the key differences between the oscillation characteristics of unshielded and magnetically-shielded HETs [54, 105].

The oscillation characteristics of the 6-kW HET remain roughly constant until the magnetic field strength reaches 150% of the nominal value. At this magnet condition the standard deviation of the discharge current and average peak-to-peak amplitude begin to increase, eventually reaching 356% and 184% of the values measured for the nominal magnet configuration at the highest magnet settings. Taken together, these changes are consistent with the transition to the “high B-field mode” observed by Sekerak with the magnetically-shielded H6 and NASA-300MS [54].

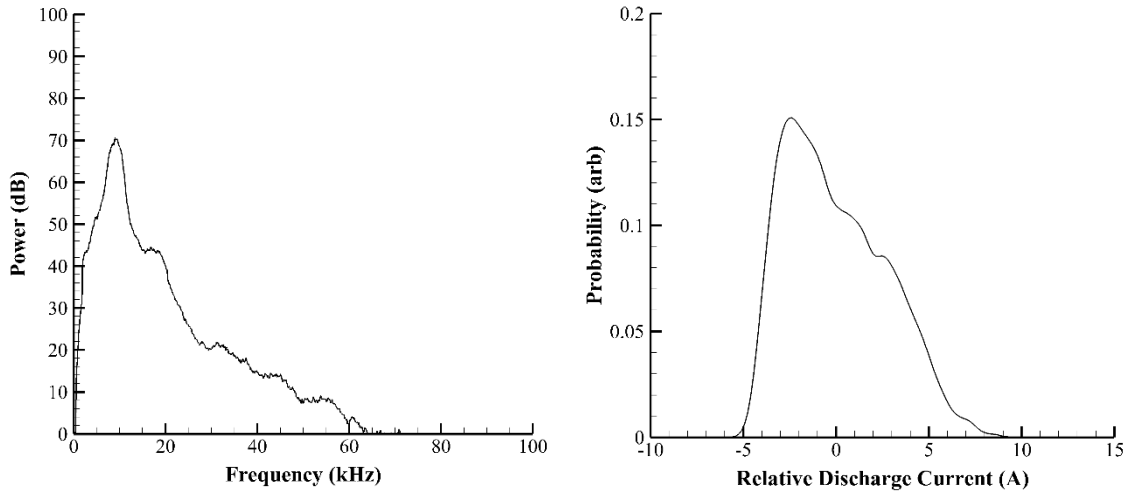

(a) **(b)**

Figure 6.26: Representative (a) power spectrum and (b) PDF of the discharge current for operation in the high B-field mode.

As noted by Sekerak, the high B-field mode is also characterized by the emergence of spokes [54]. A representative power spectrum for the high B-field mode is shown in Figure 6.26(a). The spectrum is characterized by a primary peak frequency near 9 kHz with a power of 70 dB and a secondary peak frequency near 19 kHz with a power of 44 dB. A representative PDF for this mode is shown in Figure 6.26(b). This PDF exhibits both sinusoidal and skewed characteristics with two peaks occurring near ± 2 A and a strong skew towards the positive half of the abscissa. The sinusoidal characteristics of the PDF as well as the secondary peak near 20 kHz suggest the emergence of a secondary spoke mode (which is a defining characteristic of the high B-field mode) dominated by a strong 10-kHz breaking mode while the skewed nature of the PDF is consistent with the observed increases in average peak-to-peak amplitude and standard deviation of the discharge current [54, 105].

As shown in Figure 6.25(a), unlike with the H6, the average discharge current is largely monotonic with both magnetic field strength and pressure. This is consistent with trends observed for HETs operating in a given mode [54]. However, at magnetic field strengths above 140% of nominal, the mean discharge current appears to asymptote, with the magnetic field strength corresponding to the start of the asymptotic region decreasing with increasing facility pressure. This asymptotic behavior at high magnetic field strengths has previously been observed with the H6 [54].

Also unlike the H6, the other oscillation parameters show limited sensitivity to facility pressure. The only deviation from the aforementioned trends occurs for the highest facility operating pressure of 5×10^{-5} Torr-Xe at magnetic field strengths above the nominal settings. Between 120% and 150% of the nominal magnetic field strength, the average peak-to-peak amplitude and standard deviation of the discharge current for the high-pressure condition are larger than the values observed at the other operating pressures by an average of 50% and 31%, respectively. Although the power spectrum still resembles the high-magnetic field case shown in Figure 6.26(a), the peak frequency decreases to near 4 kHz and the skew observed in the PDF shown in Figure 6.26(b) disappears, yielding a PDF closer to that shown in Figure 6.19(b).

For magnetic field strengths above 150%, the peak-to-peak amplitude and standard deviation of the discharge current are 36% and 31% lower, on average, for the high-pressure case relative to the low-pressure case. This coincides with an increase in peak frequency to approximately 8 kHz. Unlike at the lower facility operating pressures, no evidence of spoke formation occurs for the data collected at 5×10^{-5} Torr-Xe. At these magnet settings, the power spectrum returns to the nominal case (shown in Figure 6.19(a))

and the PDF is purely Gaussian. This suggests that increasing the facility pressure prevented the mode transition to the "high B-field mode" observed for the two lower operating pressures. Instead, the 6-kW HET only exhibits oscillations characteristic of the global mode for all magnetic field strengths at this pressure [54].

As noted in previous work, a coherent theory for the formation and propagation of azimuthal spokes in HET discharges has yet to be found [54]. Absent such a theory, it is not possible to explain the physical mechanisms behind the observed changes in oscillation characteristics with magnetic field strength and facility pressure. However, the results presented in this section should help inform efforts to generate a coherent model or theory for azimuthal spokes by providing insight on the previously unexplored coupling between oscillation sensitivity on magnetic field strength and facility backpressure.

6.6 Conclusions

The purpose of the data presented in this chapter was to provide answers to the final research question of this work: how does HET operation change as a function of ingestion flow rate (instead of pressure measured at a given location)? Consistent with previous work, measurements of the plume divergence half-angle, ion beam current and plasma number density showed that all three quantities increased with increasing facility pressure [14, 30–32]. However, unlike in previous work, the observed trends were not monotonic with facility pressure. Like the mean discharge current results discussed in Chapter 5, different values for the plume divergence half-angle, ion beam current, and plasma number density were obtained at a fixed facility pressure depending on how that pressure was achieved. However, once these results were plotted as a function of the empirically-measured change in ingestion mass flow rate, the trends became linear and monotonic to

within the empirical uncertainty Taken together, these results suggest that the ingestion mass flow rate due to the bulk motions of the background flow more completely describes the changes in these HET plume properties than does facility pressure magnitude.

Although able to capture the observed changes in plume divergence half-angle, ion beam current, and plasma number density, changes in HET ingestion mass flow rate were not able to fully describe the observed changes in plasma potential, electron temperature, and discharge current oscillations. This result was expected as these parameters have been shown to be complex, coupled phenomena with sensitivities related to a variety of factors including magnetic field topology and electron mobility [2, 54, 98–102].

Nonetheless, the presented data still provides unique insight into the sensitivity of cathode coupling and oscillation characteristics to facility pressure. Measurements of the plasma potential and electron temperature supported previous findings that the cathode coupling characteristics of HETs with internally-mounted cathodes are less susceptible to facility backpressure effects than those with externally-mounted cathodes [17]. Analysis of the discharge current oscillations showed the ability of facility pressure to cause mode transitions directly and alter the transition characteristics of a HET as a function of magnetic field strength. These mode transitions were observed to be severe enough to cause a breakdown in the simple ingestion approach for predicting changes in performance for the IHD2000-EM11 with changes in facility pressure. This suggests that attempts to optimize the magnetic field, oscillation, or performance characteristics of a given HET in a given facility may not hold when that HET is tested in another facility and that the technique of acquiring stability and performance surfaces by measuring changes in

discharge current as a function of discharge voltage and magnetic field strength may need to be expanded to include facility pressure as an additional independent parameter.

CHAPTER 7. CONCLUSION AND FUTURE WORK

7.1 Conclusion

The overall goal of this work was to analytically and empirically test the hypothesis that a bulk background flow of neutrals exists inside vacuum test facilities, changes as a function of facility-specific design and operating parameters (e.g., pump placement and pressure modulation technique), and is a non-negligible contributor to HET neutral ingestion and the concomitant impacts on performance and plume characteristics.

In Chapter 2, an analytical model capable of simulating the bulk background neutral flow and concomitant HET ingestion mass flow rate in ground test facilities with varying physical geometries and pump placements was developed. This model was validated in Chapter 3 by comparing the model-predicted mass flow rates of neutrals into a given HET (i.e., across a given surface in the facility) to the results from several existing empirical data sets taken using three different HETs and three different vacuum test facilities; these comparisons found that the model predictions matched the empirical observations to within the experimental uncertainty. These predictions were furthermore shown to be 40% to 70% more accurate than those generated using the thermal model most commonly used to predict and estimate neutral ingestion by HETs and equally as accurate as several published thruster-specific semi-empirical models without requiring any empirical inputs such as in-situ pressure measurements [22, 23, 29]. The physical mechanisms captured by the background flow model were also shown to offer a potentially unifying framework to explain both the results observed by Randolph *et al.* and used to develop the thermal model as well as the enhanced ingestion rates observed in subsequent facility effects studies [16,

17, 22–24, 29]. These results provided strong analytic support for the existence of the hypothesized bulk motions of the background neutrals and its contribution to HET neutral ingestion.

In Chapter 4, an experiment was designed to provide further empirical evidence to support the existence of the bulk background flow and its link to HET neutral ingestion by directly obtaining measurements of the one-directional number densities and flux rates output by the background flow model. The results are presented in Chapter 5. Measurements of the one-directional number densities confirmed the presence of an elevated number density of neutrals traveling upstream towards the HET exit plane consistent with the hypothesized bulk background flow. It was furthermore shown that the background flow model could accurately replicate both the observed one-directional number densities and the observed changes in mean discharge current for all three HETs tested. These results provide strong validation of the analytic results in Chapter 3 and further support for the proposed hypothesis regarding the presence of a bulk flow of background neutrals inside finite vacuum vessels and the impact of this flow on HET neutral ingestion.

The validated background flow model was then used to test the hypothesized sensitivity of the background flow field to parameters that often vary between different test facilities and campaigns. Analytical trade studies analyzing the impact of parameters such as pump placement and pressure modulation technique were performed in Chapter 3 and then repeated empirically in Chapter 5. In these studies, it was found that the bulk background flow is sensitive to a variety of facility-specific parameters including pump placement, bleed flow orientation, beam dump geometry, and pressure modulation technique.

Specifically, use of a conic beam dump was shown to decrease HET ingestion relative to a flat plate beam dump by increasing radial losses of background neutrals. Bleed flow orientation was only shown to impact HET neutral ingestion when used in combination with a conic beam dump, and pump placement was shown to cause only minimal changes in total HET mass flow rate. Finally, it was shown that pressure magnitude was an insufficient parameter for describing HET neutral ingestion, and that a full description of a how a give pressure was achieved was required to uniquely determine the HET neutral ingestion characteristics. Taken together, these results analytically and empirically confirm the hypothesized sensitivity of the bulk background to facility-specific design and operating parameters. These sensitivities further explain the facility-specific nature of the results generated in previous facility effects studies. The empirical confirmation and analytical description of the hypothesized bulk flow of background neutrals, its link to HET neutral ingestion, and its sensitivity to facility-specific parameters represent the major contributions from the first portion of this work.

Finally, in Chapter 6, the impact of the bulk background flow on HET performance and plume properties was assessed. Consistent with the results in Chapter 5, pressure magnitude was shown to be an insufficient parameter to describe the observed changes in ion current density, plume divergence half-angle, and plasma density. Instead, it was found that changes in these properties could be uniquely determined only by specifying the ingestion mass flow rate due to the bulk motions of the background neutrals. The contribution of these results is to confirm the hypothesized link between the ingestion mass flow rate due to the bulk motions of the background flow and the observed changes in certain HET plume properties.

However, the bulk motions of the background neutrals were shown to be insufficient to fully describe the observed changes in plasma potential, electron temperature, and discharge current oscillations due to the coupled sensitivities of these parameters to a variety of factors including magnetic field topology and electron mobility [2, 54, 98–102]. Nevertheless, the collected data did reveal the ability of facility pressure to directly cause mode transitions and alter the transition characteristics of the HETs as a function of magnetic field strength. The contribution of these results is that they suggest that attempts to optimize the magnetic field, oscillation, or performance characteristics of a given HET in a given facility may not hold when that HET is tested in another facility.

7.2 Future Work

As noted in Section 7.1, this work successfully achieved its primary research goals and confirmed the existence, impact, and sensitivities of the bulk motions of background neutrals in vacuum test facilities. However, ultimately this work was just a preliminary investigation and several unanswered questions remain about the characteristics of the bulk background flow field and the concomitant impacts on HET operation. These questions and ideas for studies to answer them are summarized in this section.

7.2.1 Background Flow Model

As discussed in Section 5.2, the collision model used in the original background flow model proved inadequate to predict some of the observed empirical trends. Although the modification developed in this work was successfully able to resolve the differences between the model predictions and the measurements, the collisional model should be further refined in future work to increase accuracy and robustness as well as incorporate

additional loss mechanisms including those related to chamber conductance. The collisional model should also be refined to incorporate changes in the velocity of unionized propellant exiting the HET with changes in discharge power as discussed in Section 3.1.2. In addition to refining the collisional model, future modeling work should look to determine the proper methods to model other common pump types such as diffusion pumps or turbomolecular pumps. This refinement would broaden the impact of the model to a wider range of vacuum test facilities.

As discussed in Section 5.3.1.2, empirical evidence suggests that while a one-dimensional model may be sufficient for predicting HET ingestion mass flow rates, it is insufficient for modeling the entire bulk background flow field, which does have non-negligible radial components. Future modeling work should look to expand the developed background flow model to incorporate radial motions. A two-dimensional version of the background flow model could provide further guidance regarding the impact of chamber aspect ratio on HET ingestion and how side wall collisions impact the bulk background motions. It could also provide further guidance on how changes to beam dump geometry or the view factor between the pumps and the bulk background neutrals (due, for instance, to graphite shielding) impacts the background flow field.

7.2.2 Background Flow Field Characterization

Although sufficient to confirm the existence of the bulk background flow field and its link to HET ingestion, the empirical data presented in Chapter 5 ultimately only quantifies the bulk flux rates and one-directional number densities at a single point. Future investigations should employ the same techniques used in this work to obtain complete two-dimensional or three-dimension maps of the directional number densities and flux

rates throughout the chamber. This data would provide additional validation for the background flow model, reveal more information about the bulk background flow field, and permit an empirical assessment of the impact of auxiliary chamber surfaces including the side walls and personnel grating on the bulk background motions. In addition to increasing the number of measurement locations, future empirical investigations into the bulk background flow field should use optical diagnostics to obtain measurements of additional bulk background flow properties including the neutral velocity distribution.

As noted in Sections 5.2.2 and 5.3.2, the facility parameter sensitivity studies performed in this work were not able to fully quantify the impact of beam dump geometry and bleed flow orientation on the bulk motions of the background neutrals. Future studies should collect additional data on these sensitivities by varying the beam dump geometry in-situ and moving the bleed flow orifice axially and radially throughout the chamber.

7.2.3 HET Performance Characterization

Although comprehensive, the probe measurements presented Chapter 6 still leave several unanswered questions regarding the impact of the bulk background flow on HET operation. Throughout this work, the internal ionization and acceleration processes of the HET were assumed to be largely unaffected by changes in ingestion mass flow rate. Future work should look to assess the validity of this simple ingestion approach by taking internal measurements of plasma properties to determine how changes in the ingestion mass flow rate ionization and acceleration zone properties and if a complete description of the HET ingestion mass flow rate can explain these changes.

Future work should also attempt to provide clearer answers to explain the observed pressure sensitivity of the discharge current oscillations. As discussed throughout Chapter

6, these investigations should employ high-speed imagery and plasma diagnostics to fully characterize the observed oscillations and mode transitions as well as analyze the previously-observed coupling of electrical facility effects to facility pressure. Studies should also be done to determine if the observed changes in oscillation characteristics with facility pressure exhibit hysteresis that could affect tuning of magnetic circuits during initial HET operation. Finally, future work should look to isolate the impact of various HET design parameters on oscillation characteristics and mode transitions. For instance, measurements should be obtained with a HET that can switch in-situ between an internally and externally-mounted cathode and between unshielded and magnetically-shielded configurations to isolate the impacts of these parameters on the observed oscillation sensitivities to both magnetic field strength and facility pressure.

REFERENCES

[1] Larson, W. J., and Wertz, J. R., Space Mission Analysis and Design, 3rd ed., Microcosm Press, El Segundo, CA, 1999, pp. 685-716.

[2] Goebel, D.M., and Katz, I., Fundamentals of Electric Propulsion: Ion and Hall Thrusters, Wiley, Hoboken, NJ, 2008, pp. 3-6, 325-384, 463-467.

[3] Brophy, J. R., and Muirhead, B., "Near-Earth Asteroid Retrieval Mission (ARM) Study," 33rd International Electric Propulsion Conference, Electric Rocket Propulsion Society, IEPC Paper 2013-082, Washington, DC, 2013.

[4] Jahn, R. G., Physics of Electric Propulsion, McGraw-Hill, New York, 1968, pp. 89-306.

[5] Zhurin, V. V, Kaufman, H. R., and Robinson, R. S., "Physics of closed drift thrusters," Plasma Sources Science and Technology, Vol. 8, No. 1, 1999.

[6] Piel, A., Plasma Physics: An Introduction to Laboratory, Space, and Fusion Plasmas, Springer, Berlin, 2010, pp. 45-50.

[7] Fossum, E., "Electron Transport in E x B Devices," Ph.D. Dissertation, Department of Mechanical Engineering-Engineering Mechanics, Michigan Technologycial University, Houghton, MI, 2009, pp. 13-52.

[8] Semenkin, A., Kim, V., Groshkov, O., and Jankovsky, R., "Development of Electric Propulsion SStandard-Current Status and Further Activity," *27th International Electric Propulsion Conference*, Electric Rocket Propulsion Society, IEPC Paper 2001-070, Pasadena, CA, 2001.

[9] Frieman, J. D., King, S. T., Walker, M. L., and Khayms, V., "Preliminary Assessment of the Role of a Conducting Vacuum Chamber in the Hall Effect Thruster Electrical Circuit," *50th AIAA/ASME/SAE/ASEE Joint Propulsion Conference*, American Institute of Aeronautics and Astronautics, AIAA Paper 2014-3712, Cleveland, OH, 2014.

[10] Frieman, J. D., King, S. T., Walker, M. L. R., Khayms, V., and King, D., "Role of a Conducting Vacuum Chamber in the Hall Effect Thruster Electrical Circuit," *Journal of Propulsion and Power*, Vol. 30, No. 6, 2014, pp. 1471–1479.

[11] Walker, J. A., Frieman, J. D., Walker, M. L.R., and Khayms, V., "Impact of Cathode Position and Electrical Facility Effects on Hall Effect Thruster Performance and Discharge Current Behavior," *50th AIAA/ASME/SAE/ASEE Joint Propulsion Conference*, American Institute of Aeronautics and Astronautics, AIAA Paper 2014-3711, Cleveland, OH, 2014.

[12] Frieman, J. D., Walker, J. A., Walker, M. L. R., Khayms, V., and King, D. Q., "Electrical Facility Effects on Hall Thruster Cathode Coupling: Performance and Plume Properties," *Journal of Propulsion and Power*, Vol. 32, No. 1, 2015, pp. 251–264.

[13] Walker, J. A., Frieman, J. D., Walker, M. L. R., Khayms, V., Peterson, P. Y., and King, D. Q., "Electrical Facility Effects on Hall Effect Thruster Cathode Coupling: Discharge Oscillations and Facility Coupling," *Journal of Propulsion and Power*, 2016, pp. 1-12.

[14] Brown, D., and Gallimore, A., "Evaluation of Plume Divergence and Facility Effects on Far-Field Faraday Probe Current Density Profiles," *31st International Electric Propulsion Conference*, Electric Rocket Propulsion Society, IEPC Paper 2009-030, Ann Arbor, MI, 2009.

[[16] Hofer, R., Peterson, P., and Gallimore, A., "Characterizing Vacuum Facility Backpressure Effects on the Performance of a Hall Thruster," *27th International Electric Propulsion Conference*, Electric Rocket Propulsion Society, IEPC Paper 01-045, Pasadena, CA, 2001.

[17] Hofer, R., and Anderson, J., "Finite Pressure Effects in Magnetically Shielded Hall thrusters," *50th AIAA/ASME/SAE/ASEE Joint Propulsion Conference*, American Institute of Aeronautics and Astronautics, AIAA Paper 2014-3709, Cleveland, OH, 2014.

[18] Huang, W., Kamhawi, H., Lobbia, R. B., and Brown, D. L., "Effect of Background Pressure on the Plasma Oscillation Characteristics of the HiVHAc Hall Thruster," *50th AIAA/ASME/SAE/ASEE Joint Propulsion Conference*, American Institute of Aeronautics and Astronautics, AIAA Paper 2014-3708, Cleveland, OH, 2014.

[19] Kamhawi, H., Huang, W., Haag, T., and Spektor, R., "Investigation of the Effects of Facility Background Pressure on the Performance and Voltag-Current Characteristics of the High Voltage Hall Accelerator," *50th AIAA/ASME/SAE/ASEE Joint Propulsion Conference*, American Institute of Aeronautics and Astronautics, AIAA Paper 2014-3707, Cleveland, OH, 2014.

[20] Nakles, M. R., and Hargus, W. A., "Background Pressure Effects on Ion Velocity Distribution Within a Medium-Power Hall Thruster," *Journal of Propulsion and Power*, Vol. 27, No. 4, 2011, pp. 737–743.

[21] Randolph, T., Kim, V., Kozubsky, K., Zhurin, V., Day, M., Fakel, and Ssl, "Facility Effects on Stationary Plasma Thruster Testing," *23rd International Electric Propulsion Conference*, Electric Rocket Propulsion Society, IEPC Paper 93-093, Seattle, WA, 1993.

[22] Reid, B. M., "The Influence of Neutral Flow Rate in the Operation of Hall Thrusters," Ph.D. Dissertation, Aerospace Engineering Dept., Univ. of Michigan, Ann Arbor, MI, 2009, pp. 306–319.

[23] Reid, B. M., "Empirically-Derived Corrections for Facility Effects in Performance and Plume Measurements of Hall Thrusters," *34th International Electric Propulsion Conference*, Electric Rocket Propulsion Society, IEPC Paper 2015-362, Kobe, Japan, 2015.

[24] Tighe, W. G., Spektor, R., Diamant, K., and Kamhawi, H., "Effects of Background Pressure on the NASA 173M Hall Current Thruster Performance," *34th International Electric Propulsion Conference*, Electric Rocket Propulsion Society, IEPC Paper 2015-152, Kobe, Japan, 2015.

[25] Byers, D., and Dankanich, J., "A Review of Facility Effects on Hall Effect Thrusters," *31st International Electric Propulsion Conference*, Electric Rocket Propulsion Society, IEPC Paper 2009-076, Ann Arbor, MI, 2009.

[26] Crofton, M. W., and Pollard, J., "Thrust Augmentation by Charge Exchange," *49th AIAA/ASME/SAE/ASEE Joint Propulsion Conference*, American Institute of Aeronautics and Astronautics, AIAA Paper 2013-4131, San Jose, CA, 2013.

[27] Diamant, K., Spektor, R., Beiting, E., Young, J., Curtiss, T., and Corporation, T. A., "The Effects of Background Pressure on Hall Thruster Operation," *48th AIAA/ASME/SAE/ASEE Joint Propulsion Conference & Exhibit*, American Institute of Aeronautics and Astronautics, AIAA Paper 2012-3735, Atlanta, GA, 2012.

[28] Huang, W., Kamhawi, H., and Haag, T., "Effect of Background Pressure on the Performance and Plume of the HiVHAc Hall Thruster," *33rd International Electric Propulsion Conference*, Electric Rocket Propulsion Society, IEPC Paper 2013-058, Washington, DC, 2013.

[29] Walker, M. L.R., and Gallimore, A. D., "Performance Characteristics of a Cluster of 5-kW Laboratory Hall Thrusters," *Journal of Propulsion and Power*, Vol. 23, No. 1, 2007, pp. 35–43.

[30] Walker, M. L. R., "Effects of Facility Backpressure on the Performance and Plume of a Hall Thruster," Ph.D. Dissertation, Aerospace Engineering Dept., Univ. of Michigan, Ann Arbor, MI, 2005, pp. 111-155.

[31] Walker, M. L. R., Hofer, R. R., and Gallimore, A. D., "The Effects of Nude Faraday Probe Design and Vacuum Facility Backpressure on the Measured Ion Current Density Profile of Hall Thruster Plumes," *38th AIAA/ASME/SAE/ASEE Joint Propulsion Conference and Exhibit*, American Institute of Aeronautics and Astronautics, AIAA Paper 2002-4253, Indianapolis, IN, 2002.

[32] Walker, M.L.R., and Gallimore, A.D., "Neutral Density Map of Hall Thruster Plume Expansion in a Vacuum Chamber," Review of Scientific Instruments, Vol. 76, No. 5, 2005, Paper 053509.

[33] Choueiri, E. Y., "Plasma Oscillations in Hall Thrusters," Physics of Plasmas, Vol. 8, No. 4, 2001, pp. 1411–1426.

[34] Dankanich, J., Swiatek, M., Yim, J., and Glenn, N., "A Step Towards Electric Propulsion Testing Standards: Pressure Measurements and Effective Pumping Speeds," *48th AIAA/ASME/SAE/ASEE Joint Propulsion Conference & Exhibit*, American Institute of Aeronautics and Astronautics, AIAA Paper 2012-373, Alanta, GA, 2012.

[35] Dankanich, J., Walker, M. L. R., Swiatek, M., and Yim, J., "Recommended Practice for Pressure Measurements and Calculation of Effective Pumping Speeds during Electric Propulsion Testing," *33rd International Electric Propulsion Conference*, Electric Rocket Propulsion Society, IEPC Paper 2013-358, Washington, DC, 2013

[36] Walker, M., Gallimore, A., Cai, C., and Boyd, I., "Pressure Map of a Facility as a Function of Flow Rate to Study Facility Effects," *38th AIAA/ASME/SAE/ASEE Joint Propulsion Conference and Exhibit*, American Institute of Aeronautics and Astronautics, AIAA Paper 2002-3815, Indianapolis, IN, 2002.

[37] Cai, C., Boyd, I. D., and Sun, Q., "Free Molecular Background Flow in a Vacuum Chamber Equipped with Two-sided Pumps," *Journal of Vacuum Science & Technology A: Vacuum, Surfaces, and Films*, Vol. 24, No. 1, 2006, pp. 9-19.

[38] Yim, J., and Burt, J. M., "Characterization of Vacuum Facility Background Gas Through Simulation and Considerations for Electric Propulsion Ground Testing," *51st AIAA/SAE/ASEE Joint Propulsion Conference*, American Institute of Aeronautics and Astronautics, AIAA Paper 2015-3825, Orlando, FL, 2015.

[39] Kamhawi, H., Huang, W., and Haag, T., "Investigation of the Effects of Cathode Flow Split and Position on the Performance and Operation of the High Voltage Hall Accelerator," *50th AIAA/ASME/SAE/ASEE Joint Propulsion Conference*, American Institute of Aeronautics and Astronautics, AIAA Paper 2014-3817, Cleveland, OH, 2014.

[40] Anderson, J. D., *Fundamentals of Aerodynamics*, McGraw-Hill Education, New York, NY, 2010, pp. 54-57.

[41] Cai, C., "Theoretical and Numerical Studies of Plume Flows in Vacuum Chambers," Ph.D. Dissertation, Aerospace Engineering Dept., Univ. of Michigan, Ann Arbor, MI, 2005 pp. 22-76.

[43] Cedolin, R. J., Hargus, W. A., Storm, P. V., Hanson, R. K., and Cappelli, M. A., "Laser-induced fluorescence study of a xenon Hall thruster," Applied Physics B: Lasers and Optics, Vol. 65, No. 4, 1997, pp. 459–469.

[44] Boyd, I., "A Review of Hall Thruster Plume Modeling," *38th Aerospace Sciences Meeting and Exhibit*, American Institute of Aeronautics and Astronautics, AIAA Paper 2000-0466, Reno, NV, 2000.

[45] Cai, C., Boyd, I., and Sun, Q., "Rarefied Background Flow in a Vacuum Chamber Equipped with One-Sided Pumps," *Journal of Thermophysics and Heat Transfer*,

Vol. 20, No. 3, 2006, pp. 524–535.

[46] Nakayama, Y., and Nakamura, M., "Electric Propulsion Propellant Flow within Vacuum Chamber," *34th International Electric Propulsion Conference*, Electric Rocket Propulsion Society, IEPC Paper 2015-360, Kobe, Japan, 2015.

[47] Sankovic, J.M., Hamley, J.A., and Haag, T. W., "Performance Evaluation of the Russian SPT-100 Thruster at NASA LeRC," *23rd International Electric Propulsion Conference*, Electric Rocket Propulsion Society, IEPC Paper 93-094, Seattle, WA, 1993.

[48] Pidgeon, D. J., Corey, R. L., Sauer, B., and Day, M. L., "Two Years On-Orbit Performance of SPT-100 Electric Propulsion," *24th AIAA International Communications Satellite Systems Conference*, American Institute of Aeronautics and Astronautics, AIAA Paper 2006-5353, San Diego, CA, 2006.

[49] Corey, R. L., and Pidgeon, D. J., "Electric Propulsion at Space Systems/Loral," *31st International Electric Propulsion Conference*, Electric Rocket Propulsion Society, IEPC Paper 2009-270, Ann Arbor, MI, 2009.

[50] Martinez, R., Dao, H., Walker, M., and Tech, G., "Power Deposition into the Discharge Channel of a Hall Effect Thruster," *Journal of Propulsion and Power*, Vol. 30, No. 1, 2014, pp. 209–220.

[51] Boyd, I. D., and Dressler, R. A., "Far Field Modeling of the Plasma Plume of a Hall Thruster," *Journal of Applied Physics*, Vol. 92, No.4, 2002, pp. 1764–1774.

[52] Reid, B. M., and Gallimore, A. D., "Review of Hall Thruster Neutral Flow Dynamics," *30th International Electric Propulsion Conference*, Electric Rocket Propulsion Society, IEPC Paper 2007-038, Ann Arbor, MI, 2007.

[53] Hofer, R., "Development and Characterization of High-Efficiency, High-Specific Impulse Xenon Hall Thrusters," Ph.D. Dissertation, Aerospace Engineering Dept., Univ. of Michigan, AnnArbor, MI, 2004, pp. 67-69.

[54] Sekerak, M. J., "Plasma Oscillations and Operation Modes in Hall Effect Thrusters," Ph.D. Dissertation, Aerospace Engineering Dept., Univ. of Michigan, Ann Arbor, MI, 2014, pp. 5-48, 55-58, 86-209.

[55] Frieman, J. D., Liu, T. M., and Walker, "Background Flow Model of Hall Thruster Neutral Ingestion," *Journal of Propulsion and Power*, 2016.

[56] Vincenti, W. G., and Kruger, C. H., *Introduction to Physcial Gas Dynamics*, Wiley, New York, 1965, pp. 1-58.

[57] Dushman, S., and Lafferty, J. M., *Scientific Foundations of Vacuum Technique*, 2nd Ed., Wiley, New York, 1962, pp. 349-359.

[58] Garner, C., Polk, J., Brophy, J., and Goodfellow, K., "Methods for Cryopumping Xenon," *32nd Joint Propulsion Conference and Exhibit*, American Institute of Aeronautics and Astronautics, AIAA Paper 1996-3206, Lake Buena Vista, FL, 1996.

[59] Huang, W., Gallimore, A. D., and Hofer, R. R., "Neutral Flow Evolution in a Six-Kilowatt Hall Thruster," *Journal of Propulsion and Power*, Vol. 27, No. 3, 2011, pp. 553–563.

[60] Pollard, J. E., and Beiting, E. J., "Ion Energy, Ion Velocity, and Thrust Vector Measurements for the SPT-140 Hall Thruster," *3rd International Conference on Spacecraft Propulsion*, ESASP-465, Cannes, France, 2000.

[61] Kieckhafer, A. W., and Walker, M. L. R., "Recirculating Liquid Nitrogen System for Operation of Cryogenic Pumps," *32nd International Electric Propulsion Conference*, Electric Rocket Propulsion Society, IEPC Paper 2011-217, Wiesbaden, Germany, 2011.

[62] Dankanich, J. W., Walker, M., Swiatek, M. W., and Yim, J. T., "Recommended Practice for Pressure Measurement and Calculation of Effective Pumping Speed in Electric Propulsion Testing," *Journal of Propulsion and Power*, 2016.

[63] Cho, S., Watanabe, H., Kubota, K., Iihara, S., Fuchigami, K., Uematsu, K., and Funaki, I., "Study of Electron Transport in a Hall Thruster by Axial–radial Fully Kinetic Particle Simulation," *Physics of Plasmas*, Vol. 22, No. 10, 2015, Paper 103523.

[64] Cho, S., Watanabe, H., Kubota, K., Iihara, S., Honda, K., Fuchigami, K., Uematsu, K., and Funaki, I., "Parametric Kinetic Simulation of an IHI High Specific Impulse SPT-Type Hall Thruster," *50th AIAA/ASME/SAE/ASEE Joint Propulsion Conference*, American Institute of Aeronautics and Astronautics, AIAA Paper 2014-3426, Cleveland, OH, 2014.

[65] Snyder, J. S., Baldwin, J., Frieman, J. D., Walker, M. L. R., Hicks, N. S., Polzin, K. A., and Singleton, J. T., "Flow Control and Measurement in Electric Propulsion Systems: Towards an AIAA Reference Standard," *33rd International Electric Propulsion Conference*, Electric Rocket Propulsion Society, IEPC Paper 2013-425, Washington, DC, 2013.

[66] Beal, B. E., Gallimore, A. D., and Hargus, W. A., "Effects of Cathode Configuration on Hall Thruster Cluster Plume Properties," *Journal of Propulsion and Power*, Vol. 23, No. 4, 2007, pp. 836–844.

[67] Xu, K. G., and Walker, M. L. R., "High-Power, Null-Type, Inverted Pendulum Thrust Stand," *Review of Scientific Instruments*, Vol. 80, No. 5 2009, Paper 55103.

[68] MKS Instruments, "Series 370 Stabil-Ion Vacuum Gague and Controller," https://www.mksinst.com/product/product.aspx?ProductID=1418 (Accessed 28

March 2017).

[69] Kamhawi, H., Huang, W., Haag, T., Shastry, R., Thomas, R., Yim, J., Herman, D., Williams, G., Myers, J., Hofer, R. R., Mikellides, I. G., Sekerak, M. J., and Polk, J. E., "Performance and Facility Background Pressure Characterization Tests of NASA's 12.5-kW Hall Effect Rocket with Magnetic Shielding Thruster," *34th International Electric Propulsion Conference*, Electric Rocket Propulsion Society, IEPC Paper 2015-07, Kobe, Japan, 2015.

[70] Kamhawi, H., Huang, W., Haag, T., Yim, J., Herman, D., Peterson, P. Y., Williams, G., Gilland, J. H., Hofer, R. R., Mikellides, I. G., and Polk, J. E., "Performance, Facility Pressure Effects, and Stability Characterization Tests of NASA's Hall Effect Rocket with Magnetic Shielding Thruster," *52nd AIAA/SAE/ASEE Joint Propulsion Conference*, American Institute of Aeronautics and Astronautics, AIAA Paper 2016-4826, Salt Lake City, UT, 2016.

[71] Absalamov, S. K., Andreev, V. B., Colbert, T., Day, M., Egorov, V. V., Gnizdor, R. U., Kaufman, H., Kim, V., Koriakin, A. I., and Kozubskii, K. N., "Measurement of Plasma Parameters in the Stationary Plasma Thruster (SPT-100) Plume and its Effect on Spacecraft Components," *28th AIAA, SAE, ASME, and ASEE, Joint Propulsion Conference and Exhibit*, American Institute of Aeronautics and Astronautics, AIAA Paper 1992-3156, Nashville, TN, 1992.

[72] King, L. B., "Transport-Property and Mass Spectral Measurements in the Plasma Exhaust Plume of a Hall-Effect Space Propulsion System," Ph.D. Dissertation, Aerospace Engineering Dept., Univ. of Michigan, Ann Arbor, MI, 1998, pp. 22-25.

[73] Hutchinson, I. H., *Principles of Plasma Diagnostics*, Cambridge University Press, Cambridge, England, U.K., 2002, pp. 55-72.

[74] Xu, K.G., "Ion Collimation and In-Channel Potential Shaping using In-Channel Electrodes for Hall Effect Thrusters," Ph.D. Dissertation, Aerospace Engineering Dept., Georgia Institute of Technology, Atlanta, GA, 2012, pp. 48-53.

[75] Reid, B., Shastry, R., Gallimore, A., and Hofer, R., "Angularly-Resolved ExB Probe Spectra in the Plume of a 6-kW Hall Thruster," *44th AIAA/ASME/SAE/ASEE Joint Propulsion Conference & Exhibit*, American Institute of Aeronautics and Astronautics, AIAA Paper 2008-5287, Hartford, CT, 2008.

[76] Industrial Netting, "BE0805 Photo Chemically Etched Screens," http://www.industrialnetting.com/be-0805.html (Accessed 28 March 2017).

[77] F.F.Chen, *Introduction to Plasma Physics and Controlled Fusion Volume 1: Plasma Physics*, 2nd Ed., Plenum Press, New York, 1974, pp. 1-43.

[78] Azziz, Y., "Experimental and Theoretical Characterization of a Hall Thruster Plume," Ph.D. Dissertation, Dept. of Aeronautics and Astronautics, Massachusetts Institute of Technology, Boston, MA, 2007, pp. 59-67.

[79] Brown, "Investigation of Low Discharge Voltage Hall Thruster Characteristics and Evaluation of Loss Mechanisms," Ph.D. Dissertation, Aerospace Engineering Dept., Univ. of Michigan, Ann Arbor, MI, 2009, pp. 104-172.

[80] Beal, B. and Gallimore, G., "Energy Analysis of a Hall Thruster Cluster," *28th International Electric Propulsion Conference*, Electric Rocket Propulsion Society, IEPC Paper 2003-035, Toulouse France, 2003.

[81] Walker, M. L. R., Victor, A. L., Hofer, R. R., and Gallimore, A. D., "Effect of Backpressure on Ion Current Density Measurements in Hall Thruster Plumes," *Journal of Propulsion and Power*, vol. 21, 2005, pp. 408–415.

[82] Frieman, J. D., Liu, T. M., Walker, M. L. R., Makela, J. M., Mathers, A., and Peterson, P. Y., "Performance Evlauation of the T-40 Low-Power Hall Current Thruster," *52nd AIAA/SAE/ASEE Joint Propulsion Conference*, American Institute of Aeronautics and Astronautics, AIAA 2016-4833, Salt Lake City, UT, 2016.

[83] Demidov, V. I., Ratynskaia, S. V., and Rypdal, K., "Electric Probes for Plasmas: The Link between Theory and Instrument," *Review of Scientific Instruments*, Vol. 73, No. 10, 2002, pp. 3409-3439.

[84] Albarède, L., Lago, V., Lasgorceix, P., Dudeck, M., Bugrova, A.I., and Malik, K., "Interaction of a Hollow Cathode Stream with a Hall Thruster," *28th International Electric Propulsion Conference*, Electric Rocket Propulsion Society, IEPC Paper 2003-333, Toulouse France, 2003.

[85] Jakubowski, A.K., "Effect of Angle of Incidence on the Response of Cylinderical Electrostatic Probes at Supersonic Speeds," *AIAA Journal*, Vol. 10, No. 8, 1972, pp. 988-995.

[86] Kim, S., "Experiemtnal Investigations of Plasma Paramters and Species-Dependent Ion Energy Distribution in the Plasma Exhaust Plume of a Hall Thruster," Ph.D. Dissertation, Aerospace Engineering Dept., Univ. of Michigan, Ann Arbor, MI, 1999, pp. 27-37.

[87] Sheehan, J.P., and Hershkowitz, N., "Emissive probes," *Plasma Sources Science and Technology*, Vol. 20, No. 6, 2011, Paper 063001.

[88] Langendorf, S., "Effects of Secondary Electron Emission on the Plasma Sheath," Aerospace Engineering Dept., Georgia Institute of Technology, Atlanta, GA, 2015, pp. 64-73.

[89] Hofer, R. R., and Gallimore, A. D., "The Role of Magnetic field Topography in Improving the Performance of High-Voltage Hall Thrusters," *38th AIAA Joint Propulsion Conference*, American Institute of Aeronautics and Astronautics, AIAA Paper 2002-4111, Indianapolis, IN, 2002.

[90] Hughes, P. C., and Leeuw, J. H., "Theory for the Free Molecule Impact Probe at an

Angle of Attack," *Rarefied Gas Dynamics: Proceedings of the Fourth International Symposium on Rarefied Gas Dynamics*, Academic Press, Vol. 1, pp. 653-676, 1965.

[91] Mikellides, I. G., Katz, I., Hofer, R. R., and Goebel, D. M., "Magnetic Shielding of a Laboratory Hall Thruster. I. Theory and Validation," *Journal of Applied Physics*, Vol. 115, 2014, Paper 043303.

[92] McVey, J., Britt, E., Engelman, S., Gulczinski, F., Beiting, E., Pollard, J., and Cohen, R., "Characteristics of the T-220 HT Hall-Effect Thruster," *39th AIAA/ASME/SAE/ASEE Joint Propulsion Conference & Exhibit*, American Institute of Aeronautics and Astronautics, AIAA Paper 2003-5158, Huntsville, AL, 2003.

[93] Hofer, R., "High-Specific Impulse Hall Thrusters, Part 1: Influence of Current Density and Magnetic Field," *Journal of Propulsion and Power*, Vol. 22, No. 4, 2006, pp. 721–731.

[94] Azziz, Y., Martinez-Sanchez, M., and Szabo, J., "Determination of In-Orbit Plume Characteristics from Laboratory Measurements," *42nd AIAA/ASME/SAE/ASEE Joint Propulsion Conference and Exhibit*, American Institute of Aeronautics and Astronautics, AIAA Paper 2006-4484, Sacramento, California, 2006.

[95] Lobbia, R. B., "A Time-resolved Investigation of the Hall Thruster Breathing Mode," Ph.D. Dissertation, Aerospace Engineering Dept., Univ. of Michigan, Ann Arbor, MI, 2010, pp. 96-145.

[96] Devore, J.L., *Probability and Statistics for Engineering and the Sciences*, Cengage Learning, Boston, MA, 2011, pp. 508-510.

[97] Sommerville, J. D., and King, L. B., "Hall-Effect Thruster--Cathode Coupling, Part I: Efficiency Improvements from an Extended Outer Pole," *Journal of Propulsion and Power*, Vol. 27, No. 4, pp. 744–753, 2011.

[98] Scharfe, M. K., Thomas, C. A., Scharfe, D. B., Gascon, N., Cappelli, M. A., and Fernandez, E., "Shear-Based Model for Electron Transport in Hybrid Hall Thruster Simulations," *IEEE Transactions on Plasma Science*, Vol. 36, No. 5, 2008, pp. 2058–2068.

[99] Meezan, N. B., Hargus, W. A., and Cappelli, M. A., "Anomalous Electron Mobility in a Coaxial Hall Discharge Plasma," *Physical Review E - Statistical, Nonlinear, and Soft Matter Physics*, Vol. 63, 2001, Paper 026410.

[100] Fossum, E. C., and King, L. B., "Design and Construction of an Electron Trap for Studying Cross- Field Mobility in Hall Thrusters," *43rd AIAA/ASME/SAE/ASEE Joint Propulsion Conference and Exhibit*, American Institute of Aeronautics and Astronautics, AIAA Paper 2007-5207, Cincinnati, OH, 2007.

[101] Smith, A. W., and Cappelli, M. A, "Single Particle Simulations of Electron Transport in the Near-Field of Hall thrusters," *Journal of Physics D: Applied*

Physics, Vol. 43, No. 4, 2010, Paper 45203.

[102] Jorns, B. A., Lopez-Ortega, A., and Mikellides, I. G., "First-principles Modelling of the IAT-driven Anomalous Resistivity in Hollow Cathode Discharges I : Theory," *52nd AIAA/SAE/ASEE Joint Propulsion Conference*, American Institute of Aeronautics and Astronautics, AIAA Paper 2016-4626, Salt Lake City, OH, 2016.

[103] Tilley, D., de Grys, K., and Myers, R., "Hall Thruster-Cathode Coupling," *35th AIAA/ASME/SAE/ASEE Joint Propulsion Conference and Exhibit*, American Institute of Aeronautics and Astronautics, AIAA Paper 1999-2865, Los Angeles, CA, 1999.

[104] Zill, D. G., and Wright, W. S., *Advanced Engineering Mathematics*, Jones and Bartlett Learning, Burlington, MA, 2014, pp. 744-773.

[105] Huang, W., Kamhawi, H., and Haag, T. W., "Plasma Oscillation Characterization of NASA's HERMeS Hall Thruster via High Speed Imaging," *52nd AIAA/SAE/ASEE Joint Propulsion Conference*, American Institute of Aeronautics and Astronautics, AIAA Paper 2106-4829, Salt Lake City, OH, 2016.

[106] Fife, J., Martinez-Sanchez, M., and Szabo, J., "A Numerical Study of Low-Frequency Discharge Oscillations in Hall Thrusters," *33rd AIAA/ASME/SAE/ASEE Joint Propulsion Conference and Exhibit*, American Institute of Aeronautics and Astronautics, AIAA Paper 1997-3052, Seattle, WA, 1997

[107] Jorns, B. A., and Hofer, R. R., "Plasma Oscillations in a 6-kW Magnetically Shielded Hall thruster," *Physics of Plasmas*, Vol. 21, No. 5, 2014, pp. 1–20.

[108] Huang, W., Kamhawi, H., and Haag, T., "Facility Effect Characterization Test of NASA's HERMeS Hall Thruster," American Institute of Aeronautics and Astronautics, AIAA Paper 2106-4828, Salt Lake City, OH, 2016.

[109] Halbach, C. R., Hill, C. S., and Yoshida, R. Y., "Life Test Summary and High-Vacuum Tests of 10-mlb Resistojets," *Journal of Spacecraft and Rockets*, Vol. 8, No. 4,1971, pp. 1970–1972.

[110] Donovan, J., Lord, W., and Sherwood, P., "Fabrication and Preliminary Testing of a 3 kW Hydrogen Resistojet," *9th Electric Propulsion Conference*, American Institute of Aeronautics and Astronautics, AIAA Paper 1972-449, Bethesda, MD, 1972.

[111] Sovey, J. S., Penko, P. F., Grisnik, S. P., and Whalen, M. V., "Vacuum Chamber Pressure Effects on Thrust Measurements of Low Reynolds Number Nozzles," *Journal of Propulsion and Power*, Vol. 2, No. 5, 1986, pp. 385–389.

[112] de Grys, K., Welander, B., Dimicco, J., Wenzel, S., Kay, B., Khayms, V., and Paisley, J., "4.5 kW Hall Thruster System Qualification Status," *41st AIAA/ASME/SAE/ASEE Joint Propulsion Coference & Exhibit*, American Institute

of Aeronautics and Astronautics, AIAA Paper 2005-3682, Tucson, Arizona, 2005.

[113] de Grys, K., Rayburn, C., and Haas, J., "Study of Power Loss Mechanisms in BPT-4000 Hall Thruster," *39th AIAA/ASME/SAE/ASEE Joint Propulsion Conference and Exhibit*, American Institute of Aeronautics and Astronautics, AIAA Paper 2003-5277, Huntsville, AL, July, 2003.